Experimental study on the thermodynamic interactions of phonons and magnetism in Fe systems

Thesis by
Stefan P. Hägeli Lohaus

In Partial Fulfillment of the Requirements for the
Degree of
Doctor of Philosophy

CALIFORNIA INSTITUTE OF TECHNOLOGY
Pasadena, California

2023
Defended May 5, 2023

Stefan P. Hägeli Lohaus

ORCID: 0000-0002-4430-3834

Acknowledgements

I want to start by thanking my advisor Brent Fultz. I'm grateful for all the insightful conversations, the advice, and the scientific rigor, while keeping a sense of lightness and calmness. Your precise balance of trust and intervention guided me through my PhD journey and allowed me to grow into the scientist I am today. I'm deeply thankful for that.

Special thanks to my thesis committee, Kathy Faber, Bill Johnson, Ercan Alp, and Valerie Scott. I had the pleasure of interacting often with Bill and Ercan in the past years, two incredibly passionate scientists who master the art of combining scientific rigor with playfulness. I always walk out inspired from our conversations. Kathy and Valerie, thank you for the discussions and the encouragement throughout my thesis defense process. I also want to acknowledge my previous mentors essential in my journey: Chiara Daraio, who catapulted me into the academic life, and Sergio Pellegrino, who first embraced me here at Caltech.

It's hard to describe the kind of excitement, stress, and sleep deprivation involved in the experimental beamtimes in national facilities. A special kind of bond is created with the people who share this experience. I'm grateful to my fellow members of the Fultz group who joined me in my experiments, in particular Pedro Guzman and Camille Bernal. The beamline scientists at the Advanced Photon Source were also essential during these times. I want to thank the staff at HPCAT, in special Guoyin Shen, and all the members of Sector 3: Jiyong Zhao, Barbara Lavina, Michael Hu, and Ercan.

I had the pleasure of sharing my years at Caltech with a handful of incredible people. I'm so grateful for the support and love from my friends Lucia de Rose, Claire Saunders, and Camille Bernal. Thank you for being with me and believing in me even when I couldn't myself.

I left home a long time ago, and only made it through this point with the help from my friends and family back home. To my Mom and Dad, Karla and Volker, I'm deeply grateful for your love and for always supporting my decisions, even when I choose to live across the world from you. To my incredible brother Thomas, and his beautiful family, I feel so embraced, safe, and at peace around you. Thank you.

I also don't underestimate the support that my therapist provided during this time in my life, particularly leading to compiling this thesis.

Lastly, none of this would be possible without funding. Basic science, so essential for the future of our world, costs (a lot of) money and relies on public investment. Resources from the National Science Foundation (NSF), under grant no. 1904714, funded most of the work presented in this thesis. The work presented in Chapter 3 was funded by the Department of Energy (DOE), under the grant DE-FG02-03ER46055. Experiments were performed at the Advanced Photon Source, a DOE Office of Science user facility operated by the Argonne National Laboratory. Neutron scattering measurements used the Spallation Neutron Source, yet another DOE user facility operated by the Oak Ridge National Laboratory.

Abstract

The macroscopic thermophysical behavior of materials is governed by their atomic level excitations and how they store heat. Most of the thermal energy excites oscillations of the atoms, quantized as phonons, but in magnetic materials a considerable amount of heat is also absorbed by fluctuations of the electronic spins. This thesis explores the thermodynamics of phonons and magnetic spins in Fe-systems: we investigate the coupling between these excitations in Fe, Fe-Ni, and Fe-C, quantify their size dependency in nanocrystalline in Ni_3Fe, and assess their individual roles in the anomalous thermal expansion of Fe-Ni Invar.

Most materials expand when heated due to enhanced atomic oscillations. However, in 1895 C.E. Guillaume combined Fe and Ni to discover a material with near-zero thermal expansion, called *Invar*. This discovery was awarded the 1920 Physics Nobel Prize and sparked thousands of scientific investigations. Since the anomalous Invar effect is associated with magnetism, nearly all studies have focused on the electronic and spin structure of Fe-Ni. But phonons are needed to complete the picture, and to date, the anomalous Invar behavior is not fully understood. Here, we explore a method for measuring thermal expansion that is capable of isolating contributions from phonons and spins. Since the thermal energy of materials is related to entropy, the thermal expansion can be indirectly determined through individual entropic contributions by using a Maxwell relation. The phonon and magnetic entropies were measured by combining two nuclear resonant x-ray scattering techniques, with samples under pressure in diamond-anvil cells. We show that the Invar behavior stems from a competition between phonons and spins, that oppose each other for near-zero thermal expansion. A spin-phonon coupling improves the precision of this cancellation, extending the range of Invar behavior.

Such a coupling of phonons and spin was also observed in pure Fe and Fe_3C cementite, as their phonon energies correlate to the change in magnetization. This motivated us to develop a magnetic quasi-harmonic model for Fe and Fe_3C, which accounts well for the deviation of phonon energies from pure volumetric effects of the conventional quasi-harmonic approximation.

The thermodynamics of materials is also affected by the size of their crystallites. We determined the size effects on the heat absorption by phonons, electrons, and spins in nanocrystalline Ni_3Fe. All excitations become enhanced in the nanomaterial. In particular, the redistribution of spectral weights amplifies the phonon entropy. This helps stabilize the nanostructure against the enthalpy from its extra grain boundaries. However, the nanostructure is metastable, and the grains will grow into their bulk counterpart when diffusion is enabled at elevated temperatures.

Published Content and Contributions

[1] P. Guzman, C. M. Quine, **S. H. Lohaus**, R. Toda, V. J. Scott, L. Schul, and B. Fultz, "A miniatuarized piezoelectric Mössbauer spectrometer with feedback control", Under review in Rev. Sci. Instrum.,
S.H.L. helped with experiments, provided intellectual input, and contributed to the manuscript.

[2] **S. H. Lohaus**, M. Heine, P. Guzman, C. M. Bernal-Choban, C. N. Saunders, G. Shen, O. Hellman, D. Broido, and B. Fultz, "A thermodynamic explanation of the Invar effect", Accepted for publication in Nat. Phys. (2023),
S.H.L. planned and performed experiments, analyzed the data, compiled and wrote the manuscript.

[3] C. N. Saunders, V. Ladygin, D. S. Kim, C. M. Bernal-Choban, **S. H. Lohaus**, G. E. Granroth, D. L. Abernathy, and B. Fultz, "Diffuse Inelastic Neutron Scattering from Anharmonic Vibrations in Cuprite", Under review in Phys. Rev. Lett. (2023),
S.H.L. provided intellectual input and contributed to the manuscript.

[4] H. L. Smith, C. N. Saunders, C. Bernal-Choban, **S. H. Lohaus**, C. J. Stoddard, L. K. Decker, J. Lin, J. L. Niedziela, D. Abernathy, J.-H. Na, M. D. Demetriou, and B. Fultz, "Vibrational dynamics in the undercooled liquid of ultra-fragile metallic glasses", Materialia **27**, 101710, 10.1016/j.mtla.2023.101710 (2023),
S.H.L. participated in the neutron scattering experiments, analyzed data, and contributed to the manuscript.

[5] **S. H. Lohaus***, L. Mauger*, and B. Fultz, "The temperature dependence of nuclear resonant X-Ray spectra of magnetic iron and cementite", Hyperfine Interact. **243**, 1, 10.1007/s10751-021-01750 (2022),
S.H.L. analyzed the data, developed the model, compiled and wrote the manuscript.

[6] C. N. Saunders, D. S. Kim, O. Hellman, H. L. Smith, N. J. Weadock, S. T. Omelchenko, G. E. Granroth, C. M. Bernal-Choban, **S. H. Lohaus**, D. L. Abernathy, and B. Fultz, "Thermal expansion and phonon anharmonicity of cuprite studied by inelastic neutron scattering and ab

initio calculations", Phys. Rev. B **105**, 1, 10.1103/PhysRevB.105.174308 (2022),
S.H.L. performed XRD experiments, and contributed to the manuscript.

[7] **S. H. Lohaus**, M. B. Johnson, P. F. Ahnn, C. N. Saunders, H. L. Smith, M. A. White, and B. Fultz, "Thermodynamic stability and contributions to the Gibbs free energy of nanocrystalline Ni_3Fe", Phys. Rev. Mater. **4**, 086002, 10.1103/PhysRevMaterials.4.086002 (2020),
S.H.L. performed experiments, analyzed the data, compiled and wrote the manuscript.

TABLE OF CONTENTS

Chapter 1

Introduction

The development and discovery of materials go hand-in-hand with human development. The naming of entire periods of time as 'Stone Age', 'Bronze Age', 'Iron Age', and the more recent 'Steel Age' are obvious reflections of that. The actual study of materials was born from the development of ceramics and metallurgy, however Materials Science did not become a rigorous inductive science until the late 19th century with the emergence of thermodynamics by Josiah Willard Gibbs. Together with James Clerk Maxwell and Ludwig Boltzmann, he also developed the field of statistical mechanics, which connected macroscopic picture of thermodynamics to the microscopic world. It is incredible that this rigorous connection to the 'micro' appeared even before the development of the atomic models, including J. J. Thomson's 'plum pudding', Rutherford's, and Bohr's models. Quantum mechanics revolutionized the study of the atomic scale, creating theories and developing a language to describe the different microscopic excitations from electrons, their spins, and phonons, for example. The connection to the 'macro' still relies on the statistical models from the 19th century, but through quantum mechanics, the 'micro' gained a renewed physical significance.

The ability to look at different scales, from atomic to macroscopic properties, makes Materials Science extremely powerful. It led to the development of sophisticated alloys, nanomaterials, energy-storage materials, ceramics, composite polymers, biomaterials, and in particular, the understanding of carbon and silicon enabled semiconductor technology, having profound implications on human civilization. We are now in the 'Silicon Age'.

On the macroscopic side, engineered applications and designs rely on the knowledge of the material properties (mechanical, electronic, magnetic, and

optical). Take the thermal expansion, for example. It describes how the volume of material changes with temperature. It is an important property for designing large metallic structures, for example, like bridges, railroads, pipelines, and power lines, since those have to maintain their structural integrity at a range of temperatures. It is also essential in medical and scientific instruments that need to be precise at different temperatures. The temperature dependence of the volume has everything to do with how the heat is absorbed in the atomic scale in the material. When heated, the thermal energy is transferred to a material in the form of vibrations of the atomic nuclei called phonons, to excitations of electrons, and their magnetic spins. And the exact amount of energy that goes into each of those different excitations dictates the overall thermal expansion. A fundamental microscopic understanding of materials allows to tune their properties for different applications. Most materials expand when heated, however some can also contract, or by mixing different types of atoms at specific proportions, materials with no thermal expansion can be created.

While all scales of Materials Science, from quantum to practical engineering applications, are essential, I am particularly interested in the bridge from the micro to the macro scale. Observing the quantum world of phonons and magnetic spins, and translating them into the macroscopic language of thermodynamics is fascinating. It also reflects the reverse course of my personal academic path, from a mechanical engineer into a materials physicist. This thesis is a snapshot of my personal understanding and contribution to the field of Materials Science, through an experimental study of phonons and their interactions with magnetism in transition metals, explaining thermophysical properties via a thermodynamic lens.

This thesis studies different magnetic transition metals. In these materials, thermal energy is absorbed and stored mainly in three forms: as lattice vibrations (or phonons), as electronic excitations, and as excitations of magnetic spins. We first look at nanocrystalline Ni_3Fe (Chapter 3), to study how these three different excitations contribute to the free energy and the thermodynamic stability, and how they are dependent on the size of the crystalline structure. We then explore iron and cementite (Fe_3C) in Chapter 4, to see how the excitations from lattice vibrations and magnetic spins can be coupled and dependent on each other. Such interactions of spins with phonons can re-

sult in an anomalously low thermal expansion, know as the *Invar* effect. The main part of this thesis (Chapter 5) looks into the Invar effect, and how the thermal expansion in $Fe_{65}Ni_{35}$ is affected by vibrational and magnetic degrees of freedom, as well as their coupling.

But first, we continue this introductory chapter with the 'micro', looking at the bonding between atoms in transition metals, and the different excitations that exist at a quantum-mechanical level. We then focus on phonons and magnetism and move from the atomistic behavior into a thermodynamic description. The thermal expansion is explored at a qualitative level, by looking at the individual contributions to the entropy from phonons, electrons and spin. This chapter is concluded with a discussion of the phase diagram of iron, which offers a great example of effects from lattice vibrations, magnetism, and their coupling to the phase stability of materials.

1.1 Metallic bonding and structure

Atoms are comprised by a small nucleus with most of the atomic mass, and an essentially massless electronic cloud around them. When different atoms are brought together in a condensed matter system, they exert forces on each other through the electrons. It is usually energetically favorable for atoms to stick together, so they end up forming molecules and materials. Metallic atoms usually form large periodic crystals, and prefer a tight packing of atoms. Since the forces between atoms are dictated by electrons, to understand the bonding in metals, we need to look into their electronic structure.

Quantum mechanics provides analytical solutions for the distribution of electrons (or wavefunctions) for isolated atoms. In condensed matter systems, the electronic distribution is different, but a lot can be understood from the wavefunctions of free atoms. Transition metals are known for having d orbitals that are only partially filled by electrons. Take nickel, for example, with the valence electronic structure: $4s^2\,3d^8$. The s orbital is full, but only 8 out of 10 possible electrons occupy the d orbital. The wavefunction $\psi(r,\theta)$ describing its distribution of electrons, can be separated in radial and angular components $\psi(r,\theta) = R(r) \cdot Y(\theta)$. The former describes the amplitude of the distribution as we move away from the nucleus, and the latter the shape of the orbitals. Both are shown in Fig. 1.1.

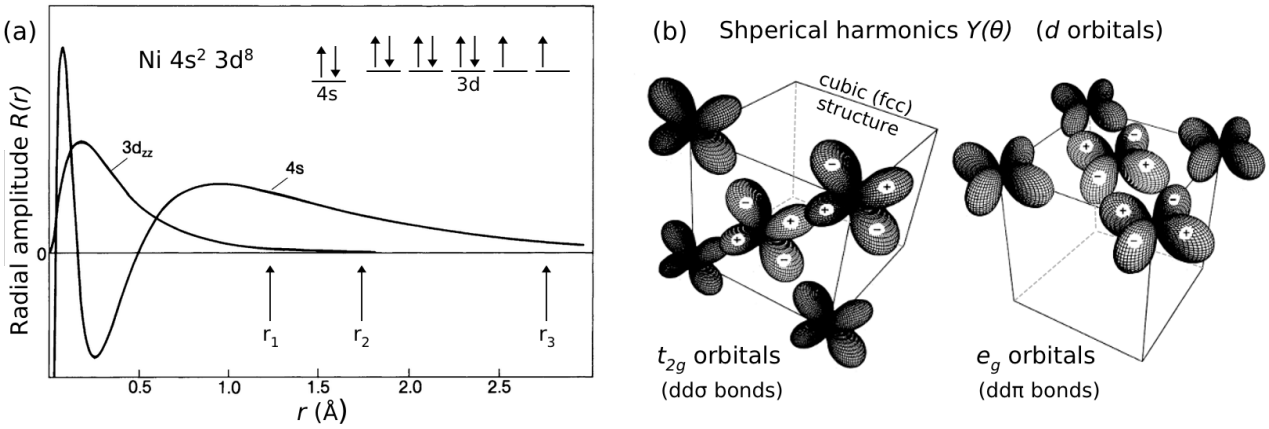

Figure 1.1: Electronic wavefunction of fcc transition metals. **(a)** Radial distribution of the $3d_{zz}$ and $4s$ wavefunctions of an isolated Ni atom [1]. The electronic configuration of the valence shell of Ni has two unpaired electrons in the d shell. Arrows mark the half-distances to the first, second and third nearest neighbors (r_1, r_2 and r_3) [1]. **(b)** Spherical harmonics of the t_{2g} and e_g orbitals of d electrons. They are overlaid at the atomic positions of an fcc crystal structure, showing their bonding directions [2].

The amplitude of the $4s$ orbital in (Fig. 1.1 a) is large close to the nucleus near $r = 0$, but a second node extends far into the material, at least up to the 3rd nearest neighbor. This results in a substantial overlap of wavefunctions of neighboring atoms, reducing their energies compared to isolated atoms. The s orbital takes, therefore, an important role in the bonding energy [3]. On the other hand, the $3d$ orbitals are more localized, they only have a single node and are concentrated relatively close to the nucleus. These orbitals are less affected when the atom is placed in a solid. Since they are only partially occupied, the unpaired electrons in the $3d$ orbitals result in a net magnetic moment and are the source of magnetism in transition metals (see the electronic configuration of Ni in Fig. 1.1 a with two unpaired 'spin-up' electrons).

The $3d$ electrons have a smaller contribution to the bonding energy, but unlike the radially symmetric $4s$ orbitals, d orbitals are directional as shown in Fig. 1.1 b. They form a covalent-like framework that dictates the structure of transition metals. Nickel, for example, is stable in a face-centred cubic (fcc) structure. This arrangement of atoms directly reflects the directions of the orbital lobes of the $3d$ shell, which becomes clear when overlaying t_{2g} orbitals on the fcc structure, for example. These orbitals point towards each other and overlap, which reduces their energy to form $dd\sigma$ bonds between the atoms. The e_g orbitals have a different orientation, forming $dd\pi$ bonds.

Similar geometric arguments can result in another common structure of transition metals, the body-centered cubic (bcc) crystal. The electronic orbitals need somewhat more space in the bcc structure, resulting is larger local volumes compared to fcc. Metallic bonding usually favours the closest possible spherical packing of atoms [4], since it results in larger overlaps of the wavefunctions and stronger bonding (especially because of the radially symmetric s orbitals responsible for most of the bonding energy). The fcc configuration is therefore often preferred, but as discussed below, phonons and magnetism also interfere with the bonding energy, and can cause the bcc phase to become stable.

1.2 Elementary excitations

The microscopic excitations in condensed matter systems can be studied by shooting a probing particle with different energies on a material and observing which energies are absorbed. Absorption implies that energy is being transferred into internal excitations in the material. In experiments, x-rays (photons) or neutrons are usually used as probing particles. Figure 1.2 shows the energy range of the most important excitations in materials.

Starting at zero energy transfer in Fig. 1.2, the material does not exchange energy with the probing particle (elastic interaction). However, the specific

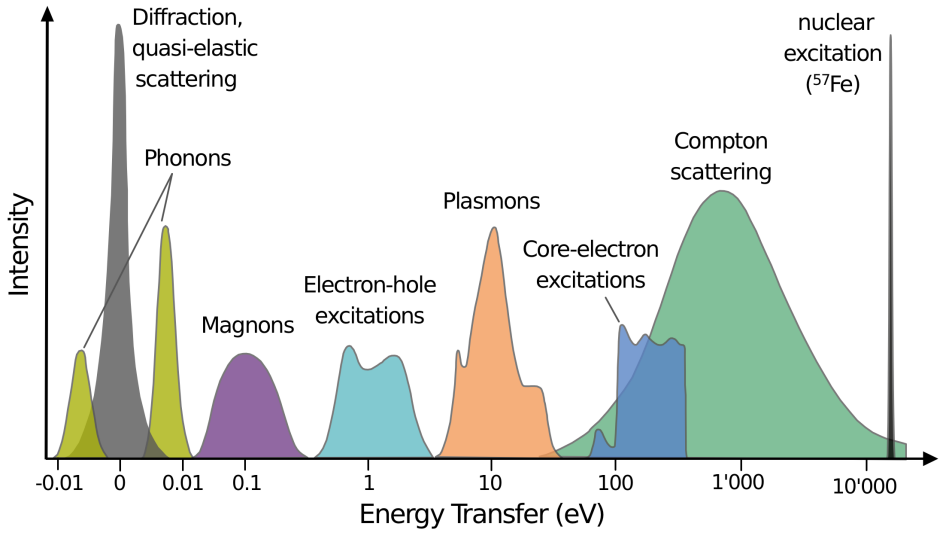

Figure 1.2: Approximate energy scales (on a logarithmic axis) of different elementary excitations in condensed matter systems. Adapted with permission from [5].

arrangement of atoms in the material can scatter the incoming radiation into different angles. Elastic diffraction gives, therefore, information about the atomic arrangement and the crystal structure of the sample.

Away from zero energy transfer, energy is actually absorbed by the material (inelastic scattering). In the meV range, it is absorbed in the form of oscillations of the atoms. These are called lattice vibrations, or phonons. In fact, most of the thermal energy in materials, $E = k_{\mathrm{B}}T$, is stored as phonons. Room temperature corresponds to roughly E=25 meV exactly at a the absorption range of phonon excitations. As discussed further below, about 80-90% of the thermal energy at room temperature goes into lattice vibrations. Phonons have absorption lines at both positive and negative energy transfers, since they can be excited by the probe, but also annihilated by losing energy to the probing particle. Since phonons need to already exist in the material for the latter to happen, phonon annihilation is less likely than the creation of a phonon, resulting in a lower intensity in the negative side of Fig. 1.2.

By increasing the energy transfer to around the 0.1 eV range, the electronic spins can be excited in the form of spin-waves, called magnons. Around 1 eV the electrons themselves can get excited into higher energy levels within the atoms. And several other types of excitations are possible at larger energies, like plasmons or completely knocking electrons out of the atoms (Compton scattering).

At even higher energies, in the keV range, we reach the nuclear excitations (depicted for iron at 14.41 keV). Nuclear states are very narrow in energy resulting in sharp absorption lines. While nuclear transitions are usually not important for the thermodynamics, they are relevant to the experimental techniques used in this thesis, as discussed in Chapter 2.

Lattice vibrations are the main focus of this work. Essentially all the mass of an atoms is focused in the point-like nucleus. The electronic cloud is over three orders of magnitude lighter, and therefore, move much faster than the nuclei. In the Born-Oppenheimer approximation, inter-atomic forces are assumed to respond instantaneously to nuclear displacements. This allows us to treat electronic excitations and nuclear vibrations independently. As we will see, however, they are not truly independent, and their interactions can have significant thermodynamic effects. For instance the energy between electronic spins depend on the local volumes through exchange interactions. Atomic dis-

placements of phonons cause the volume to fluctuate, which in turn affects the exchange energies of spins, and vice-versa.

In the remainder of this chapter we will look into phonon excitations, starting from from their quantum mechanical character up to their macroscopic average. We then turn to the electronic spins and their magnetic effects in materials, from micro to macro. Thermodynamics binds both these excitations into a theory that can predict macroscopic thermophysical properties, such as thermal expansion.

1.3 Phonons

Atoms are not static, they vibrate around their equilibrium positions in the lattice. This is pictured in Fig. 1.3 a with the electronic forces between nuclei represented by springs. In quantum mechanics, the lattice vibrations are quantized as 'phonons' of energy $\varepsilon = \hbar\omega$, where ω is the angular frequency of the oscillation and $\hbar$ the Planck constant. The stronger the atoms vibrate, corresponding to larger amplitudes in the classical world, the more phonons are excited in the quantum picture. What is completely new with respect to classical world is that even at 0 K, phonons still exist in materials, corresponding to a zero-point energy [6] ($E_0 = \hbar\omega/2$ for a harmonic oscillator).

The nuclei do not vibrate isolated from their neighbors, the forces in between them cause oscillatory waves to propagate in the material (see Fig. 1.3 b).

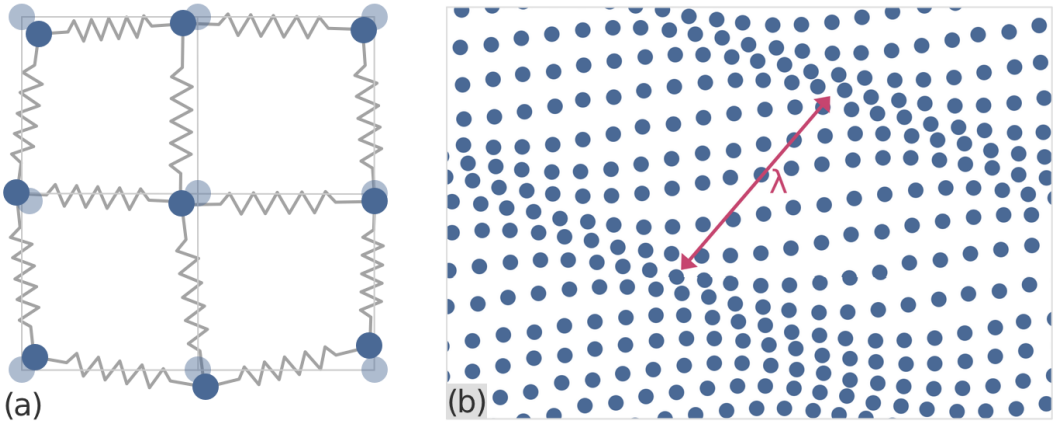

Figure 1.3: Phonon vibrations of a lattice. **(a)** Representation of atomic displacements from their equilibrium positions on a square lattice. Springs correspond to the forces between nuclei. **(b)** Collective oscillation of nuclei propagating as phonon waves in the lattice with wavelength λ.

Phonon constitute therefore a collective motion of the nuclei, and are classified as 'quasi-particles', as opposed to particles that can exist isolated. They are bosons because there is no limit on the amount of phonons that can exist at the same energy. In fact, most phonons in a material occur at low energies. The statistical Planck distribution $n(\varepsilon, T)$ (plotted further below in Fig. 1.5) represents the probability of a phonon of energy ε being excited at a certain temperature T. It is more probable to excite a lower energy phonon, but as the temperature is increased, higher vibrational frequencies can be reached, changing the energy distribution of phonons.

Harmonic model

The phonon waves can be modeled by a Born-von Kármán model [7], assuming nuclear masses that are connected by massless electronic 'springs' as in Fig. 1.3 a. Within the Born-Oppenheimer approximation, the nuclear motion is independent from the electrons. The Hamiltonian for the nuclei in a lattice with l atoms becomes [7, 8]:

$$H = -\sum_{l} \frac{\mathbf{p}_l^2}{2m_l} + V \tag{1.1}$$

where the first term is the kinetic energy of an atom of mass m_l and momentum $\mathbf{p}_l$. Transition metals form periodic crystals, so the equilibrium coordinates of all the atoms are multiples of the basis vectors, that describe the location the primitive unit cells:

$$\mathbf{l} = l_1\mathbf{a_1} + l_2\mathbf{a_2} + l_3\mathbf{a_3}\,. \tag{1.2}$$

Phonons describe the oscillations of nuclei out of their equilibria, so the actual atomic positions are

$$\mathbf{r}_l = \mathbf{l} + \mathbf{u}(l)\,, \tag{1.3}$$

and $\mathbf{u}(l)$ describes the deviation from the equilibrium position of the lth atom. Here we assumed one atom per unit cell (as is the case for pure metals or random solid solutions in a cubic structure). If there were more than one atom, Eq. 1.3 could be expanded to $\mathbf{r}_{lm} = \mathbf{l} + \mathbf{m} + \mathbf{u}(lm)$, where $\mathbf{m}$ describes the coordinate of the mth atom in the unit cell.

The kinetic energy can be rewritten as:

$$\frac{1}{2}\sum_{\alpha,l} m_l \left(\frac{\partial u_\alpha(l)}{\partial t}\right)^2 \tag{1.4}$$

where the spacial coordinates are given by $\alpha = x, y, z$.

The displacements out of equilibrium are small, so the potential energy V can be expanded in a Taylor series as

$$V = V_0 + \sum_{\alpha,l} \Phi_\alpha(l) u_\alpha(l) + \sum_{\alpha,l} \sum_{\beta,l'} \Phi_{\alpha\beta}(l,l') u_\alpha(l) u_\beta(l') + \dots , \tag{1.5}$$

with

$$\Phi_\alpha(l) = \left. \frac{\partial V}{\partial u_\alpha(l)} \right|_0 , \tag{1.6}$$

$$\Phi_{\alpha\beta}(l,l') = \left. \frac{\partial^2 V}{\partial u_\alpha(l) \partial u_\beta(l')} \right|_0 . \tag{1.7}$$

We set $V_0 = 0$ for the equilibrium conditions. The potential needs to be symmetric, otherwise the forces do not disappear at the equilibrium and the atoms would move. So the first derivative also vanishes: $\Phi_\alpha(l) = 0$.

If the nuclei displacements are small, we can approximate the bottom of their potential wells with parabolic potentials, and ignore higher order terms ($\sim \mathcal{O}^3$) of the Taylor expansion. This gives the harmonic model. Atomic nuclei are treated like oscillators with harmonic springs in between them, with spring forces that are proportional to the atomic displacements. In the harmonic approximation, Newton's law leads to a set of second-order differential equations. For the lth atom they are

$$m_l \frac{\partial^2 u_\alpha(l)}{\partial t^2} = - \sum_{\beta,l'} \Phi_{\alpha\beta}(l,l') u_\beta(l') . \tag{1.8}$$

Solutions have the form of plane waves with j normal modes. Each vibrational mode has angular frequency ω_j and propagates with a wavevector $\mathbf{k}$. The displacement of a nucleus in the lattice with N atoms is given by

$$u_\alpha(l) = \sum_{\mathbf{k},j} \sqrt{\frac{2\hbar}{N m_l \omega_j(\mathbf{k})}} \tilde{u}_\alpha(\mathbf{k}j) \mathrm{e}^{i[\mathbf{k}\cdot\mathbf{l} - \omega_j(\mathbf{k})t]} . \tag{1.9}$$

The displacements of the nuclei result, therefore, in a collective motion of all atoms in the lattice that propagates as waves. For materials with one atom per unit cell, there are three phonon modes ($j = 1, 2, 3$). In normal coordinates the polarization of the atomic oscillations $\tilde{u}(\mathbf{k}j)$ are either transverse to

the wave propagation direction **k** (there are two such transverse modes), or along the propagation direction, corresponding to a longitudinal mode. These correspond to shear and compression waves, or sound waves that propagate in the material, and are therefore referred to as acoustic phonon modes. They have different sound velocities, as compression waves propagate faster than shear ones.

Additional coordinates exist if there are more than one atom per unit cell. With m atoms per cell, the number of modes scales as $3m$, and three additional optical modes exists in systems with two atoms per cell, for example.

By ignoring higher order terms of the potential, the harmonic models assumes that different modes do not interact with each other. In a quantum picture this means that phonons are independent and cannot exchange energy with each other through scattering. The vibrational frequencies ω_j remain unchanged (even with increasing temperature) and phonons have infinite lifetimes. This is a good first-order approximation and allows an analytical theoretical treatment of phonons as independent modes. Real materials however, do not behave like this. Phonons energies change with temperature. They scatter on defects, interact with each other, and exchange energy with electrons and electronic spins. These can often be treated as small perturbations. As we will see further below, however, interactions of phonons with other excitations can have significant effects.

Phonon dispersion and density of states

Phonon waves have dispersion relations, since the vibrational energies depend on the propagation direction. This can be visualized by plotting the phonon energy (or frequency) as a function of their momentum Q. For simplicity these are usually plotted only in specific high symmetry directions of the crystal structure. Fig. 1.4 b shows such a dispersion of phonons in Fe-Ni Invar. Three different branches, corresponding to the two transverse and the longitudinal modes can be seen. Longitudinal phonons reach larger energies and propagate faster (larger slopes near Γ) than transverse phonons.

Inelastic neutron scattering experiments can measure dispersion relations (overlaid in Fig. 1.4 b as markers). These experiments are performed by shooting neutrons in specific directions of single crystalline samples and detecting the

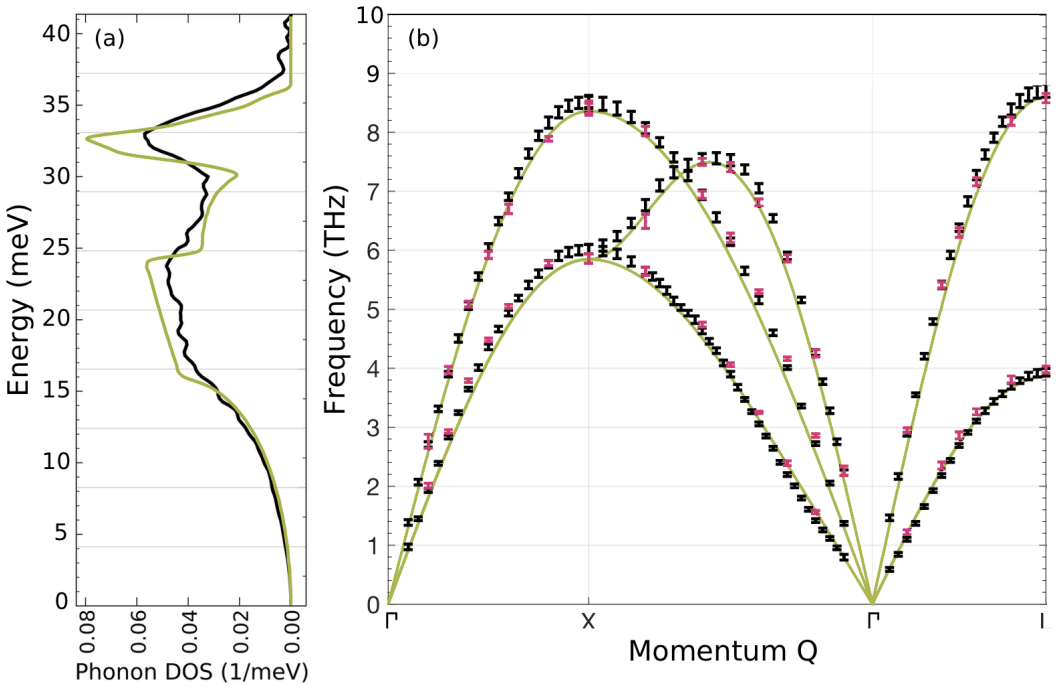

Figure 1.4: Phonon spectrum of $Fe_{65}Ni_{35}$ (Invar). **(a)** Phonon density of states (DOS) at ambient conditions. Black curve was experimentally determined through NRIXS (see Chapter 2), and green curve by integrating the calculated phonon dispersion of panel b over all momenta. **(b)** Phonon dispersion of along a few high symmetry momentum directions of the Brillouin zone. Solid line is from TDEP calculations (see Chapter 5). Markers are experimental data from inelastic neutron scattering (black markers from [9], and magenta are measurements on $Fe_{70}Ni_{30}$ [10]). Three phonon branches are seen. The maximum of each branch corresponds to large numbers of phonon states in a narrow energy range, resulting in peaks of the DOS (panel a).

energy and momentum transfer to the material as a function of the crystal orientation [11].

The energy spectrum of phonons, can be computed by integrating the phonon dispersions over all momenta (see Fig. 1.4 a). It gives the energy distribution of the lattice vibrations, or the relative number of phonon states available at a certain energy. It is therefore called the phonon density of states (DOS). By looking closely at Fig. 1.4 a some features of the different modes can be observed in the DOS. No phonons exist at zero energy, and they scale as ε^2 at low energies. Where the dispersion of the low transverse modes reach their maximum (around 4 THz at the L point), several phonon states are available, corresponding to the first 'peak' in the DOS (a Van Hove singularity). It is followed by a peak from the high transverse modes around 6 THz and a pronounce peak from the longitudinal vibrations around 8 THz. No phonons exist above approximately 9 THz or 37 meV.

Phonon statistics and Boltzmann entropy

The macroscopic behavior is the average of the atomistic excitations over large length scales and long time scales, and statistical mechanics offers tools for bridging over the scales. The key is Boltzmann's entropy relation:

$$S = k_{\mathrm{B}} \ln \Omega, \tag{1.10}$$

which relates number of microstates Ω to the entropy S (k_{B} is the Boltzmann constant). This relation is of astounding generality as it is simply a statistical model and works for any kind of microscopic excitation. All we need to figure out is the number of microstates or the number of ways that the internal coordinates can be arranged to give a thermodynamically equivalent macrostate. The entropy is a thermodynamic function that is often described as a measure of disorder, since it scales as (the logarithm of) the number of internal degrees of freedom. A state with larger entropy is more probable to occur, since there are more microscopic configurations that lead to that state.

For phonon excitations, we need to count the number of ways that phonons can be arranged into the different vibrational modes at a certain energy. For such a combinatoric treatment of phonons, we need to assume that each phonon is independent and does not interact with other modes, i.e., we assume a harmonic model. Let us say that there are N different modes (or oscillators) at a certain energy, and m phonons are excited into these different oscillators. Phonons are bosons so several phonons are able to occupy the same oscillator. Combinatorically, this raises the number of possible sites from N to $N + m$ (see [7]), and Ω becomes the number of ways to distribute m indistinguishable phonons into $N + m$ sites:

$$\Omega = \binom{N+m}{m} = \frac{(N+m)!}{N!\,m!}\,. \tag{1.11}$$

Using Stirling's approximation ($\ln x! \approx x \ln x - x$) we obtain the entropy for all oscillators at a certain energy:

$$S_{osc} = k_{\mathrm{B}} \left[(N+m)\ln(N+m) - N \ln N - m \ln m \right]\,. \tag{1.12}$$

The occupancy of each oscillator is the number phonons per number of oscillators $n = m/N$, so the entropy for each oscillator becomes

$$\frac{S_{osc}}{N} = k_{\mathrm{B}} \left[(1+n)\ln(1+n) - n \ln n \right]\,. \tag{1.13}$$

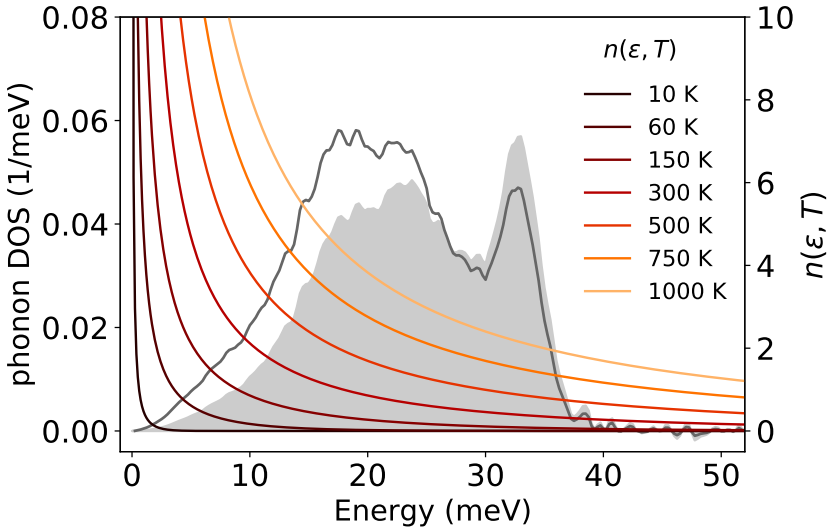

Figure 1.5: Phonon spectrum and occupation. left axis: phonon density of states $g(\varepsilon)$ measured for $Fe_{65}Ni_{35}$ at 300 K (shaded), and same DOS after weighting by the Planck distribution at 300 K (dark gray curve), corresponding to the integrand of Eq. 1.14. right axis: Planck distribution $n(\varepsilon, T)$ describing the occupation of phonon modes as a function of energy for different temperatures. Since more phonons exist at low energies (larger Planck distribution), the low energy portion of the phonon DOS has a larger weight when computing the entropy.

As discussed in the previous section, the energy distribution of phonons is given by the density of states, $g(\varepsilon)$, so the total phonon entropy of a material can be computed as [7, 12]

$$S_{ph} = 3k_{\mathrm{B}} \int_0^\infty g(\varepsilon) \left[(1 + n_T(\varepsilon)) \ln(1 + n_T(\varepsilon)) - n_T(\varepsilon) \ln n_T(\varepsilon) \right] \mathrm{d}\varepsilon \,, \quad (1.14)$$

where $g(\varepsilon)$ is normalized to 1, and the factor of 3 comes from the three spacial dimensions or polarization of the oscillations. The occupation of the phonon modes is given by the Planck distribution $n_T(\varepsilon)$, where the subscript T means that it is evaluated at a certain temperature. Even though Eq. 1.14 was derived from the harmonic model, when using experimentally determined $g(\varepsilon)$, it also includes nonharmonic effects to first order [12].

Since phonons are boson semi-particles, it is energetically favorable to excite low-energy phonons, and the Planck distribution is larger at lower energies as shown in Fig. 1.5 (right axis). As the temperature is increased, more phonons with higher energies can get excited, causing a shift of the Planck distribution. Figure 1.5 also visualizes the different pieces of Eq. 1.14: when phonon DOS (shaded, left axis) is weighted by the Planck distribution at 300 K it results in the gray solid curve. This weighted DOS corresponds to the function that

is integrated in Eq. 1.14 to compute the entropy. The takeaways is that since more phonons exist at lower energies (larger Planck distribution), the low energy portion of the DOS has a larger weight and a larger contribution to the entropy.

Physical interpretation of the phonon entropy

In context of atomic vibrations, the number of microstates of the Boltzmann entropy can be interpreted as the space explored by the nuclei while vibrating. The stronger the oscillations, the larger is the volume explored by the atoms and the greater the number of ways of finding the system [7]. The explored volume consists of a multi-dimensional hyperspace, with a spatial but also a momentum component.

Take a harmonic spring with an oscillator of mass m. The force F is proportional to the displacement u of the oscillator ($F = k\,u$, where k is the spring constant). The equation of motion becomes

$$m\ddot{u} + ku = 0 \qquad \rightarrow \qquad \omega = \sqrt{\frac{k}{m}}\,, \tag{1.15}$$

where ω is the resonant angular frequency of the oscillator. The potential energy can be calculated as $E_p = 1/2\,ku^2$. Now lets compare two different oscillators with the same potential energy,

$$\begin{aligned} k_1 u_1^2 &= k_2 u_2^2 \\ \frac{u_2}{u_1} &= \sqrt{\frac{k_1}{k_2}} = \frac{\omega_1}{\omega_2}\frac{\sqrt{m_1}}{\sqrt{m_2}}\,. \end{aligned} \tag{1.16}$$

There are three ways to control the displacement amplitudes (as pictured in Fig. 1.6). Weak spings with small spring constants (or weak interatomic force constants in a lattice), small masses, and low vibrational frequencies all result in a larger oscillation amplitudes. Similar arguments, through the kinetic energy, result in the same dependencies for the momentum (see [7]). The difference in vibrational entropy between the two oscillators, taken at the high temperature limit for simplicity, is [7]

$$S_2 - S_1 = k_\mathrm{B} \ln\left(\frac{\omega_1}{\omega_2}\right)\,. \tag{1.17}$$

The entropy difference scales inversely with the frequency.

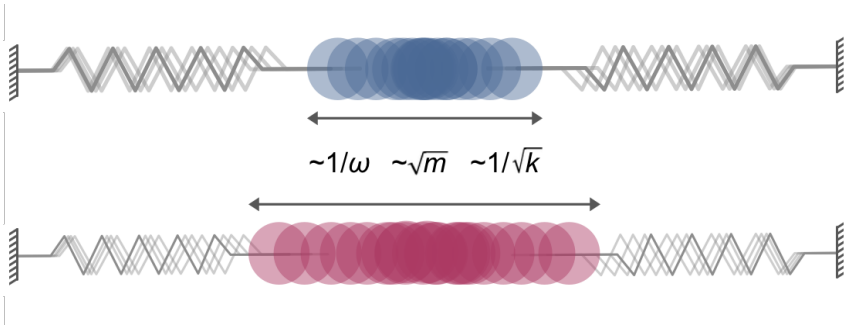

Figure 1.6: Two harmonic oscillators with different amplitudes u. Larger amplitudes correspond to lower vibrational frequencies ω, and can result from a lager mass m or a weaker spring constant k. Enhanced amplitudes are also correlated to larger vibrational entropies: the mass explores more space/momentum, which corresponds to a larger number microstates in Boltzmann's entropy (Eq. 1.10)

The masses are constants for a specific material, but the vibrational frequencies and the interatomic force constants are not. This gives us a physical picture of why low energy vibrations (low frequencies) result in larger entropy contributions compared to high energy modes. In Eq. 1.14 this was accomplished by weighting the phonon DOS with the Planck distribution. The simple picture of Fig. 1.6 also gives an intuition for the temperature and pressure dependence of the phonon entropy. As temperature is increased, the frequency of phonon modes tend to decrease because the forces between atoms decrease (weaker springs), resulting in larger oscillatory amplitudes and larger entropies. The opposite happens as materials are placed under high pressures, which increases their vibrational frequencies causing an entropy reduction.

In reality, phonons are quantum mechanical excitations. The nuclei have zero-point motion, and explore the space and momentum hyperspace in ways that a harmonic classical spring can not capture. The vibrational entropy can, for example, increase without a increase of vibrational amplitudes (see negative thermal expansion materials [6]). What seems to be always true, at least up to first order, is that the entropy depends inversely on the vibrational frequency. The lower the frequency, the larger the vibrational entropy.

1.4 Magnetism

Electrons are charged particles that move around the nucleus, so they create a magnetic field. In quantum mechanics, electrons have quantized orbital momenta $\hbar\mathbf{l}$, corresponding to their motion around the nuclei, and spin-orbital

momenta $\hbar\mathbf{s}$, representing their internal rotational degree of freedom around their own axes. For an atom as a whole, the total magnetic moment arises from the sum of the momenta from individual electrons: $\mathbf{M} = \mu_{\mathrm{B}}(\mathbf{L} + \mu_g \mathbf{S})$, where capital variables represent sums, $\mu_{\mathrm{B}} = e\hbar/2mc$ is the Bohr magneton, and $\mu_g \approx 2$ the g-factor of electrons. When all orbitals of an atom are fully occupied by electrons, the individual momenta cancel each other out and $\mathbf{L} = \mathbf{S} = \mathbf{0}$. This is not the case for the d orbitals of transition metals, however, resulting in a net magnetization.

When atoms are condensed into a solid, their magnetic fields of neighboring atoms have an effect on each other's magnetic moments through the 'exchange interaction'. Pauli's exclusion principle states that two electrons cannot occupy the same quantum state, so electrons in d orbitals with parallel spins have to avoid each other. These interactions between the magnetic spins of different atoms give rise to interesting magnetic effect in transition metals.

Heisenberg localized magnetism

The partially filled $3d$ orbitals are strongly bound to the nucleus as shown previously for the case of nickel in Fig. 1.1. This localized picture of unpaired electrons led to a model of local magnetic moments at each atom, know as the Heisenberg model.

Placing atoms in a solid creates an electric field in the crystal. This field and the partial covalency of neighboring d orbitals result in a net quenching of the orbital momenta $\mathbf{L}$. So the magnetic exchange interaction between neighboring atoms i and j is assumed to depend solely on the dot product of their spins [3]:

$$H_{exch} = -\sum_{i,j} J_{ij}(\mathbf{S}_i \cdot \mathbf{S}_j), \tag{1.18}$$

where J_{ij} is the interatomic exchange constant. J_{ij} can in theory be computed from the overlap integral between orbitals, having a positive sign for ferromagnetic interactions and a negative sign for anti-ferromagnetism. This local model with magnetic spins localized at each atom can be pictured as is Fig.1.7 a. As temperature is increased, the local spins become progressively disordered and their dot products smaller. This disorder between pairs of spins then alters the interactions with other neighboring atoms, making spin

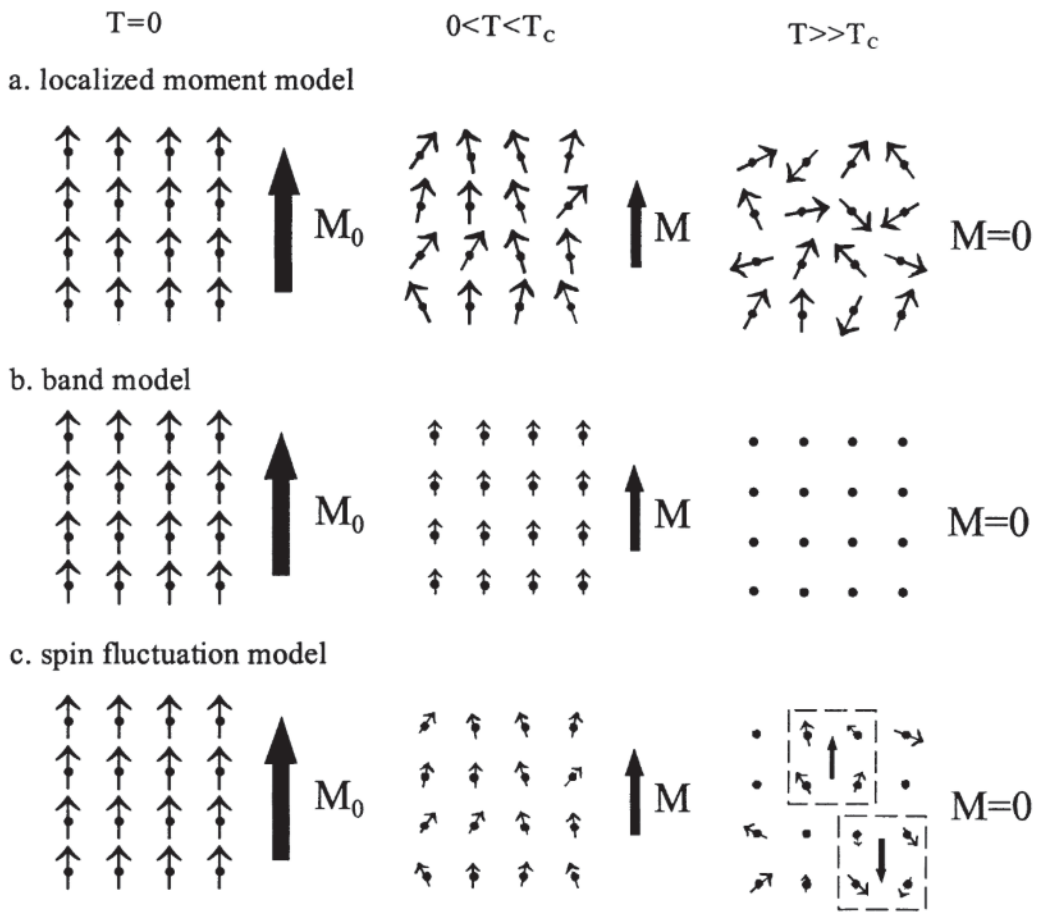

Figure 1.7: Models for magnetism in solid-state systems and their temperature dependence, where M denotes the net magnetization [4]. **(a)** Localized Heisenberg model. **(b)** Delocalized itinerant electron model. **(c)** Spin fluctuation model combining both local and itinerant pictures.

disorder a many-body effect. As a result, the net magnetization decreases up to the Curie temperature T_{C}.

It is too complicated and computationally expansive, however, to calculate the exchange energy by dot products between all individual atoms. A Weiss molecular field model can be introduced, where each spin interacts with a mean magnetic field produced collectivelly by all spins [13]:

$$H_{exch} = -2J \sum_i \mathbf{S}_i \cdot \mathbf{B}_{MF}, \tag{1.19}$$

where the mean magnetic field $\mathbf{B}_{MF} = \lambda \mathbf{M}$, is proportional to the mean magnetization, and J is the mean exchange constant. This model is able to calcu-

late the temperature dependence of the magnetization, the Curie temperature, and magnetic susceptibility, for example.

Calculating the magnitude and sign of J for ferromagnetic transition metals is very challenging computationally. Additionally, perfectly localized moments would result in whole numbered magnetic moments, as is the case for isolated atoms. This is not observed for transition metals with magnetic moments of $2.2\mu_B$, $1.7\mu_B$ and $0.6\mu_B$ for Fe, Co, and Ni, respectively. The Heisenberg model is justified for well-defined local moments, which can be valid for magnetic insulators and many rare-earth metals. It cannot provide an accurate microscopic description of the collective magnetic behavior of transition metals, with d orbitals that overlap with their neighbors. Nonetheless, the Heisenberg model as a phenomenological magnetic model has been extremely important for understanding the magnetic properties of materials. Variations of it will be used further below in this thesis.

Itinerant electron magnetism

The electronic behavior in transition metals is better described by a model in which the electrons are not closely bound to a single nucleus. They can be transferred from atom to atom, known as an itinerant behavior. The concept of an atomic magnetic spin is no longer well defined in this picture.

When individual atoms are brought together into a crystal, their electronic energy levels broaden and become bands of energy. This results in a continuous density of states (DOS) for the electrons. Band theories usually use a tight binding model, which is appropriate for describing the fairly localized d orbitals of transition metals. The energy of s electrons broaden more than d electrons, as depicted in Fig. 1.8 a, resulting in distinct properties of transition metals. For instance, the d electrons provide a large number of electronic states near the Fermi energy, E_F. It is therefore easy for an electron to be excited into an unoccupied state above E_F. This electron can then move between atoms (itinerant behavior) and contributes to the large electrical conductivity of transition metals.

The electronic bands can be split into two sub-bands representing two possible spin orientations, ‘spin-up’ and ‘spin-down’ (this model ca not support noncollinear spins). It can be visualized by plotting the electronic DOS in two separate spin-polarized bands as in Fig. 1.8. If a material is ferromagnetic,

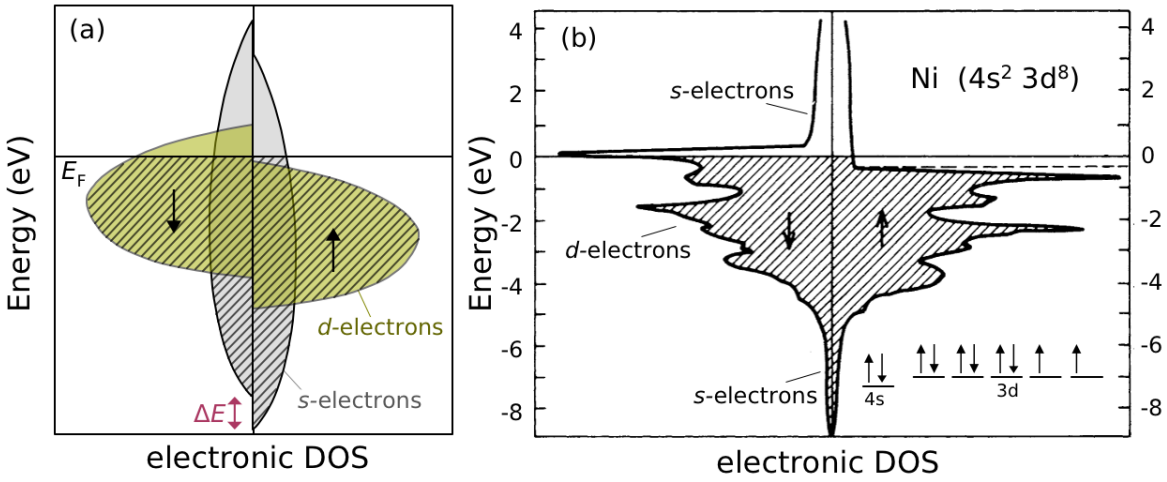

Figure 1.8: Spin-polarized electronic density of states (DOS). **(a)** Schematic representation of the DOS showing the energy distribution of the s and d electrons, for the spin-up (↑) and spin-down (↓) bands. Dashed lines represent the states occupied by electrons up to the Fermi energy E_F. In Stoner magnetism the bands are split by ΔE and more states are occupied by ↑-electrons than ↓-electrons resulting in a net magnetization. **(b)** Calculated eDOS of ferromagnetic nickel, with an exchange splitting of ΔE = 0.6 eV [1].

there are more electrons with 'spin-up', and the 'spin-down' bands are less occupied. This is represented by a splitting of the sub-bands by an amount ΔE, know as the exchange splitting. It creates a net magnetic field in the material and electrons with 'spin-up' and 'spin-down' experience different forces within the crystal.

Electrons, due to their charges and irrespective of their spins, experience repulsive forces between each other (Coulomb repulsion). If they have parallel spins they have to avoid each other due to the Pauli exclusion principle, which keeps them at larger distances and in turn reduces their Coulomb repulsion. However, electrons are fermions, so by having the same spins, they also have to progressively occupy higher energetic states, which raises their kinetic energy. If more electrons have 'spin-up', the overall Coulomb repulsion is lower, but the kinetic energy is larger. Therefore a balance between a reduced Coulomb repulsion and an increased kinetic energy determines if it is energetically favorable for the bands to split, and for the material to become ferromagnetic. This is known as the Stoner criterion for ferromagnetism. For the case of nickel, shown in Fig. 1.8 b, the overall energy is reduced by splitting the bands by ΔE = 0.6 eV, making it ferromagnetic.

The itinerant band model provides a completely different picture of ferromagnetism than the Heisenberg model. It describes accurately the ground state of ferromagnets and can also be modified to handle anti-ferromagnetism and other complex magnetic structures. Even though the moments are not localized at the atoms, their temperature dependence can be pictured as in Fig.1.7 b. The moments preserve their parallel alignment (in each of the sub-bands), however their magnitude progressively decreases up to the Curie temperature. The decreasing magnitudes can be thought of as thermal spin-flip excitations of electrons across the Fermi surface, which changes the occupancy of the sub-bands.

Spin waves and spin fluctuations

Magnetic spins interact with each other, and fluctuations of the spins with increasing temperatures can cause a collective excitation at long-range scales. At low temperatures, the gradual disruption of the magnetic alignment is well described by spin fluctuations that travel coherently as waves in the crystal. This spin-waves, or magnons (in analogy to phonons) are depicted in Fig. 1.9 for γ-Fe. The temperature dependence of the magnetization due to magnons obeys Block's law:

$$\frac{M_0 - M(T)}{M_0} = AT^{3/2}. \tag{1.20}$$

For iron $A = 3.4 \times 10^{-6}\mathrm{K}^{3/2}$, and the magnons holds up to about 200 K [4]. At higher temperatures, there are too many interactions and scattering between spins and phonons, which disrupts the propagation of such coherent spin-waves.

In reality, both localized and itinerant behaviors happen simultaneously. Several attempts have been made to merge both models [3, 4]. The spin fluctuation model divides the electronic correlations into two time scales: quantum fluctuations at small time scales ($\sim 10^{-15}s$) cause electrons to hop between nearby orbitals in the lattice, affecting the correlation of nearby spins and creating local magnetic effects. Over a longer time-scale ($\sim 10^{-13}s$) the short-range magnetization is averaged, and slower fluctuations can travel in the lattice in the form of spin-waves, creating long-range delocalized magnetic effects.

There is no contradiction between local and itinerant behaviors in the spin fluctuation model (Fig.1.7 c). The ground state is given by the band theory.

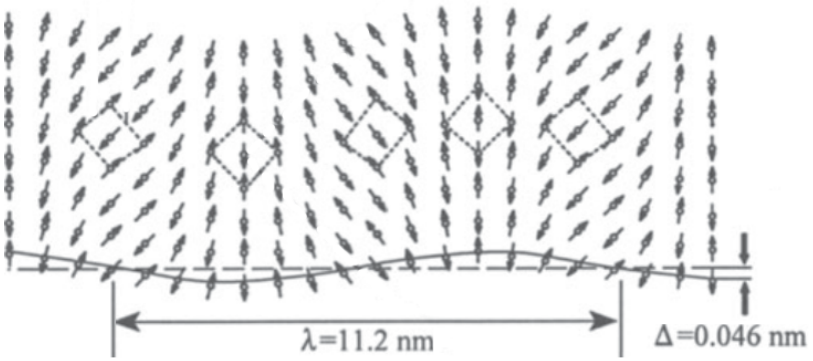

Figure 1.9: Schematic representation of the periodic lattice distortion and the propagation of a spin wave in anti-ferromagnetic γ-Fe particles. The magnon wavelength is 11.2 nm extending over tens of atoms in the lattice [4].

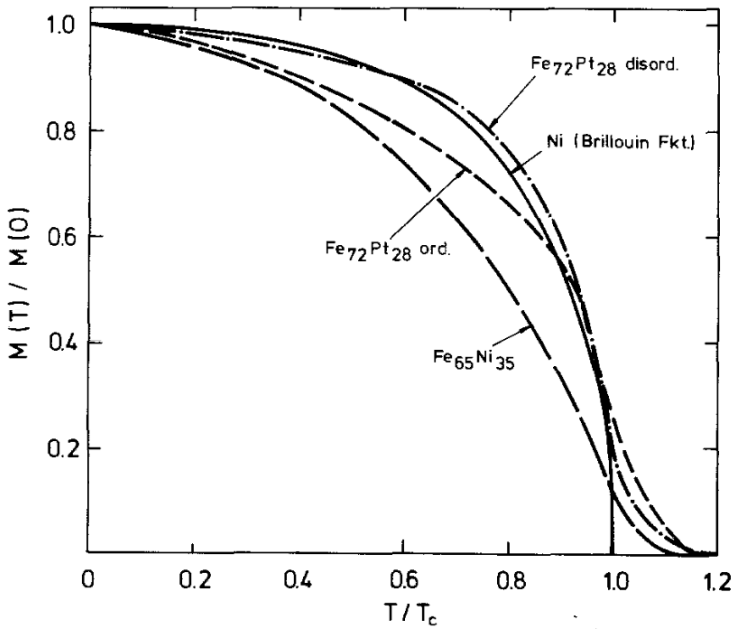

Figure 1.10: Temperature dependence of magnetization in Ni and Invar materials ($Fe_{65}Ni_{35}$ and $Fe_{72}Pt_{28}$) [14].

As temperature is increased, directional fluctuations of the moments occur up to T_C, and at the same time electronic spin-flip transitions allow the magnitude of the moments to decrease. Long-range order is lost above T_C, with a zero average magnetization, but local spin correlations can result in a lingering short-range magnetic order.

Magnetization

The individual magnetic moments result in a net macroscopically measurable magnetization. The temperature dependence of the magnetization, $M(T)$,is shown in Fig. 1.10 for Ni and two Invar alloys. At low temperatures, the demagnetization of pure nickel (and similarly of pure iron) has a $T^{3/2}$ dependence. As temperature increases, magnetic moments start interacting with each other and the wave-like propagation of spin fluctuations is disrupted. Near the Curie temperature they collectively collapse, resulting in a rapid decrease of $M(T)$. Invar alloys ($Fe_{65}Ni_{35}$ and $Fe_{72}Pt_{28}$) seem to behave differently. The spins start disordering earlier, resulting in a lower $M(T)$ at low temperatures, especially in $Fe_{65}Ni_{35}$. They also have a tail above the Curie transition, corresponding to short-range ordering of the spins.

Spin statistics

As for phonons, we want to correlate the microscopic arrangement of spin to a macroscopic thermodynamic quantity, such as the entropy. We use a simplified version of the local Heisenberg model for describing ferromagnetism, called the Ising model, where spins can either be 'up' ($\sigma = +1$) or 'down' ($\sigma = -1$). At low temperatures, the spins are perfectly aligned, as shown in the left panel of Fig. 1.11, and become progressively disordered with increasing temperature through local spin flips.

The number of microstates Ω of the Boltzmann entropy, $S = k_B \ln \Omega$, are the number of ways that $N_\uparrow$ spin-up atoms can be arranged on N lattice sites (or equivalently how to arrange $N_\downarrow = N - N_\uparrow$ spin-down atoms in the lattice).

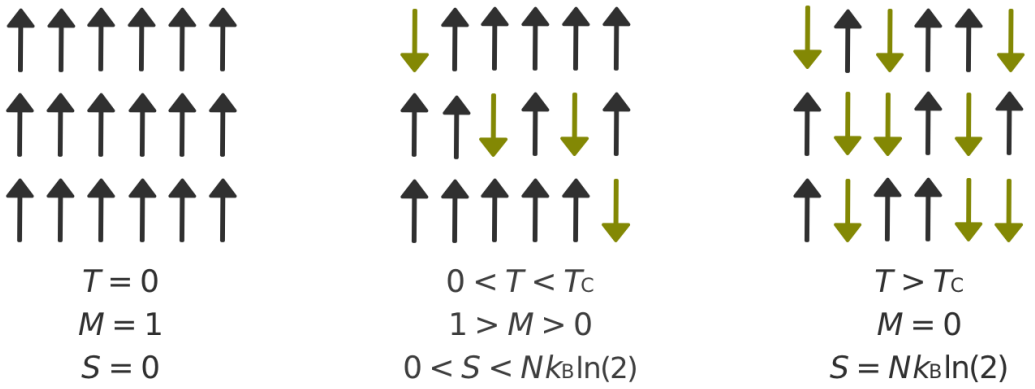

Figure 1.11: Mean-field Ising model of a magnetic lattice.

Using a binomial distribution:

$$S = k_{\mathrm{B}} \ln \binom{N}{N_{\uparrow}} = k_{\mathrm{B}} \ln \left(\frac{N!}{N_{\uparrow}!\,(N - N_{\uparrow})!} \right). \tag{1.21}$$

The total magnetic moment is simply the number $N_{\uparrow}$ of up spin, minus the number $N_{\downarrow}$ of spin downs. And a mean-field order parameter, M, is defined as the average magnetization per atom [3, 15]:

$$M = \frac{N_{\uparrow} - N_{\downarrow}}{N} = \frac{N_{\uparrow} - (N - N_{\uparrow})}{N}. \tag{1.22}$$

Using Stirling's approximation ($\ln x! \approx x \ln x - x$) and $N_{\uparrow} = N(1 + M)/2$, the Boltzmann entropy becomes:

$$S = -\frac{N k_{\mathrm{B}}}{2} \left[(1 + M) \ln \frac{1 + M}{2} + (1 - M) \ln \frac{1 - M}{2} \right]. \tag{1.23}$$

This is often called the entropy of mixing or configurational entropy, as it can also describe the entropy of mixing two types of atoms in a lattice (instead of two 'types' of spins). It ranges from $S = 0$, when all spins are aligned with $M = 1$ (left panel in Fig. 1.11), up to $S = N k_{\mathrm{B}} \ln 2 = 0.69 k_{\mathrm{B}}$/atom, when half of the spins point in each direction (right panel). The latter is the maximum disorder captured by the Ising model, and corresponds to the total loss of long-range magnetic order at the Curie transition. Mean-field models can, therefore, not account for local effects of short-range order. They are still useful since most of the magnetization below the Curie transition arises from long-range order [7]. This simple Ising model allows us to compute the entropy associated with the magnetic disordering from a measured magnetization curve, $M(T)$, as those of Fig. 1.10.

In such a local moment model, the magnetic entropy can be understood as a measure of spin disorder. When spins are perfectly ordered, in a ferromagnetic state, there is no entropy. In contrast, when the spins are fully disordered in a paramagnetic state, there are several equivalent configurations for arranging the spins on the lattice with M=0, corresponding to a large magnetic entropy.

1.5 Thermodynamics

One of the most fundamental ways that nature operates is through the principle of energy minimization, or equivalently, of entropy maximization. It is

based on the universal experience that heat (or thermal energy) always flows spontaneously from hotter objects (high energy state) to colder objects (low energy state) unless external energy is supplied to reverse the heat flow. This leads to the first law of thermodynamics where the change in the internal energy U of a system is given by the change of the thermal energy Q plus the external work W [16]:

$$\mathrm{d}U = \delta Q + \delta W \,. \tag{1.24}$$

For a closed system with a fixed number of particles, the external work results from the change of the volume of the system, $\delta W = -P\mathrm{d}V$, and the thermal energy originates from a change in entropy as $\delta Q = T\mathrm{d}S$, so

$$\mathrm{d}U = T\mathrm{d}S - P\mathrm{d}V \,. \tag{1.25}$$

Entropy is associated with thermal energy, which originates from microscopic excitations of phonons, electrons, and spins. For a closed system in equilibrium, the internal energy is at a minimum and $\mathrm{d}U = 0$.

Materials, however, are rarely isolated in a true closed system. They exist in equilibrium with their environment at a certain temperature and pressure. There is an exchange of energy with the environment and the principle of energy minimization needs to be reformulated. The equilibrium of a system in contact with a temperature and pressure reservoir minimizes, instead, the Gibbs free energy [16]:

$$\begin{aligned} G &= U - TS + PV \\ &= H - TS \,, \end{aligned} \tag{1.26}$$

where $H = U + PV$ is the enthalpy. Most of the enthalpy of materials originates from the bonding energy of the electronic orbitals between atoms. In the ground state at T=0 K, it constitutes the entire Gibbs free energy. As temperature is increased, however, the entropy term becomes important. Because of the minus sign of Eq. 1.26, high entropy states help to reduce the free energy at high temperatures, stabilizing the material.

Entropy is also the variable that connects the macroscopic thermodynamic behaviour to the microscopic excitations through the Boltzmann relation $S = k_\mathrm{B} \ln \Omega$ (Eq. 1.10). More phonons and larger spin disorder increase the number of microstates, and hence the entropy. High entropy states have a larger probability to occur, since there are several microscopic configurations that

result in that same macroscopic state. The principle of entropy maximization is a statistical statement, that a system will take the most likely configuration with the highest number of microstates.

Entropy contributions

Most of the entropy in materials comes from phonons. As the temperature is raised, more phonons are excited, which increases the entropy and decreases the free energy. At room temperature, lattice vibrations account for about 80-90% of the total entropy in Fe-Ni alloys, for example.

As previously discussed, thermal energy can also be absorbed by disordering the magnetic spins. As temperature is increased, the alignment of spins gets disrupted, which contributes to a magnetic entropy. Therefore a disordered spin state is usually more stable at high temperatures than a state with magnetic order.

Electrons can also get thermally excited to higher energetic states. The electronic entropy is associated with the occupation of electronic states near the Fermi energy E_{F}. As previously discussed, the d orbitals of transition metals result in a large density of states at E_{F}, and there is no energy gap between the highest occupied electronic state and the lowest unoccupied state. Broadening of the Fermi-Dirac distribution with increasing temperatures, allows a larger number states to be populated by electrons just above E_{F}. It increases the number of microstates available for electron, and therefore, contributes as an electronic entropy.

The last piece of entropy is configurational. When combining different types of atoms into a material (as in an alloy) there are different ways to arrange those atoms on the lattice. Analogously to the magnetic entropy, it can be viewed as a measure of the disorder of atomic configurations, or the entropy of mixing. Some materials experience order-disorder transitions as a function of temperature due to the configurational entropy [7]. All materials studied in this thesis, however, are random solid solutions of atoms in the lattice. In theory, they have a configurational entropy, but it is constant as the atomic configurations cannot be further randomized. The atomic configurations, therefore, do not change in the temperature range of this study and do not contribute to change

the entropy. The total entropy change can be described by

$$\mathrm{d}S = \partial S_{ph} + \partial S_{mag} + \partial S_{el} \,. \tag{1.27}$$

Thermal expansion

The thermal expansion is a measure of the volumetric change of a material when heated. The coefficient of thermal expansion, β, is the fractional change of volume with temperature:

$$\beta = \frac{1}{V}\left(\frac{\partial V}{\partial T}\right)_P \,. \tag{1.28}$$

Metals usually expand their volumes when heated. This happens because their thermal energy is mostly stored as atomic vibrations. As the temperature is increased, the bonds between atoms soften, lowering their vibrational frequencies, and allowing the nuclei to explore a larger volume in space and momentum. As the nuclei vibrate more strongly, they can be found in a larger range of locations and momenta. This increases the entropy as previously discussed with Fig. 1.6), and is usually associated with a lattice expansion. Thermal expansion is, therefore, directly linked to the phonon entropy. This vibrational contribution to the thermal expansion is qualitatively depicted in Fig. 1.12 a, for the case of a material with positive thermal expansion.

Figure 1.12 a is intended to provide an intuitive connection between vibrational entropy and thermal expansion. But is might also be a little misleading, since such a classical picture cannot capture the full quantum mechanical nature of phonons. While it is always true that the entropy increases with temperature (since that is the role of entropy in minimizing the Gibbs free energy with temperature), it does not always lead to an expansion of the lattice. Phonons can be enhanced without requiring a larger net volume. Accordingly, materials with negative thermal expansion are known [6, 17–19]. These are further discussed in Chapter 5.

A softening of the bonding forces and vibrational energies with temperature is out the scope of the harmonic model. Since it assumes non-interacting modes of constant energies, the harmonic model cannot account for thermal expansion. A simple fix (and somewhat limited one [6, 17]) is achieved by extending the model to allow vibrational modes to shift in frequency. The

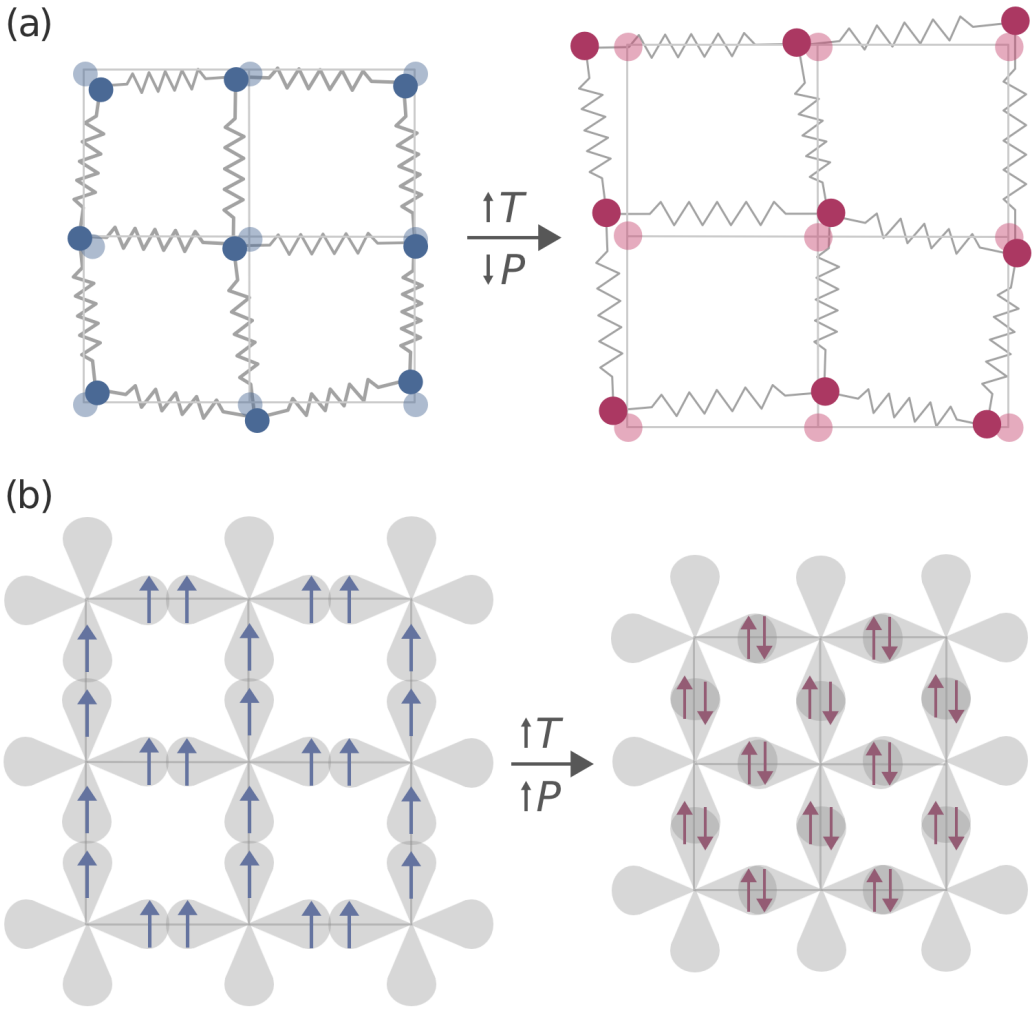

Figure 1.12: Qualitative connection between entropy and thermal expansion on a 2-dimensional lattice. **(a)** Schematic representation of phonon displacements on a lattice for a material with positive thermal expansion. As the temperature is increased (or pressure is decreased), the interatomic forces soften, lowering the vibrational energies, and causing an increase of the phonon entropy. As the nuclei vibrate more strongly, they explore a larger volume in space and momentum which usually causes an expansion of the lattice. **(b)** Representation of the d orbitals and spin configurations on a lattice. As the temperature (or pressure) is increased, the electronic orbitals overlap more. This disrupts the magnetic ordering due to the Pauli exclusion principle and increases the magnetic entropy. The increase of magnetic entropy is tied to a volume contraction.

quasiharmonic approximation (QHA) includes the temperature dependence of the phonon energies, but only implicitly through the volume: $\omega = \omega(V(T))$. For a harmonic spring (see Eqs. 1.15 and 1.16) there is a linear relationship between the oscillation amplitude and frequency. In the QHA, the change in vibrational frequency is also assumed to be linear with volume. A constant Grüneisen parameter, γ, is typically defined for describing the fractional change in frequency of mode i per fractional change in volume V

$$\gamma = -\frac{V_0}{\omega}\frac{\partial \omega}{\partial V} \,, \tag{1.29}$$

where V_0 is an initial volume. The volume dependency of the energies become:

$$\omega(V) = \omega(V_0 + \Delta V) = \omega_0 \left(1 - \gamma\, \Delta V / V_0\right) \,. \tag{1.30}$$

The QHA can often describe the thermal expansion of real materials, but does not include true anharmonic effects. The different modes still do not interact with each other resulting in infinite phonon lifetimes, as in the harmonic model. And as discussed in Chapter 5, thermal expansion is inherently an anharmonic effect. This model will be also further explored in Chapter 4, where we apply the QHA to the phonon behavior of iron and cementite. There we extend it to include the dependence of phonons energies on the magnetization, a *magnetic QHA*.

The magnetic structure is also linked to the entropy, and also affects the thermal expansion. However, temperature effects of magnetism on volume tend to be opposite of those from phonons. Increasing temperatures affects the electronic structure. In a band (itinerant) model, temperature causes spin-flip transitions from the majority (spin-up) to the minority (spin-down) band, resulting in a decrease of the net magnetization through the Stoner criterion. In a localized moment model, the magnetic spins become progressively disordered with increasing temperatures. Changing the electronic structure has an effect on the lattice parameter. Such a connection between temperature and volume due to magnetic interactions can be gained from the Pauli exclusion principle. In a ferromagnetic material, the unpaired electrons in the d orbitals of different atoms have aligned spins. Their wave-functions, therefore, are not allowed to overlap due to the Pauli repulsion (upper panel in Fig. 1.12 b). As the temperature is increased, the spins progressively lose their ferromagnetic alignment, allowing the electronic orbitals of neighboring atoms to overlap,

which enables a contraction of the volume as pictured in the lower case of Fig. 1.12 b.

The increase of magnetic entropy through the disorder of the spins is linked to a decrease in volume, while the increase of vibrational entropy with temperature usually causes a thermal expansion. In both cases temperature increases the entropy. Figure 1.12 also offers a connection of the phonon and magnetic entropies to the pressure, as it directly controls the volume. For phonons, increasing the pressure constricts the vibrational amplitudes and reduces the entropy. And for the magnetism, increasing the pressure makes the electronic orbitals overlap, which causes an increase in entropy through the spin disorder. A balance of the effect of phonon and magnetism (and electrons) give the net volumetric dependence of magnetic materials on the temperature and pressure.

Thermal expansion and entropy

We can explicitly relate the entropy to the thermal expansion by looking at derivatives of the Gibbs free energy ($\mathrm{d}G = V\mathrm{d}P - S\mathrm{d}T + \mu\mathrm{d}N$):

$$\begin{aligned} \frac{\partial G}{\partial P} &= V & \qquad \frac{\partial G}{\partial T} &= -S \\ \frac{\partial^2 G}{\partial T \partial P} &= \frac{\partial V}{\partial T} & \qquad \frac{\partial^2 G}{\partial P \partial T} &= -\frac{\partial S}{\partial P}\,. \end{aligned} \tag{1.31}$$

Since the mixed derivatives have to be equal, we obtain the Maxwell relation:

$$\left(\frac{\partial V}{\partial T}\right)_P = -\left(\frac{\partial S}{\partial P}\right)_T . \tag{1.32}$$

This holds true when the material is in thermodynamic equilibrium, which is the case since equilibration between phonons, electrons and spins is much faster than the times of macroscopic measurements of β. The thermal expansion of Eq. 1.28 can therefore be expressed as:

$$\beta = -\frac{1}{V}\left(\frac{\partial S}{\partial P}\right)_T . \tag{1.33}$$

Phonons, spins and electrons contribute simultaneously to the change of entropy as S_{ph}, S_{mag}, S_{el}, so the thermal expansion can be broken down into these individual components:

$$\beta = -\frac{1}{V}\left[\left(\frac{\partial S_{\mathrm{ph}}}{\partial P}\right)_T + \left(\frac{\partial S_{\mathrm{mag}}}{\partial P}\right)_T + \left(\frac{\partial S_{\mathrm{el}}}{\partial P}\right)_T\right] . \tag{1.34}$$

Note that by using a Maxwell relation we move from a temperature to a pressure dependence. As described previously with Fig. 1.12, temperature causes both the phonon and magnetic entropies to increase. Pressure, however, increases the magnetic entropy and decreases the phonon entropy, so they have opposing effects on the thermal expansion through Eq. 1.34.

1.6 Phase stability of iron

We conclude this chapter with an example of how phonons and magnetism can have consequences on the morphology of materials. The following excursion into the stability of the different phases of iron gives a glimpse into the thermodynamics of magnetic materials. It reiterates the content of this chapter, and serves in and serves as a building block for the following chapters of this thesis.

Iron is usually described as a ferromagnetic (FM) metal, which might understates the complexity and richness of its different magnetic phases. At ambient conditions it is indeed FM in the body-centered cubic (bcc) structure. However at different conditions, when alloyed to other elements, or in the face-centered cubic (fcc) crystal structure, for example, it can present antiferromagnetic (AF), non-collinear, partially disordered, spin-spiral, spin-glass like, and nonmagnetic states (NM) [20]. The existence of several competing magnetic states, results in the polymorphism of iron, and its rich phase diagram of Fig. 1.13 a. The strong magnetic interactions in iron also offers a good system to study couplings between phonons and spins. From an experimental perspective, iron has the advantage of having an isotope, ^{57}Fe, suitable for Mössbauer spectroscopy, a powerful technique to study magnetism.

As discussed in section 1.1, the delocalized and symmetric s orbitals in transition metals favor the closest possible spherical packing of atoms [4]. The d orbitals provide a covalent-like framework and the close-packed fcc configuration is often preferred as the ground state by minimizing the enthalpy. However, iron atoms have four unpaired electrons in the d shell, leading to fairly strong local moments. These magnetic moments exert forces on each other through exchange interactions, resulting in an additional contribution to the enthalpy. The Pauli repulsion between spins in a ferromagnetic alignment, for example, leads to an internal pressure that would require larger volumes, and could result in a more open atomic configuration such as in the bcc structure.

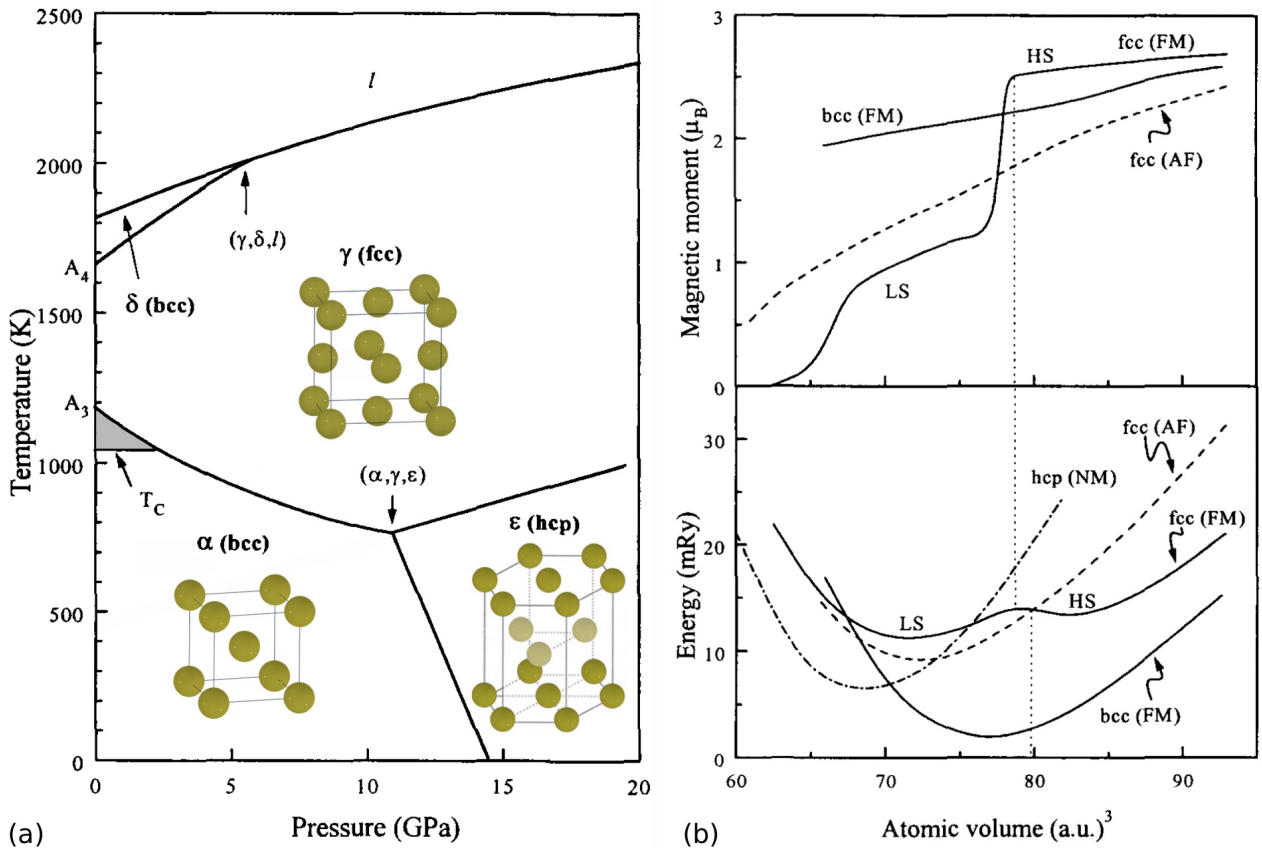

Figure 1.13: Phase stability of Fe. **(a)** Structural phase diagram of iron showing its different crystal structures as a function of temperature and pressure. **(b)** Total energy and magnetic moments as a function of volume at T=0 K calculated for Fe in the bcc, fcc and hcp crystal structures [21].

The enthalphy (or energy) and magnetic moments of iron in different crystal structures (fcc, bcc, and hexagonal closed-packed hcp) were computed by first-principles band calculations at 0 K (no entropic effects) [21]. As shown in Fig. 1.13 b, the (FM) bcc structure provides the lowest ground state energy for iron. This means that the exchange interactions between spins in Fe, overcome the tendency of a close-packed structure from the electronic bonding. Indeed, the atomic volume of the bcc structure is larger than those from the fcc (AF) and hcp (NM) ones. This is not always the case for FM metals, however. The lower magnetization of FM nickel for example ($0.6\mu_B$), favors the low-volume fcc structure up to the melting temperature.

As pressure is increased, the atoms are forced into smaller volumes and the electronic orbitals start to overlap. The Pauli repulsion forces intensify and a ferromagnetic alignment of spins is no longer energetically favorable. With the loss of ferromagnetism, the exchange interactions can not stabilize the bcc

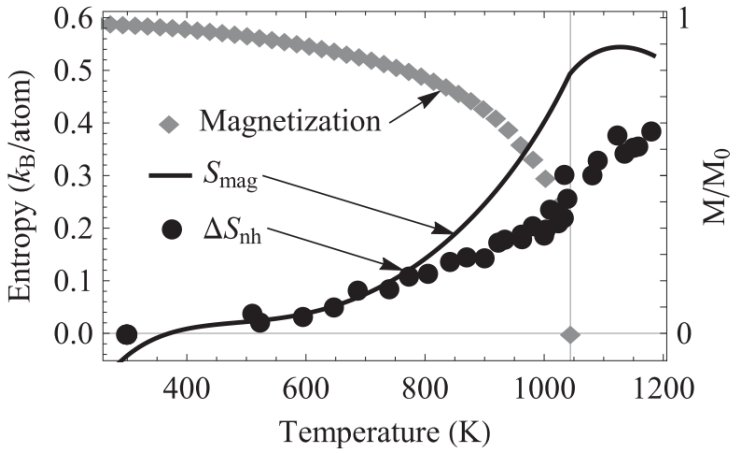

Figure 1.14: Nonharmonic phonon entropy ($\Delta S_{\mathrm{nh}} = S_{\mathrm{tot}} - S_{\mathrm{QHA}}$) from measured phonon DOS spectra, compared to the magnetization of bcc Fe (right axis), and its magnetic entropy [24]. Vertical line marks the Curie transition at 1044 K.

phase. At a pressure of about 14 GPa in the phase diagram, or a volume of 70 (a.u.)^3 in Fig. 1.13 b, the nonmagnetic hcp structure becomes stable. The transition into the high-pressure ϵ phase does not seem to have substantial phonon contributions. It is rather an effect of pressure on the magnetism than a dynamic instability of phonons [22].

As the temperature is increased, spin fluctuations progressively disrupt the magnetic order. This gives rise to a magnetic entropy that helps reducing the free energy (Eq. 1.26) to stabilize the bcc structure. Above the Curie temperature, the bcc phase is no longer stabilized by magnetism and transforms martensitically into a paramagnetic fcc phase.

Although the fcc phase of iron is anti-ferromagnetic (see Fig. 1.13 b) its Néel transition happens at around 67 K, so it becomes paramagnetic by the temperature at which the fcc becomes stable. The other (meta-stable) ferromagnetic fcc phases of iron, HS and LS, are essential to understanding the Invar effect and will be discussed in detail in Chapter 5.

As the temperature is increased further, the entropy becomes even more relevant for reducing the free energy. And phonons, as the largest entropy contributors, take the main role. By having a lower packing density, the bcc structure allows for larger oscillations of the nuclei, which results in a larger phonon entropies. Above 1667 K, this vibrational entropy is responsive for stabilizing the nonmagnetic bcc phase [23]. At 1811 K the bond between atoms become to soft to sustain thermal fluctuations and iron melts.

The stability of the lower temperature bcc phase (α-Fe) is generally attributed to the magnetic entropy as described above. Phonons, however, are also essential. Magnetism alone cannot explain how the bcc phase is stable even beyond the Curie transition (shaded area in Fig. 1.13 a). Measurements of both the phonon dispersions [25] and the phonon DOS [24] in α-Fe show strong softening of the vibrational energies, especially those from transverse modes (we will later discuss this in Fig. 4.1). It results in a large contribution to the entropy, that departs from the quasi-harmonic model as shown in Fig. 1.14. In fact, this excess (nonharmonic) phonon entropy is of the same order as the magnetic entropy. This excessive phonon amplitudes are a result of a coupling with magnetism, as described in [26]. The increase of magnetic disorder interacts with the lattice to soften the phonon vibrations. It is, therefore, not surprising that the nonharmonic vibrational entropy has a very similar shape to the magnetic entropy. This interaction of phonons and spins holds even beyond the loss of magnetic long-range order at the Curie temperature of 1044 K. The coupling with short-range magnetism continues to raise the phonon entropy, stabilizing the bcc phase up to 1185 K. Prior to the discovery of coupled interactions of phonons and magnetism, the stability of the bcc phase above its Curie transition could not be explained.

The coupling between the vibrational and magnetic degrees of freedom is central in this thesis. It will be further explored in the case of in α-Fe in Chapter 4, where the nonharmonic contributions of Fig. 1.14 are modeled by a magnetic quasi-harmonic approximation. Chapter 5 explains how such a spin-phonon coupling can result in anomalous thermal behaviour of Invar, with near-zero thermal expansion. The size of the crystalline structure of a material is also essential, as it influences all kinds of thermal excitations. Chapter 3 explores the size dependence of phonons, spins and electrons in nanocrystalline Ni_3Fe, and their effects on its thermodynamic stability. But first, in the coming chapter, we discuss some of the critical experimental methods used in these studies.

References

[1] H. Ibach and H. Lüth, *Solid-State Physics* (Springer, 2009).

[2] P. Entel, E. Hoffmann, P. Mohn, K. Schwarz, and V. L. Moruzzi, Phys. Rev. B **47**, 8706 (1993).

[3] T. Moriya, *Spin Fluctuations in Itinerant Electron Magnetism* (Springer, 1985).

[4] W. Pepperhoff and M. Acet, *Constitution of Iron and its Alloys* (Springer, 2001).

[5] G. Shen and H. K. Mao, Rep. Prog. Phys **80** (2017).

[6] D. S. Kim, O. Hellman, J. Herriman, H. L. Smith, J. Y. Y. Lin, N. Shulumba, J. L. Niedziela, C. W. Li, D. L. Abernathy, and B. Fultz, Proc. Natl. Acad. Sci. U.S.A. **115** (2018).

[7] B. Fultz, *Phase Transitions in Materials* (Cambridge University Press, 2014).

[8] Y.-L. Chen and D.-P. Yang, *Mössbauer Effect in Lattice Dynamics* (Wiley, 2007).

[9] E. Maliszewski and S. Bednarski, Phys. Status Solidi B **211**, 621 (1999).

[10] E. D. Hallman and B. N. Brockhouse, Can. J. Phys. **47**, 1117 (1969).

[11] B. Fultz, JOM **58**, 58 (2006).

[12] D. C. Wallace, *Thermodynamics of Crystals* (Dover, 1998).

[13] K. H. J. Buschow and F. R. de Boer, *Physics of Magnetism and Magnetic Materials* (Springer, 2003).

[14] E. F. Wasserman, in *Handbook of Ferromagnetic Materials*, Vol. 5 (Elsevier, 1990).

[15] P. M. Chaikin and T. C. Lubensky, *Principles of Condensed Matter Physics* (Cambridge University Press, 1995).

[16] H. B. Callen, *Thermodynamics* (Wiley, 1962).

[17] C. N. Saunders, D. S. Kim, O. Hellman, H. L. Smith, N. J. Weadock, S. T. Omelchenko, G. E. Granroth, C. M. Bernal-Choban, S. H. Lohaus, D. L. Abernathy, and B. Fultz, Phys. Rev. B **105**, 1 (2022).

[18] J. S. Evans, W. I. David, and A. W. Sleight, Acta. Crystallogr. B **55**, 333 (1999).

[19] A. W. Sleight, Endeavour **19**, 64 (1995).

[20] I. A. Abrikosov, A. E. Kissavos, F. Liot, B. Alling, S. I. Simak, O. Peil, and A. V. Ruban, Phys. Rev. B **76**, 1 (2007).

[21] E. F. Wassermann, M. Acet, P. Entel, and W. Pepperhoff, J. Magn. Soc. Jpn. **23**, 385 (1999).

[22] S. Klotz and M. Braden, Phys. Rev. Lett. **85**, 3209 (2000).

[23] J. Neuhaus, M. Leitner, K. Nicolaus, W. Petry, B. Hennion, and A. Hiess, Phys. Rev. B **89**, 184302 (2014).

[24] L. Mauger, M. S. Lucas, J. A. Muñoz, S. J. Tracy, M. Kresch, Y. Xiao, P. Chow, and B. Fultz, Phys. Rev. B **90**, 064303 (2014).

[25] J. Neuhaus, W. Petry, and A. Krimmel, Physica B Condens. **234-236**, 897 (1997).

[26] F. Körmann, B. Grabowski, B. Dutta, T. Hickel, L. Mauger, B. Fultz, and J. Neugebauer, Phys. Rev. Lett. **113**, 165503 (2014).

Chapter 2

Experimental methods

Here I review the most relevant experimental techniques and their data analyses. All data presented in this chapter were collected for Fe-Ni Invar ($Fe_{65}Ni_{35}$), and relates to Chapter 5 where the Invar effect is discussed.

2.1 High pressures in diamond-anvil cells

Pressure is an important thermodynamic variable, describing the volume dependence of the internal energy U, and Helmoltz free energy F ($F = U - TS$):

$$P = -\left(\frac{\partial U}{\partial V}\right)_S = -\left(\frac{\partial F}{\partial V}\right)_T . \tag{2.1}$$

Being able to experimentally control the pressure enables us to better understand the interactomic interactions. Pressure alters all chemical, structural, mechanical, electronic, magnetic and phonon properties. Studying geological conditions at planetary core conditions requires extreme pressures up to hundreds of GPa, for example (100 GPa $\approx 10^6$ atmospheres). Pressure can even be used to look at temperature dependencies, such as the thermal expansion, through the Maxwell relation described in section 1.5 (Eq. 1.32):

$$\left(\frac{\partial V}{\partial T}\right)_P = -\left(\frac{\partial S}{\partial P}\right)_T .$$

Diamond-anvil cells (DACs) provide a well establish technique for *in-situ* pressure control. DACs are able to pressurize materials to pressures as low as ~ 0.1 GPa and up to 750 GPa [1], about twice the pressure of the Earth's core. An excellent review of diamond-anvil cell techniques is provided in [2].

The operation of a symmetric piston-cylinder DAC is depicted in Fig. 2.1. The sample is placed in between two opposing diamond anvils, within a chamber

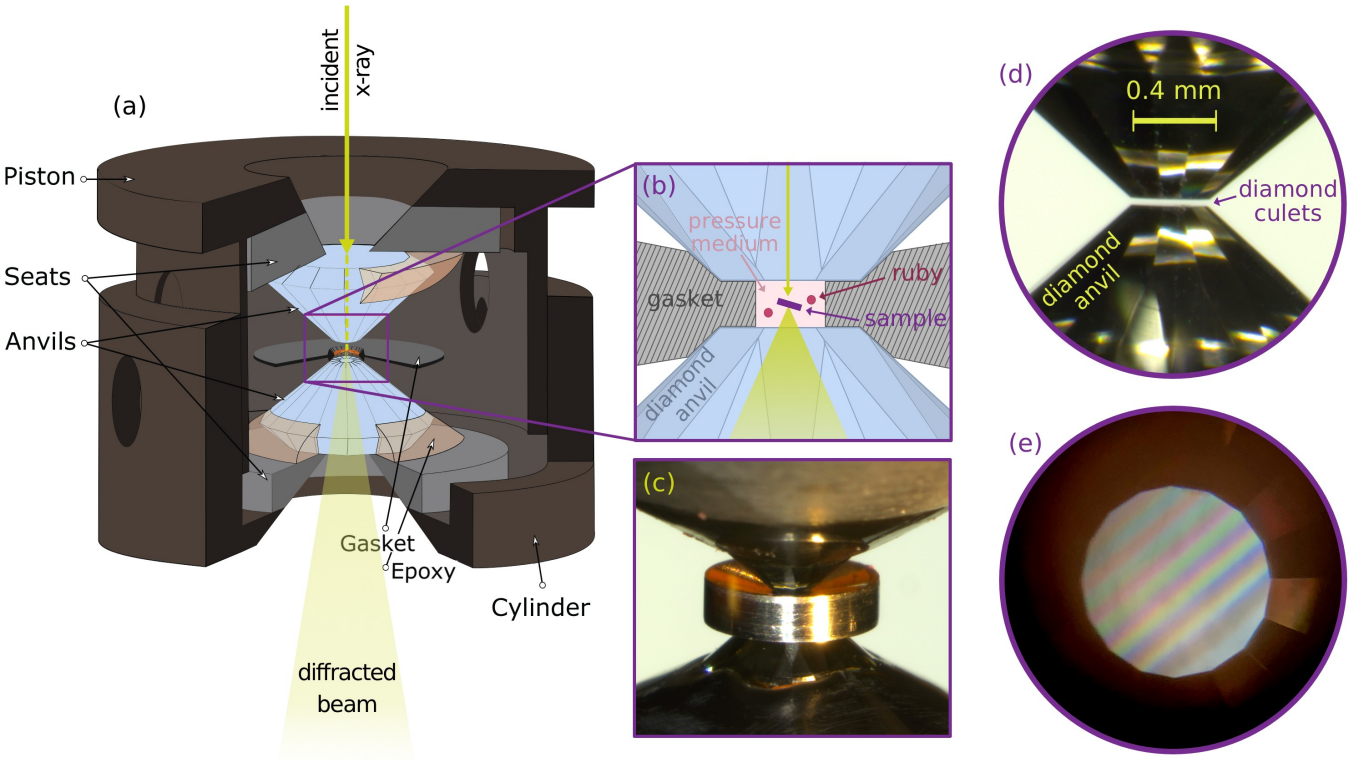

Figure 2.1: Operation of a diamond-anvil cell (DAC). **(a)** Schematic of a symmetric-type DAC [2]. **(b)** Detailed view of diamond culets indenting the gasket and pressurizing the sample chamber, which is filled with a pressure transmitting medium. The fluorescence spectrum of ruby spheres is used to determine the pressure. **(c)** Photo of diamond anvils pressing on a beryllium gasket. Beryllium is used for phonon measurements, because it is transparent to x-rays allowing the collection of the inelastic incoherent signal from the sides of the DAC. **(d)** Close-up view of the diamond-anvils showing the precise alignment of the culets. **(e)** Top view (through the diamonds) of the culets touching each other. If these Newton fringes are seen, the culets are not precisely parallel.

drilled in a gasket material. By pressing the piston against the cylinder (using screws or a pressurised bladder), high pressures are achieved at the sample environment. Diamonds are mostly transparent to x-rays, so the incident beam goes through a hole in the piston side, diffracts at the sample, continues through an opening in the cylinder and into the detectors. The diamonds do not press directly on the sample, but on the gasket, indenting the material and reducing the gasket hole (see Fig. 2.2 e and f). A pressure medium is used to fill the chamber and transmit hydrostatic pressure to the sample. The pressure is monitored by placing a reference material inside the pressure chamber. Measuring the x-ray diffraction of gold, or the fluorescence spectrum of ruby with a Raman spectrometer are typical methods to measure the pressure.

The tip of the diamonds are cut into a culet to provide a flat surface where the experiment can be built. Typical culet sizes range between 50 and 800 um, depending on the desired pressure. In any case, they are small, requiring small samples. Diamond-anvil cells are therefore ideal for experiments in synchrotrons, with small x-ray beam sizes, or with lasers such as Raman spectroscopy. The culets must be extremely well aligned (see Fig. 2.1 d), otherwise pressure concentrations will crack the diamonds. A technique to check if they are parallel to each other, is touching the culets and looking for Newton interference rings (shown in Fig. 2.1 e). Their appearance indicates that the light path length is not the same everywhere and that the culets are not precisely parallel.

Desirable materials for the gaskets are strong and stiff, able to withstand high pressures without cracking. Rhenium is a favorite. Our diffraction measurements used them as gaskets. To collect the incoherent inelastic spectrum for measuring phonons (described below), detectors are placed around the sides of the DACs, very close to the sample. Panoramic DACs with large side openings, as shown in Fig. 2.2 a and b, are used for these experiments. The diffracted signal has to travel sideways through the gasket to reach the detectors, so the gasket material has to be chosen carefully. Beryllium has a low x-ray absorption down to 5 keV, and has been used as high pressure gaskets up to 153 GPa [3]. We used beryllium for our inelastic phonon experiments. Beryllium is toxic, however, especially as fine powders or fumes. Indenting the gaskets and drilling the sample chamber hole needs to be done with care. We used the laser micro-machining system at the Advanced Photon Source (APS) [4].

Different pressure media can be used in DACs. Solids such as aluminum or magnesium oxides have been used [5]. They do not provide isotropic pressures at the sample, however, so liquid and gas media are preferred. A mixture of methanol–ethanol (4:1 ratio) is commonly used as a fluid medium, but its strength rises sharply above 10 GPa [6]. Gas media are preferred, especially inert gases that produce quasi-hydrostatic conditions up to 8 GPa in argon, 20 GPa in neon, and over 100 GPa in helium [2]. At high pressures, these gases transition into supercritical states, and even solidify. The hydrostatic limit and its distribution within a DAC were reviewed for 11 pressure media in [6]. Helium provides the best pressure transmission medium, even in its solid state above 12.1 GPa at 300 K. We therefore used helium in our experiments.

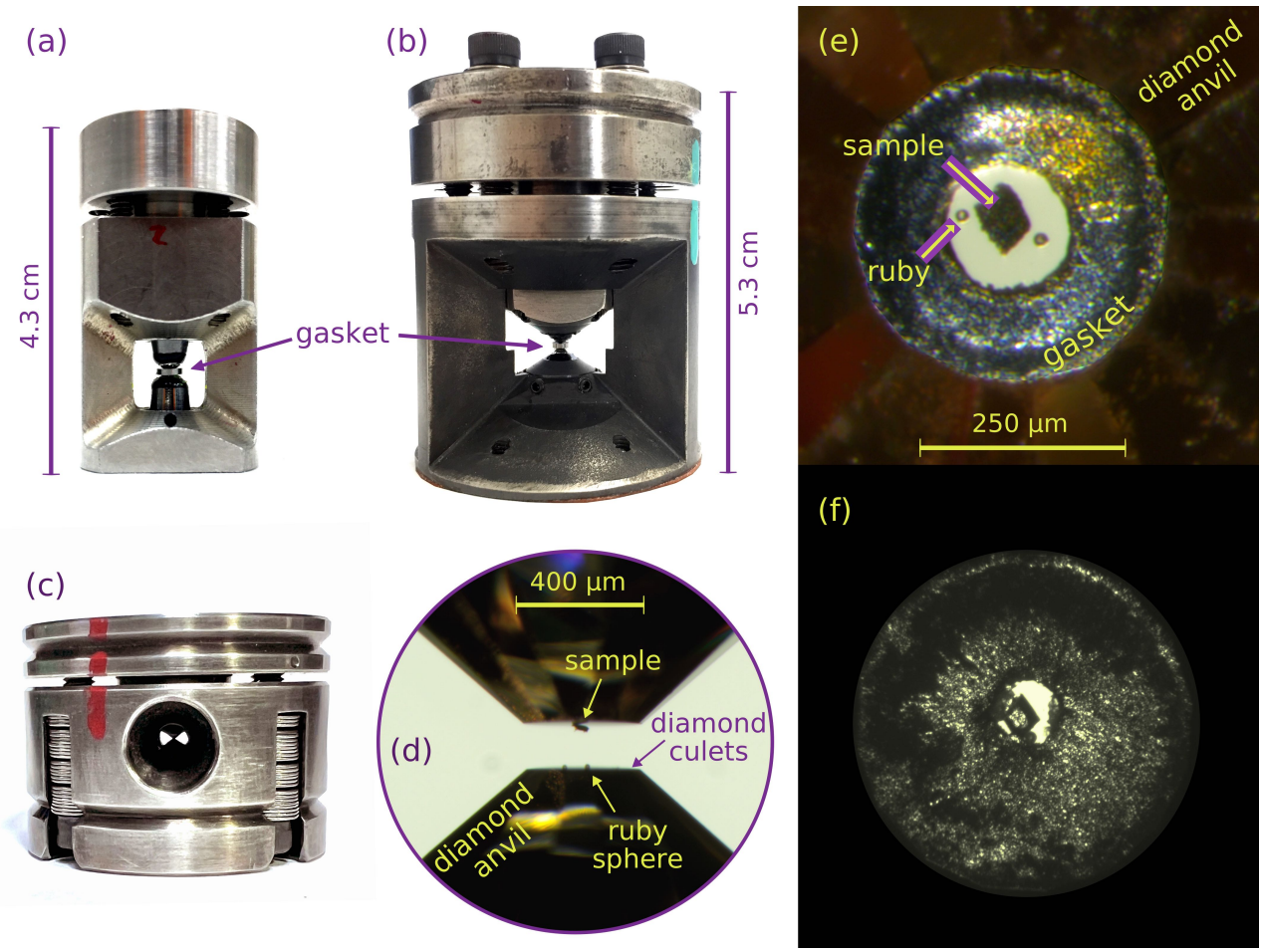

Figure 2.2: Diamond-anvil cells (DACs) used in this thesis. **(a)** Mini panoramic DAC for low-temperature NRIXS and NFS experiments, designed to fit inside the cold finger of a cryostat [7]. **(b)** Panoramic DAC for NRIXS and NSF. Large openings around the gasket allow APD detectors to get very close to the sample for collecting the weak inelastic signal. **(c)** Symmetric-type DAC for XRD experiments. **(d)** Close-up view of the diamond anvils (without gasket), showing the sample and rubies holding onto the diamonds by electrostatic forces. **(e)** Top microscope view of DAC. The sample and ruby spheres are placed inside the gasket hole, filled with helium gas for transmitting the pressure isotropically. When the pressure is increased, the diamonds compress the gasket and reduce the sample chamber volume. **(f)** Final state of a gasket with a shrunken chamber after achieving high pressures (~ 20 GPa).

To load the DACs for the experiments, we first indent the gaskets with the diamond culets. This ensures a well-sealed sample chamber. The gasket is then drilled by EDM or using a laser drilling system [4]. The small sizes of the diamonds limit the size of the samples, which were cut into squares of approximately 50 μm across. We then carefully placed the sample and the ruby spheres on the diamond culets (see Fig. 2.2 d) using tungsten needles under a microscope. The gasket is then placed on the anvil and the DAC is closed, such that the diamonds lightly touch the gaskets from both sides. The helium pressure medium must be loaded into the DACs at a high pressure (around 25,000 psi), otherwise the gasket hole will shrink too much to achieve high pressures. Our cells were gas-loaded with the help of beamline scientists at Argonne National Laboratory. The gas it trapped in the sample chamber medium by engaging the DAC screws which seals the gasket by the diamonds.

Simultaneous P & T control

The temperature of the sample can be controlled by heating or cooling the DACs. This is not straightforward, however. DACs are made out of different components with different thermal expansions. At high temperatures the stress bearing components, including the gasket, the seats for diamaond anvils, and the diamond anvil itself, limit the maximum attainable temperature and pressure [2]. There is also an intrinsic temperature limit from the rapid graphitization of diamonds above 1900 K, even in vacuum.

External furnaces provide precise and well-controlled temperature conditions. An example of a heating block design that encloses the entire DAC is shown in Fig. 2.3 a. These can be used to heat the DACs up to 700 K [2], and was used for our diffraction experiments of Chapter 5. For higher temperatures, a smaller resistive heater around the diamonds can offer a localized heat source [8]. Temperatures up to 1200 K have been achieved with this method. This works well for diffraction experiments where the diffracted beam is detected in the forward direction. For measuring the inelastic spectrum, however, the detectors need to have access to the sides of the DACs. Heating blocks and resistive heaters are not yet available for measuring phonons.

A cooling system designed for inelastic phonon experiments is shown in Fig. 2.3 b. [7]. The specially designed mini-DAC (Fig. 2.2 a) fits into a compact liquid helium flow cryostat system. Temperatures down to 9 K are achieved by flowing

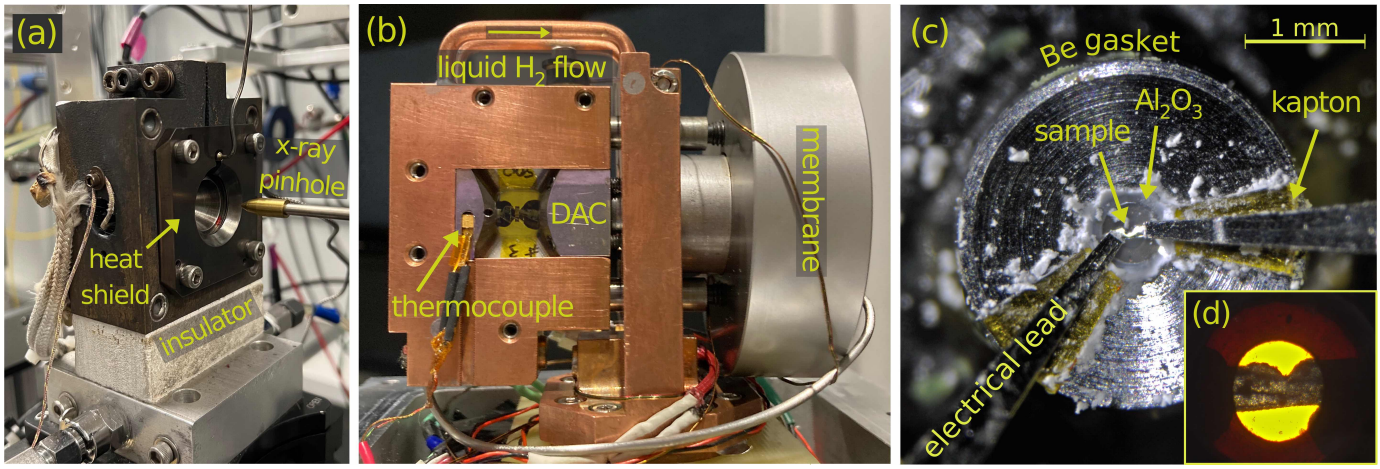

Figure 2.3: Controlling the temperature of DACs. **(a)** Heating block used at beamline 16 BM-D of the APS for diffraction experiments. The symmetric-type DAC (Fig. 2.2 c) is not visible inside the heat shield, and its pressure is controlled by a bladder membrane system. **(b)** Liquid helium flow-cryostat for cooling mini-DAC (Fig. 2.2 a) at beamline 3 ID-D of the APS [7]. The pressure is controlled remotely by a membrane system. A thermocouple monitors the temperature at the DAC, which is shielded inside a vacuum chamber (shielding and vacuum shroud not shown). **(c)** Internal resistive heating setup (gasket and sample are shown). Platinum electrical leads touch the iron sample to create an electrical circuit. The sample is notched to increase the local resistance and ensure localized heating. Leads are insulated from the beryllium gasket by kapton tapes and by using a boron insert in the center of the gasket (not visible). Aluminum oxide was used as the pressure medium. **(d)** View of the closed DAC with notched sample and partially transparent boron-insert.

helium through the DAC holder, which is shielded inside a vacuum chamber. A gas membrane system enables *in situ* tuning of the pressure without direct access to the DAC screws. Side windows allow detectors to get close to the diamond anvils from both sides.

Laser heating can provide very localized sample temperatures up to 7000 K [2], and has been used for inelastic techniques [9]. The temperature measurements are usually limited to above 1000 K, however [2]. For temperatures in the range of 300-1000 K an alternative internal resisitive heating method that heats the sample inside the pressure chamber of a DAC is possible [10, 11]. The sample itself can used as the conductive heating element and heating is controlled by the applied voltage through electrical leads in contact with the sample. Placing heating components in the 100 µm size DAC sample chambers has proven extremely challenging however [2]. I tried reproducing the heating setup described in [5], as shown in Fig. 2.3 c. Platinum leads touching the iron sample provide the electrical current from a power supply. They are insulated from the beryllium gasket by kapton tape and by using a boron insert for the

indented portion of the gasket (not visible). Additional electrical and heat insulation is provided by the aluminum oxide pressure medium. The sample has a notch to increase its resistance, ensuring a localized heat, and minimizing the heat flow into the beryllium gasket. Figure 2.3 d shows the closed DAC with the notched sample. It was extremely challenging to prepare this setup, and even after several attempts the electrical contact between the lead and the sample was lost. This happened either because the leads move or become damaged upon closing the DAC and pressurizing the diamonds. I strongly recommend an alternative heating design for anyone who might attempt this.

2.2 Inelastic neutron scattering (INS)

INS is a powerful and well established technique to measures the phonon dispersion of materials [12, 13]. Neutrons are heavy particles, able to transfer both a wide range of energy and momentum to the sample. Since neutrons do not have an electric charge, they do not interact with electrons, but can "hit" the nuclei and excite phonons. (They do posses a spin, making them also suitable for measuring the magnetic states of materials.)

By interacting with the lattice, neutrons can lose or gain energy depending on the frequency, ω, of the phonons created or annihilated by the incoming neutron (the energy of a phonon is given by $E = \hbar\omega$). Neutrons also exchange momentum with the sample depending on the orientation and wavelength of the phonon waves (the momentum of a phonon is $\mathbf{p} = \hbar\mathbf{k}$, where $|\mathbf{k}| = 2\pi/\lambda$ is its wavevector of wavelength λ). One neutron can sometimes create (or annihilate) more than one phonon, referred to as multi-phonon scattering.

We measured the phonon dispersions with the time-of-flight Wide Angular-Range Chopper Spectrometer, ARCS, at the Spallation Neutron Source (SNS) at Oak Ridge National Laboratory [14]. The wide angle of the detector bank at ARCS, ranging from -28° to 135° with respect to the incident beam, allows the collection of radiation with a large range of momentum transfers. At the SNS, neutrons are created through a spallation reaction, where a high-energy proton beam hits a liquid mercury target creating neutrons. The created neutrons are then slowed down by scattering in a water moderator, which reduces their energies to the thermal range. At ARCS, the energy is monochromated by passing the neutron beam through two Fermi choppers. These are cylinders with vertical slits, that rotate at certain frequencies, letting only a burst of

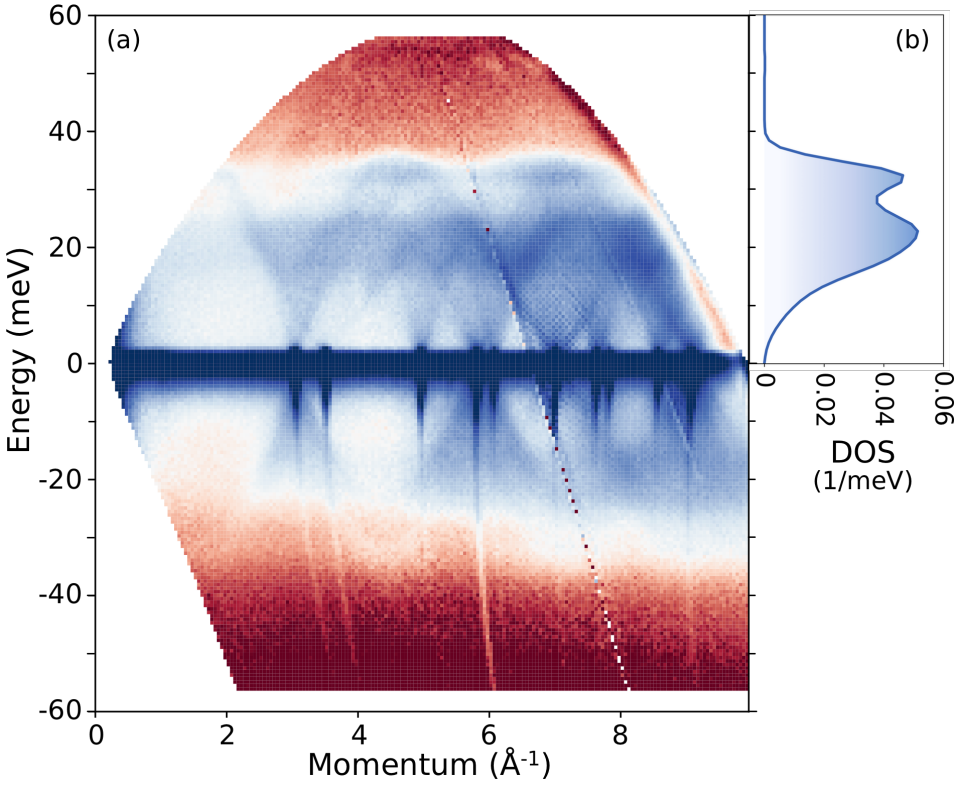

Figure 2.4: Phonon spectrum of polycrystalline Fe-36%Ni (Invar) measured by inelastic neutron scattering at ambient conditions. **(a)** Dispersion map showing the energy of phonons as a function of their momenta. **(b)** Energy spectrum of phonons, computed by integrating their dispersion intensities (of panel a) over the momentum axis.

neutrons of a certain energy pass through. The inelastic spectrum, i.e., the amount of energy transferred between neutrons and phonons, is measured by timing. Neutrons are heavy particles and their energy can be classically determined from their velocity ($E = 1/2mv^2$) [13]. The inelastic interaction with the sample are therefore determined by their speed, which is measured by the time it takes for a neutron to travel from the choppers, through the sample, and into the detectors.

The resulting data form a dispersion map, $S(Q, E)$, with momentum transfer, Q, on the horizontal axis and the energy transfer, E, on the vertical axis, as shown in Fig. 2.4 a for the case of Fe-Ni Invar. For these experiments we monochromated the incoming neutron beam to 60 meV, which sets the limit of the measured phonon energy and also the energy resolution of the experiment. The data cutoffs (white portions of the plot) correspond to the kinematic limits of the ARCS instrument. At zero energy transfer, E=0, we measure the elastic scattering, giving Bragg peaks from neutrons diffracted off the nuclei at

their equilibrium positions (analogous to x-ray diffraction). The inelastic spectrum ($E \neq 0$) follows specific directions in momentum space, corresponding to specific propagation directions of phonons in the material. Our measurements on a polycrystalline Invar plate capture the average of phonons propagating in all direction, as opposed to sharp dispersions of single crystals. This results in the superposition of modes and 'blurred' dispersions are seen in Fig.2.4. Nevertheless different branches from low- and high-transverse, and longitudinal modes are visible.

The intensities of the $S(Q, E)$ dispersion can be integrated over all momenta to give the energy spectrum of the atomic vibrations, the phonon density of states (DOS). The DOS gives the total number of states, or oscillator modes, available for phonons at a certain energy. It can therefore only consist of single phonon events, where one neutron interacts with one phonon. Corrections for multi-phonon and multiple scattering of phonons were performed using Mantid and the Multiphonon package [15, 16].

If the sample is placed inside a container, the scattering from the container has to be separately measured and subtracted as a background. The data are normalized by the proton current on target, and bad detector pixels are identified and masked. Corrections for detector efficiency are carried out using measurements from an incoherent scatterer (independent from momentum), such as vanadium. The resulting phonon DOS of $Fe_{65}Ni_{35}$ is shown in Fig. 2.4 b.

Inelastic neutron scattering requires large samples, because of the limited neutron flux and its large dimensions (about 5 cm x 5 cm at ARCS), compared to x-rays. The viability of experiments at high pressures, which usually requires small samples, is therefore also limited. High pressure neutron-diffraction measurements have traditionally used large sample volumes of at least $\sim 25\,\mathrm{mm}^3$ [17]. Correspondingly, large pressure Paris-Edinburgh cells, weighting about 200 tons, have been used with toroidal anvils reaching up to 10-20 GPa [18]. The high fluxes at the Spallation Neutron Source combined with newly developed methods to collimate and focus the beam into into small sizes, have allowed for neutron diffraction up to 94 GPa [17] and 115 GPa [19].

For measuring the inelastic spectrum, however, large samples are still required. Additionally, the pressure cell needs to allow for scattering at large angles to include a wide range of momentum transfers of phonons. Some preliminary experiments have been performed at ARCS with Paris-Edinburgh cells, how-

ever accounting for the background of neutrons scattering at the cell remains a challenge. We opt for well-established nuclear resonant x-ray scattering techniques described below.

2.3 Mössbauer spectroscopy

Mössbauer spectroscopy is a powerful resonant scattering technique to study the local environment of a resonant nucleus, giving information about its electronic, magnetic and structural properties [20]. Being resonant to the nuclear energies and sensitive to fluctuations in the nuclear environment, Mössbauer spectroscopy provides a view from the inside out of a material.

A Mössbauer spectrum shows the absorption energies of γ-rays by a resonant nucleus, such as ^{57}Fe, ^{191}Ir, ^{119}Sn, or ^{151}Eu. These absorption lines correspond to the transitions between different nuclear energy levels as shown in Fig. 2.5. An isolated ^{57}Fe nucleus has its first excited state ($I = 3/2$) at 14.41 keV from the ground state ($I = 1/2$). Interactions between the nucleus and its electronic environment, called hyperfine interactions, cause shifts and splittings of the nuclear energy spectrum.

The characteristic lifetime of the excited state of an ^{57}Fe atom is 141 ns, a relatively long time, especially compared to electronic transitions on the order of pico-seconds. According to the uncertainty principle, $\Delta E \sim \hbar/\Delta t$, these long lived states are extremely narrow in energy with $\Delta E = 4.7 \times 10^{-9}$ eV (see energy scale of Fig. 2.5 b). This unprecedented precision can be used with hyperfine interactions to quantify small changes in the environment of the resonant nuclei.

The probability density of s-electrons, and some relativistic p-electrons, is non-zero at the nucleus (revisit Fig. 1.1 a). Coulomb interactions of these electrons inside the volume of the nucleus with the nuclear charge give rise to an *isomer shift* of the nuclear energies. When the nuclear volume is known, the strength of isomer shift provides direct information about the electron density at the nucleus, and is useful to extract information about the electronic structure [21, 22]

The nuclear states have spins, associated with their magnetic dipole moments. When the nucleus experiences a magnetic field, such as in a ferromagnetic material, the energy of the nuclear states depends on orientation of the spins

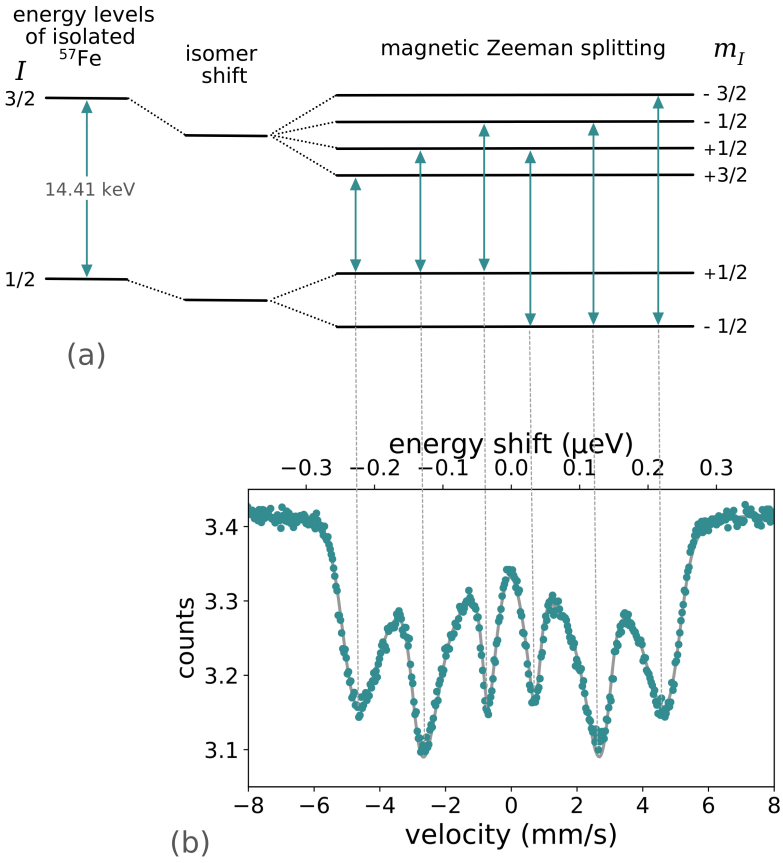

Figure 2.5: Mössbauer spectrum of Fe-Ni Invar. **(a)** Shifts of the nuclear energy levels of ^{57}Fe (with principal quantum number I) by an isomer shift and by the presence of a magnetic hyperfine field. States with different spins m_I with respect to the magnetic field shift by different amounts, resulting in a splitting of the energy levels. **(b)** Mössbauer spectrum of ferromagnetic $^{57}Fe_{65}Ni_{35}$ at ambient conditions measured with a conventional Doppler drive (velocity of the drive is the lower axis). It has the six absorption lines corresponding to the different nuclear transitions of panel a. The isomer shift is seen as a shift of the entire spectrum from zero energy shift (only a very weak effect for $Fe_{65}Ni_{35}$)

with respect to the magnetic field. Analogously to the Zeeman splitting of electrons, a magnetic field raises the spin degeneracy, and the nuclear states with different spins are split. For ^{57}Fe, there are six possible transition between the ground and the first excited states, as shown in Fig. 2.5. Since the splitting of the spectral lines is directly proportional to the magnetic field experienced by the nucleus, called the hyperfine magnetic field (HMF), Mössbauer spectroscopy is an effective method to measure this field [22].

Figure 2.6 a shows the effect of ferromagnetism on the Mössbauer spectrum of Fe-Ni Invar in different conditions. As the magnetization of the material decreases from a fully ferromagnetic state at 20 K, to ambient conditions, the

strength of the HMF decreases and the absorption lines are closer together. At 21 GPa, with the magnetism squeezed out by the high pressures, the material is paramagnetic and there is only a single absorption line.

In ^{57}Fe, the magnetic field experienced at the nucleus originates from unpaired d-electrons. The spin density of these outer unpaired electrons, polarize the core electrons, resulting in a net magnetic field at the nucleus [23–25]. The effective field at the nucleus is negative, or opposite to the direction of magnetization. Its intensity, however, is proportional to the bulk magnetization [26], so measurements of the hyperfine field can be used to determine the net magnetization of a material.

Mössbauer spectra can be fit to models of the hyperfine interactions, to extract hyperfine parameters such as isomer shifts, and strength of the HMF. We fitted our measurements using the CONUSS software package [27, 28]. The distribution of the HMF, $P(B_{hf})$, was approximated by two assymmetric Gaussian distributions, giving the field distributions of Fig. 2.6 b. At 20 K, the mean of the distribution is 33.7 Tesla (26.2 T at ambient conditions). This is a remarkably strong field; much stronger the field produced by an MRI magnet of about 1.5-3 T, and comparable to the 45 T field of the strongest (superconducting) magnet ever build.

In this thesis we use Mössbauer experiments to determine the magnetic state and the strength of the magnetic field of our materials. It can, however, be used to extract other parameters such as recoil-free fractions, isomer shifts and quadrupole splitting (which occurs in the presence of an electric field gradient) [21, 22]. These are sensitive to the chemical environments and can be used for quantitative phase analyses and determinations of the concentrations of resonant element in different phases, even for amorphous or nanostructured materials [20].

Experimental observation of nuclear resonance

In a conventional Mössbauer experiment, the resonant nuclei in the sample are excited by γ-radiation emitted from a source. For exciting ^{57}Fe nuclei, a ^{57}Co radioisotope embedded in a Rh matrix is typically used as a radiation source. The unstable ^{57}Co nucleus absorbs an inner-shell electron, and decays into a ^{57}Fe nucleus while emitting a 122 keV γ-ray [20]. The new ^{57}Fe nucleus is formed in the excited state ($I = 3/2$), and decays to the ground state emitting

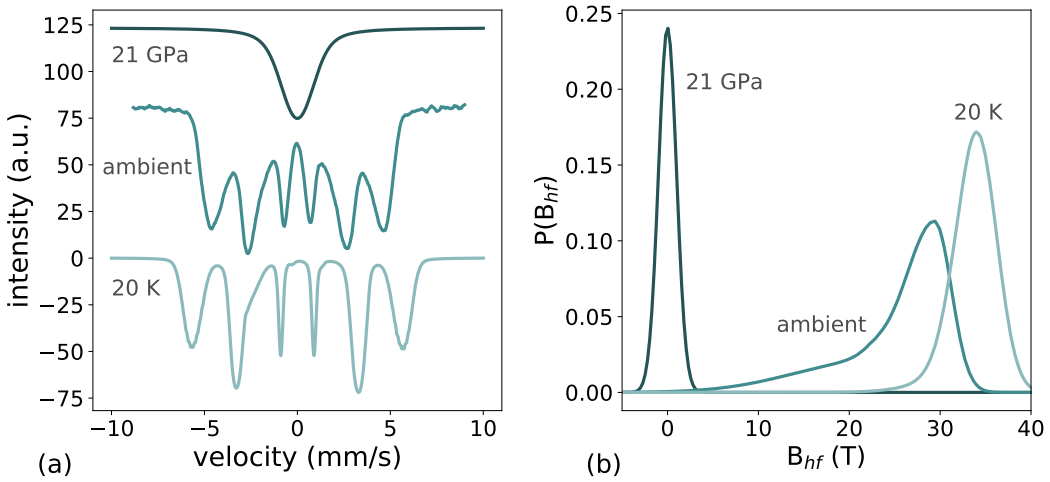

Figure 2.6: Dependence of Mössbauer spectra and hyperfine magnetic field of $^{57}Fe_{65}Ni_{35}$ on temperature and pressure. **(a)** Energy spectra at different conditions. At 20 K the material is strongly ferromagnetic, with well defined nuclear absorption lines. The magnetization is reduced at ambient conditions, so the nuclear energies are less split. At high pressures (21 GPa) well above the Curie transition, the material is paramagnetic with a single nuclear transition energy. **(b)** Distribution of the hyperfine magnetic field, showing the strength of the field experienced by the ^{57}Fe nuclei. They were computed from the spectra of panel a using CONUSS [27, 28].

another γ-ray of 14.41 keV. This is the useful emission which can be resonantly absorbed by the ^{57}Fe in the sample.

Experiments are usually performed in a transmission geometry, as depicted in Fig. 2.7, with the radiation from the source going through thin samples and into detectors. When the sample resonantly absorbs the γ-ray from the source, it re-emits radiation in all directions, removing intensity from the forward direction and lowering the count rate. We can correlate the measured count rate with the velocity of the Doppler drive to get the Mössbauer spectrum of Fig. 2.5.

As mentioned previously, these nuclear energies are extremely narrow with $\Delta E \sim 5\,\text{neV}$. Any disturbance in the nuclear environments of either the source of the sample would cause a mismatch and hinder the resonant absorption of the γ-rays, even the recoil of a nucleus when emitting or absorbing the radiation. Therefore recoilless emission by the source and absorption by the sample are necessary. An isolated nucleus cannot be in resonance because it recoils. If embedded in a solid, the recoil energy can be transferred to the entire lattice and resonance becomes possible.

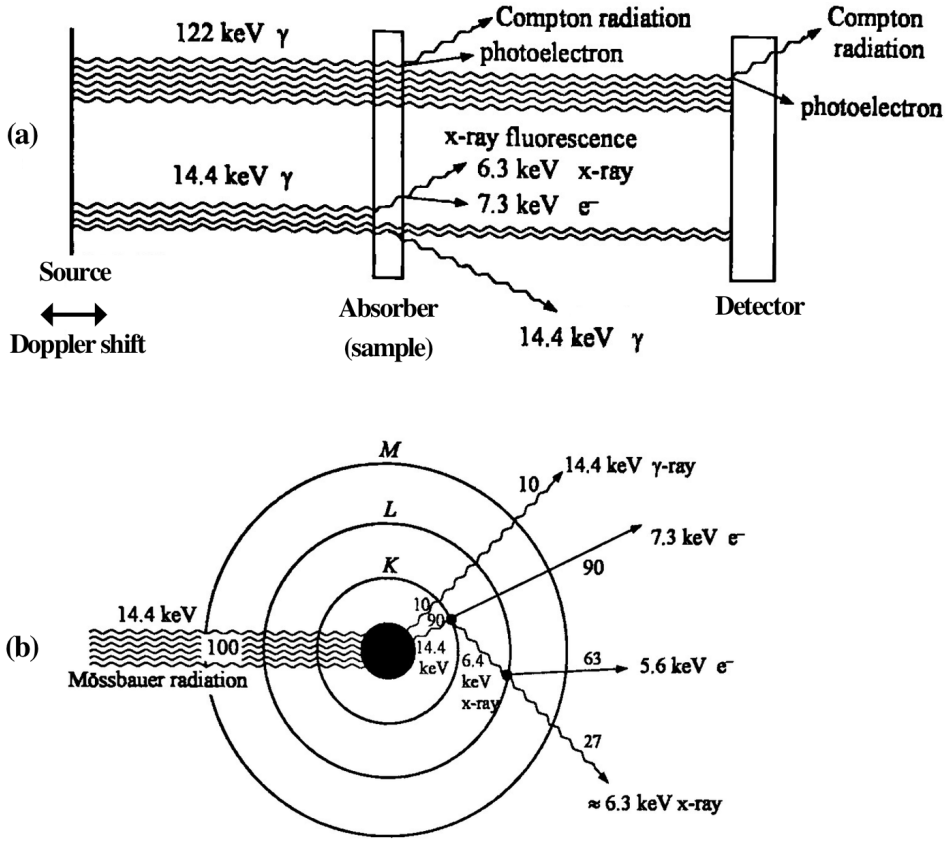

Figure 2.7: Schematic of Mössbauer experiment. **(a)** Conventional experimental setup in transmission geometry. γ-radiation is produced by a ^{57}Co source, placed on a Doppler drive to provide an energy scan. The radiation is partially absorbed by the sample, whenever the energy matches precisely an absorption line of the ^{57}Fe nuclei. The absorbed radiation is re-emitted in all directions through different channels (see panel b for details). This reduces the intensity of the radiation reaching the detectors, causing a dip in the count rate and resulting in the spectrum of Fig. 2.5. **(b)** Resonant absorption at the ^{57}Fe nuclei and re-emission through different channels. Only part of the radiation is emitted as 14.4 keV γ-rays. Most of it decays through the internal conversion channels interacting with the inner electronic shells (see text). Adapted with permission from [29].

Such a recoil-free resonance of γ-radiation was first observed in 1957 at the Max Planck Institute in Heidelberg, Germany. Its discoverer, a 29 year old PhD student named Rudolf Mössbauer, was quickly awarded the 1961 Nobel Prize in physics. Shortly after hearing the news about the resonant γ-ray absorption in $^{1}91$Ir, Richard Feynman invited Mössbauer to come work in California. Mössbauer was a researcher at Caltech when the Nobel Prize was announced, and after an emergency faculty meeting, he was promoted to full professor in early 1962, the fastest promotion case in Caltech history.

In order to see such a recoil-free absorption we need to scan the incident energy around 14.413 keV. An energy scan in the sub μeV range is achieved by placing the ^{57}Co source on a electromagnetic Doppler drive. It shifts the energy of the emitted radiation depending on the relative speed of the source to the sample by $\Delta E = (v/c) \cdot 14.41\,\text{keV}$. The velocity of the oscillating drive is typically plotted as the horizontal axis in a Mössbauer spectrum.

After resonantly absorbing γ-rays, only 10.9% of the energy is re-emitted by the ^{57}Fe nuclei as γ-rays [20, 29]. Most of it is transferred to the electrons through *internal conversion* processes, where an electron is ejected from the atom and a lower energy x-ray is emitted. Figure 2.7 b shows more details of these different decay channels. Gas-filled proportional counters or solid-state detectors are used for detecting such electrons and x-rays. A backstatter (reflection) geometry is also possible, where electrons emitted from the sample surface are counted by detectors. This is especially useful when thin samples are difficult to prepare. Backscatter geometry was also used for the miniature Mössbauer spectrometers that are on board the Mars Exploration Rovers (Spirit and Opportunity), to probe the landscape of and provide evidence of water on the surface of Mars [30, 31].

Mössbauer experiments are solely sensitive to the resonant isotopes. There is no background from other materials placed in the experimental setup, although an uniform and constant background occurs from other x-ray processes and detector noise. The samples, however, have to be prepared with such isotopes. The natural abundance of ^{57}Fe is 2.2%, so samples are often made with 95-99% enriched ^{57}Fe to shorten the collection time.

With due care and the use of point-sources, it is possible to perform Mössbauer spectroscopy at high pressures, with samples in diamond-anvil cells. Due to the small sample sizes, however, long acquisition times are necessary resulting

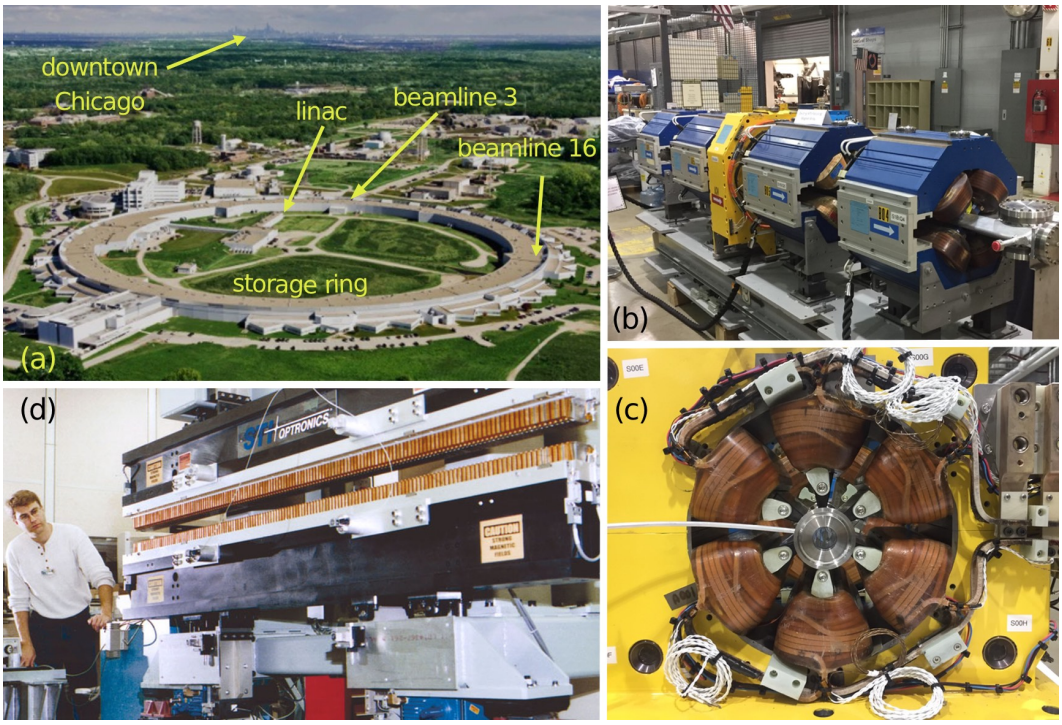

Figure 2.8: Advanced Photon Source (APS) at the Argonne National Laboratory. **(a)** Aerial view of the APS. **(b)** Electromagnets used to keep the electrons in a narrow beam while traveling around the storage ring. **(c)** Cross-sectional view of a sextupole electromagnet, showing the vacuum tubes in which the electrons travel close to the speed of light. **(d)** Undulator insertion device. The series of magnets with alternating polarity make the electrons wiggle along their path, creating a coherent beam of x-rays in the propagation direction.

in lower signal-to-noise ratios. The strong and narrow x-ray beam produced at synchrotron provides a better alternative.

2.4 Synchrotron radiation - Advanced Photon Source

X-ray creation

High energy x-rays are created from high speed electrons at synchrotrons. At the Advanced Photon Source (APS) of the Argonne National Laboratory (see Fig. 2.8 a), the electrons are first emitted from a hot cathode and accelerated by a high-voltage in the linear accelerator (linac). The electrons are injected into an accumulator ring which compresses the electron bunches into short pulses of less than 1 ns. The booster synchrotron then accelerates these pulses using electromagnets up to 7 GeV, with electrons traveling at >99.999999% of the speed of light.

The high-energy electron bunches are injected into a 1104 m circumference storage ring [32]. They are kept in vacuum into a narrow beam by electromagnets (shown in Fig. 2.8 b and c). The storage ring is not a perfect circle, but a consists of 40 straight sections. Between each of these sections, the beam is bent by bending magnets. When electrons undergo such accelerations to change path directions, they emit radiation. X-rays with a wide range of energies are created (white beam) [33, 34], which can be monochromated depending on the specific use. The x-ray diffraction measurements presented in Chapter 5 used 27 keV x-rays produced by such a bending magnet (BM) at beamline 16 BM-D.

An alternative way to create x-rays in the storage ring uses undulators (see Fig. 2.8 d). A sequence of magnets with alternating polarity makes electrons oscillate along their path. At each oscillation, x-rays are created and interfere coherently in the beam direction. The x-rays interfere constructively at specific energies depending on the spacing of the magnets [32, 33]. Such an undulating insertion devices were used for nuclear resonant scattering experiments at beamlines 3 ID-D and 16 ID-D of the APS.

Beamlines for nuclear resonant spectroscopy

For nuclear resonant absorption, the x-rays must be monocromated. At beamlines 3 ID-D and 16 ID-D of the APS, this is performed by a series of two monochrometors [32, 35–37]. The x-ray created at the undulator is reflected by two single crystal of silicon mirrors, as depicted in Fig. 2.9 a. Only the (111) Bragg reflection is selected by the second mirror, so only a narrow energy width of about 1.5 eV proceeds. These mirrors must be actively cooled, since they absorb most of the high energy beam. The x-rays are then sent into a second monochromator consisting of four sillicon crystals. Here, higher order Bragg reflections are selected, resulting in an even narrower energy width of about 1 meV. Selecting such a monochromated beam out of a high energy 14.41 keV x-ray is a remarkable feat. It corresponds to a precision of $2 \cdot 10^{-5}$ % of the incident energy.

After being monochromated, the beam is focused by Kirkpatrick–Baez (KB) mirrors into the diamond-anvil cell (DAC) and irradiates the sample. Avalanche photon diode (APD) detectors in the forward direction record the nuclear absorption spectrum, while three APD detectors placed around the DAC collect

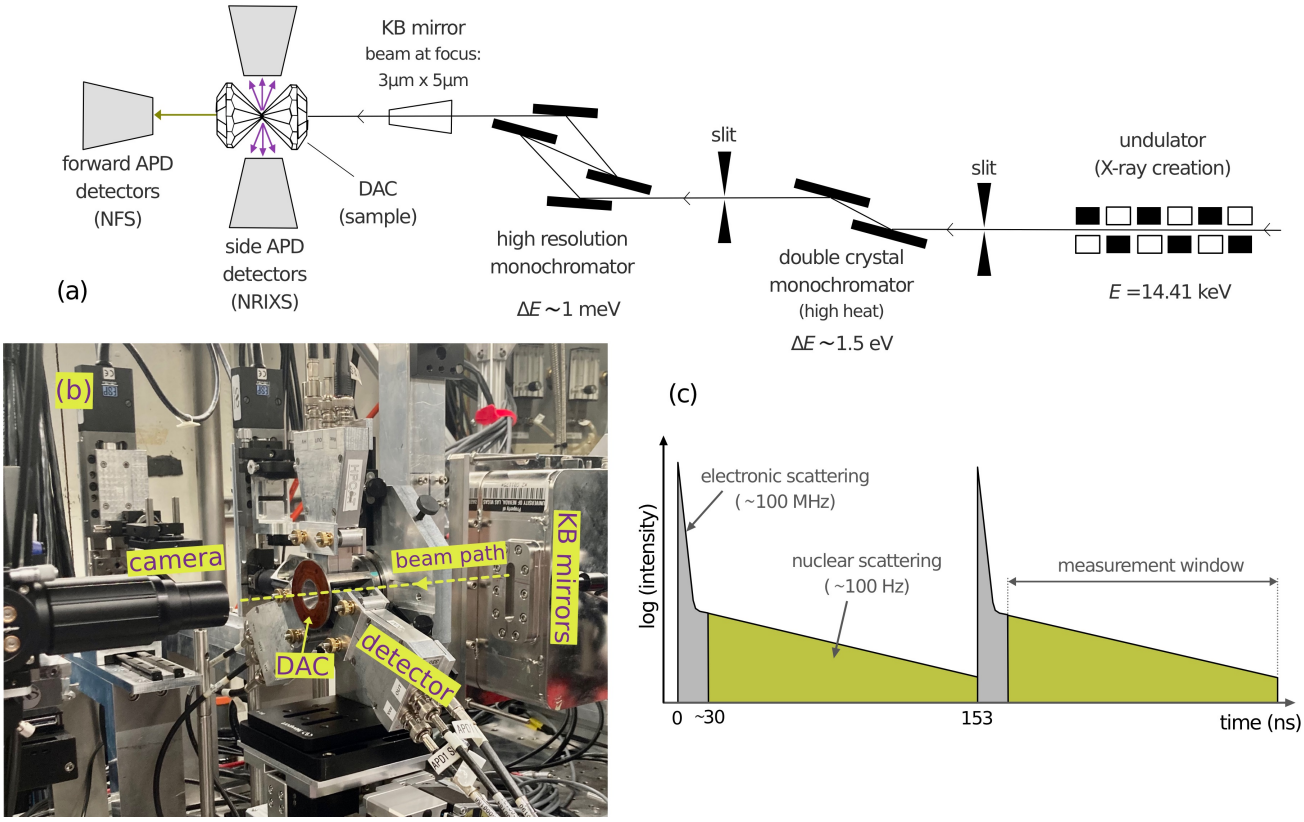

Figure 2.9: Experimental setup for nuclear resonant experiments at beamlines 3 ID-D and 16 ID-D of the APS. **(a)** From right to left: the electrons pass through undulators and create x-ray around 14.41 keV. The beam passes first through a high heat monochromator and then through a high-resolution monochromator for an energy resolution of about 1 meV. The beam is then focused into the sample with KB mirrors. Side APD detectors collect the NRIXS spectrum, with the forward detector measures the NFS. **(b)** Photo of the experimental hutch of beamline 3 ID-D. Three APD detectors are placed around the opening of a panoramic DAC (Fig. 2.2 b). The forward detector is not shown. A camera with a microscope and a Raman spectrometer can be moved in and out of the beam. They are used to monitor the sample and determine the pressure inside the DAC through the fluorescence spectrum of a ruby reference (see Fig. 2.2 e). **(c)** Timing of the x-ray radiation hitting the sample, created by electronic bunches separated by 153 ns.

the inelastic spectrum (discussed below). APD detectors are nearly ideal for time-resolved x-ray measurements. They have a large dynamic range, sensitive to x-rays in the 5-20 keV range, and importantly, have a good time resolution (< 1 ns) with low noise [38].

The timed nature of the synchrotron radiation, with x-ray bunches hitting the sample every 153 ns at the APS [39], is essential for the nuclear resonant experiments. X-rays excite all sort of electronic transitions in the material along with nuclear excitations, and detectors cannot discern between their energies. However, while the electrons decay back to their ground states quickly, on the order of pico-seconds, the nuclear states have a much longer lifetime, as depicted in Fig. 2.9 c. Their narrow energy width of $\Delta E = 4.7 \times 10^{-9}$ eV for ^{57}Fe, corresponds to characteristic lifetimes of 141 ns. Since the detectors have good time resolution, we can wait for the electronic transitions to decay to start collecting data[1].

2.5 Synchrotron Mössbauer spectroscopy

In conventional Mössbauer spectroscopy, the absorption lines of a resonant nucleus are measured as a function of energy, as previously discussed in detail. While high-resolution monochromators at synchrotrons have an impressive energy precision of $\sim$1 meV, they are off by three orders of magnitude for Mössbauer experiments, which require a sub-μeV energy scan.

By keeping the incoming energy fixed and oscillating the sample position (analogous to using a Doppler drive for the γ-ray source), Gerdau et al. [40] were able to observe nuclear absorption at a synchrotron for the first time in 1985. While this was exciting, the energy resolution at synchrotrons is inherently too low for quantitative analyses of Mössbauer spectra in energy domain.

A more suitable technique used the timed nature of synchrotron radiation, with short x-ray pulses every 153 ns, to circumvent the need of energy scans altogether [39]. The nuclear decay can be measured as a function of time instead of Doppler-shifting the energy. The synchrotron radiation excites all

[1] The Advanced Photon Source is about to be upgraded (starting in April 2023). To increase the brightness of the x-rays by up to 500 times, the number of electron bunches in the storage ring will be doubled from 24 to 48. While a stronger beam is favorable for most experiments, the upgrade will reduce the time window available to measure the nuclear decay by half [34].

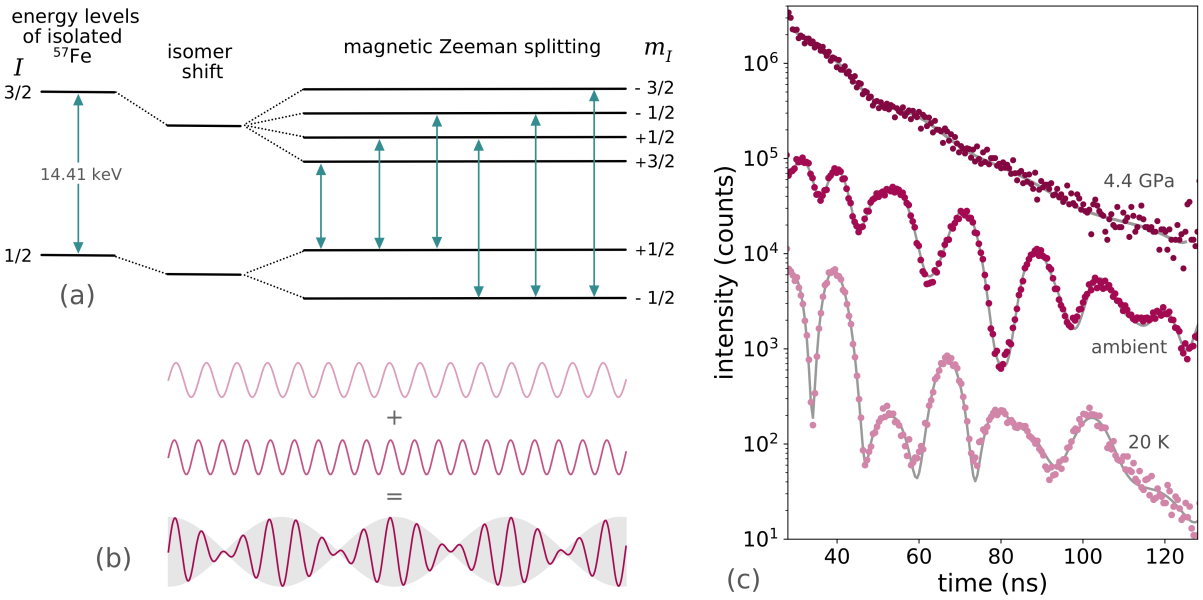

Figure 2.10: Mössbauer spectroscopy in time domain. **(a)** Splitting of nuclear energies of ^{57}Fe due to a magnetic field (from Fig. 2.5). **(b)** The sum of two sinusoidal waves with slight different frequencies results in a wave with intensity modulations, or "beats". **(c)** Measured NFS spectra showing the intensity modulation due to interference of the six energy lines of ^{57}Fe (panel a). The period of the modulations is used to infer the strength of the hyperfine magnetic field. Solid lines are fits to data using CONUSS [27, 28]. At low temperatures, the sample is strongly ferromagnetic resulting in NFS spectra with well defined beats of short periods. With increasing temperatures (or pressures) the magnetic beats are broadened in time. At 4.4 GPa, close to the Curie transition, the NFS spectrum is almost an exponential decay at a single energy.

nuclear states at once, and the interference of the six energy transitions of ^{57}Fe is observed in time. Unlike the insufficient energy resolution of the monochromators, the APD detectors have an excellent time response [36].

When two sinusoidal waves with slight different frequencies are added together, as shown in Fig. 2.10 b, they result in a wave with intensity modulations, or "beats". You may have heard such binaural beats to relax, or to enter a meditative state, where the intensity modulation is perceived as a ringing of the volume. What is important here is that by measuring the period of the modulation, the difference in frequency of the two waves can be quantified.

For the nuclear decay of ^{57}Fe, waves with six slight different energies interfere with each other coherently [39, 41]. This results in complicated interference beats, but the idea is the same: we can determine the magnetic Zeeman splitting by measuring the modulation period. The shorter the beat period, the larger the energy separation between the states, and the stronger the mag-

netic field. Examples of such intensity modulations of the nuclear transition are shown in Fig. 2.10 c. At 20 K the material is ferromagnetic with a strong field, so the beats have short periods (this time spectrum corresponds to the energy-Mössbauer spectrum of Fig. 2.6 a). At ambient conditions, the material is less magnetic and the beats are slightly broader in time. The Curie transition in $Fe_{65}Ni_{35}$ happens near 4.4 GPa, giving a nearly exponential decay from a single nuclear transition (straight line in the logarithmic plot). This corresponds to a absorption line of a paramagnetic material, without any magnetic Zeeman splitting.

The same information can be extracted from Mössbauer measurements in either the time or energy domains. One is simply the Fourier transform of the other. We used the CONUSS [27, 28] software package to fit these time spectra and extract the distribution of the the hyperfine magnetic field (as those shown in Fig. 2.6 b). The fits are included as solid lines in Fig. 2.10 c.

The coherent time interference is measured in a transmission geometry at the synchrotron, with an APD detector placed in the forward direction. The time-domain synchrotron Mössbauer technique is, therefore, also known as nuclear forward scattering (NFS).

2.6 Nuclear resonant inelastic x-ray scattering (NRIXS)

NRIXS is a technique that exploits the narrow resonant nuclear absorption by a Mössbauer active isotope to measure the inelastic spectrum of phonons [39, 41]. By scanning incoming x-ray energy around the nuclear absorption energy, the full phonon spectrum of the resonant nucleus can be observed, as shown in Fig. 2.11. X-rays can be focused into very small beams, making this technique ideal for high pressure experiments, with materials inside DACs.

Being a resonant technique, only the active isotope is excited and there is no background signal. Figure 2.11 therefore, arises from the partial phonon DOS of ^{57}Fe in the Fe-Ni lattice. This resonant selection can be extremely useful. It enables, for example, the probe of a single atom at the active site of a complex biomolecule, while avoiding interference from thousands of other atoms [42]. It can also be a nuisance, when computing bulk thermodynamic quantities, for example. For our Fe-Ni alloys, this turn out not to be a problem. Since both Fe and Ni have very similar masses and similar vibrational properties, the partial

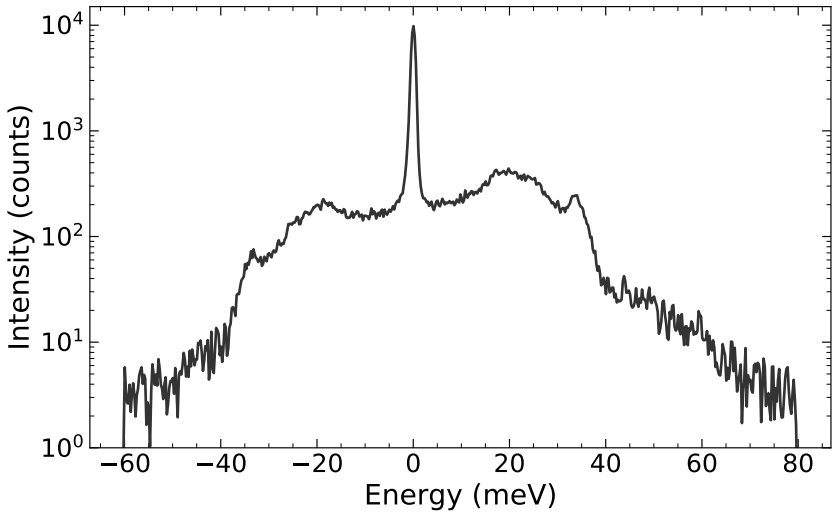

Figure 2.11: NRIXS spectrum of $^{57}Fe_{65}Ni_{35}$ at ambient conditions. The resonant absorption of the ^{57}Fe through the Mössbauer effect gives the strong elastic line at E=0. The inelastic phonons spectrum of ^{57}Fe is prominent up to about ± 40 meV. Beyond this, the spectrum is dominated by multi-phonon scattering (discussed below).

DOS of ^{57}Fe is representative of the full phonon DOS [43]. We confirmed this for our materials by preforming inelastic neutron scattering (results shown in Chapter 5). This is not universal. Fe and V, for example, have very different partial vibrational spectra [44].

Development of NRIXS

The idea of using the resonant absorption to measure the inelastic phonon spectrum is not new. In fact, it was proposed immediately after Mössbauer was able to collect the first nuclear resonant spectrum [45]. Resonant absorption has such a narrow width ($\sim$ neV), that it would offer an ideal resolution to measure the inelastic spectrum. We "only" need to provide an energy scan around the resonant energy for collecting the phonon spectrum. A Doppler drive, typically used in Mössbauer experiments, would have to reach velocities in the order of 1 km/s to scan an energy range of about $\pm$ 5 meV. Such a setup has been attempted by using high speed centrifuges [46]. However, there is another inherent problem. Since the nuclear spectrum is so narrow, the probability of an inelastic excitation at that precise energy is very low [39]. It requires, therefore, a strong radiation with 10^6-10^7 photons/s to be measurable [47].

Fortunately, both problems have been solved. Very intense radiation is available at third generation synchrotrons. The APS, for example, is able to provide 10^9 photons/s at 14 keV [48]. The energy scanning problem was solved by developing high-resolution monochromators with $\Delta E \sim$1 meV [35–37, 49]. The monochromator crystals can be slowly rotated to provide the energy scan. The first inelastic spectra using nuclear resonant absorption at a synchrotron were observed in Japan [50, 51]. Sturhan et al. [51] recognized the incoherent nature of the inelastic interactions, and placed the detectors next to the sample, perpendicular to the incident beam, as it is done nowadays (see Fig. 2.9).

When a photon is scattered inelastically by the sample, as is the case for NRIXS, it acquires a certain phase shift and loses coherence with the incident radiation [39, 41]. If the phase shift is random for different nuclei it also becomes specially incoherent, and the signal has no phase information (in contrast to the phonon dispersions measured by inelastic neutron scattering). The data can therefore be collected from any solid angle. In the forward direction, for time-domain Mössbauer, the elastically scattered beam is coherent. The detector is placed far away from the sample, so the path lengths of waves emitted from different nuclei are indistinguishable and they have the same phase (spatially coherent). Without coherence, no interference would take place and the intensity modulations of Fig. 2.10 c would not be seen.

The NRIXS spectrum & data analysis

To collect the inelastic spectrum, the crystals of the high-resolution monochromator are slowly rotated, shifting the energy of the incoming x-ray beam. Since the nuclear absorption is very narrow, resonance with the ^{57}Fe is lost. The only way to detect a signal is if phonons are created or annihilated in the material by interactions with the x-rays. For example, an incoming photon with energy of E_0 + 25 meV, can excite both the nucleus and a phonon of 25 meV. By performing an energy scan around resonance, we can collect the full phonon spectrum. Figure 2.12 shows representative NRIXS spectra of $^{57}Fe_{65}Ni_{35}$ under pressure in a diamond-anvil cell at room temperature and 30 K.

At positive energy transfer, phonons are created in the material, while negative energies correspond to annihilation of phonons. In order to annihilate a phonon, it has to exist in the material. At 30 K, practically no phonons

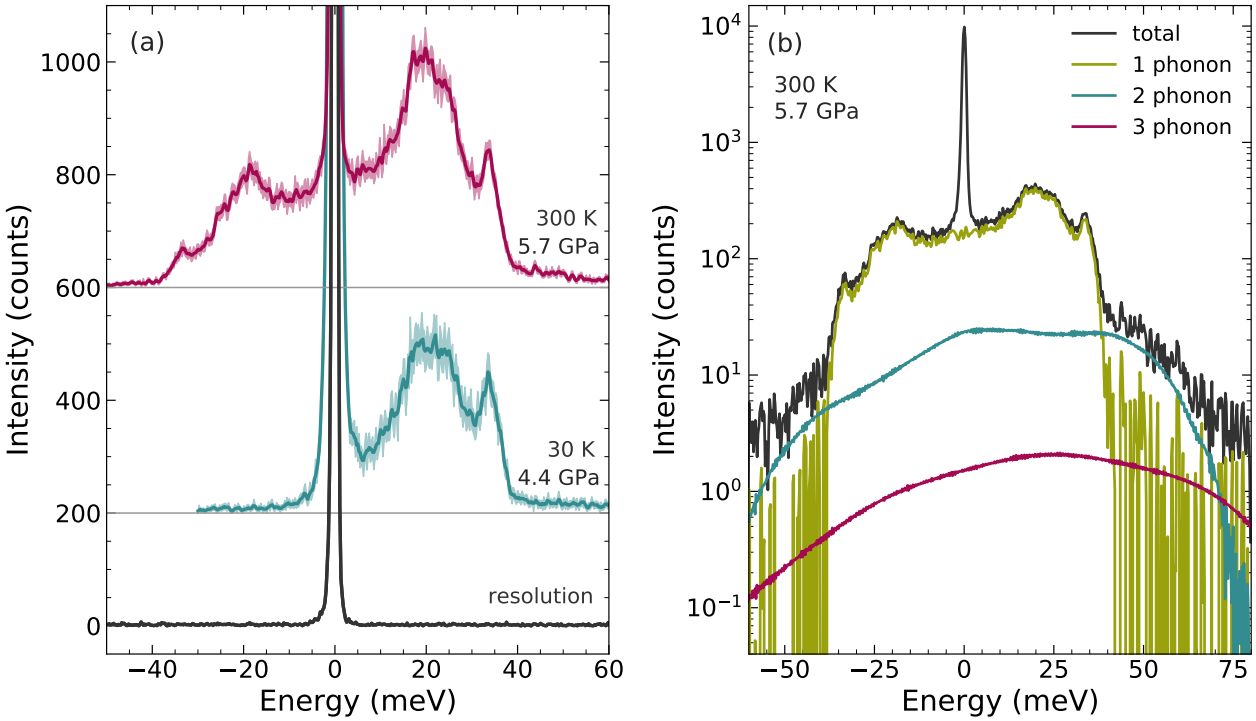

Figure 2.12: NRIXS spectra of $^{57}Fe_{65}Ni_{35}$. **(a)** Representative raw NRIXS data showing the inelastic spectrum at different conditions (full elastic peak not shown). Positive energies represent the creation of phonons by x-rays, and negative energies their annihilation. The probabilities of these events follow the Boltzmann factor of Eq. 2.2. At 30 K practically no phonons exist to be annihilated. The resolution function has a full-with half-maximum of 1.1 meV. **(b)** NRIXS spectrum in a logarithmic scale showing excitations of 1, 2, and 3-phonons (multi-phonon scattering). Only 1-phonon events are useful for computing the density of states.

exist above $\sim$ 3 meV, so the inelastic spectrum consists only of the creation of phonons at positive energies. The creation and annihilation processes follow detail balance; they are analogous to Stokes and anti-Stokes lines in Raman spectroscopy. Their scattering probabilities $S(\pm E)$ are balanced by the Boltzmann factor as [39]:

$$S(+E) = e^{E/k_B T}\, S(-E)\,. \tag{2.2}$$

The measured spectrum has an elastic and an inelastic component $S'(E)$. They can be separated as [51, 52]:

$$S(E) = f_{LM}\left[\delta(0) + S'(E)\right]\,, \tag{2.3}$$

where $\delta(E = 0)$ is a delta-function describing the resonant absorption and f_{LM} is the Lamb-Mössbauer factor, or the probability of a recoil-free resonant

absorption. For $^{57}Fe_{65}Ni_{35}$ at ambient conditions, $f_{LM} = 0.69$. This elastic line, $\delta(0)$, is broadened by the instrument resolution, with a full-width half-maximum (fwhm) of 1.1 meV in our experiments. For further analysis of the inelastic spectrum, the elastic peak is removed by fitting the resolution function to the measured spectrum $S(E)$, as shown in Fig. 2.12 b.

The inelastic spectrum $S'(E)$ consists of mostly one-phonon processes, where an incoming photon interacts with a single phonon. However some photons can excite multiple phonons, giving rise to a non-zero signal above the vibrational cutoff energy of about ± 40 meV. The total inelastic spectrum consist of one-phonon and multi-phonon contributions:

$$S'(E) = S'_1(E) + S'_2(E) + S'_3(E) + ... \tag{2.4}$$

In the harmonic approximation, the higher order terms can be expanded in terms of the one phonon contribution as [27, 39, 41, 52]:

$$S'_n(E) = \frac{1}{n}\int_{-\infty}^{+\infty} S'_1(E')S'_{n-1}(E-E')\mathrm{d}E' \,. \tag{2.5}$$

The one-phonon contribution is extracted from the measured NRIXS spectrum through a Fourier-log method described in [27]. This was performed using the PHOENIX software [28] after removal of the elastic line. The resulting 1, 2, and 3-phonon contributions to the NRIXS spectrum are presented in Fig. 2.12 b. The 2-phonon processes become prominent above 40 meV, while the 3-phonon contribution dominates the spectrum above 70 meV.

Phonon DOS and entropy

The phonon density of states, $g(E)$, is computed from the 1-phonon contribution as [27, 39, 41, 52]:

$$g(E) = \frac{E}{E_R} S'_1(E)(1 - e^{-E/k_B T}) \,, \tag{2.6}$$

with E_R being the recoil energy of the free nucleus (1.956 meV for ^{57}Fe). The resulting phonon DOS of Fe-Ni Invar at 5.7 GPa is shown in Fig. 2.13. A constant background is subtracted from the NRIXS signal, such that the noise of the DOS above a cutoff energy has a zero mean (details in the appendix of Chapter 5).

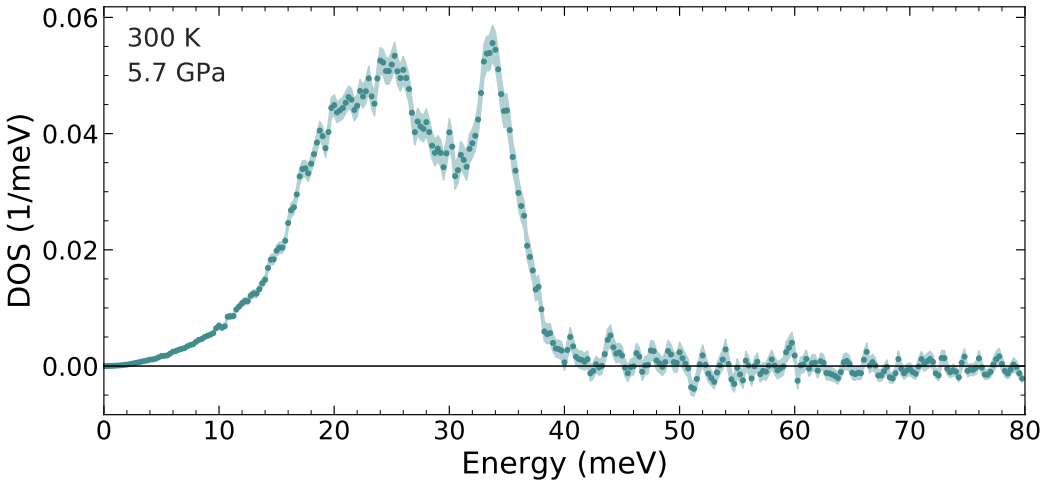

Figure 2.13: Phonon density of states (DOS) of $^{57}Fe_{65}Ni_{35}$ at 5.7 GPa and room temperature. It was computed using PHOENIX [27] from the one-phonon NRIXS spectrum of Fig. 2.12 b, after a background subtraction. The error bars were propagated from the standard deviation of Fig. 2.12 a, with a Monte-Carlo method. (Details about background subtraction and error propagation are found in the appendix of Chapter 5).

To compute the phonon entropy, we integrate the phonon DOS with a weighting factor of the energy distribution of phonons (as discussed in section 1.3). Within the harmonic model, the entropy is (Eq. 1.14):

$$S_{ph} = 3k_{\mathrm{B}} \int_0^\infty g(\varepsilon) \left[(1 + n_T(\varepsilon)) \ln(1 + n_T(\varepsilon)) - n_T(\varepsilon) \ln n_T(\varepsilon) \right] \mathrm{d}\varepsilon \,. \qquad (2.7)$$

However, experimental data are not harmonic. The measured phonon energies depend on the temperature and pressure of the sample. Fortunately Eq. 2.7 for the phonon entropy includes non-harmonic effects to first order if $g(\varepsilon)$ is the experimental DOS at finite temperatures and pressures [53].

Since the entropy is an integrated quantity (a weighted average of the DOS) the statistical errors are reduced upon integration. For the spectrum of Fig. 2.13 at 5.7 GPa, the entropy and its standard deviation are $3.32 \pm 0.01\, k_{\mathrm{B}}$/atom. The appendix of Chapter 5 discusses the error propagation and background subtraction in more detail.

References

[1] L. Dubrovinsky, N. Dubrovinskaia, E. Bykova, M. Bykov, V. Prakapenka, C. Prescher, K. Glazyrin, H. P. Liermann, M. Hanfland, M. Ekholm, Q.

Feng, L. V. Pourovskii, M. I. Katsnelson, J. M. Wills, and I. A. Abrikosov, Nature **525**, 226 (2015).

[2] G. Shen and H. K. Mao, Rep. Prog. Phys **80** (2017).

[3] H. K. Mao, J. Xu, V. V. Struzhkin, J. Shu, R. J. Hemley, W. Sturhahn, M. Y. Hu, E. E. Alp, L. Vocadlo, D. Alfè, G. D. Price, M. J. Gillan, M. Schwoerer-Böhning, D. Häusermann, P. Eng, G. Shen, H. Giefers, R. Lübbers, and G. Wortmann, Science **292**, 914 (2001).

[4] R. Hrubiak, S. Sinogeikin, E. Rod, and G. Shen, Rev. Sci. Instrum. **86**, 072202 (2015).

[5] G. Shen, W. Sturhahn, E. E. Alph, J. Zhao, T. S. Toellnner, V. B. Prakapenka, Y. Meng, and H. R. Mao, Phys. Chem. Miner. **31**, 353 (2004).

[6] S. Klotz, J. C. Chervin, P. Munsch, and G. Le Marchand, J. Phys. D **42** (2009).

[7] J. Y. Zhao, W. Bi, S. Sinogeikin, M. Y. Hu, E. E. Alp, X. C. Wang, C. Q. Jin, and J. F. Lin, Rev. Sci. Instrum. **88** (2017).

[8] Z. Jenei, H. Cynn, K. Visbeck, and W. J. Evans, Rev. Sci. Instrum. **84**, 095114 (2013).

[9] J. Zhao, W. Sturhahn, J.-f. Lin, G. Shen, E. E. Alp, and H.-k. Mao, High Press. Res. **24**, 447 (2004).

[10] R. Boehler, Geophys. Res. Lett **13**, 1153 (1986).

[11] C.-S. Zha and W. A. Bassett, Rev. Sci. Instrum. **74**, 1255 (2003).

[12] A. T. Boothroyd, *Principles of Neutron Scattering from Condensed Matter* (Oxford University Press, 2020).

[13] B. Fultz, Inelastic Scattering (2020).

[14] D. L. Abernathy, M. B. Stone, M. J. Loguillo, M. S. Lucas, O. Delaire, X. Tang, J. Y. Y Lin, and B. Fultz, Rev. Sci. Instrum **83**, 15114 (2012).

[15] O. Arnold, J. Bilheux, J. Borreguero, A. Buts, S. Campbell, L. Chapon, M. Doucet, N. Draper, R. Ferraz Leal, M. Gigg, V. Lynch, A. Markvardsen, D. Mikkelson, R. Mikkelson, R. Miller, K. Palmen, P. Parker, G. Passos, T. Perring, P. Peterson, S. Ren, M. Reuter, A. Savici, J. Taylor, R. Taylor, R. Tolchenov, W. Zhou, and J. Zikovsky, Nucl. Instrum. Methods. Phys. Res. A **764**, 156 (2014).

[16] J. Y. Y. Lin, F. Islam, and M. Kresh, J. Open Source Softw. **3**, 440 (2018).

[17] R. Boehler, M. Guthrie, J. Molaison, A. dos Santos, S. Sinogeikin, S. Machida, N. Pradha, and C. Tulk, High Press. Res. **33**, 546 (2013).

[18] M.-E. Donnelly, E. K. Y. Wu, J. J. Molaison, M. Frontzek, and B. Haberl, High Press. Res. **42**, 213 (2022).

[19] B. Haberl, M. Guthrie, and R. Boehler, Sci. Rep., 1 (2023).

[20] B. Fultz, in *Characterization of Materials* (Wiley, 2011).

[21] R. L. Cohen, *Applications of Mössbauer Spectroscopy* (Elsevier, 1976).

[22] D. Dickson and F. Berry, *Mössbauer Spectroscopy* (Cambridge University Press, 1986).

[23] R. E. Watson and A. J. Freeman, Phys. Rev. Lett. **6**, 227 (1961).

[24] R. E. Watson and A. J. Freeman, Phys. Rev. **123**, 2027 (1961).

[25] R. E. Watson and A. J. Freeman, Phys. Rev. **131**, 250 (1963).

[26] M. A. Kobeissi, Phys. Rev. B **24** (1981).

[27] W. Sturhahn, Hyperfine Interact. **125**, 149 (2000).

[28] W. Sturhahn, NRIXS Scientific Software (website).

[29] Y.-L. Chen and D.-P. Yang, *Mössbauer Effect in Lattice Dynamics* (Wiley, 2007).

[30] G. Klingelhöfer, R. V. Morris, B. Bernhardt, D. Rodionov, P. A. de Souza Jr., S. W. Squyres, J. Foh, E. Kankeleit, U. Bonnes, R. Gellert, C. Schröder, S. Linkin, E. Evlanov, B. Zubkov, and O. Prilutski, J. Geophys. Res. Planets **108** (2003).

[31] R. V. Morris, G. Klingelhöfer, C. Schröder, D. S. Rodionov, A. Yen, D. W. Ming, P. A. de Souza Jr., I. Fleischer, T. Wdowiak, R. Gellert, B. Bernhardt, E. N. Evlanov, B. Zubkov, J. Foh, U. Bonnes, E. Kankeleit, P. Gütlich, F. Renz, S. W. Squyres, and R. E. Arvidson, J. Geophys. Res. Planets **111** (2006).

[32] E. Alp, T. Mooney, T. Toellner, and W. Sturhahn, Hyperfine Interact. **90**, 323 (1994).

[33] Argonne National Laboratory, 7-GeV Advanced Photon Source Instrumentation Initiative Conceptual Design Report (1992).

[34] Argonne National Laboratory, Advanced Photon Source Upgrade Project, Final Design Report (2019).

[35] E. E. Alp, T. M. Mooney, T. Toellner, W. Sturhahn, E. Witthoff, R. Röhlsberger, E. Gerdau, H. Homma, and M. Kentjana, Phys. Rev. Lett. **70**, 3351 (1993).

[36] T. Mooney, T. Toellner, W. Sturhahn, E. Alp, and S. Shastri, Nucl. Instrum. Methods Phys. Res. A **347**, 348 (1994).

[37] T. S. Toellner, M. Y. Hu, W. Sturhahn, K. Quast, and E. E. Alp, Appl. Phys. Lett. **71**, 2112 (1997).

[38] T. S. Toellner, W. Sturhahn, E. E. Alp, P. A. Montano, and M. Ramanathan, Nucl. Instrum. Methods Phys. Res. A **350**, 595 (1994).

[39] W. Sturhahn, J. Phys. Condens. Matter **16**, 497 (2004).

[40] E. Gerdau, R. Rüffer, H. Winkler, W. Tolksdorf, C. P. Klages, and J. P. Hannon, Phys. Rev. Lett. **54**, 835 (1985).

[41] A. I. Chumakov and W. Sturhahn, Hyperfine Interact. **123**, 781 (1999).

[42] J. T. Sage, C. Paxson, G. R. A. Wyllie, W. Sturhahn, S. M. Durbin, P. M. Champion, E. E. Alp, and W. R. Scheidt, J. Phys. Condens. Matter. **13**, 7707 (2001).

[43] M. S. Lucas, L. Mauger, J. A. Muñoz, I. Halevy, J. Horwath, S. L. Semiatin, S. O. Leontsev, M. B. Stone, D. L. Abernathy, Y. Xiao, P. Chow, and B. Fultz, J. Appl. Phys **113**, 17 (2013).

[44] M. S. Lucas, J. A. Muñoz, O. Delaire, N. D. Markovskiy, M. B. Stone, D. L. Abernathy, I. Halevy, L. Mauger, J. B. Keith, M. L. Winterrose, Y. Xiao, M. Lerche, and B. Fultz, Phys. Rev. B **82**, 144306 (2010).

[45] H. J. Lipkin, Ann. Phys. **9**, 332 (1960).

[46] H. Weiss and H. Langhoff, Phys. Lett. A **69**, 448 (1979).

[47] A. I. Chumakov and R. Rüffer, Hyperfine Interact. **112**, 59 (1998).

[48] HPCAT Technical Notes.

[49] A. I. Chumakov, J. Metge, A. Q. Baron, H. Grünsteudel, H. F. Grünsteudel, R. Rüffer, and T. Ishikawa, Nucl. Instrum. Methods Phys. Res. A **383**, 642 (1996).

[50] M. Seto, Y. Yoda, S. Kikuta, X. W. Zhang, and M. Ando, Phys. Rev. Lett. **74**, 3828 (1995).

[51] W. Sturhahn, T. S. Toellner, E. E. Alp, X. Zhang, M. Ando, Y. Yoda, S. Kikuta, M. Seto, C. W. Kimball, and B. Dabrowski, Phys. Rev. Lett. **74**, 3832 (1995).

[52] E. E. Alp, W. Sturhahn, and T. S. Toellner, J. Phys. Condens. Matter **13**, 7645 (2001).

[53] D. C. Wallace, *Thermodynamics of Crystals* (Dover, 1998).

Chapter 3

Thermodynamic stability and heat absorption of nanocrystalline Ni_3Fe

This chapter is based of the following published article:

S. H. Lohaus, M. B. Johnson, P. F. Ahnn, C. N. Saunders, H. L. Smith, M. A. White, B. Fultz. Thermodynamic stability and contributions to the Gibbs free energy of nanocrystalline Ni3Fe. *Physical Review Materials* 4 (2020).

Thermodynamic quantities, and hence the properties of materials, depend on their structure. It is important to know how the individual atoms are consolidated into a material, because the excitations on the atomic scale from phonons, electrons, and their spins, dictate how the material behaves on a macroscopic scale. From a thermodynamic perspective, we aim to understand how the structure affects the free energy through the enthalpy and entropy. Here, the size of the crystalline structure matters.

Bulk metals usually form large periodic crystals, with grain boundaries in between the individual crystallites. Having different crystals, as opposed to a single crystalline lattice, raises the configurational degrees of freedom and hence the entropy. This extra entropy helps to lower the Gibbs free energy at finite temperatures and helps stabilizing a structure with several individual crystallites. Each crystal is usually several hundreds of atoms across, so for an atom sitting in the middle of the crystal, the lattice seems infinite. For the atoms at the edge of the crystallite, near a grain boundary, their neighbors appear at unusual positions or coordinations. This leads to a weaker bonding between them and a larger enthalpy. Having several crystallites raises, therefore, both the entropy and enthalphy. The stability of such a material

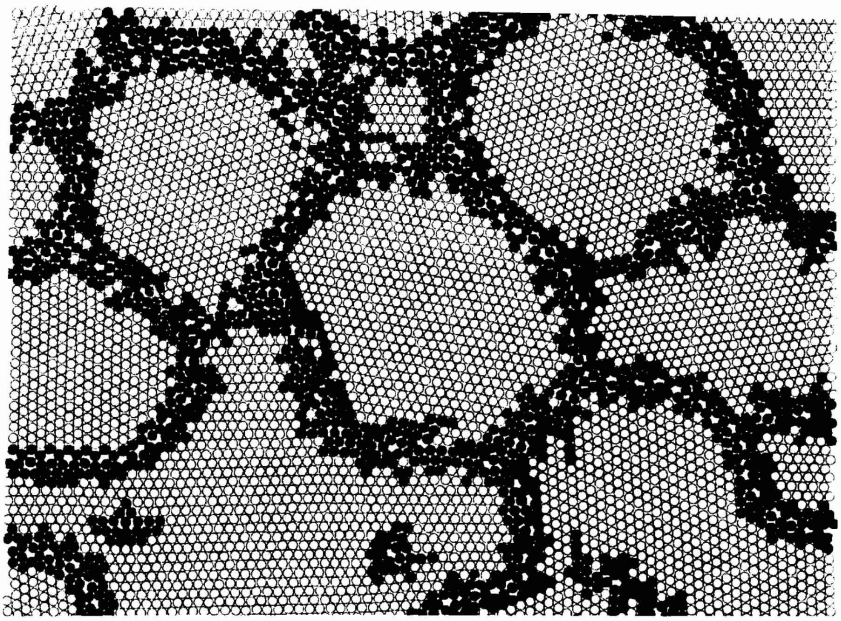

Figure 3.1: Two dimensional atomic structure of a nanocrystalline material, computed using a Morse potential. Black atoms are at grain boundaries, at sites which deviate by over 10% from the corresponding lattice sites at regular coordinations (white atoms) [1]. Additional orientational disorder between the grains is expected in real three dimensional materials.

becomes a balance between lowering the free energy through the extra entropy and raising it as a result of the extra enthalphy.

What happens to the thermodynamic stability if we reduce the size of the individual crystallites from hundreds to tens of atoms? The nanoscale is often a bridge between atomistic behavior and continuum properties, so what happens to the individual quantum excitations (phonons, electrons, magnons) when the crystallites themselves are on the nanoscale? In this chapter we study the thermodynamic stability of nanocrystalline Ni_3Fe, synthesized by high-energy ball milling. We determine the individual contributions to the heat capacity from phonons, electrons and magnetism, and see how their behavior is altered when they are spatially confined to a nanostructure.

For thermodynamic purposes, nanostructured materials can be defined as materials with structural features on the order of 10 nm or smaller, some tens of atoms across. The limited size confines phonons, electrons, and defects, affecting their energies and thermodynamics. The small crystalline regions in a nanocrystalline material are separated by grain boundaries as depicted in Fig. 3.1. A large number of atoms (black atoms in the figure) located near

these grain boundaries are forced into irregular local environments, raising their internal energy (and enthalpy) compared to bulk materials with larger grains. Extra contributions to the enthalpy from elastic fields and internal defects are also expected in many as-synthesized nanomaterials. Because smaller particles have larger surface-to-volume ratios and higher internal energy per atom, adding an atom to a small particle is less favorable than adding it to a large one. This "Gibbs-Thomson effect" raises the chemical potential of atoms in small particles. When a nanocrystalline material is heated and diffusion enables atoms to move, these differences in chemical potential cause the grains to grow and defects to be annihilated. The nanomaterial releases energy during this process and transforms into a material with larger crystallites and lower energy. The excess enthalpy of nanomaterials can therefore be measured by heating in a calorimeter to high temperatures [2–4].

Entropy, S_p, completes the thermodynamic picture. It opposes the enthalpy, H_p, by reducing the Gibbs free energy, G, as:

$$G(T) = H_p(T) - TS_p(T) \ , \tag{3.1}$$

where the subscript p denotes a constant (ambient) pressure. The spatial confinement of phonons and electrons alters their energy, affecting the entropy of nanocrystals. Most of the entropy in nanostructured materials is vibrational in origin [5], so important thermodynamic questions include how atomic vibrations become heat, and how this affects the Gibbs free energy and the stability of a nanomaterial. How stable or unstable do nanostructures become at finite temperatures? To date the Gibbs free energy of nanostructured materials is poorly understood, even though it underlies their stability, and their suitability for applications in engineered devices.

Here we report new thermodynamic results from cryogenic calorimetry measurements on a nanocrystalline material and its bulk counterpart with larger crystallites. The results are analyzed to obtain the enthalpy, entropy, and Gibbs free energies, and their difference for the two materials. Additional inelastic neutron scattering measurements allow us to quantify the effect of nanocrystallinity on the vibrational entropy and the phonon contribution to the thermodynamics of Eq. 3.1. The neutron scattering experiments measured the phonon density of states of control and nanocrystalline materials, showing that the difference in entropy of nanocrystalline and bulk Ni_3Fe is dominated

by vibrational entropy. We also assess the electronic and magnetic contributions to the free energy of Ni_3Fe, and how these are changed by nanocrystallinity. We show an excess entropy of the nanocrystalline Ni_3Fe that lowers its Gibbs free energy, but this entropic stabilization is opposed by the excess enthalpy from grain boundaries and defects. Altogether, the nanocrystalline material has a larger Gibbs free energy than the bulk control material at 300 K, making it thermodynamically unstable at ambient conditions.

3.1 Thermodynamics of nanoparticles

Both the enthalpy and entropy of Eq. 3.1 can be determined from the heat capacity, C_p, with the relationships:

$$H_p(T) = H_0 + \int_0^T C_p(T')\mathrm{d}T' \,, \tag{3.2}$$

$$S_p(T) = S_0 + \int_0^T \frac{C_p(T')}{T'}\mathrm{d}T' \,. \tag{3.3}$$

The thermodynamic stability of a nanomaterial with respect to a bulk control material is determined by the difference $\Delta G^{\mathrm{n-c}}$ (a positive $\Delta G^{\mathrm{n-c}}$ makes the nanomaterial unstable with respect to the control material):

$$\begin{aligned} \Delta G^{\mathrm{n-c}}(T) &= G^{\mathrm{n}}(T) - G^{\mathrm{c}}(T) \\ &= \Delta H_p^{\mathrm{n-c}}(T) - T\Delta S_p^{\mathrm{n-c}}(T) \,, \end{aligned} \tag{3.4}$$

$$\Delta H_p^{\mathrm{n-c}}(T) = \Delta H_0^{\mathrm{n-c}} + \int_0^T \Delta C_p^{\mathrm{n-c}}(T')\mathrm{d}T' \,, \tag{3.5}$$

$$\Delta S_p^{\mathrm{n-c}}(T) = \Delta S_0^{\mathrm{n-c}} + \int_0^T \frac{\Delta C_p^{\mathrm{n-c}}(T')}{T'}\mathrm{d}T' \,, \tag{3.6}$$

where a notation such as $\Delta C_p^{\mathrm{n-c}}$ denotes the difference in heat capacity of the nanocrystalline material and the control bulk material at constant pressure.

The larger H_0 of the nanocrystalline material originates from grain boundaries, internal stresses, and defects. Grain boundaries force atoms into irregular local coordinations, increasing their internal energies (the black atoms of Fig. 3.1). The weaker bonding of atoms near these grain boundaries has other macroscopic consequences, such as lowering their melting temperature [1]. Metals with stronger bonding and higher melting temperatures are also expected to have grain boundaries with higher energies. From work on a number of grain

boundary structures in fcc metals, the grain boundary energy varies from approximately 0.4 to 1.2 $\mathrm{J/m^2}$ in the sequence Au, Ag, Al, Pd, Cu, Co, Ni, Pt [6, 7]. For fcc Ni metal, however, grain boundaries between crystals with various orientations have energies that span much of this entire range [8]. We measured this enthalphy in nanocrystalline Ni_3Fe by heating it up in calorimeter, and measuring the heat released while the grains grow and defects are recovered.

Sources of entropy

Entropy counteracts the enthalpy to lower the Gibbs free energy, and has configurational, magnetic, electronic and vibrational contributions. The large number of individual crystallites at different relative orientations give nanocrystalline materials additional structural degrees of freedom. This results in a somewhat larger configurational entropy compared to materials with large grains. As derived in [5] however, this extra configurational entropy falls off extremely fast with increasing grain size. For nanocrystals with 20 atoms across (which corresponds approximately to our materials), the configurational entropy should be lower than 0.01 k_B/atoms, or about 0.3% of the total entropy at 300 K. On top of that, during our cryogenic calorimetric measurements, atom mobilities are suppressed. So we expect no changes in the atomic configurations, and therefore do not measure differences in the configurational entropy between the nanostructured material and the control samples.

As the temperature approaches absolute zero, all excitations are suppressed, but the structural disorder remains. Does this mean that nanostructured materials have a residual configurational entropy (S_0 in Eq. 3.6). The answer is not necessarily clear, and has been the topic of heated debate in the case of amorphous materials, which are also metastable with a large number of structural degrees of freedom [9–16]. From a thermodynamic perspective, what matters is if a materials is able to access and change its configuration. When the nanomaterial is cooled down, its atomic mobility is impaired and it becomes kinetically trapped in a specific configuration. This metastable nanomaterial cannot access all its degenerate configurational microstates as $T \to 0$ [12, 15, 16]. According to Boltzmann's entropy, $S = k_\mathrm{B} \ln \Omega$, the number of accessible microstates (or configurations) becomes $\Omega = 1$, and the entropy vanishes at 0 K. We therefore adopt $\Delta S_0^{\mathrm{n-c}} = 0$.

Most of the entropy in materials stem from atomic vibrations. Nanocrystallinity changes the dynamical degrees of freedom, which affects the phonon spectrum. Vibrations of nanoparticles have been studied for some time, and the large literature on this subject is reviewed in the next section. The additional degrees of freedom from individual nanocrystallites causes their phonon spectrum to have more low-energy vibrations than its bulk counterpart. This results in larger oscillatory amplitudes of atoms in the nanomaterial, and therefore larger vibrational entropies. The Gibbs free energy of nanomaterials is lowered by this additional entropy, helping to stabilize against their extra enthalpy from grain boundaries. Quantifying the thermodynamic consequences remains a challenge, however, and is the main goal of this study.

The spatial confinement also alters the bonding between atoms, and hence the electronic structure. Our low temperature heat capacity data show an enhancement of the heat absorbed by electrons in nanostructured materials by about 40%, which is reflected in a larger electronic entropy.

Lastly, the structural disorder in nanocrystalline materials also affects the magnetic ordering of spins. The magnetization of consolidated nanocrystals seem to become weaker with decreasing grain sizes in Fe and Ni [17–19] (see Fig. 3.2 a), and also in Ni_3Fe [2, 20]. This makes sense since magnetic ordering depends on exchange interactions between neighboring atoms, which can be disrupted at the grain boundaries. Additionally, the individual grains can act as different magnetic domains and reduce the net magnetization.

More importantly for the thermodynamics, the irregular local environments of atoms near grain boundaries cause their spins to be more susceptible to thermal excitations. This leads to a stronger dependence of the magnetism on temperature as shown in Fig. 3.2 b for iron nanoparticle [17]. This is reflected in the lower Curie temperatures observed in nanostructured materials. For Ni_3Fe, nanocrystallinity can reduce the Curie temperature from 871 K, [21] down to 728 K [22]. In thin films of Ni, with two monolayers, the Curie transition can be suppressed down 325 K [23].

Most of the magnetic disorder, and hence most of the magnetic entropy, increases near the Curie transition. Only a small amount of magnetic entropy is expected below 300 K, where our cryogenic heat capacity measurements were carried out. Nonetheless, due the stronger temperature dependence of the

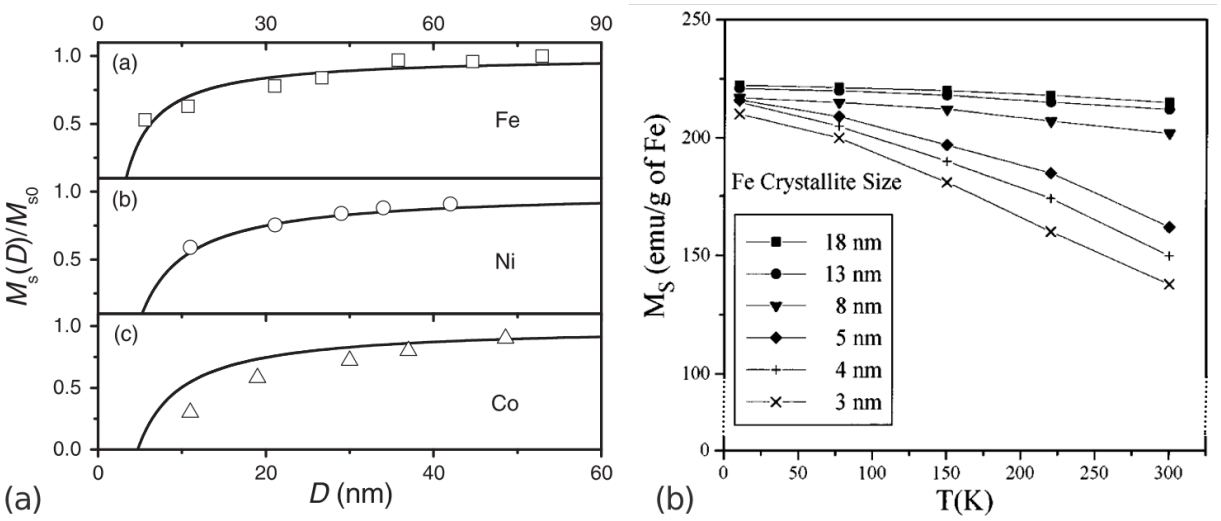

Figure 3.2: Size effects on magnetization. **(a)** Size dependence of the satruration magnetization, M_s, of ferromagnetic nanoparticles [18]. **(b)** Size and temperature dependence of M_s for iron crystallites (coated in Mg) [17].

magnetic spins in nanocrystalls, we do expect them to have a larger magnetic entropy than our control samples.

3.2 Prior work on vibrations in nanomaterials

From prior work, we know that the phonon density of states (DOS), $g(\varepsilon)$, of a nanocrystalline material differs from that of bulk materials in three ways. These three features have been found for isolated nanoparticles, and for consolidated nanoparticles with grain boundaries between them. They are found in metals, semiconductors, and insulators, and all three are shown in Fig. 3.3 a. These features are:

1. An enhancement of $g(\varepsilon)$ at low energies (below 15 meV in Fig. 3.3 a).
2. A general broadening of sharp features in $g(\varepsilon)$ (e.g., at 24 and 33 meV).
3. A longer tail in $g(\varepsilon)$ that extends to high energies above the usual cutoff frequency of longitudinal phonon modes (above 36 meV).

Feature 1 is understood best. An enhancement of $g(\varepsilon)$ at low energies is expected from the degrees of freedom of a nanostructure, as depicted in Fig. 3.3 b. Nanostructures have additional vibrational modes from nanocrystals oscillating against each other, from their relative rotations, and also from the partial

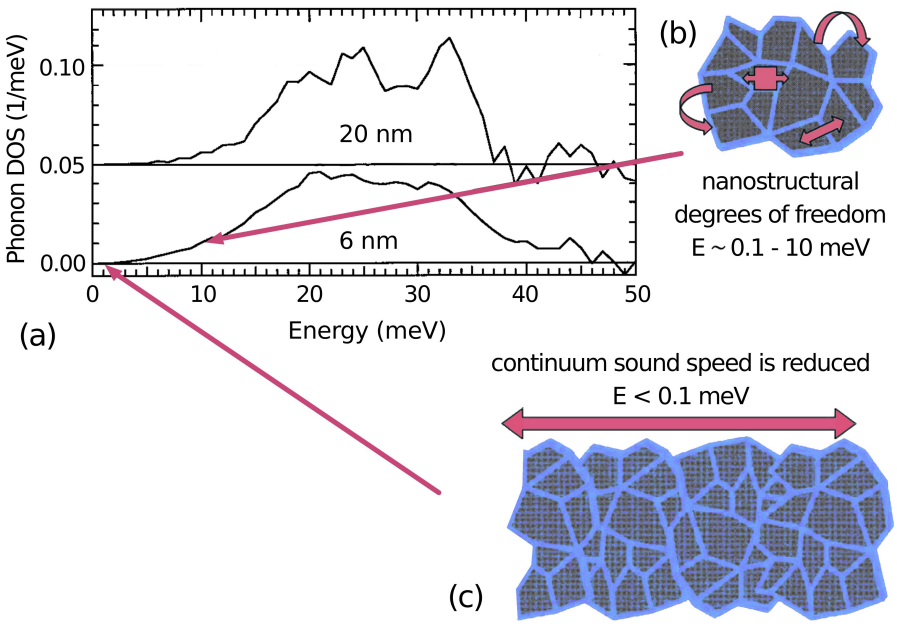

Figure 3.3: Size effects on phonons. **(a)** Phonon DOS from a polycrystalline powder of an fcc Ni-Fe alloy. Compared to the DOS from the material with the larger 20 nm crystallite size, the 6 nm DOS shows three features: (1) enhancement of the intensity below 15 meV, (2) broadening of all features, (3) a tail of spectral weight above 36 meV. **(b)** Representative vibrational modes of the nanocrystalline microstructure, with energies of order 1 meV and wavelengths of 10 nm. **(c)** Continuum behavior at long wavelengths.

confinement of vibrational waves to boundary regions, similar to Rayleigh waves at surfaces with elastic discontinuities. At very low energies, this enhancement disappears. The wavelengths become longer than the nanostructural features (Fig. 3.3 c), and they can not excite modes within individual nanocrystals. At this point the material moves as a continuum with altered elastic constants [24–29]. The enhanced number of modes at low energies have been observed both in calculations and measurements on either isolated nanocrystals or nanocrystals with rigid constraints [13–42].

This low-energy regime can be indicative of a change in the dimensionality of the vibrational modes. For three-dimensional bulk crystalline materials the $g(\varepsilon)$ scales as ε^2 at low energies. Fitting the DOS of nanocrystals to ε^n has given $n < 2$ at these low energies [30, 31], and even $n \approx 1$ in some cases, which corresponds to two-dimensional vibrations [32–34]. This is not universally true, however, and n is often found to be close to 2 in consolidated nanocrystals [35, 36]. What is universally accepted, is that nanostructured materials have more vibrational modes at low energies, up to a factor of five compared to bulk materials [31, 33, 35–43].

Transferring phonon spectral weight from higher energies to lower energies can have a significant effect on the vibrational entropy. Phonons are bosonic quasi-particles, so more of them occupy the lowest energy modes (as shown previously in Fig. 1.5). The enhanced phonon DOS of nanoparticles at low energies enhances the number of phonons that are able to be excited, resulting in larger vibrational amplitudes and larger entropies.

Feature 2, the broadening of features in the $g(\varepsilon)$ of nanomaterials, is less understood. This broadening has been attributed to the shortening of phonon lifetimes, which could explain both features 2 and 3 [39]. As oscillatory waves propagate within a nanostructured material, they often encounter a surface or grain boundary and can be (anharmonically) scattered. In a 10 nm crystal, a phonon propagates only tens of atomic distances before it hits a grain boundary, so its lifetime may only be tens of vibrational periods or less. Such a shortened lifetime results in an energy broadening according to the energy-time uncertainty principle ($\Delta E \Delta t \geq \hbar/2$). The broadening of spectral features in the phonon DOS can often be captured by simple models like damped harmonic oscillators, which have an asymmetrical broadening about their central frequency [33, 35, 39, 41, 44–49].

Feature 3 may be attributable to the same phonon lifetime broadening, but other explanations have been proposed. Some prior work indicated that these tails in $g(\varepsilon)$ may originate from harmonic modes at high frequencies caused by surface oxides or impurities [33, 42, 43, 50]. High energy tails of the phonon DOS have also been reported in a number of molecular dynamics simulations on materials without any impurities [30, 43, 51], and were attributed to higher frequency harmonic vibrations of atoms at surfaces of nanoparticles.

3.3 Materials

We chose a magnetic Fe-Ni alloy for this study, with 75 atomic % nickel and 25 atomic % iron, Ni_3Fe. As seen from the phase diagram of Fig. 3.4, the Ni-rich alloys are fcc solid solutions at most temperatures. However below 773 K, Ni_3Fe can become chemically long-range-ordered with the $L1_2$ structure (where Fe atoms occupy the corners, and the Ni atoms the faces, of the standard fcc cube) [53]. The $L1_2$ order develops sluggishly by a first-order phase transition [21, 54]. Heat treatments of over two months of annealing time have been reported for transforming into the $L1_2$ phase [53], so usually Ni_3Fe retains

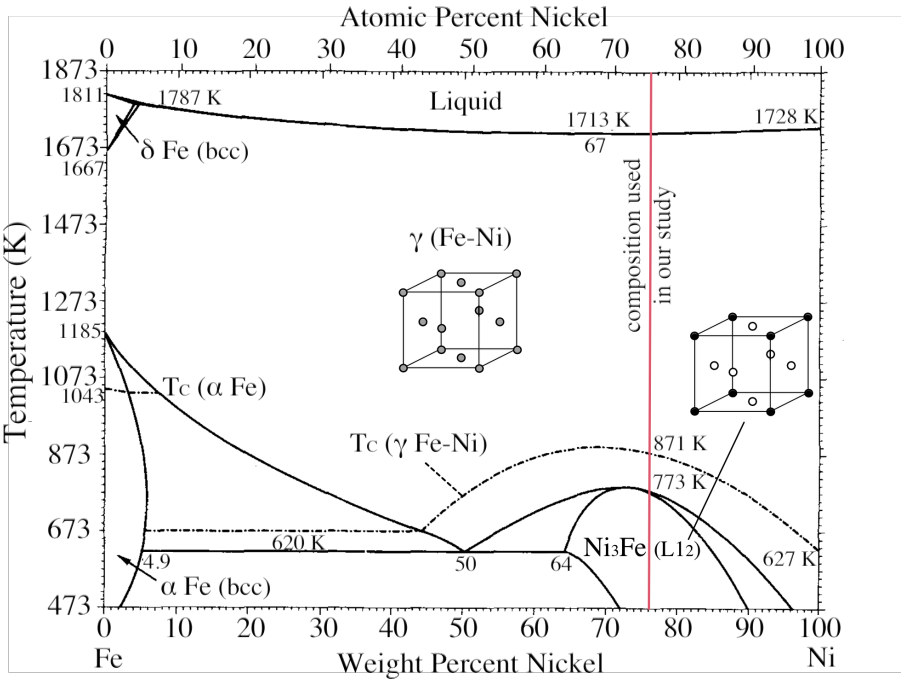

Figure 3.4: Phase diagram of Ni-Fe compounds. Adapted with permission from [52].

the randomized arrangement of Fe and Ni atoms in the fcc structure at room temperature and below (no configurational contributions to the entropy).

Fcc solid solutions of Ni_3Fe have advantages for studying the thermodynamics of nanocrystals. Some of the smallest nanocrystalline sizes in metals, around 6-7 nm, can be obtained in Ni_3Fe prepared by high energy ball milling [55]. Ball milling of Ni_3Fe has been shown to produce disordered fcc structure [20], and no signs of $L1_2$ ordering was observed in our samples. These alloys also collect less oxygen and hydrogen than other materials, which could be introduced during ball milling, and impair inelastic neutron scattering measurements.

Ball milling and nanostructure

One way to produce nanocrystals is by breaking down the (bulk) crystallites of a material through mechanical plastic deformation. In high-energy ball milling, powder of the material is shaken together with steel balls inside a vial for several hours (see Fig. 3.5). This method is able to produce the relatively large quantities of nanocrystalline powder required for neutron scattering experiments. The nanocrystals are consolidated into larger particles of powder, lowering their surface area, and making them less susceptible to adsorbing gases and water, which would impede neutron scattering measurements.

Figure 3.5: Ball milling vial prior to milling, with steel balls, sample powders, and stearic acid (white powder).

The large strains introduced during ball milling create microstructural features and defects that contribute to the internal energy, and consequently increase the enthalpy of nanomaterials. Point defects such as vacancies are likely, although they have not been reported. Impurities such as interstitial atoms are introduced during ball milling, and line defects such as dislocations are responsible for some of themlow-angle boundaries between crystallites, although their density within the crystals may be low [2, 3]. Twin boundaries are also possible [4]. Microstructural features give a distribution of internal energies to the different crystallites of both bcc and fcc phases of Ni-Fe alloys [56]. These microstructural sources of internal energy contribute to H_0 of Eq. 3.2.

To prepare the nanocrystalline Ni_3Fe samples, powders of Ni (75 atomic%) and Fe (25 atomic%) were mixed with 5 wt.% stearic acid or ethanol and sealed in a steel vial. Ball milling was performed with a Fritsch Planetary Mono Mill for 20 h at 650 rpm using steel ball-to-powder weight ratios between 20:1 and 40:1. After milling, the material was sonicated in isopropyl alcohol and centrifuged to remove the stearic acid. In what follows, we call the nanomaterials prepared by high energy ball milling "as-milled" samples. Control samples of bulk material with larger crystallites can be prepared by milling the powder for shorter times, by milling with a lower ball-to-powder ratio or by annealing the as-milled material inside sealed quartz ampoules under vacuum.

In previous work, nanocrystalline Ni_3Fe samples prepared by a similar method were well characterized by inelastic neutron scattering, small-angle neutron

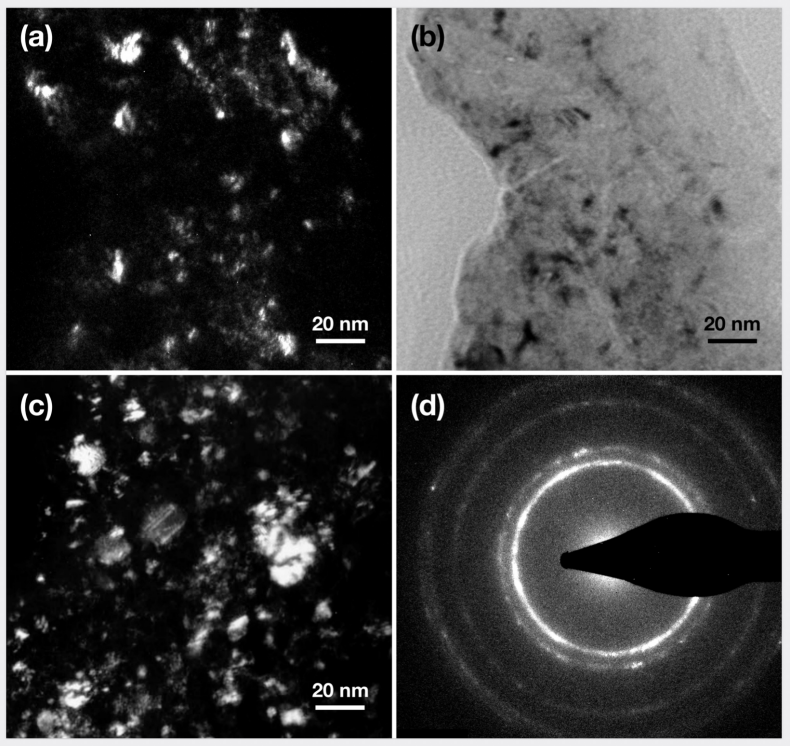

Figure 3.6: Transmission electron microscopy images of the as-milled Ni_3Fe. The dark-field (DF) and bright-field (BF) images were obtained from the (111) fcc diffraction. **(a)** DF and **(b)** BF images of the as-milled sample, compared to **(c)** DF image from previous work, with crystallites of 6 nm [35]. **(d)** Electron diffraction pattern.

scattering, transmission electron microscopy, x-ray diffractometry, Mössbauer spectrometry, and magnetization [2, 35, 44].

The nanocrystals of our materials were imaged through transmission electron microscopy (TEM). Figure 3.6 shows the dark-field and bright-field images of the as-milled samples collected from the (111) diffraction. The high contrast speckles represent the individual crystalline grains and are direct evidence of their nanocrystallinity. The TEM analysis from previous work (Fig. 3.6 c) determined a mean crystallite size of 6 nm [35], and as shown below, those are comparable to the grain sizes of our as-milled material. The five diffraction rings of Fig. 3.6 d show the characteristic diffraction pattern of an FCC crystal structure.

3.4 X-ray diffraction

The diffraction patterns were also collected through x-ray diffraction (XRD) using Cu K_α radiation in a x-ray powder diffractometer (PANalytical X'Pert Pro). Figure 3.7 shows the XRD data obtained from a sample in the as-milled (nano) state, and from the same sample with larger grains (control) after annealing at 873 K for 1 h. Both diffraction patterns show the main peaks from an fcc solid solution. There is evidence for some $L1_2$ chemical order in a few of the annealed control samples, seen as very weak superlattice peaks in the XRD pattern (e.g., at $2\theta = 36°,62°$). Such a low content of $L1_2$ ordering, however, does not alter the phonon DOS significantly [53, 57, 58], and therefore does not affect our study. Other control samples did not show this $L1_2$ chemical order and all control samples gave very similar heat capacity measurements, as shown below.

The diffraction peaks from the nanocrystalline material are broadened. Due to their nanostructured nature, only tens of atomic layers contribute coherently to the interference pattern measured in x-ray diffraction. This results in a reduction of constructive interference, and a loss of sharpness in their diffraction peaks. As described in detail in the appendix, the width of the diffraction peaks are inversely proportional to their grain sizes. By comparing to previous work, we determined that our nanomaterials and control samples have grain sizes of 6-7 nm and 25-35 nm, respectively.

Since nanomaterials have more grain boundaries and many atoms at unusual coordinations, their lattice parameter is larger than those of bulk materials. The lattice parameters depend inversely on the grain sizes of the material as shown in Fig. A.1 of the appendix. Our lattice parameters were determined from the x-ray diffraction using Nelson-Riley method (see appendix). The as-milled samples have lattice parameters between 3.587 – 3.604 Å, in good agreement with values reported for ball-milled Ni_3Fe (3.590 Å [20] and 3.600 Å [59]). The annealed control samples have a lattice parameter of 3.5599 Å, slightly larger than the lattice parameter of 3.5533 Å reported for a Ni_3Fe single crystal [60].

Nanomaterials also have larger internal strains than their bulk counterparts. Strains result both from the large number of grain boundaries and from defects introduced during ball milling. These internal strains also affect the XRD

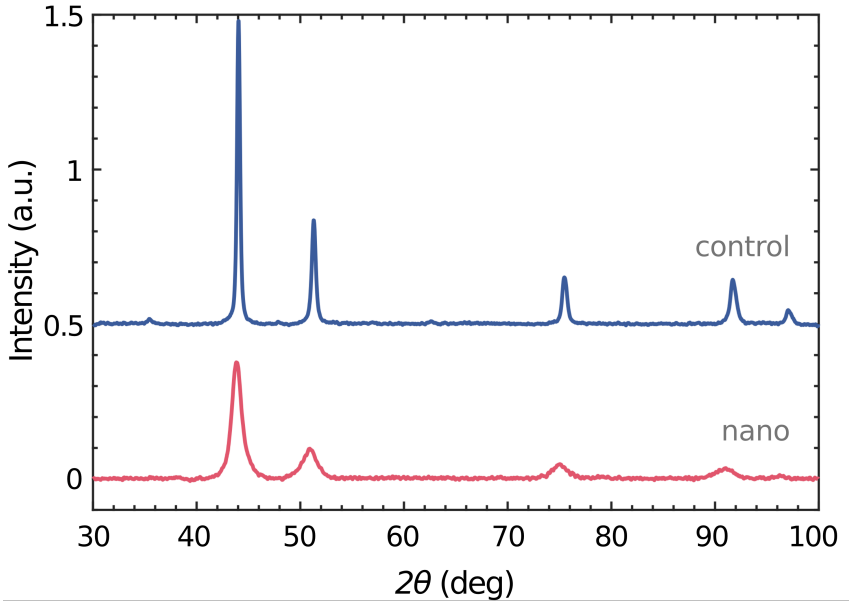

Figure 3.7: X-ray diffraction patterns of the as-milled material and of the bulk control sample after annealing at 873 K for 1 h.

patterns by broadening the diffraction peaks. Luckily, these effects can be separated from grain size broadening since they have different 2θ dependencies. The Williamson-Hall method is derived in the appendix, to show the effects of grain sizes and strains in our materials (Figs. A.4 and A.5).

Grain growth and defect recovery

Ball-milling produces metastable nanostructured crystals, with atoms that are kinetically trapped into a certain configuration at low temperatures. Due to the extra enthalphy from grain boundaries, their free energy is larger, and they are less stable than bulk materials. When the material is heated, enabling atoms to move by diffusion, the grains grow and the grain boundaries are gradually broken down. This process returns the material to its more stable configuration with larger grains and lower free energy.

We can observe the grain growth by annealing the nanocrystalline material to different temperatures. Their XRD patterns show progressively narrower peaks as the temperature is increased, corresponding to larger grains (see Fig. A.2 of the appendix). To avoid oxidation, these materials were sealed inside quartz tubes under vacuum to be heated in a furnace.

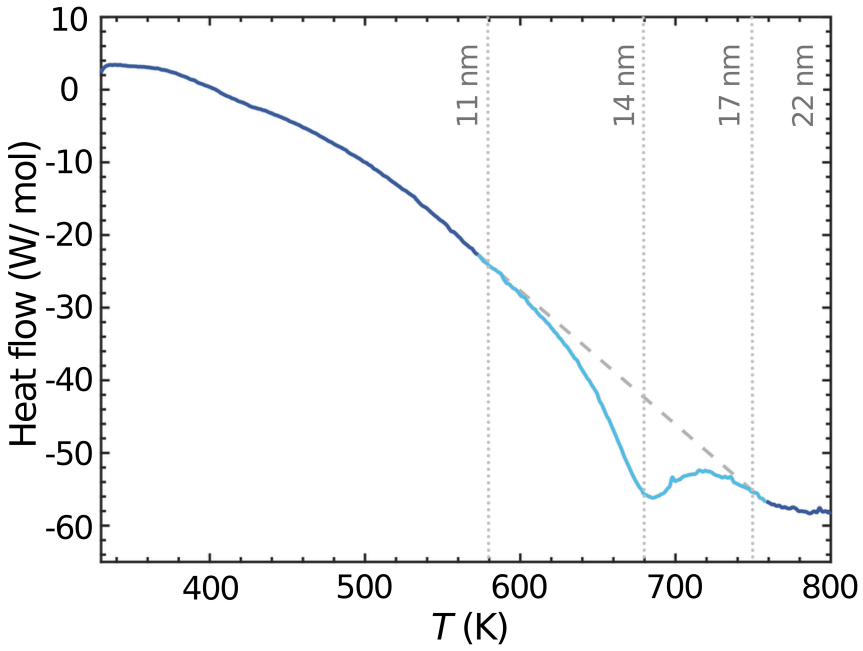

Figure 3.8: Heat flow measured by DSC while heating the nanocrystalline sample at 20 K/min. Positive values correspond to endothermic heat flows. The release of internal energy from defects and grain growth is highlighted and its enthalpy of $H_0^{\mathrm{n-c}}$ = 2.3 kJ/mol was calculated using a linear baseline (dashed line). The labeled grain sizes were determined from measured XRD patterns of Fig. A.2.

For thermodynamics, we are more interested in the energy released by the nanomaterial as the grains grow. Calorimetry experiments enable us to measured this energy. At the same time as the grain growth happens, other kinetically assisted processes such as defect recovery, and stress release, are also enabled at high temperatures. All these make up the excess enthalpy, $\Delta H_0^{\mathrm{n-c}}$, of the nano with respect to the bulk material of Eq. 3.5.

Differential Scanning Calorimetry (DSC) was performed using a Perkin Elmer DSC 7. The as-milled nanomaterial with grain sizes of 7 nm was placed in the DSC sample holder inside alumina crucibles. We used a N_2 purge gas flowing at $20 - 30$ ml/min to reduced oxidation and to enhance heat transfer. The differential heat flow to the sample was measured while heating it from 320 K to 800 K at 20 K/min. The heat evolution of the nanomaterial measured by DSC is shown in Fig. 3.8. The instrument has a baseline, which varies somewhat for every measurement, so the overall negative slope of the heat flow should not lead to any quantitative interpretations. We also did not use a reference material, since we do not need absolute values of the heat capacity.

A distinct deviation from the baseline is observed between 580 and 800 K (highlighted in the figure). This corresponds to an a exothermic heat flow as the energy is released from the sample. It corresponds to the excess enthalpy of the nanocrystalline material, released during annealing. The defect recovery and grain growth are exothermic and irreversible processes, so subsequent DSC runs on the same sample lack this exothermic peak, indicating that the entire defect recovery occurred during the first run. The grain sizes obtained from the XRD analysis of Fig. A.2 (in appendix), are included in Fig. 3.8. They confirm that most of the grain growth takes place indeed between 580 and 800 K, corresponding to the heat release.

To quantify the internal enthalpy difference $\Delta H_0^{\mathrm{n-c}}$ of Eq. 3.5 associated with defects and grain boundaries, the heat flow, $\dot{Q}$, can be integrated as

$$\Delta H_0^{\mathrm{n-c}} = \int_{T_i}^{T_f} \frac{\dot{Q} - B}{c} dT \tag{3.7}$$

where c is the heating rate of 20 K/min and B is the instrument baseline. For a linear baseline (dashed line in Fig. 3.8) we obtain $\Delta H_0^{\mathrm{n-c}} = 2.3\,\mathrm{kJ/mol}$. This result is in very good agreement with the re-crystallization enthalpy of 2.2 kJ/mol of ball-milled Ni_3Fe reported in [61].

It should be noted that the Curie transition of nanocrystalline $Ni_{0.7}Fe_{0.3}$ was reported to occur at 728 K [22]. Even though we did not measure the thermal evolution of the magnetism in our samples, some endothermic signal seen around 720 K could correspond to the ferromagnetic transition. The Curie temperature of nanocrystalline materials, however, is sensitive to the exact grain size [62], and it might be different in our materials. If part of the highlighted signal of Fig. 3.8 includes the magnetic transition, our calculation of $\Delta H_0^{\mathrm{n-c}}$ would be affected. To estimate this possible error, we calculated the enthalpy of the magnetic transition by integrating the heat capacity measurement of Ni_3Fe by Kollie, et al. [53]. The resulting magnetic enthalpy is 0.12 kJ/mol, or 5% of $\Delta H_0^{\mathrm{n-c}}$.

3.5 Heat capacity

We now turn to the remaining contributions to the enthalphy and entropy of Eqs. 3.2 and 3.3, determined from heat capacity measurements at cryogenic temperatures up to ambient conditions. Heat capacity measures the total

enthalphy and entropy of the material, associated with phonons, electrons, and electronic spins (magnetism). Further below, we will break it down into the individual contributions from each of those excitations.

Specific heat measurements were carried out by collaborators M. B. Johnson[1] and M. A. White[1,2]. These measurements were made by relaxation microcalorimetry using a commercial instrument (a PPMS from Quantum Design). Measurements were conducted in the temperature range between 0.4 and 300 K over which accuracy, with due care, can be within 1% from 5 K to 300 K, and 5% from 0.4 K to 5 K [63]. Measurements were taken in two modes: ^{4}He cooling for the $2-300$ K temperature interval and ^{3}He cooling for the interval from $0.5-10$ K. To enhance the thermal contact between the sample and the microcalorimeter, a thin layer of grease was applied to the sample stage and its contribution to the specific heat was quantified prior to each sample measurement. All measurements were conducted under high vacuum (10^{-5} Torr) to minimize convective heat losses. For the relaxation calorimetry measurements, the as-milled powder samples were consolidated into pellets by pressing them in a die with a pressure of approximately 0.44 GPa. The consolidated samples had better thermal contact and heat transfer. The sample masses ranged from 10 to 27 mg.

Several heat capacity measurements were performed on nanocrystalline (as-milled) and control samples (less milled or annealed). The results are shown in Fig. 3.9. There are some variations between samples of each type, but in all cases the heat capacity curves for the nanocrystalline material exceeded the heat capacity of the control samples. This difference is most evident at low temperatures, as expected owing to the enhanced phonon DOS of nanocrystals at low energies.

The heat capacity of the as-milled nanocrystalline material was also enhanced at temperatures above 200 K. We were concerned that this could be from interstitial impurities, carbon and oxygen, that can be introduced into the material by milling. This motivated the preparation of control samples by annealing the as-milled material at 873 K to increase the crystallite size and eliminate defects, resulting in a bulk control sample with the same amount

[1]Clean Technologies Research Institute, Dalhousie University, Halifax, Nova Scotia, Canada B3H 4R2

[2]Department of Chemistry, Dalhousie University, Halifax, Nova Scotia, Canada B3H 4R2

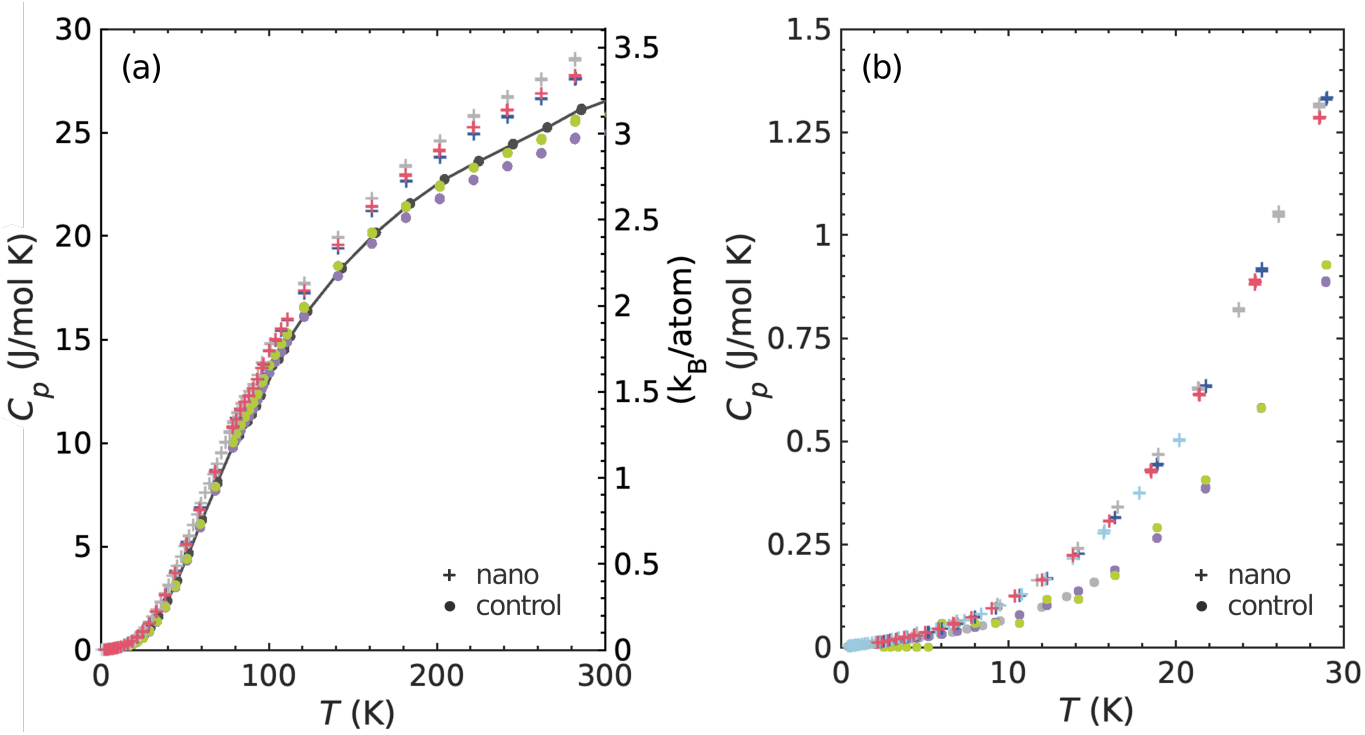

Figure 3.9: Heat capacity of Ni_3Fe measured by calorimetry for the as-milled materials (+) and large-grained control samples (•), normalized by the number of moles of atoms. Different colors represent results from different samples. **(a)** Full data set. The solid black curve is from the annealed control material (see text). **(b)** Low-temperature data.

of interstitial atoms as the nanomaterial. The concentration of impurities in both the as-milled and annealed samples were indeed the same as measured by an instrumental gas analysis (IGA) performed by a commercial laboratory (the results are shown in table 3.1). The heat capacity of this annealed control sample, shown in Fig. 3.9 as a solid line, is similar to that of the other samples of Ni_3Fe with large crystals, however, indicating that the enhanced heat capacity above 200 K does not originate from interstitial impurities, but from its the noncrystalline nature.

Figure 3.10 compares our heat capacities with those found in the literature. Our measured heat capacity for the control sample is similar to the heat capacity measured on fcc Ni [64] and in good agreement with the heat capacity of 25.5 J/(mol K) measured for Ni_3Fe at 300 K [53]. Low temperature measurements on disordered Ni_3Fe [65] are in excellent agreement with the heat capacity of our control sample.

Element	Nanomaterial (wt%)	Control (wt%)
O	2.8	2.4
C	1.7	1.6
N	0.0064	0.0063
S	0.0018	0.0034

Table 3.1: IGA measurements on the as-milled nanomaterial, and the control sample prepared by annealing the as-milled material, showing their concentration of impurities.

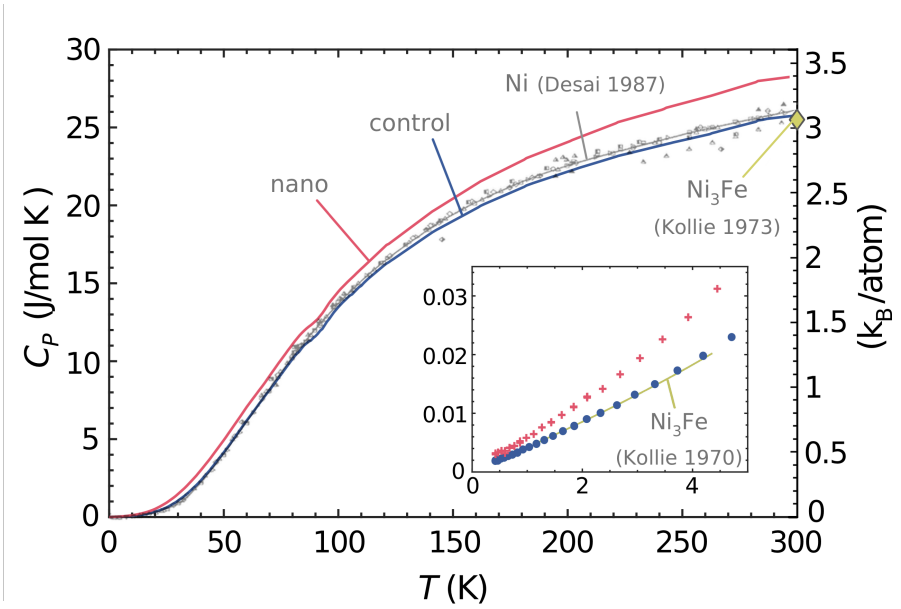

Figure 3.10: Mean heat capacities of the as-milled nanomaterial and control bulk sample compared to literature. The heat capacity of bulk disordered Ni_3Fe reported by Kollie and Brooks [53] is shown at 300 K (♦). Data compiled by Desai for fcc Ni are shown as small markers, and the recommended curve as a thin solid line [64]. The insert compares our low temperature data (< 5 K) with the fit reported by Kollie, et al. [65]

.

A complete $L1_2$ ordering transition in this material would reduce the heat capacity by approximately $0.1\,k_B$/atom (0.8 J/mol K) at 300 K [53], with most of this from phonons [58]. However, the $L1_2$ ordering in Ni_3Fe is very sluggish. It is a first-order transition, so with partial order, the change in heat capacity would be reduced proportionately. We therefore neglect the effects of partial chemical ordering on the heat capacity of our samples.

3.6 Contributions at low temperatures

Phonons, electrons, and magnetism all contribute to the heat capacity in the low temperature region around $0.4 - 10$ K as

$$\begin{aligned} C_p(T) &= C_{p,\mathrm{el}} + C_{p,\mathrm{mag}} + C_{p,\mathrm{ph}} \\ &= \gamma T + \alpha T^{3/2} + \beta T^3 \,, \end{aligned} \tag{3.8}$$

where the heat of the magnetic disorder is assumed to contribute as spin-waves ($\sim T^{3/2}$) following Block's law of Eq. 1.20. At low temperatures, phonons are accurately described by Debye's law, where the phonon DOS, $g(\varepsilon)$, scales as ε^2 resulting in a T^3 dependency for the heat capacity [5].

The linear temperature dependence from electrons can be directly observed in our data plotted in Fig. 3.11 a. Below 3 K, the data is well described by linear fits. Above 3 K the T^3 dependency from phonons takes over and the data deviates from a linear behavior. Below 1 K the $T^{3/2}$ effects from magnons also become visible as slight (upward) deviations from the linear fits in Fig. 3.11 a.

By the plotting the data as C_p/T vs. T^2, we can visualize each contribution more clearly and improve the fitting accuracy to determine the parameters γ, α, and β of Eq. 3.8. Figure 3.11b shows vertical offsets from conduction electrons, with linear behaviors from phonons. The contribution from magnons becomes pronounced only at very low temperatures below 1 K [65] (seen as downward curvatures in the plots). Nonetheless, including the spin wave term, $\alpha T^{3/2}$, in fits to Eq. 3.8 reduces the overall RMS errors of the fits by 20% for the bulk material, and 15% for the nanocrystalline material. The fitted parameters are presented in table 3.2. The nanocrystalline material has clearly larger parameters for all three contributions from electrons, magnons, and phonons, compared to the control samples. In particular, the enhanced degrees of freedom of the nanomaterial at low vibrational energies are manifested as larger β parameters and hence a larger slope in Fig. 3.11 b.

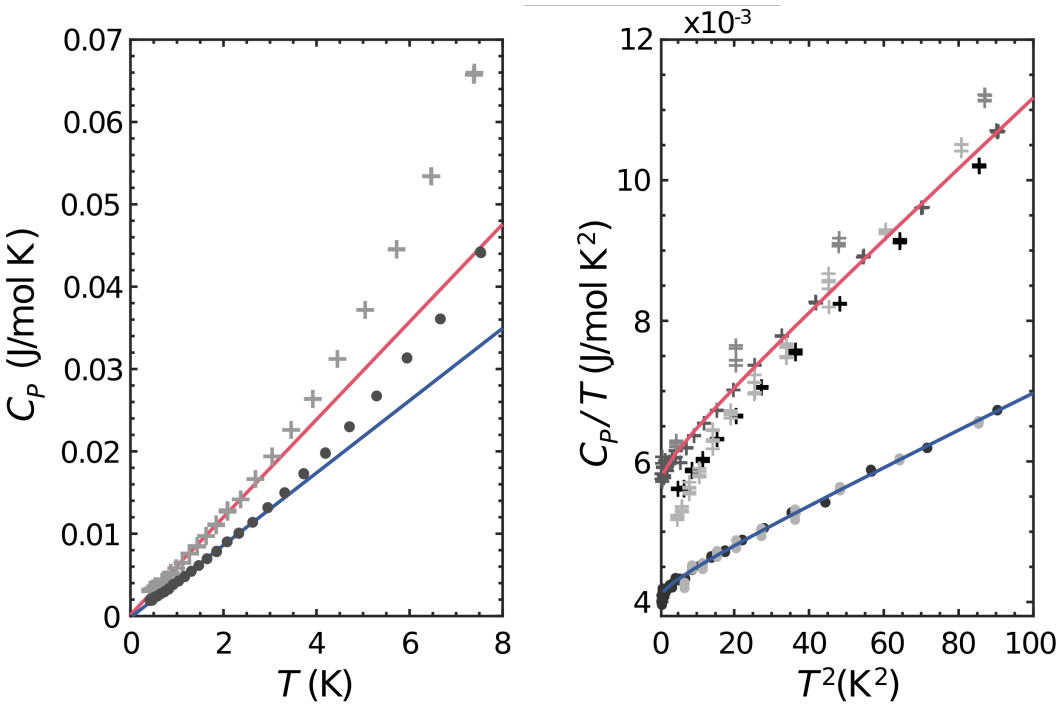

Figure 3.11: Low temperature heat capacities of the nanocrystalline (red) and control materials (blue) plotted as **(a)** C_p vs. T and **(b)** C_p/T vs. T^2. Solid curves are fits to the data using Eq. 3.8.

3.7 Phonon contributions

We quantified the phonons density of states (DOS), through inelastic neutron scattering (INS). The measurement we performed on powder samples with the time-of-flight Wide Angular-Range Chopper Spectrometer, ARCS, at the Spallation Neutron Source at Oak Ridge National Laboratory (see methods in Section 2.2). Neutrons used for this experiment were monochromated to an incident energy of 70 meV, setting the highest energy of phonon excitations. The powder samples, both as-milled (nano) and annealed (control), were placed in aluminum cans with a cylindrical insert to create an annulus of sample 1 mm in thickness, with 30 mm of outer diameter and 50 mm of height. Measurements were performed in a low-background closed cycle refrigerator (CCR 16) between 190 K and 300 K. The data were normalized by the proton current on target, and corrected for detector efficiency using a measurement from vanadium. The phonon DOS were obtained after subtraction of the signal from an empty aluminum can and corrections for multiphonon and multiple scattering (using the Multiphonon package in Mantid [67, 68]).

	γ (mJ/mol K^2)	β (10^{-2} mJ/mol K^4)	α (mJ/mol K$^{5/2}$)	RMS error (10^{-4} J/mol K)
$\gamma T + \beta T^3$				
control	4.2	2.71	-	1.90
nano	5.9	5.14	-	3.56
Kollie et al. [65] (bulk Ni_3Fe)	4.18	2.43	-	-
$\gamma T + \alpha T^{3/2} + \beta T^3$				
control	3.96	2.51	0.16	1.59
nano	5.55	4.81	0.27	3.11
Kollie et al. [65] (bulk Ni_3Fe)	4.05	1.89	0.10	-
Dixon et al. [66] (bulk 68.7% Ni)	3.90	1.87	0.12	-

Table 3.2: Low temperature fits the heat capacity data of in Fig. 3.11 b to Eq. 3.8, including and excluding the contributions from magnons α. These are compared to fitting parameters from the literature.

The resulting phonon DOS at 300 K from nanocrystals and bulk control samples are presented in Fig. 3.12 a as solid curves. As expected, the nanomaterial (red curve) has a phonons DOS with broadened features and enhanced intensities at low and high energies compared to the control sample.

The data is overlaid with measurements from prior work as markers and a grey solid curve calculated with a Born–von Kármán model [35]. These spectra were obtained by neutron scattering on a triple axis spectrometer, at only two values of momentum Q (3.54 and 4.60 Å^{-1}). This resulted in an underestimation of the DOS at low energies especially for the large grained materials, due to the sharper features in their spectra. Both spectra obtained for the nanocrystalline material ('nano' and '6 nm') are in good agreement.

The vibrational contribution from phonons to the entropy, S_{vib}, and heat capacity $C_{p,\mathrm{vib}}$ can both be determined from the phonon DOS, $g(\varepsilon)$, as [5, 69]

$$S_{\mathrm{vib}}(T) = 3k_{\mathrm{B}} \int_0^\infty g(\varepsilon) \left[\, (1 + n_{\varepsilon,T}) \ln(1 + n_{\varepsilon,T}) - n_{\varepsilon,T} \ln n_{\varepsilon,T} \, \right] \mathrm{d}\varepsilon \, , \qquad (3.9)$$

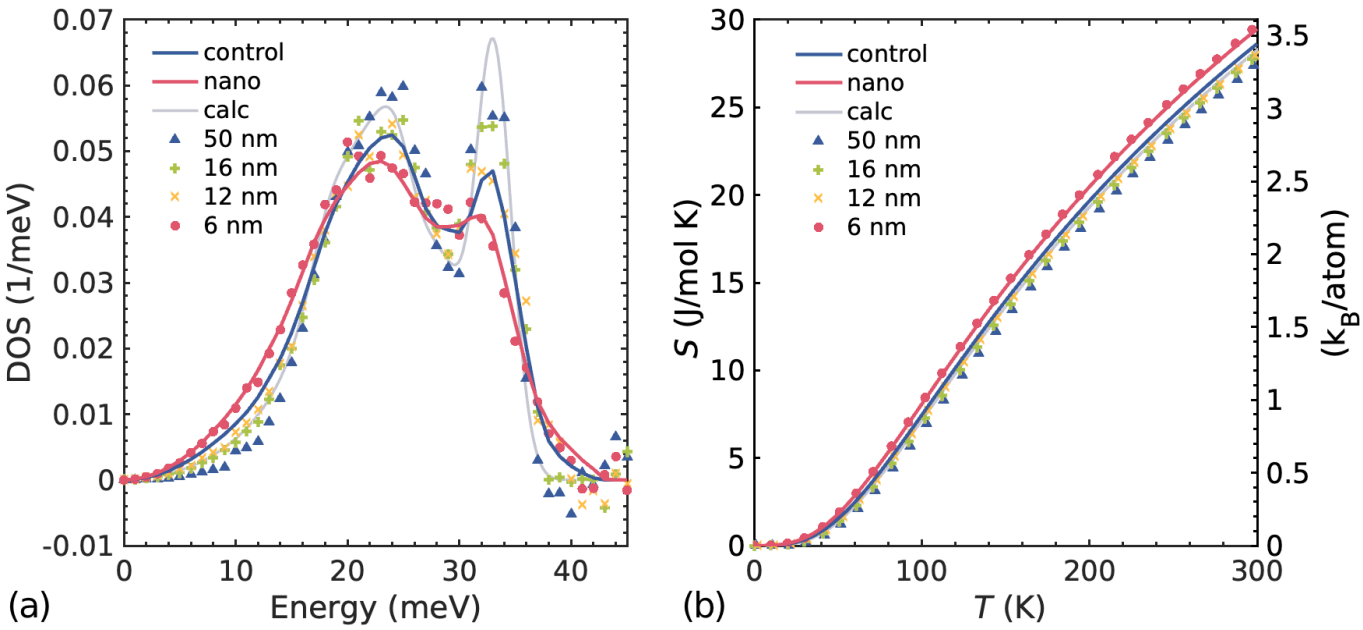

Figure 3.12: Phonon energy spectrum and entropy. **(a)** Phonon DOS curves measured by inelastic neutron scattering at 300 K. Solid curves correspond to the new measurements performed at ARCS, while the markers are measurements from previous work [35]. The solid light curve (Calc), also from previous work, was calculated with a Born–von Kármán model using force constants from [57], and broadened by instrument resolution. **(b)** Phonon entropies calculated with the curves of panel a, using Eq. 3.9.

$$C_{p,\mathrm{vib}}(T) = 3N\,k_\mathrm{B}\int_0^\infty g(\varepsilon)\left(\frac{\varepsilon}{k_\mathrm{B}T}\right)^2\frac{\mathrm{e}^{\varepsilon/k_\mathrm{B}T}}{\left(\mathrm{e}^{\varepsilon/k_\mathrm{B}T}-1\right)^2}\,\mathrm{d}\varepsilon\,, \tag{3.10}$$

where ε is the phonon energy and $n_{\varepsilon,T} = (\exp(\varepsilon/k_\mathrm{B}T) - 1)^{-1}$ the Planck distribution of phonon occupancy. The phonon DOS, $g(\varepsilon)$, is normalized to 1, and N is the number of atoms in the sample.

Figure 3.12 b shows the resulting vibrational entropies, which as expected, are enhanced with increasing nanocrystallinity due to their extra degrees of freedom. The entropy obtained for our control sample is larger than that from previous work ('50 nm'). The previous underestimation of the DOS at low energies causes a reduction of the vibrational entropy as calculated by Eq. 3.9, because the Planck factor, $n_{\varepsilon,T}$, is largest at low ε.

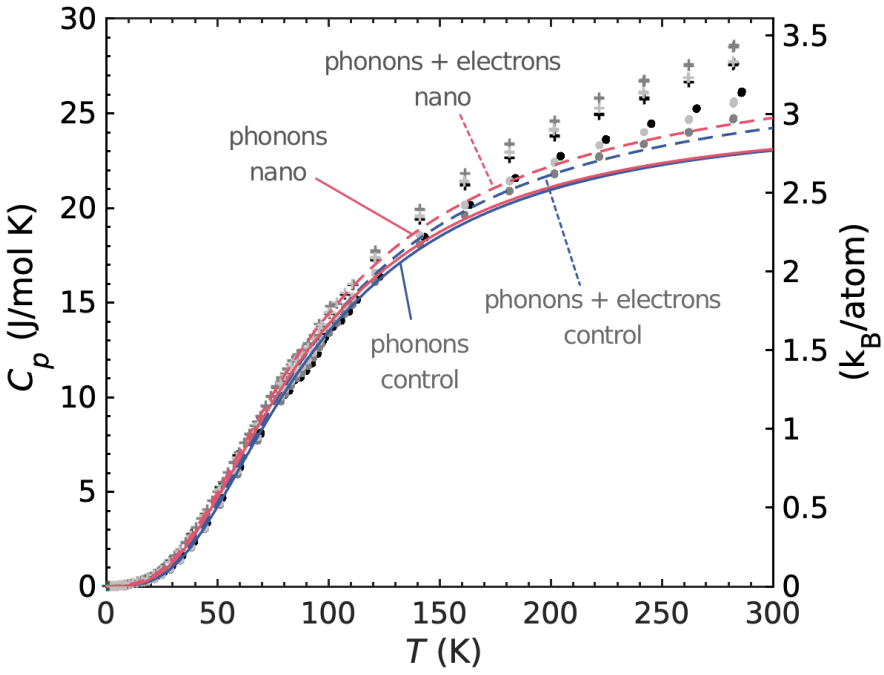

Figure 3.13: Heat capacities of nanomaterial (+) and control samples (•) from calorimetry shown in Fig. 3.10, superposed with phonon heat capacities calculated from the phonon DOS using Eq. 3.10 (solid lines) and with vibrational plus electronic heat capacities (dashed lines).

3.8 Contributions to the heat capacity at higher temperatures

Phonons & electrons

The phonon contribution to the heat capacity was calculated from the phonon DOS measured at 300 K by inelastic neutron scattering using Eq. 3.10. The resulting vibrational heat capacities for the nanocrystalline and control samples are compared in Fig. 3.13 to the total heat capacities measured by calorimetry. About 90% of the heat capacity originates from phonons for the control material approximately and 80% for the nanomaterial. The increase of heat capacity above the classical limit of $3\,k_B$/atom at high temperatures requires more than harmonic or quasiharmonic phonons as calculated by Eq. 3.10, as discussed further below.

Adding the contributions from electrons and spins to the phonon contribution brings the heat capacity closer to the results from calorimetry. The electronic contribution to the heat capacity is estimated by extrapolating the low temper-

ature electronic contribution ($C_{p,\mathrm{el}} = \gamma T$) to higher temperatures. The results for both the nanocrystalline and control materials are included in Fig. 3.13. At 300 K, the electronic heat capacities for the nanocrystalline and control samples are 0.20 k_B/atom and 0.14 k_B/atom, respectively.

Magnetism

The spin-wave model of magnetic fluctuations does not hold at elevated temperatures, so estimating the magnetic contribution at 300 K is not straightforward. For instance the energy to create a magnon becomes dependent on the number of magnons already present in the material. This many-body aspect of spin waves, makes the concept of individual and independent magnons inapplicable at 300 K. Elevated temperatures can also enhances other scattering events with phonon for example. Since spin-waves can not propagate coherently at elevated temperatures, a magnetic contribution as $C_{p,\mathrm{mag}} = \alpha T^{3/2}$ is not applicable at elevated temperatures.

Most of the change in magnetization occurs near the Curie temperature, so the magnetic thermal disorder is small at 300 K. For disordered bulk Ni_3Fe the ferromagnetic transition occurs at 871 K [21]. Measurements show a decrease of only 5% in the spontaneous magnetization between 0 K and 300 K [70], so the magnetic contribution to the entropy at room temperature is small.

Nanostructured materials, however, have lower Curie temperatures [19] and a stronger temperature dependence of the magnetization [17], so we expect a larger entropy. Ball-milled nanocrystals have a lower magnetization than their bulk counterpart as measured by Mössbauer experiments [55]. Previous measurements on our nanocrystalline samples at 300 K showed that the magnetization is 7% lower than that of the control samples [2]. In other work, at 4 K, the magnetization of a nanocrystalline sample (12.5 nm) was found to be 2% lower than that of a sample with larger grain sizes [71]. The Curie temperature reported for nanocrystalline Ni_3Fe, ranges between 728 K [22] and 848 K [71]. Nanomaterials have, therefore, a larger contribution from magnetism to the heat capacity and entropy, even at 300 K and below.

The disordering the spins requires heat and contributes to the heat capacity as an endothermic signal. The total entropy associated with the disordering of spins can be quantified by from the magnetic heat capacity as $S^{tot}_{\mathrm{mag}} = \int C_{P,\mathrm{mag}}/T \, \mathrm{d}T$. The magnetic heat capacity is reported in [72] up to 1400 K

for bulk Ni_3Fe, giving $S^{tot}_{\mathrm{mag}} = 0.61\,k_\mathrm{B}$/atom. At 300 K and below, the magnetic entropy is only a fraction of this total. To estimate this fraction we use the mean-field model derived previously in Eq. 1.23, giving the entropy of 'mixing' spin-up and spin-down atoms on an Ising lattice:

$$S_{mix} = -\frac{Nk_\mathrm{B}}{2}\left[(1+M)\ln\frac{1+M}{2} + (1-M)\ln\frac{1-M}{2}\right].$$

The maximum entropy in this model is $Nk_\mathrm{B}\ln 2 = 0.69k_\mathrm{B}$/atom (when M=0). For Ni_3Fe this has to be equivalent to the total measured magnetic entropy of $0.61\,k_\mathrm{B}$/atom. For partial magnetization, the magnetic entropy becomes:

$$\begin{aligned} S_{\mathrm{mag}}(M) &= \frac{S_{\mathrm{mix}}}{Nk_\mathrm{B}\ln 2} S^{tot}_{\mathrm{mag}} \\ &= -\frac{S^{tot}_{mag}}{2\ln 2}\left[(M+1)\ln\frac{M+1}{2} + (1-M)\ln\frac{1-M}{2}\right]. \quad (3.11) \end{aligned}$$

The magnetization $M(T)$ has been measured for bulk Ni_3Fe [70], so we can compute the magnetic entropy from 0−300 K. At 300 K it is $S^{\mathrm{c}}_{\mathrm{mag}} = 0.09\,k_\mathrm{B}$/atom.We can also compute the magnetic contribution to the heat capacity, as plotted in Fig. 3.14 a together with the other contributions for the control samples. The magnetic contribution at 300 K ($0.12\,k_\mathrm{B}$/atom) is in good agreement with the magnetic heat capacity of Ni_3Fe reported by Kollie ($0.14\,k_\mathrm{B}$/atom) [72] and the magnetic contribution calculated by Körmann et al. for Ni ($0.11\,k_\mathrm{B}$/atom) [73]. As seen from the small residual of Fig. 3.14 a, the sum of magnetic, electronic and phononic contributions agrees well with the total heat capacity measured by calorimetry.

Magnetization data were available for the nanomaterial only at 4 K [71] and 300 K [2]. At 300 K Eq. 3.11 gives $S^{\mathrm{n}}_{\mathrm{mag}} = 0.15\,k_\mathrm{B}$/atom. By assuming that it follows the same temperature dependence as the control material, we can estimate its magnetic heat capacity between $0-300$ K (shown Fig. 3.14 b). As suggested by the larger residual heat capacity at 300 K, the nanocrystalline material has additional contributions, besides the electronic, magnetic and vibrational heat capacities. This residual heat capacity is $0.22\,k_\mathrm{B}$/atom at 300 K, corresponding to a residual entropy of $0.14\,k_\mathrm{B}$/atom. Its origin is discussed below.

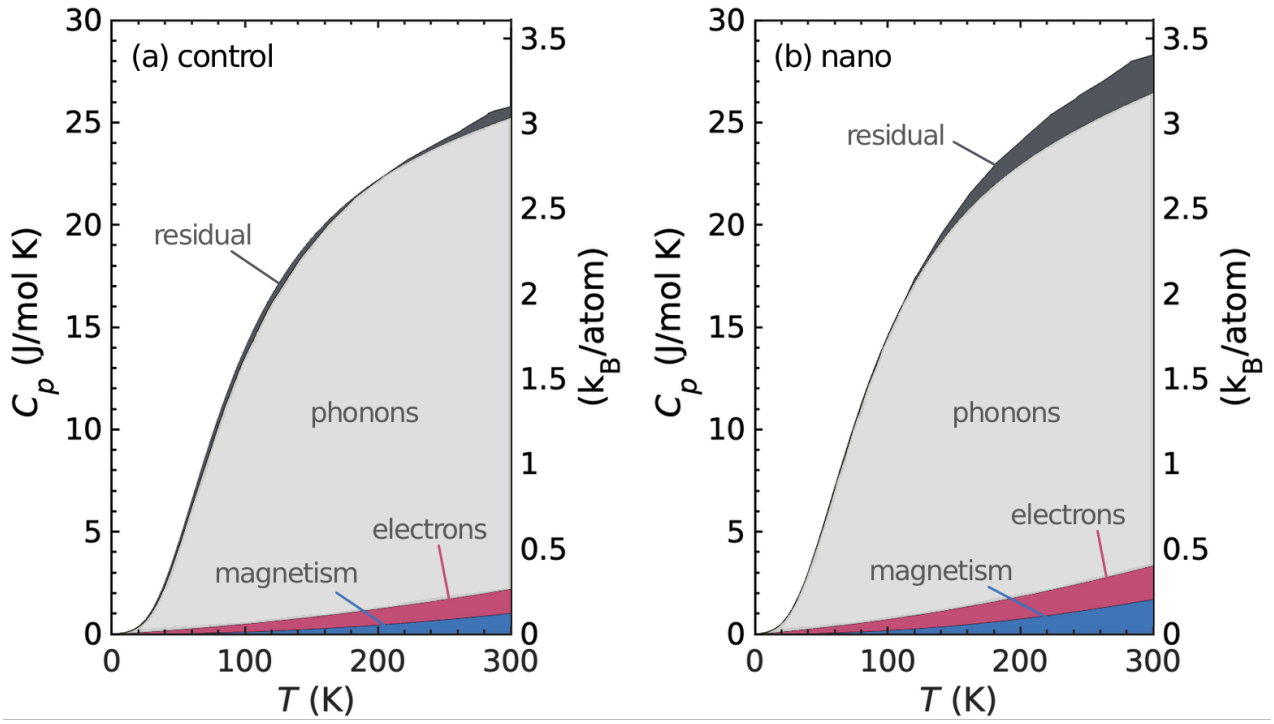

Figure 3.14: Individual contributions to the heat capacity of **(a)** the control and **(b)** nanocrystalline samples. The residual is the difference between the sum of the labeled contributions and the total heat capacity measured by calorimetry.

Anharmonic contributions

The vibrational contribution to the heat capacity was computed from the phonon DOS measured at 300 K using Eq. 3.10, based on a harmonic model. In reality, phonons are not harmonic: their vibration frequencies vary with temperature and their propagation has a finite lifetime. Here we discuss the effects of these two types of anharmonicity.

A general trend is the softening of phonons (lowering of the vibrational frequencies) with increasing temperature. This increases the phonon entropy and is often related an expansion of the lattice volume. Magnetism and electrons can also affect the volume, as will be explored in more depth in Chapter 5. Their contributions and variations with temperature are usually much less important than those from phonons, however. It is straightforward to estimate the contribution from thermal expansion to the heat capacity [5]:

$$\Delta C_{th}(T) = C_p(T) - C_v(T) = Bv\beta^2 T \; . \tag{3.12}$$

Using a bulk modulus of 179 GPa, molar volume of 6.75 cm^3/mol, volume thermal expansion of $3.3{\cdot}10^{-5}K^{-1}$ (values for Ni_3Fe at 300 K taken from [60]), gives ΔC_{th}=0.05 k_B/atom, about 1% of the total heat capacity at 300 K and about 20% of the residual heat capacity of the nanomaterial. Thermal expansion alone can not account for the excess residual heat capacity of Fig. 3.14 b.

Another possible contribution comes from the reduced lifetimes of phonons, resulting from their scattering at grain boundaries or other defects of nanomaterials. Reduced lifetimes are compatible with the broadening the features of the DOS as shown in Fig. 3.12 a. According to the energy-time uncertainty principle ($\Delta E \Delta t \geq \hbar/2$), when the lifetime is reduced, the energy uncertainty has to increase. Lifetime broadening can be modeled by damped harmonic oscillators. Introducing damping causes a shift of the vibrational spectrum to higher energies, giving an apparent reduction in the entropy when calculated with Eq. 3.9. A correction for this effect, given in [74], predicts an increase of the phonon entropy by 0.15 k_B/atom for a damped harmonic oscillator with a damping factor of $\mathcal{Q} = 6$, which is consistent with the broadened phonon DOS of the nanocrystalline material. An anharmonic contribution of a fraction of one k_B/atom is typical for metals at high temperatures [69]. Shortened phonon lifetimes are consistent with the larger amount of grain boundaries and defects of the nanomaterial, and account well for its residual entropy of 0.14 k_B/atom at 300 K.

3.9 Free energy and thermodynamic stability

Now we turn to the stability of the nanocrystals with respect to the bulk material. Nanostructured materials have both a larger enthalpy and entropy contributions to the free energy of Eq. 3.1, which can be computed from the measured heat capacity.

The H_0 term in Eq. 3.2 is an important contribution to the enthalpy of the nanocrystalline material. It arises from their extra grain boundaries and defects compared to bulk materials, and was determined to be $\Delta H_0^{n-c} = 2.3\,kJ/mol$ by heating the nanocrystals in a calorimeter to 800 K (Fig. 3.8). The remaining enthalpy, $H_p(T)$, is temperature dependent and was determined from measurements of the heat capacity with Eq. 3.2. As shown in Fig. 3.15 a, the difference of enthalphy between the nanocrystalline and control material

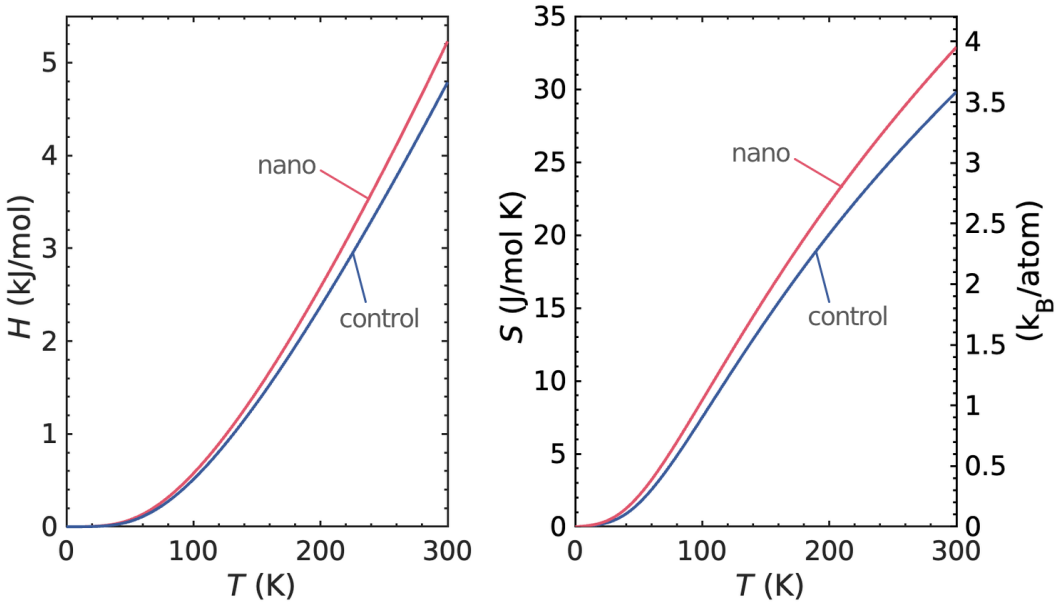

Figure 3.15: Total enthalpy **(a)** and entropy **(b)** of nanocrystalline material and control sample computed from calorimetry measurements of the heat capacity using Eq. 3.2 and 3.3. The grain boundary enthalpy H_0 is not included.

increases with temperature, making the nanomaterial more energetically unfavorable at higher temperatures

On the other hand, the entropy of formation of a grain boundary is positive, helping to stabilize nanomaterials at finite temperatures. The excess entropy of the nanomaterial with respect to the control sample can be seen in Fig. 3.15 b. At 300 K it is 0.37 k_B/atom (3.0 J/mol K). An early report gave a larger excess entropy for nanocrystalline Pd [24], and isolated iron nanoparticles showed an increase of phonon entropy of 0.5 k_B/atom [4]. Our measured excess entropy contributes to the Gibbs free energy with $-T\Delta S^{n-c} = -0.9\,\mathrm{kJ/mol}$ at 300 K. The excess entropy increases with temperature, so its contribution to the Gibbs free energy should be larger at 600 K where the grain growth starts.

Figure 3.16 shows the resulting Gibbs free energy as a function of temperature for both the nanomaterial and control samples. The excess free energy of the nanocrystalline samples $\Delta G^{n-c}(T)$ (labeled "difference") is positive at all temperatures, meaning that is it less stable then the bulk material. It has a larger entropy that helps to reduce the $\Delta G^{n-c}(T)$ with temperature somewhat, but not enough to overcome the enthalpy H_0 from grain boundaries and defects in the nanocrystalline material. By extrapolating the measured Gibbs free

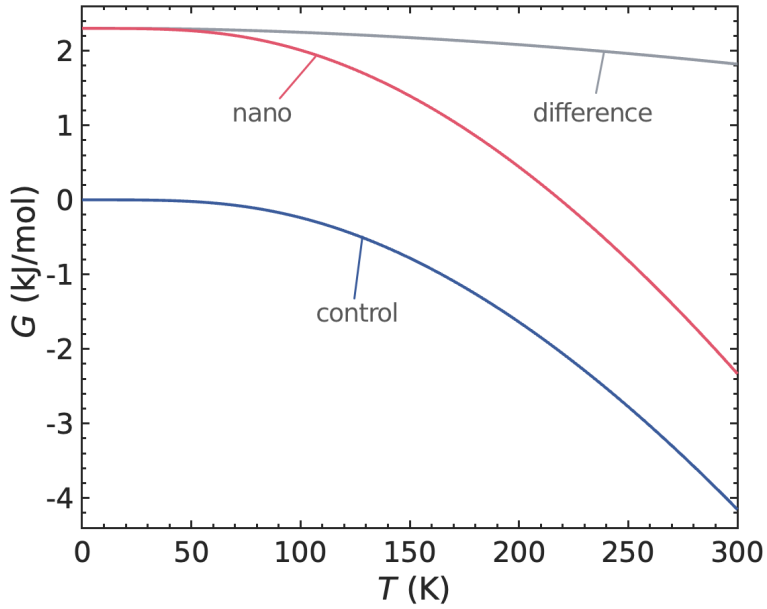

Figure 3.16: Gibbs free energies of as-milled nanocrystalline Ni_3Fe and control sample, using enthalpies and entropies of Fig. 3.15, and $\Delta H_0^{n-c} = 2.3\,\mathrm{kJ/mol}$.

energies to 600 K, we predict that the nanomaterial would still be thermodynamically unstable. Its larger excess entropy at 600 K would be insufficient to overcome the enthalpy of its grain boundaries (2.3 kJ/mol). Since diffusion is thermally activated, the grains start to grow at 600 K, transforming the metastable nanomaterial into its stable counterpart with larger crystallites.

3.10 Conclusions

The heat capacities of nanocrystalline and large-grained fcc Ni_3Fe alloys were measured between $0.4 - 300\,\mathrm{K}$. The heat capacity of the nanocrystalline material was consistently larger, especially at temperatures below 100 K. This difference originates from its larger phonon density of states (DOS) at energies below 15 meV, as shown inelastic neutron scattering measurements. Phonons accounted for most of the heat capacities of the Ni_3Fe samples, and for most of the difference between the nanocrystalline and control samples. The remaining heat capacity of the control sample was accounted for by electronic and magnetic contributions. Adding all components of the nanocrystalline material (phonons, electrons and magnetism) gave a result that was about 7% lower than the total measured by calorimetry at 300 K. This difference is

attributed to a larger phonon anharmonicity in the nanocrystalline material, which could also cause the observed broadening of features in its measured phonon spectrum. The larger entropy of the nanocrystalline material with respect to the control sample is counteracted by its larger enthalpy, so the difference in Gibbs free energy between the nanocrystalline and control sample decreases only modestly with temperature. The nanocrystalline material is thermodynamically unstable at temperatures to 300 K, and is probably unstable to higher temperatures where grain growth occurs.

References

[1] H. Gleiter, Nanostruct. Mater. **6**, 3 (1995).

[2] H. Frase, "Vibrational and Magnetic Properties of Mechanically Attrited Ni_3Fe Nanocrystals", PhD thesis (1998).

[3] H.-J. Fecht, Nanostruct. Mater. **6**, 33 (1995).

[4] B. Roldan Cuenya, L. K. Ono, J. R. Croy, K. Paredis, A. Kara, H. Heinrich, J. Zhao, E. E. Alp, A. T. DelaRiva, A. Datye, E. A. Stach, and W. Keune, Phys. Rev. B **86**, 165406 (2012).

[5] B. Fultz, *Phase Transitions in Materials* (Cambridge University Press, 2014).

[6] H. Van Swygenhoven, D. Farkas, and A. Caro, Phys. Rev. B **62**, 831 (2000).

[7] M. Yuasa, T. Nakazawa, and M. Mabuchi, J. Condens. Matter Phys. **24**, 265703 (2012).

[8] D. L. Olmsted, S. M. Foiles, and E. A. Holm, Acta Mater. **57**, 3694 (2009).

[9] M. Goldstein, J. Chem. Phys. **128**, 373 (2008).

[10] M. Goldstein, J. Chem. Phys. **134**, 124502 (2011).

[11] S. A. Langer, J. P. Sethna, and E. R. Grannan, Phys. Rev. B **41**, 2261 (1990).

[12] J. C. Mauro, R. J. Loucks, and S. Sen, J. Chem. Phys. **133**, 139 (2010).

[13] D. P. B. Aji and G. P. Johari, J. Phys. Chem. B **114**, 9578 (2010).

[14] P. K. Gupta and J. C. Mauro, J. Chem. Phys. **126**, 234503 (2007).

[15] P. K. Gupta and J. C. Mauro, J. Chem. Phys. **129**, 224504 (2008).

[16] D. Kivelson and H. Reiss, J. Phys. Chem. B **103**, 8337 (1999).

[17] D. Zhang, K. J. Klabunde, C. M. Sorensen, and G. C. Hadjipanayis, Phys. Rev. B **58**, 14167 (1998).

[18] H. M. Lu, W. T. Zheng, and Q. Jiang, J. Phys. D **40**, 320 (2007).

[19] H. M. Lu, P. Y. Li, Y. N. Huang, X. K. Meng, X. Y. Zhang, and Q. Liu, J. Appl. Phys. **105**, 5903 (2009).

[20] C. Chinnasamy, A. Narayanasamy, N. Ponpandian, K. Chattopadhyay, and M. Saravanakumar, Mater. Sci. Eng. A **304-306**, 408 (2001).

[21] R. J. Wakelin and E. L. Yates, Proc. Phys. Soc. B **66**, 221 (1953).

[22] P. Y. Li, H. M. Lu, Z. H. Cao, S. C. Tang, X. K. Meng, X. S. Li, and Z. H. Jiang, Appl. Phys. Lett **94**, 213112 (2009).

[23] Y. Li and K. Baberschke, Phys. Rev. Lett. **68**, 1208 (1992).

[24] D. Korn, A. Morsch, R. Birringer, W. Arnold, and H. Gleiter, J. Phys. Colloques **49**, C5 (1988).

[25] T. Shen, C. Koch, T. Tsui, and G. Pharr, J. Mater. Res. **10**, 2892 (1995).

[26] G. Fougere, L. Riester, M. Ferber, J. Weertman, and R. Siegel, Mater. Sci. Eng. A **204**, 1 (1995).

[27] P. Sanders, J. Eastman, and J. Weertman, Acta Mater. **45**, 4019 (1997).

[28] H. Tanimoto, S. Sakai, E. Kita, and H. Mizubayashi, Mater. Trans. **44**, 94 (2003).

[29] A. F. Yue, A. B. Papandrew, O. Delaire, B. Fultz, Z. Chowdhuri, R. M. Dimeo, and D. A. Neumann, Phys. Rev. Lett. **93**, 205501 (2004).

[30] A. Kara and T. S. Rahman, Phys. Rev. Lett. **81**, 1453 (1998).

[31] H. L. Smith, B. Hornbuckle, L. Mauger, B. Fu, S. Tracy, G. Thompson, M. Lucas, Y. Xiao, M. Hu, J. Zhao, E. Ercan Alp, and B. Fultz, Acta Mater. **61**, 7466 (2013).

[32] U. Stuhr, H. Wipf, K. H. Andersen, and H. Hahn, Phys. Rev. Lett. **81**, 1449 (1998).

[33] B. Roldan Cuenya, A. Naitabdi, J. Croy, W. Sturhahn, J. Y. Zhao, E. E. Alp, R. Meyer, D. Sudfeld, E. Schuster, and W. Keune, Phys. Rev. B **76**, 195422 (2007).

[34] N. Spiridis, M. Zając, P. Piekarz, A. I. Chumakov, K. Freindl, J. Goniakowski, A. Kozioł-Rachwał, K. Parliński, M. Ślęzak, T. Ślęzak, U. D. Wdowik, D. Wilgocka- Ślęzak, and J. Korecki, Phys. Rev. Lett. **115**, 186102 (2015).

[35] H. Frase, B. Fultz, and J. L. Robertson, Phys. Rev. B **57**, 898 (1998).

[36] A. B. Papandrew, A. F. Yue, B. Fultz, I. Halevy, W. Sturhahn, T. S. Toellner, E. E. Alp, and H.-k. Mao, Phys. Rev. B **69**, 144301 (2004).

[37] J. Trampenau, K. Bauszus, W. Petry, and U. Herr, Nanostruct. Mater. **6**, 551 (1995).

[38] B. Fultz, J. L. Robertson, T. A. Stephens, L. J. Nagel, and S. Spooner, J. Appl. Phys. **79**, 8318 (1996).

[39] B. Fultz, C. C. Ahn, E. E. Alp, W. Sturhahn, and T. S. Toellner, Phys. Rev. Lett. **79**, 937 (1997).

[40] E. Bonetti, L. Pasquini, E. Sampaolesi, A. Deriu, and G. Cicognani, J. Appl. Phys. **88**, 4571 (2000).

[41] B. Roldan Cuenya, J. R. Croy, L. K. Ono, A. Naitabdi, H. Heinrich, W. Keune, J. Zhao, W. Sturhahn, E. E. Alp, and M. Hu, Phys. Rev. B **80**, 125412 (2009).

[42] B. Roldan Cuenya, L. K. Ono, J. R. Croy, A. Naitabdi, H. Heinrich, J. Zhao, E. E. Alp, W. Sturhahn, and W. Keune, Appl. Phys. Lett. **95**, 143103 (2009).

[43] S. Stankov, M. Miglierini, A. I. Chumakov, I. Sergueev, Y. Z. Yue, B. Sepiol, P. Svec, L. Hu, and R. Rüffer, Phys. Rev. B **82**, 144301 (2010).

[44] H. N. Frase, L. J. Nagel, J. L. Robertson, and B. Fultz, Philos. Mag. B **75**, 335 (1997).

[45] P. Machnikowski and L. Jacak, Phys. Rev. B **71**, 115309 (2005).

[46] S. Stankov, Y. Z. Yue, M. Miglierini, B. Sepiol, I. Sergueev, A. I. Chumakov, L. Hu, P. Svec, and R. Rüffer, Phys. Rev. Lett. **100**, 235503 (2008).

[47] B. Roldan Cuenya, W. Keune, R. Peters, E. Schuster, B. Sahoo, U. von Hörsten, W. Sturhahn, J. Zhao, T. S. Toellner, E. E. Alp, and S. D. Bader, Phys. Rev. B **77**, 165410 (2008).

[48] S. De, K. Kunal, and N. R. Aluru, J. Appl. Phys. **119**, 114304 (2016).

[49] R. Röhlsberger, W. Sturhahn, T. S. Toellner, K. W. Quast, P. Hession, M. Hu, J. Sutter, and E. E. Alp, J. Appl. Phys. **86**, 584 (1999).

[50] L. Pasquini, A. Barla, A. I. Chumakov, O. Leupold, R. Rüffer, A. Deriu, and E. Bonetti, Phys. Rev. B **66**, 073410 (2002).

[51] D. Wolf, J. Wang, S. R. Phillpot, and H. Gleiter, Phys. Rev. Lett. **74**, 4686 (1995).

[52] L. Swartzendruber, V. Itkin, and C. Alcock, JPE **12**, 288 (1991).

[53] T. G. Kollie and C. R. Brooks, Phys. Status Solidi A **19**, 545 (1973).

[54] A. Khachaturyan, Prog. Mater. Sci. **22**, 1 (1978).

[55] H. Ouyang, "Grain Boundaries of Nanophase Materials", PhD thesis (1993).

[56] L. B. Hong and B. Fultz, J. Appl. Phys. **79**, 3946 (1996).

[57] E. D. Hallman and B. N. Brockhouse, Can. J. Phys. **47**, 1117 (1969).

[58] M. S. Lucas, L. Mauger, J. A. Muñoz, I. Halevy, J. Horwath, S. L. Semiatin, S. O. Leontsev, M. B. Stone, D. L. Abernathy, Y. Xiao, P. Chow, and B. Fultz, J. Appl. Phys **113**, 17 (2013).

[59] C. Chinnasamy, A. Narayanasamy, K. Chattopadhyay, and N. Ponpandian, Nanostruct. Mater. **12**, 951 (1999).

[60] P. Turchi, Y. Calvayrac, and F. Plicque, Phys. Status Solidi A **45**, 229 (1978).

[61] F. Popa, O. Isnard, I. Chicinaş, and V. Pop, J. Alloys Compd. **554**, 39 (2013).

[62] H. M. Lu, P. Y. Li, Y. N. Huang, X. K. Meng, X. Y. Zhang, and Q. Liu, J. Appl. Phys. **105**, 023516 (2009).

[63] C. A. Kennedy, M. Stancescu, R. A. Marriott, and M. A. White, Cryogenics **47**, 107 (2007).

[64] P. Desai, Int. J. Thermophys. **8**, 763 (1987).

[65] T. G. Kollie, J. O. Scarbrough, and D. L. McElroy, Phys. Rev. B **2**, 2831 (1970).

[66] M. Dixon, F. E. Hoare, T. M. Holden, and E. C. Stoner, Proc. R. Soc. Lond. A **303**, 339 (1968).

[67] J. Y. Y. Lin, F. Islam, and M. Kresh, J. Open Source Softw. **3**, 440 (2018).

[68] O. Arnold, J. Bilheux, J. Borreguero, A. Buts, S. Campbell, L. Chapon, M. Doucet, N. Draper, R. Ferraz Leal, M. Gigg, V. Lynch, A. Markvardsen, D. Mikkelson, R. Mikkelson, R. Miller, K. Palmen, P. Parker, G. Passos, T. Perring, P. Peterson, S. Ren, M. Reuter, A. Savici, J. Taylor, R. Taylor, R. Tolchenov, W. Zhou, and J. Zikovsky, Nucl. Instrum. Methods. Phys. Res. A **764**, 156 (2014).

[69] D. C. Wallace, *Thermodynamics of Crystals* (Dover, 1998).

[70] J. Went, Physica **17**, 596 (1951).

[71] I. Chicinas, V. Pop, and O. Isnard, J. Magn. Magn. Mater. **242-245**, 885 (2002).

[72] T. Kollie, "Contributions to the Specific Heat Capacity of Nickel, Iron, and the Alloy Ni_3Fe", PhD thesis (1969).

[73] F. Körmann, A. Dick, T. Hickel, and J. Neugebauer, Phys. Rev. B **83**, 165114 (2011).

[74] M. Palumbo, B. Burton, A. Costa e Silva, B. Fultz, B. Grabowski, G. Grimvall, B. Hallstedt, O. Hellman, B. Lindahl, A. Schneider, P. E. A. Turchi, and W. Xiong, Phys. Status Solidi B **251**, 14 (2014).

Chapter 4

Magnetic quasi-harmonic model for Fe and Fe_3C

This chapter is based of the following published article:
S. H. Lohaus*, L. Mauger*, and B. Fultz. The temperature dependence of nuclear resonant x-ray spectra of magnetic iron and cementite. *Hyperfine Interactions* 243, 1 (2022).

Magnetism plays an essential role in the thermodynamics of materials. It influences their phase stability, the electronic, and mechanical properties. Magnetic spins can couple to phonons and affect their energy, resulting in thermodynamic relevant effects. Magnetism is especially prominent in transition metals. Their electronic d-orbitals are partially filled and unpaired, so the local magnetic moments add up to a net magnetization.

As previously discussed in sections 1.4 and 1.5, the magnetic moments are strongly correlated to the local environments at the atoms, in particularly the volume through the Pauli exclusion principle. Parallel spins in ferromagnetic materials create strong Pauli repulsion forces requiring a larger local volume, as shown in Fig. 1.12. These larger volumes, however, result in lower electrostatic repulsion forces between electrons, which can lower the enthalpy and help stabilizing the ferromagnetic ordering of the spins. A careful balance between Pauli exchange interactions and electrostatic forces between electrons define the enthalpy of magnetic materials. As temperature is increased, thermal fluctuations lead to a progressive reduction of the spin ordering and an increase in the magnetic entropy. Magnetism is therefore essential for thermodynamics and phase stability of materials. This was showcased for iron in section 1.6, where magnetism helps stabilizing its bcc-α phase at low temperatures and pressures.

The effect of the local environments on the magnetic spins was also explored in Chapter 3. In nanostructured materials, a large number of atoms are at grain boundaries with irregular coordinations. This results in a weaker magnetization, with lower Curie transitions, and magnetic spins that are more susceptible to thermal excitations.

Since the ordering of magnetic spins depends strongly on the local environment, it is hard to imagine that they behave independently from atomic vibrations. Phonons cause volume fluctuations that can alter the exchange interactions between spins, and vice-versa. As temperature (or pressure) is increased, more interactions between phonons are induced, as well as between magnons. So the coupling between phonons and spins might also be enhanced by increasing the temperature. The remainder of this thesis explores the coupling between the vibrational and magnetic degrees of freedom in magnetic materials.

In this chapter, our window is through phonons, which are measured by nuclear resonant inelastic x-ray scattering (NRIXS). We look into two magnetic materials: pure iron and an alloy of iron with carbon, Fe_3C, called cementite, which is extensively used in metallurgy. In section 1.6 we discussed how a coupling between magnetism and phonons stabilizes the bcc phase of iron even above the Curie transition. This chapter focuses on modeling this coupling through a magnetic quasiharmonic model for the phonons.

The measurements shown in this chapter we performed previously by Lisa Mauger [1–3]. See Chapter 2 for details on the experimental methods. Lisa analyzed the phonon data and fitted the shifts of phonon energies by the conventional QHA shown in Figs. 4.1 and 4.2. However, as discussed below, these fits cannot capture the full behavior of phonons. I take over from there, recognizing that the deviation from the QHA is correlated to magnetism. This led us to develop a *magnetic* QHA, that accounts well for the deviation of phonons from pure volumetric effects included in the conventional QHA.

4.1 Experiments

The phonon density of states (DOS) of iron in the bcc phase have been previously measured at temperatures between 30-1180 K at beamline 16 ID-D of the Advanced Photon Source [1]. Pure iron has one atom in its primitive unit

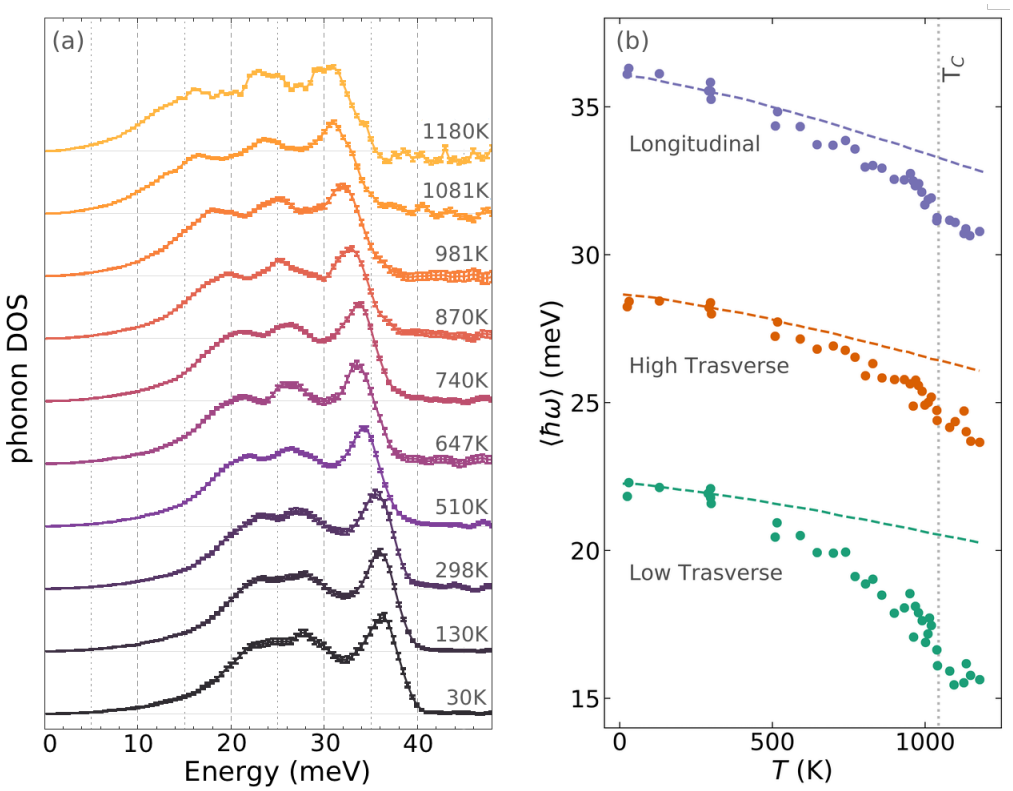

Figure 4.1: Phonon energies of bcc Fe. **(a)** Phonon densities of states (DOS) of ^{57}Fe from 30 K to 1180 K. **(b)** Mean phonon energies for the three vibrational modes of Fe, found by fitting three Lorentzians to the phonon DOS peaks of panel (a). The dashed curves show the QHA, and the vertical dotted line the Curie transition temperature.

cell, so there are 3 possible phonon branches, two transverse acoustic modes and one longitudinal acoustic mode. They can be identified in Fig. 4.1 a as three distinct peaks in the phonon DOS. The distinct modes were fitted by three Lorentzians, giving the energy shifts of the vibrational modes with temperature, as shown in Fig. 4.1 b. All three phonon modes of iron shift to lower energies with increasing temperature.

A quasiharmonic approximation (QHA), briefly described in section 1.5, accounts for phonon shifts due to volumetric changes. Since the volume is affected by temperature, it also indirectly includes thermal shifts of phonon energies $\omega(V(T))$. However, as shown by the dashed curves of Fig. 4.1 b, the QHA is not able to fully capture the phonon behavior, particularly as the temperature approaches the Curie transition. This means that besides the volumetric shifts, the phonon energies are affected by another thermal excitation. This effect cannot explained by anharmonic phonon effects alone, because many-body theory for 3- and 4-phonon processes predicts thermal

shifts of phonon energies that are linear in T [4, 5]. As shown later in Fig. 4.4, the deviations from the QHA seem to track the change in magnetization with temperature, $M(T)$. We therefore attribute this anharmonic effect of phonons to a coupling of vibrational motion with the magnetic spins [1, 6]. This chapter develops a QHA for magnetism, where the deviations of the phonon energies from the volumetric QHA are attributed to the disordering of the spins with temperature, through a spin-phonon coupling.

For a comparison to iron and a further validation of the model presented below, we also quantified the temperature dependence of the phonon modes in cementite, Fe_3C. Cementite has an orthorhombic crystal structure, containing 12 Fe and 4 C atoms per unit cell. The Fe atoms occupy two distinct sites in the lattice with different local environments and bond lengths with their neighbors. Partial phonon densities of states of ^{57}Fe in cementite, $^{57}Fe_3C$, were obtained by Mauger et al. from cryogenic temperatures through the Curie transition at 460 K by NRIXS [2, 3]. The low temperature DOS at 14 K is compared to the one at 463 K in Fig. 4.2 a. The rich crystal structure of cementite results in complex phonon dispersions containing 48 different phonon modes. Unlike iron, we cannot observe distinct peaks from individual modes in the phonon DOS cementite. It rather represents the average energy distribution of all vibrational modes.

The thermal behaviour of phonons in cementite is more subtle than in iron and the phonon modes do not shift much up to the Curie transition. The frequencies of a few phonon branches, notably the acoustic modes of energies below 12 meV, increase with temperature (see insert of Fig. 4.2 a). The energies of most phonons, however, decreased with temperature. The resulting overall mean phonon energy of cementite remains largely constant with temperature below T_C, as shown in Fig. 4.2 b. This behavior is not captured by the QHA, which predicts a stronger thermal softening of phonon frequencies.

The evolution of the magnetic state of $^{57}Fe_3C$ with temperature was measured by nuclear forward scattering (NFS), shown in Fig. 4.3. As the temperature is increased, the intensity modulation of the NFS spectra become broader, corresponding to lower sample magnetizations (see section 2.5). Above 463 K the sample is paramagnetic, the hyperfine levels are no longer split, and the spectrum is close to an exponential decay.

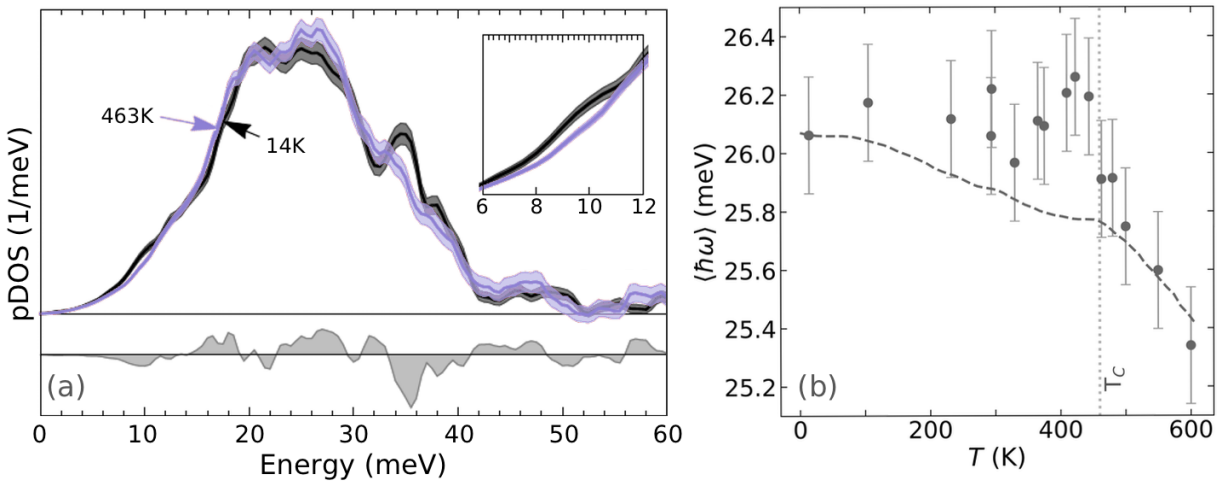

Figure 4.2: Phonon energies of orthorhombic Fe_3C (cementite). **(a)** Partial phonon densities of states of ^{57}Fe in $^{57}Fe_3C$ obtained through NRIXS at 14 K and 463 K. **(b)** Mean phonon energies vibrational modes of Fe_3C. The dashed curve shows the QHA, and the vertical dotted line the Curie transition temperature.

I fitted the NFS spectra using the CONUSS software package [7, 8]. The distribution of the hyperfine magnetic field (HMF) around the ^{5}7Fe atoms was approximated by two Gaussian distributions, corresponding to the two distinct Fe sites in the Fe_3C crystal. Fits are shown as solid curves in Fig. 4.3 a. The mean of these fitted HMF distributions, B_{hf}, are plotted in Fig. 4.3 b below the Curie transition, compared to data from the literature. The HMF, $B_{\mathrm{hf}}(T)$, is proportional to the magnetization, $M(T)$, of the Fe atoms in the material [9]. At room temperature we find a mean HMF of $B_{\mathrm{hf}} = 20.8\,\mathrm{T}$, in good agreement with [10] and [11]. A mean-field model was used to extrapolate the decreasing magnetic field and determine a Curie transition temperature of f$T_{\mathrm{C}} = 460\,\mathrm{K}$. It agrees with [12] and is about 20 K lower than [10].

4.2 Standard phonon quasiharmonic approximation

The simplest model for describing vibrations of atoms in materials is the harmonic model. The nuclei are assumed to be bound together by harmonic springs, and oscillate around their equilibria in parabolic potentials (see Fig. 1.3). Phonons are treated as independent harmonic oscillators, at fixed energies, and without any damping. The partition function for a single

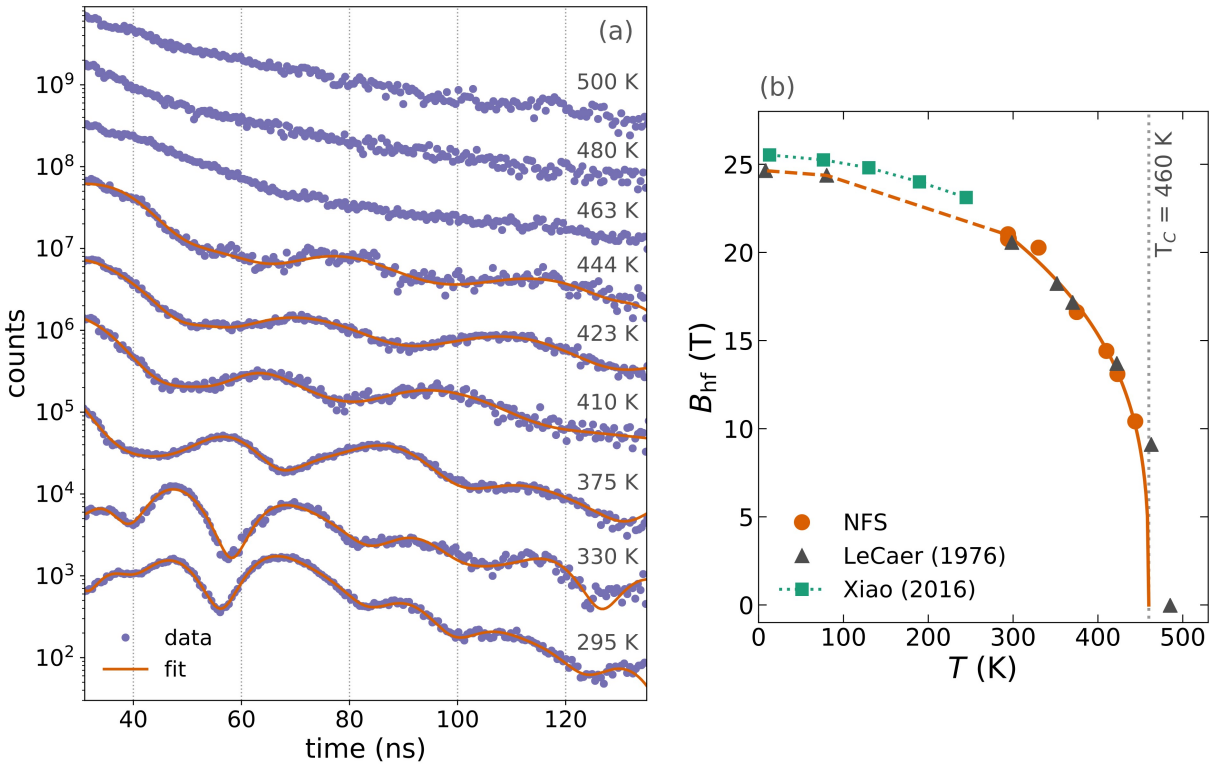

Figure 4.3: Temperature dependence of magnetism in Fe_3C (cementite). **(a)** Nuclear forward scattering (NFS) spectra of Fe_3C at several temperatures. The spectra were fitted using CONUSS, displayed on a log scale, and are offset for clarity. **(b)** Mean hyperfine magnetic fields B_{hf}, from fitted NFS curves of panel a compared to measurements by Le Caër, et al. [10], and Xiao, et al. [11]. Solid orange curve is a power law fit, and dashed orange curve is the extrapolation to low temperatures using [10].

harmonic oscillator of energy $\varepsilon_i = \hbar\omega_i$ can be written as [13]

$$Z_i = \sum_{n=0}^{\infty} \mathrm{e}^{-(n+1/2)\frac{\varepsilon_i}{k_B T}}, \tag{4.1}$$

where n is the occupancy of the oscillator. Expanding the sum as a geometric series gives

$$Z_i = \frac{\mathrm{e}^{-\varepsilon_i/2k_B T}}{1 - \mathrm{e}^{-\varepsilon_i/k_B T}}. \tag{4.2}$$

The assumption that phonons oscillate at fix energies would result in an unchanging phonon DOS. A quick look at Fig. 4.1 a is enough to realize that the phonon modes of iron do shift considerably with temperature to lower energies. The quasiharmonic approximation (QHA) relaxes this assumption, allowing the phonon energies to shift as function of the unit cell volume. The temperature dependence is included only implicitly through the volume, i.e.,

$\omega = \omega(V(T))$, but this is often enough to capture important thermophysical properties of materials, such as thermal expansion.

In the QHA, a Grüneisen parameter, γ_i, is typically used for describing the fractional change in frequency of mode i per fractional change in volume V

$$\gamma_i = -\frac{V_0}{\omega_i}\frac{\partial \omega_i}{\partial V} \,, \tag{4.3}$$

where V_0 is an initial volume. If we simplify the problem by using an average γ for all modes,

$$\omega(V) = \omega(V_0 + \Delta V) = \omega_0 \left(1 - \gamma\, \Delta V/V_0\right) \,. \tag{4.4}$$

A linear dependence between the phonon energy and volume is typically assumed in the QHA, giving a constant Grüneisen parameter.

The harmonic phonon free energy[1], F, can be obtained from the partition function of Eq. 4.2 as $F = -k_\mathrm{B}T \ln Z$ [13]. For a 3D material with N atoms it becomes

$$F(T) = \int_0^\infty \frac{\hbar\omega}{2} 3N g(\omega)\,\mathrm{d}\omega + k_\mathrm{B}T \int_0^\infty \ln\!\left(1 - \mathrm{e}^{-\frac{\hbar\omega}{k_\mathrm{B}T}}\right) 3N g(\omega)\,\mathrm{d}\omega \,, \tag{4.5}$$

where the phonon DOS, $g(\omega)$, is normalized to 1. In the high T limit, this is simplified to

$$F_0(T) = 3N k_\mathrm{B}T \int_0^\infty \ln\!\left(\frac{\hbar\omega}{k_\mathrm{B}T}\right) g(\omega)\,\mathrm{d}\omega \,. \tag{4.6}$$

For the QHA we use $\omega(V)$ from Eq. 4.4, and then expand the logarithm to its leading term, giving

$$F(T) = 3N k_\mathrm{B}T \int_0^\infty \ln\!\left(\frac{\hbar\omega_0\left(1 - \gamma\,\Delta V/V_0\right)}{k_\mathrm{B}T}\right) g(\omega)\,\mathrm{d}\omega \,, \tag{4.7}$$

$$F(T) = F_0(T) - 3N k_\mathrm{B}T \int_0^\infty \gamma\,\Delta V/V_0\, g(\omega)\,\mathrm{d}\omega \,, \tag{4.8}$$

$$F(T) = F_0(T) - 3N\gamma k_\mathrm{B}T\,\Delta V/V_0 \,, \tag{4.9}$$

where $F_0(T)$ is given by Eq. 4.6 and the last line used the normalization of $g(\omega)$ and an average γ for all modes. Since we are relying on the formalism of the harmonic model (Eq. 4.2), phonons in the QHA are still non-interacting

[1] We refer to the free energy with an F here to be consistent with our publication [14]. It is, however, equivalent to the Gibbs free energy G used elsewhere in this thesis.

and there are no 3-phonon processes that give rise to finite phonon life-times and broadening of phonon modes. There are also no anharmonic effects that arise from a direct temperature dependence, and no coupling between different excitations.

Thermal expansion is efficiently predicted with methods of density functional theory that implement the QHA [15]. But the reliability of the QHA is uncertain because with true anharmonicity, phonon frequencies have an explicit dependence on T and V as $\omega(V,T)$ [4, 5, 16], which differs from the $\omega(V(T))$ used in the QHA [17, 18]. With a volume coefficient of thermal expansion β and a change of temperature ΔT, the crystal expands by the amount $\Delta V = \beta \Delta T V_0$. For computing thermal expansion, the total free energy will include an additional term for the elastic energy as

$$F(T+\Delta T) = F_0(T) - 3Nk_{\mathrm{B}}T\gamma\,\beta\,\Delta T + \frac{1}{2}B\left(\beta\,\Delta T V_0\right)^2 \ , \tag{4.10}$$

where B is the bulk modulus. In a typical case with $\gamma \simeq +2$, F is reduced by expanding the crystal as the decreasing phonon free energy (2nd term) competes with the increasing elastic energy (3rd term). Minimizing Eq. 4.10 gives an equilibrium value of thermal expansion $\beta = \gamma 3Nk_{\mathrm{B}}/B$. With $c_V = 3Nk_{\mathrm{B}}/\mathrm{atom}$ in the classical limit, we obtain the widely-stated result

$$\beta = \frac{\gamma c_V}{B} \ . \tag{4.11}$$

Equation 4.11 has been previously used to define a "magnetic Grüneisen parameter" when β and c_V are attributed to magnetism (early examples are [19, 20]).

As shown in Fig. 4.1 b, the QHA describes well the shift of phonon modes below 500 K for iron. As we approach the Curie transition at 1044 K, however, the actual shift of the phonon energies is much larger than predicted by the QHA, suggesting an additional contribution to the thermal shifts. Temperature causes more interactions between phonons (anhamonicity), as well as between spins. Additionally, atomic displacements due to phonons can affect the exchange interactions between spins, and vice-versa. Such a spin-lattice coupling could be the cause of the deviation from the QHA as the spins disorder as the Curie transition is approached.

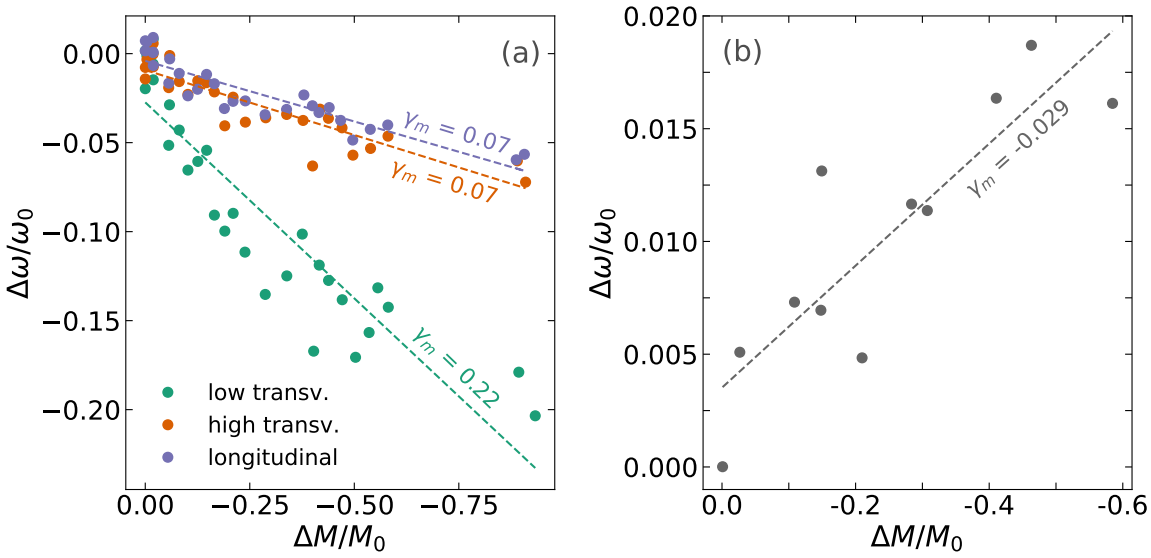

Figure 4.4: Fractional deviation of the phonon energy from the QHA ($\Delta\omega/\omega_0$) vs. fractional change of the magnetization ($\Delta M/M_0$) for **(a)** Fe and **(b)** Fe_3C. Magnetization data for Fe are from [21]. Dashed lines and labeled values are results of linear fits to the data, corresponding to magnetic Grüneisen parameters γ_m of Eq. 4.12.

4.3 Magnetic quasiharmonic approximation

Now we look further into the deviation between the phonon QHA and the measured phonon energy shifts of Fig. 4.1 b and 4.2 b. There is a direct correlation between the deviation, $\Delta\omega$, and the change in magnetization, ΔM, for both iron and cementite as shown in Fig. 4.4. The linear relationship between $\Delta\omega$ and ΔM suggests a coupling between phonon and spins, and motivates the development of a magnetic QHA. We describe the shift of vibrational energies with magnetization using a new magnetic Grüneisen parameter, γ_m. In analogy to the standard QHA for phonons, γ_m gives the fractional change in frequency per fractional change in magnetization,

$$\gamma_\mathrm{m} = +\frac{M_0}{\omega_0}\frac{\partial\omega}{\partial M}\ , \tag{4.12}$$

which can be compared to Eq. 4.3. This gives a magnetization dependence to the phonon energy ω

$$\omega(M_0 + \Delta M) = \omega_0\,(1 + \gamma_\mathrm{m}\,\Delta M/M_0)\ . \tag{4.13}$$

To develop a magnetic QHA for $F(T)$, we need the temperature-dependent magnetization $M(T)$. For ferromagnets the general behavior is well known,

and $\partial M/\partial T$ has a negative sign. This $\partial M/\partial T$ is largest near the Curie temperature, as measured by NFS and shown in Fig. 4.3 for the case of cementite. The magnetization of iron is well know, and follows the same behavior [21]. Using $\omega(M)$ of Eq. 4.13 and following the analysis of the previous section for the standard QHA, the dependence of the free energy on the magnetization is

$$F(M_0 + \Delta M) \;=\; F(M_0) + 3N\gamma_{\rm m} k_{\rm B} T\, \Delta M/M_0 \; . \tag{4.14}$$

For a change in temperature of ΔT

$$F(T + \Delta T) = F_0(T) + 3N\gamma_{\rm m} k_{\rm B} T\, \frac{1}{M_0}\frac{\partial M}{\partial T}\Delta T \; . \tag{4.15}$$

If $\gamma_{\rm m}$ is independent of temperature, as we assume, Eq. 4.15 can be integrated from $T' = 0$ to $T' = T$

$$F(T) = F_0(T) + 3N\gamma_{\rm m} k_{\rm B} T\, \frac{M(T) - M_0}{M_0} \; , \tag{4.16}$$

so the interaction term in Eq. 4.16 is zero at $T = 0$, and causes F to decrease until the Curie temperature. For a more complete free energy, we expect a contribution from magnetic short-range order above the Curie temperature, even though the long-range order is zero.

In the classical thermodynamic limit of this magnetic QHA, the effect of magnetism on the phonon free energy, $F = E - TS$, is entirely through the phonon entropy S. Here the phonon energy E remains as $k_{\rm B}T$ per mode, and is unchanged by magnetism. These are the same roles played by E and S in the standard QHA, but in the magnetic QHA it is M instead of V that alters the phonon entropy and free energy.

4.4 Magnetic QHA for Fe and Fe_3C

The linear dependence between $\Delta\omega$ and ΔM for both iron and cementite shown in Fig. 4.4, suggests that a constant magnetic Grüneisen parameter $\gamma_{\rm m}$ captures the phonon behavior for the entire temperature range up to the Curie transition, and a magnetic QHA seems promising. The dashed lines are linear fits that give values of $\gamma_{\rm m}$ for each mode of iron and for cementite. Such a temperature independent correlation between the demagnetization and the shift of phonon energies, with a constant $\gamma_{\rm m}$, is essential for the QHA and was assumed in Eq. 4.16.

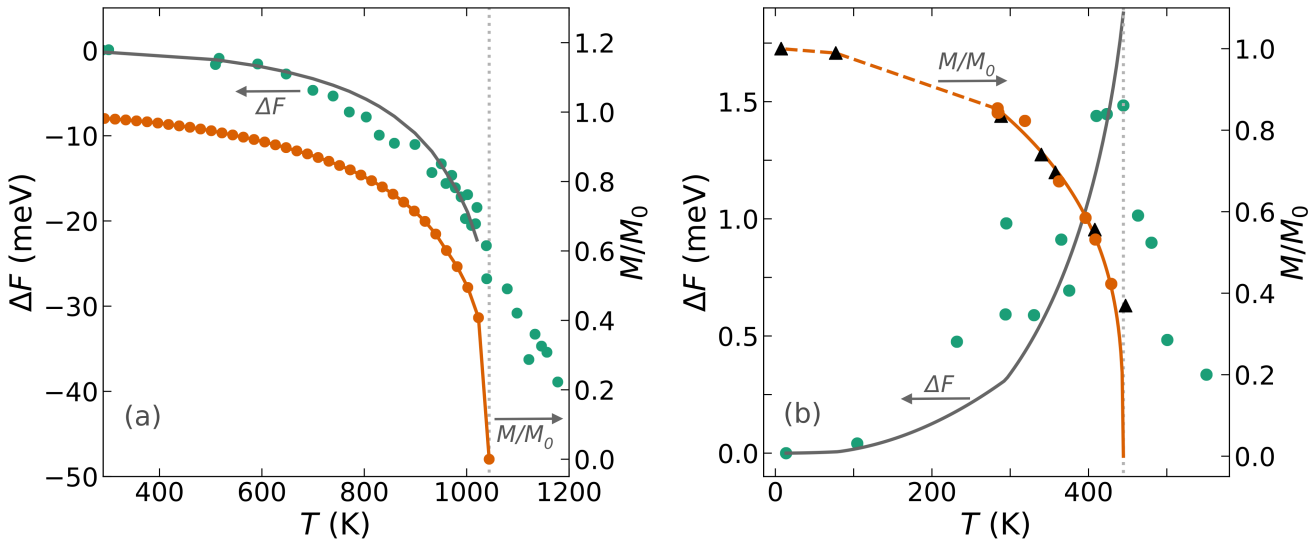

Figure 4.5: Deviation of the phonon free energy from the QHA (ΔF, left axes) and evolution of the magnetization (M/M_0, right axes) with temperature for **(a)** Fe and **(b)** Fe_3C. Magnetization data for Fe are from [21], and magnetization of Fe_3C is the reduced mean hyperfine magnetic field B_{hf} of Fig. 4.3. Solid dark curves are fits of the magnetic QHA (Eq. 4.16) to ΔF from NRIXS data, resulting in $\gamma_{m,Fe} = 0.15$ and $\gamma_{m,Fe_3C} = -0.028$.

To further test the magnetic QHA, magnetic Grüneisen parameters were obtained by fitting Eq. 4.16 to the phonon free energy differences for iron and cementite. In the classical limit, this phonon free energy difference is simply $\Delta F = -T\,\Delta S$, where ΔS is the difference of the experimental phonon entropy from NRIXS and the quasiharmonic phonon entropy. The difference ΔS for iron and cementite are reported in [1] and [2], respectively. Figure 4.5 shows ΔF and the fits of the magnetic QHA, together with magnetization curves $M(T)$. For iron, the magnetic quasiharmonic model (solid dark gray curves) generally captures the behavior of the free energy. Its temperature dependence is proportional to $T(M(T) - M_0)$, as predicted by Eq. 4.16. The fit is less reliable for cementite because the difference between the phonon free energy from QHA calculations and NRIXS measurements (ΔF) is small and hard to measure (see scatter in Figs. 4.2 b and 4.5 b). Nonetheless, cementite shows a magnetic Grüneisen parameter of the opposite sign than iron, where the measured phonon energies from NRIXS are larger than from QHA predictions. As seen from the fit of Fig. 4.5 b, the behavior of cementite is also captured adequately by the magnetic QHA approximation, using a small and negative value of γ_m.

	Standard QHA	**Magnetic QHA**	
	$V(T)$, $\omega(V)$, γ	$M(T)$, $\omega(M)$, γ_m	
		Fig. 4.4 (Eq. 4.12)	Fig. 4.5 (Eq. 4.16)
Fe	$\gamma = 2.18$	$\gamma_{\mathrm{m,LT}} = 0.22$	$\gamma_\mathrm{m} = 0.15$
		$\gamma_{\mathrm{m,HT}} = 0.07$	
		$\gamma_{\mathrm{m,L}} = 0.07$	
		$\langle\gamma_\mathrm{m}\rangle = 0.13^*$	
Fe_3C	$\gamma = 2.24$	$\gamma_\mathrm{m} = -0.029$	$\gamma_\mathrm{m} = -0.028$

Table 4.1: Grüneisen parameters in the QHA and magnetic QHA. The quantities for the standard QHA are from [3]. The magnetic γ_m were determined from fits of the phonon energy shifts with magnetization (Fig. 4.4, Eq. 4.12) and from fits of the phonon free to the magnetic QHA (Fig. 4.5, Eq. 4.16).
* This is the weighted average of the three iron modes in the phonon DOS.

The values of γ_m determined by fitting the phonon energy shifts with magnetization (Fig. 4.4), and the γ_m from fitting the phonon free to the magnetic QHA of Eq. 4.16 (Fig. 4.5) are very similar, both for iron and for cementite. These values are listed in Table 4.1, along with the standard phonon Grüneisen parameters.

Origin of magnon-phonon interactions

Why a phonon frequency would depend on magnetization has been a topic of interest for many years. With many-body theory, in 1969 Silberglitt [22] considered the creation of magnons from phonons, and commented that a spin zero phonon would create two magnons of opposite spin, in addition to satisfying kinematical requirements of energy and momentum conservation for the interaction. For band magnetism, in 1989 Kim [23] considered how the electron-phonon interaction involving free electrons would affect magnetism, and vice-versa.

For ferromagnetic iron, the band structure is polarized, with more electrons in the ↑-band than the ↓-band. A transfer of electrons with temperature from the ↑-band to the ↓-band leads to changes in the density of electron states at the Fermi level. Such changes alter the number of electrons that are available to screen the ion displacements in atom vibrations, altering the interatomic forces. Changes of phonon frequencies with electron density at the Fermi level

are well-known [13]. A net gain of electron density at the Fermi level can occur as magnetization is lost near the Curie transition of a ferromagnet. In other words, the electron-phonon interaction will tend to soften the interatomic forces and reduce phonon energies as magnetism is lost. This increases the phonon entropy and reduces the free energy.

The large difference of γ_{m} between iron and cementite is not readily explained with the simple electronic DOS at the Fermi level – the polarized electronic DOS curves are similar for both, and of course the difference in γ_{m} for the different phonon branches in iron cannot be explained with this simple approach. More subtle effects of the magnetization on phonons are needed to explain the difference in the γ_{m} of bcc iron and cementite. Different phonon branches often have very different changes with temperature. In the standard QHA there is a substantial cancellation of phonon effects from the different mode Grüneisen parameters $\{\gamma_i\}$, with their different signs and magnitudes. This may be true for the different phonon responses to magnetism, requiring individual mode magnetic Grüneisen parameters $\gamma_{\mathrm{m},i}$. Finally, from work with mode Grüneisen parameters in non-magnetic materials, it is known that when the γ_i take large values of 10 or so, or have negative signs, the QHA is generally unreliable and many-body theory of anharmonicity is needed for quantitative explanations [13, 17, 18, 24]. Many-body theory may also be necessary for the interactions of phonons with magnetic spins. Nevertheless, the magnetic QHA does predict approximately the shape of the phonon free energy curves beyond the standard QHA for phonons. It is easy to use, and makes a good case that phonons in iron and cementite depart from the standard phonon QHA owing to magnon-phonon interactions.

4.5 Conclusions

NRIXS measurements show that both bcc iron and cementite have phonon free energies that deviate from the standard QHA for phonons, with deviations being largest near the Curie temperature. In the case of iron this extra free energy makes a substantial contribution to stabilizing the bcc phase near the Curie temperature and slightly above [3]. We propose a magnetic quasiharmonic theory, analogous to the QHA for phonons, using a magnetic Grüneisen parameter, γ_{m}, that is the fractional change in phonon frequency per fractional change in magnetization. This formalism redicts a deviation from the QHA

in proportion to $T(M(T) - M_0)$. It accounts for the thermal trends of the phonon free energy beyond the QHA for iron and cementite. It helps to identify the presence of magnon-phonon interactions. In practice, it requires only data from NFS and NRIXS, and a comparison of their trends. The physical origins of their different γ_m remain a challenge to explain, however.

References

[1] L. Mauger, M. S. Lucas, J. A. Muñoz, S. J. Tracy, M. Kresch, Y. Xiao, P. Chow, and B. Fultz, Phys. Rev. B **90**, 064303 (2014).

[2] L. Mauger, J. E. Herriman, O. Hellman, S. J. Tracy, M. S. Lucas, J. A. Muñoz, Y. Xiao, J. Li, and B. Fultz, Phys. Rev. B **95**, 024308 (2017).

[3] L. M. Mauger, "Phonon thermodynamics of iron and cementite", PhD thesis (2015).

[4] A. A. Maradudin and A. E. Fein, Phys. Rev. **128**, 2589 (1962).

[5] D. C. Wallace, *Thermodynamics of Crystals* (Dover, 1998).

[6] F. Körmann, B. Grabowski, B. Dutta, T. Hickel, L. Mauger, B. Fultz, and J. Neugebauer, Phys. Rev. Lett. **113**, 165503 (2014).

[7] W. Sturhahn, Hyperfine Interact. **125**, 149 (2000).

[8] W. Sturhahn, NRIXS Scientific Software (website).

[9] M. A. Kobeissi, Phys. Rev. B **24** (1981).

[10] G. Le Caer, J. Dubois, and J. Senateur, J. Solid State Chem. **19**, 19 (1976).

[11] X.-W. Liu, S. Zhao, Y. Meng, Q. Peng, A. K. Dearden, C.-F. Huo, Y. Yang, Y.-W. Li, and X.-D. Wen, Sci. Rep. **6** (2016).

[12] H. K. D. H. Bhadeshia, Int. Mater. Rev. **65**, 1 (2020).

[13] B. Fultz, *Phase Transitions in Materials* (Cambridge University Press, 2014).

[14] S. H. Lohaus*, L. Mauger*, and B. Fultz, Hyperfine Interact. **243**, 1 (2022).

[15] A. Togo and I. Tanaka, Scr. Mater. **108**, 1 (2015).

[16] O. Hellman, I. A. Abrikosov, and S. I. Simak, Phys. Rev. B **84** (2011).

[17] Y. Shen, C. N. Saunders, C. M. Bernal, D. L. Abernathy, M. E. Manley, and B. Fultz, Phys. Rev. Lett. **125**, 085504 (2020).

[18] D. S. Kim, O. Hellman, J. Herriman, H. L. Smith, J. Y. Y. Lin, N. Shulumba, J. L. Niedziela, C. W. Li, D. L. Abernathy, and B. Fultz, Proc. Natl. Acad. Sci. U.S.A. **115** (2018).

[19] M. A. Simpson and T. F. Smith, J. Phys. F **11**, 397 (1981).

[20] E. Fawcett, J. Condens. Matter Phys. **1**, 203 (1989).

[21] J. Crangle and G. Goodman, Proc. Roy. Soc. Lond. A **321**, 477 (1971).

[22] R. Silberglitt, Phys. Rev. **188**, 786 (1969).

[23] D. J. Kim, Phys. Rep. **171**, 129 (1988).

[24] C. W. Li, X. Tang, J. A. Muñoz, J. B. Keith, S. J. Tracy, D. L. Abernathy, and B. Fultz, Phys. Rev. Lett. **107**, 195504 (2011).

Chapter 5

Thermodynamic origin of the Invar effect

This chapter is based of the following article:

S. H. Lohaus, M. Heine, P. Guzman, C. M. Bernal-Choban, C. N. Saunders, G. Shen, O. Hellman, D. Broido, B. Fultz. A thermodynamic explanation of the Invar effect. *Accepted for publication in Nature Physics (2023).*

Invar is a magnetic alloy of iron and nickel with an anomalous near-zero thermal expansion at ambient conditions. Since its discovery in 1985, it has been used in precision instrumentation and mechanical devices that require dimensional stability against changes in temperature [1]. However, the microscopic origins of the Invar effect of anomalously low thermal expansion are still not fully understood. Its electronic and magnetic structures have been extensively studied, but the role of phonons is missing in the picture. Without phonons, the thermal expansion cannot be quantitatively understood.

Until now, we looked into how thermal energy is stored in matter. When increasing the temperature of a material, thermal energy causes vibrations of atomic nuclei, interacts with the electronic structure, and excites their spins. Most of the entropy is associated with thermal vibrations of the lattice. The more strongly the atoms vibrate, the larger the phonon entropy. As a result, increasing the temperature usually causes materials to expand as discussed in the introduction (Fig. 1.12).

Here, we look at thermal expansion in more depth. In Invar, phonons alone cannot explain anomalous thermal expansion behavior, so we need to include the contributions from all individual excitations. Interactions between phonons and magnetic spins explain the anomalous Invar effect, and the meth-

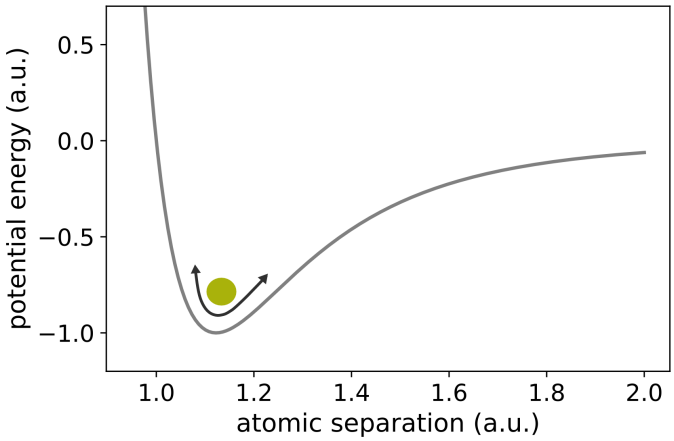

Figure 5.1: Lennard-Jones potential as an example of an anharmonic potential. As the temperature is increased, the atoms explore larger amplitudes, resulting in a larger atomic separations due to the skewness of the potential. The potential itself changes with temperature, so for computing the thermal expansion, the volume that minimizes the total Gibbs free energy needs to be found.

ods proposed here can be extended to understand thermophysical behaviors in other magnetic materials as well.

5.1 Anomalous thermal expansion

Metals usually have a pronounced thermal expansion. Especially those with lower bonding energies and melting points. The thermal expansion of glasses tends to be larger than of crystals, and liquids expand slightly more than solids. The conventional textbook description starts from the potential between atoms, like atoms connected by springs. The potential in not symmetric and harmonic, however. Pauli exclusion principle prevents atoms from coming very close to each other, so the energy raises sharply at low atomic separations. Think of a Lennard-Jones potential, for example (shown in Fig. 5.1). When temperatures increase, most of the thermal energy goes into atomic vibrations, so the atoms explore larger amplitudes in their potential energy. Due to the skewed potential, the atomic separation tend to increase a little, causing the thermal expansion. Thermal expansion is inherently an anharmonic effect. For actual computations of thermal expansion, the free energy $G(V, T)$ must be minimized, giving an equilibrium volume $V(T)$.

Negative thermal expansion

Thermal contraction is fairly rare, but we are all familiar with an example: water. Ice floats on liquid water, because it is less dense (has a larger volume) than the warmer liquid. The volume of water therefore contracts when it melts. You should not forget a beer can in the freezer because the expansion of the freezing water might cause the can to explode and make a mess.

Negative thermal expansion (NTE) is found in several oxides, such as $Si0_2$ [2], ZrW_2O_8 [3], and many perovskites [4–6]. Geometric arguments are often used to explain the anomalous NTE. Transverse vibrations of the central atom in a linear chain like O-S-O (in SiO_2 or CO_2 [2]) can decrease the distance between the outer O atoms (as in a vibrating guitar string). Rigid unit modes of tetrahedra in SiO_4 [7], and octahedra in ZrW_2O_8 [3] or layered perovskites [6], can distort the lattice causing NTE.

Geometric explanations sound appealing and may be intuitive, but they usually focus on specific modes. The entire phonon spectrum has to be accounted for to quantify the thermal expansion, however. Cuprite, Cu_2O, contracts when heated up to about 500 K. While the O atoms soften and oscillate more strongly, the phonon energies of the Cu increase with temperature, and they vibrate less. Details require anharmonic interactions between phonons, but the net effect is a thermal contraction [8]. Pure silicon also contracts at low temperatures. A full anharmonic picture, that includes the zero point motion of phonons, is necessary for understanding this anomalous thermal expansion behavior [9].

Invar behavior

Invar is a face-centered cubic (fcc) random solid solution of Fe and Ni, with 65 atomic % Fe and 35 atomic % Ni. Geometric and symmetry explanations have no chance of success for explaining its anomalous thermal expansion. Pure Fe and Ni both have a well behaved positive thermal expansion. When alloyed, both show a similar phonon spectra [10]. But in a narrow range near a composition of 65% Fe, Invar shows an anomalously low thermal expansion (see Fig. 5.2). Why does this happen? Phonons alone cannot explain it, we need to bring other excitations into the picture.

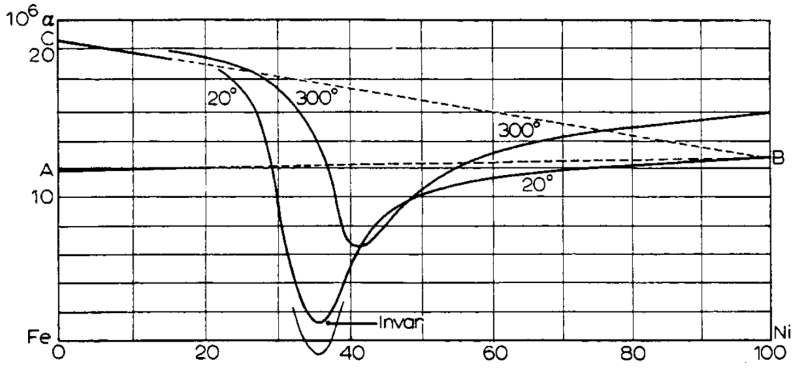

Figure 5.2: Linear thermal expansion coefficient α of Fe-Ni alloys measured by Guillaume. The minimum, close to $\alpha = 0$, corresponds to the Invar composition [11].

Fe-Ni Invar was discovered in 1895 by the Swiss physicist C.E. Guillaume. It was named *Invar* due to the invariance of its volume with temperature. Although the Invar effect of anomalously low thermal expansion was discovered in $Fe_{65}Ni_{35}$, it has since been found in Fe-Pd, Fe-Pt, Fe-Mn, Ni-Mn, Co-Mn, Fe-Cr and several other crystalline and amorphous alloys of iron with transition metals [1, 12]. Such a property can be exploited in numerous in engineered devices to have structural stability against temperature, and allow for tight tolerances [1]. Large structures such as pipelines or tanks that require cryogenic cooling use Invar alloys. Invar has been used in composite molds in the aerospace industry to achieve tight dimensional tolerances in curing processes. Invar is used for structural components in precision instrumentation, such as laser and optical measuring systems. Invar materials appear in microscopes, in support systems for mirrors in telescopes, and in orbiting satellites [13].

Guillaume himself presented applications for Invar and Fe-Ni alloys [11]. He demonstrated how Invar can be used for precision measurements of length in the late 1800s. By using a long Invar wire, he tracked the vertical motion of the Eiffel Tower, while it expands and contracts in the course of a day. He attached a wire from the ground up to the second platform of the tower and recorded its height variation as the iron structure, but not the Invar wire, expands and contracts with the changing temperature. Invar-like alloys also allow for precise measurement of time. A material with thermally-invariable elasticity modulus, named *Elinvar*, is achieved when the Ni content is changed to about 45%. Guillaume designed compensating springs for watches using Elinvar, reducing their error by five times. By 1927, over 100 million watches were made with Elinvar springs.

The discovery of Invar was so important that Guillaume was awarded the physics Nobel Prize in 1920 "in recognition of the service he has rendered to precision measurements in Physics by his discovery of anomalies in nickel steel alloy". Because of Guillaume, Albert Einstein had to wait another year for his Nobel, awarded in 1921.

So why is the volume of Invar not affected by temperature? Guillaume knew it had something to do with the magnetic nature of Fe-Ni alloys. The Invar effect disappears when heating above the Curie transition. This is seen in Fig. 5.3, where the coefficient of thermal expansion, α, is plotted against temperature. For the classic Invar composition of 65% Fe, the thermal expansion is close to zero up to about 450 K (roughly $0.25/T_{\mathrm{m}}$). This is in striking contrast to the expected thermal expansion of the 'lattice' from the thermally enhanced phonon vibrations in an anharmonic potential. Above the Curie temperature, $T_{\mathrm{C}} = 515\,\mathrm{K}$, the Invar behavior vanishes, and the measured thermal expansion matches that from the 'lattice'.

The term *Invar* has since been generalized for all alloys that present a lower thermal expansion than expected from phonons. At 70% Fe the Invar behavior is also observed at low temperatures, but above its Curie transition, the thermal expansion is larger than 'normal'. This excessive thermal expansion became know as the *anti-Invar* effect. It is observed at all compositions above 70% Fe. It seems like the thermal expansion behaviour can be tuned by the alloy composition. At large Fe content, the plot is cut off at the Curie temperature because the magnetic transition is accompanied by a martensite transformation into the bcc phase.

The anomalous properties of Invar are by no means limited to the anomalous thermal expansion [1]. They include an anomalous softening of the elastic constants, affecting both the bulk and shear moduli. Invar has a strong temperature dependence of the magnetization, and an anomalous specific heat, with excessive magnetic contributions even well below the Curie transition. And a Curie temperature that collapses near the Invar composition.

5.2 Alloying iron and nickel

Iron has a complex magnetic structure, with spin configurations ranging from ferromagnetic (FM), to anti-ferromagnetic (AF), and non-collinear partially

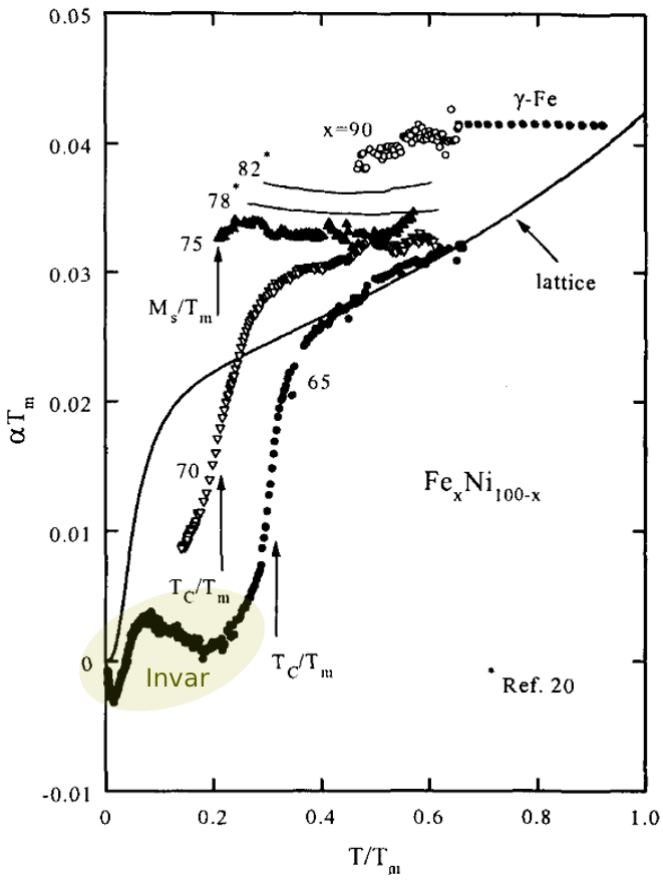

Figure 5.3: Anomalous thermal expansion of Fe-Ni alloys, compared to the expected thermal expansion from anharmonic phonons, labeled 'lattice' [14]. Both axes are scaled by the melting temperature T_{m}.

disordered states [15]. This gives rise to a rich phase diagram as previously described in section 1.6. The stable bcc (FM) phase has a magnetic moment of $2.2\,\mu_{\mathrm{B}}$/atom at 0 K. Nickel, on the other hand, is FM with a much lower moment of $0.6\,\mu_{\mathrm{B}}$/atom. Its weaker magnetism allows nickel to have a closed-packed fcc structure up until melting. It is not surprising that the magnetic properties and magneto-volume effects of Fe-Ni alloys stem mostly from the iron atoms.

The phase diagram of Fe-Ni alloys is shown in Fig. 5.4. Below 70% Fe content it has a fcc (γ) structure. The Invar region ($\sim$50 - 70% Fe) is marked by a sharp collapse of the both the magnetic moments M and the Curie temperature T_{C}. This region also exhibits strong magneto-volume effects, being strongest at 65% Fe. Above 70% Fe, the fcc structure transforms into bcc (α), and the Invar effect is no longer observed. However, as the temperature is in-

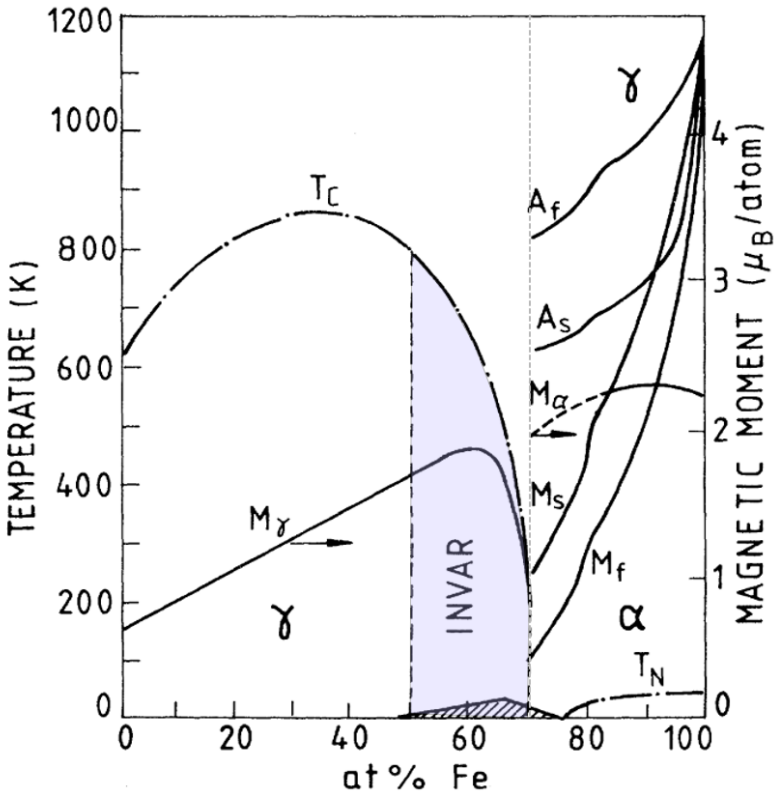

Figure 5.4: Fe-Ni phase diagram, as a function of the atomic % of Fe [16]. The γ (fcc) phase is stable up to 70% Fe, above which the α (bcc) becomes favorable. The shaded area shows the region of Invar behavior. The dashed area at low-temperatures represents spin-glass states [17]. Left axis: concentration dependence of the Curie temperature (T_C) and the Néel temperature (T_N) in the γ phase. Martensite transformation temperatures (start and finish) into the austenite γ phase, A_s and A_f, and back into the martensite α phase, M_s and M_f, are also included. Right axis: Concentration dependence of the magnetic moments in both the γ and α phases (M_γ and M_α).

creased, a martensite transformation back into the γ phase (called austenite) is observed. This transformation happens between temperatures A_s and A_f (Austenite start and finish temperatures). The anti-Invar effect is observed at this high temperature γ phase. The transformation back into the α phase, called martensite, has a hysteresis and occurs at a lower temperature between M_s and M_f.

5.3 Interpretations and theories of the Invar effect

The wide applicability of Invar and the curiosity about the role of magnetism in its anomalous thermal expansion, have stimulated thousands of scientific studies of the Invar effect. Here we review the key theories that led to our current interpretation of its anomalous behavior. Because of the complex and

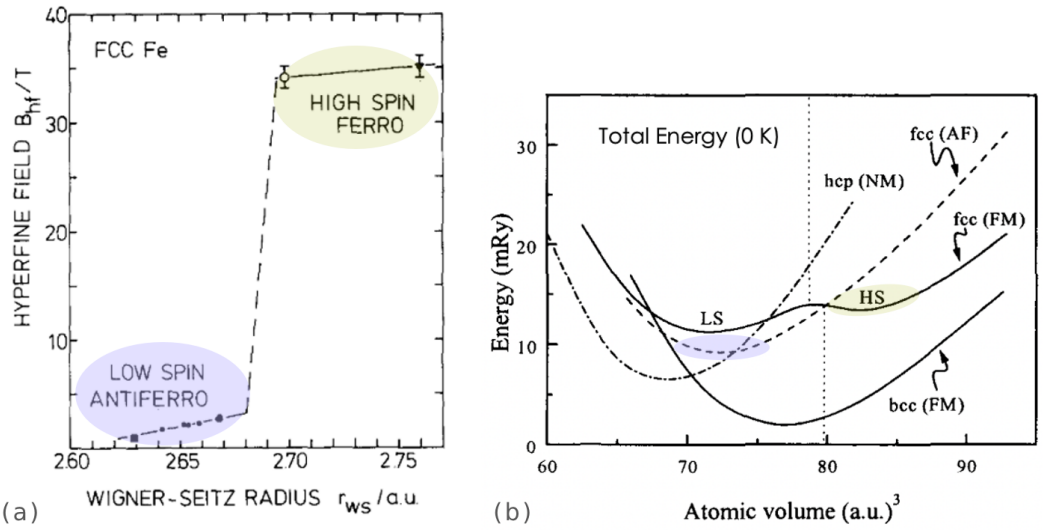

Figure 5.5: States of fcc γ-Fe. **(a)** Hyperfine field of fcc Fe as a function of volume from Mössbauer spectroscopy, giving the strength of magnetic moments. These were measured on γ-Fe precipitates and samples on Cu and Cu-Au substrates to force Fe into the fcc phase [20]. **(b)** Bonding energy as a function of volume at T=0 K of pure Fe in the bcc, fcc and hcp crystal structures [14].

important role of magnetism, most theories focused on the electronic structure of Fe-Ni alloys. Phonons are rarely part of the picture.

γ phases of iron

Pure iron is stable in the FM bcc phase. Its meta-stable fcc (γ) phase, however, has very interesting magnetic properties, and becomes stable when alloyed with nickel, palladium, or platinum, for example. Understanding the γ phase of iron is key to understanding earlier models of the Invar effect.

Fcc Fe is anti-ferromagnetic (AF) at low temperatures. The AF spin ordering results is fairly low magnetic moments, so it often called a 'low-spin' phase. It also has a 'high-spin' ferromagnetic (FM) phase, close by in energy and stable at larger volumes. These phases, shown in Fig. 5.5, have been observed both by ab initio calculations [18, 19] and by Mössbauer spectroscopy at 4.2 K [20].

The Pauli exclusion principle provides a qualitative connection between atomic volumes and the magnetic ordering. When neighboring atoms have parallel spins, wave-functions have less overlap, requiring a larger volumes. Whereas AF coordinations, allow overlapping orbitals and hence, lower volumes.

The FM phase does not always have a large moment, however. Both high-spin (HS) and low-spin (LS) phases have been calculated for FM γ-Fe [21] (and for FM Fe-Ni alloys [16, 22]). Fig. 5.5 b shows, accordingly, a double well for the FM phase. There are hence two different low-spin states in γ-Fe, a FM and a AF one. They both appear nearby in energy and volume, and are interchangeably referred to as the low-spin (or low-moment) state in the literature.

Two-state model

The first widely used model to explain the Invar effect was proposed in 1963 by J. Weiss [23]. It is based on the observation of Fig. 5.5 that γ-Fe has two distinct phases, a high-spin-high-volume, and a low-spin-low-volume phase. Unlike Fe, Fe-Ni Invar is stable in the HS phase at 0 K (with a magnetic moment of about 2.8 μ_B/atom). The LS phase has a lower equilibrium volume (about 8% lower), lower magnetization (about 0.5 μ_B/atom), and is separated in energy from the HS phase by only about 2.6 mRy according to Weiss.

As temperature is increased, electrons can be thermally excited from the HS into the LS state. Besides the reduction in magnetization, this transition results in a volumetric contraction. It counteracts the expansion from anharmonic phonons and can yield an apparent near-zero expansion.

The simplicity of this model and its capability of fitting experimental observations (e.g., in [24]), made this model very popular and it is still widely used. But it is a purely phenomenological statistical model, and the co-existence of these two states has never been experimentally verified [22].

Electronic band-structure

Similarly to γ-Fe, *ab initio* calculations on ordered and disordered Fe-Ni found an energy landscape with two minima [14, 16, 22, 25]. These are shown in Fig. 5.6 a for Fe_3Ni. Unlike γ-Fe however, the state at larger volumes and higher magnetic moments (HM) is the stable one, whereas the low magnetic moment (LM) state is meta-stable at lower volumes.

These calculations laid out important microscopic mechanisms to explain the Invar effect. Their spin-polarized electronic density of states is shown in Fig. 5.6 b. In the HM state (upper panel), electrons occupy the orbitals asym-

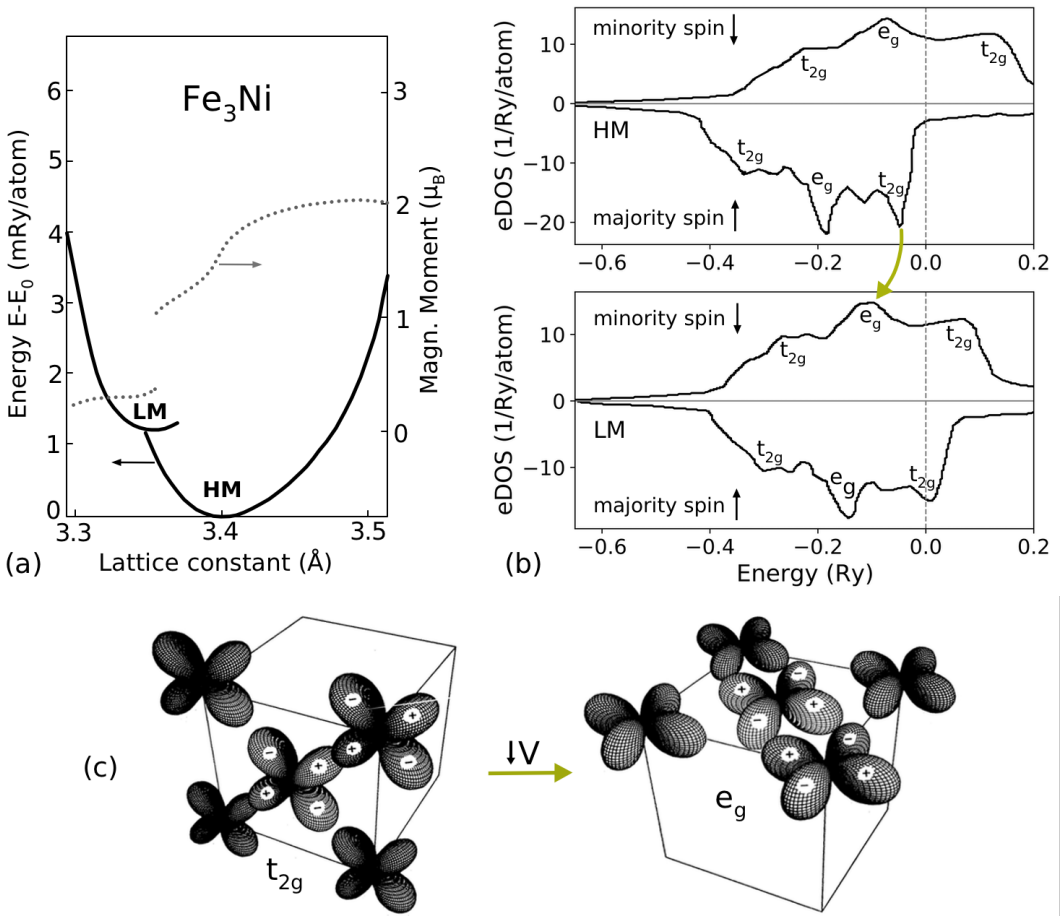

Figure 5.6: Electronic structure of Fe-Ni Invar. **(a)** Energy landscape of Fe_3Ni from *ab initio* band structure calculations (data from [25]). The two minima correspond to the low-moment (LM) and high-moment (HM) states. Right axis shows the strength of their magnetic moments. **(b)** Spin-polarized electronic density of states, with majority (spin-up) and minority (spin-down) bands [16, 22]. Upper plot shows the high-moment (HM) and lower plot the low-moment (LM) state. The thermal spin-flip transition from t_{2g} to e_g orbitals is marked by an arrow. **(c)** t_{2g} and e_g orbitals on a fcc crystal. The charge densities in the t_{2g} configuration point towards each other forming ddσ bonds. For FM ordering, they require a larger volume than ddπ bonds of e_g orbitals [22].

metrically, filling mostly the spin-up bands, and resulting in a ferromagnetic material. The mean magnetization of $Fe_{60}Ni_{40}$ was reported as $1.6\,\mu_B$/atom ($1.9\,\mu_B$ per Fe atom and $0.6\,\mu_B$ per Ni atom) [16]. A much lower magnetization of $0.25\,\mu_B$/atom was obtained for the LM state of Fe_3Ni [22] (lower panel), as a result from the more symmetric occupation of the bands.

The Invar effect was attributed to the thermal excitation of electrons from the spin-up band just below the Fermi energy (with mostly t_{2g} orbitals) into the spin-down band (mostly e_g orbitals). This is illustrated by an arrow in Fig. 5.6 b. The spin-flip excitations reduce the mean magnetization, and cause a volume contraction. For FM ordering, the e_g orbitals require a lower volume than t_{2g} orbitals, because their their lobes are not directed towards their nearest neighbour in an fcc lattice (see Fig. 5.6 c). As temperatures are increased, fluctuation theories predict that the equilibrium volumes of the HM and LM states gradually merge into a single minimum [16].

This picture of a double well potential, with thermal excitation of electrons, might resemble the two-state model, and has been used extensively to corroborate Weiss' phenomenological two-state model. Schröter, Entel et al. disagree and think it "differs greatly from Weiss". It considers the state of the entire system, with an itinerant electron model, in contrast to the local theory of Weiss, that implies a co-existence of two kinds of Fe atoms, a high-spin-high-volume and a low-spin-low-volume variety [16].

Anti-Invar and martensite transformation

There seems to be a connection between Invar, anti-Invar, and the martensite transformation [16, 25, 26]. The relative stability of the HM and LM states is controlled by the alloy composition, and increasing the concentration of Fe favors gradually the LM state. Figure 5.7 shows the energy surface with lattice parameter vs. magnetic moment for 60% (a) and 70% Fe (b). At 60% Fe, the Invar effect is seen: the HM is more stable, and spin-flip transitions to the LM phase cause a volume contraction. Above 70% Fe content, the stability of the HM and LM phases switch. Now, electrons are excited from the LM to the HM phase (from e_g to t_{2g} orbitals). This causes an increase of the net magnetization as well as an excessive volume expansion: the anti-Invar effect.

Beyond 70% Fe, however, the bcc structure is more energetically favorable, as show in Fig. 5.7 c. Instead of the anti-Invar effect, there is a transformation into

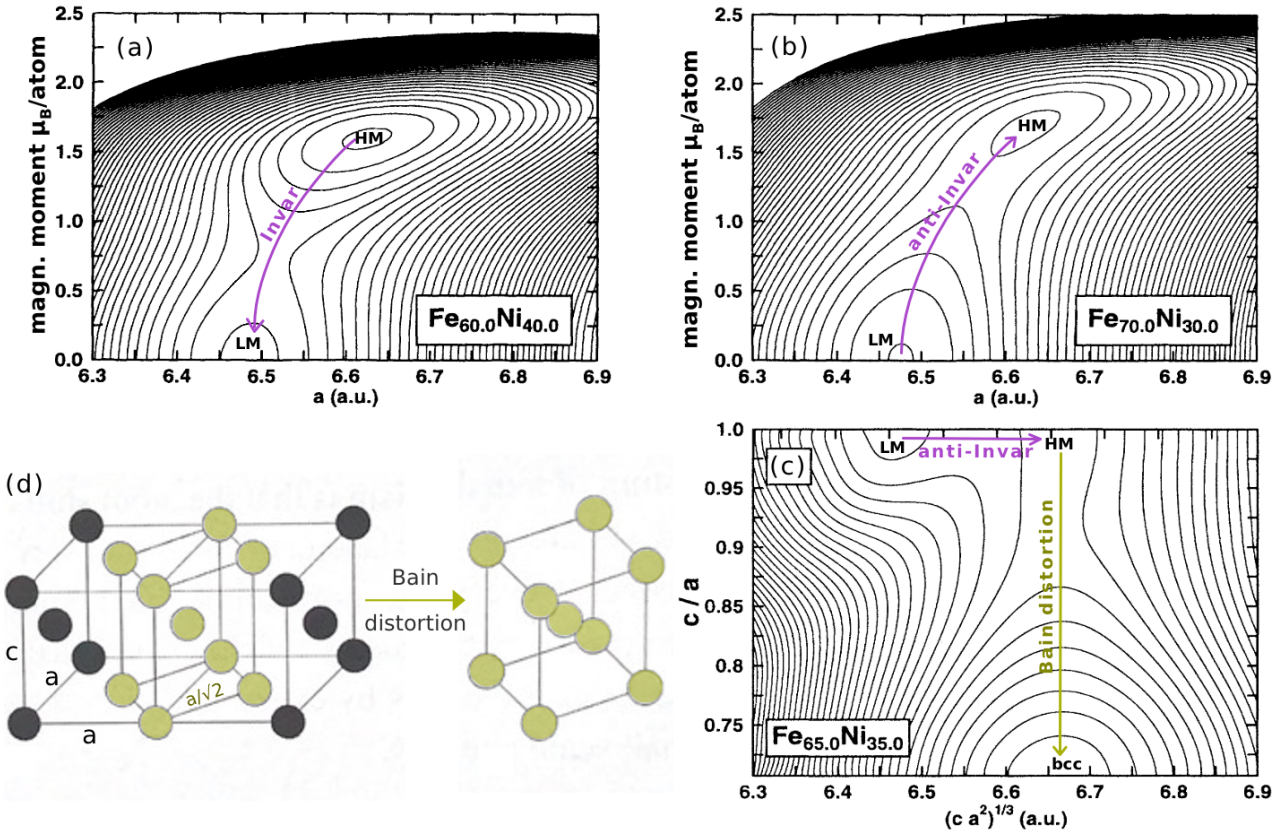

Figure 5.7: Energy surfaces with magnetic moment vs. lattice parameter in the **(a)** Invar and **(b)** anti-Invar regions [16]. **(c)** Energy surfaces with height-to-width ratio of the unit cell (c/a) vs. normalized cell volume. The martensite transformation happens in two parts: from the LM minimum to the HM saddle point (anti-Invar effect), and then through a Bain distortion into a bcc phase. [16]. **(d)** Highlight: body-centered tetragonal coordination within the fcc structure. By changing the c/a ratio (Bain distortion) it can be transformed into a bcc structure.

the bcc phase. It is a martensite transformation mediated by a Bain distortion of the structure [26, 27]. The most efficient path for this transformation is through a saddle point as marked by arrows in the figure. The anti-invar transition, from the LM minimum into the HM saddle point, seems to be the precursor of the martensite transformation. (The structural details of the Bain distortion are shown in panel d).

The anti-Invar effect is only observed at high temperatures, once the structure transforms into the fcc γ phase (revisit Fig. 5.4). At these high temperatures, the LM phase is stable, and the anti-Invar effect can occur. Polarized neutron scattering measurements have indeed observed an increase of the magnetic moments as the temperature was increased from 700 to 1000 K for Fe-Ni at 85% and 90% Fe content [28].

This same behavior with Invar and anti-Invar regions being separated by a martensite transformation has been observed in Fe-Pd and Fe-Pt. It might be a general feature of Invar materials.

Multiple states & continuous transition

Even though band-structure calculations laid out microscopic mechanisms to explain the Invar effect, they were not able to quantify the thermal expansion.

For several fcc alloys (including Fe-Ni, Fe-Pt, Fe-Pd, Co-Mn, and others) there is an unambiguous relation between the *d*-electron concentration per atom (e/a) and the magnetic ordering: above $\sim 8.4\,\mathrm{e/a}$ the ordering is FM, below it is AF, and in between, spin-glass behavior is observed [25]. Interestingly, the Invar behavior (and anti-Invar) happens only near this region, where there is no strong preference for FM ordering over AF.

The Invar behaviour might be governed by non-collinear spins with partial AF exchange, which can lead to frustrated Fe-Fe bonds. Spin-glass states have indeed been measured in Fe-Ni between 55-70% Fe [17]. Competing FM and AF interactions freeze into a frustrated spin-state below a glass transition temperature of around 30 K. Partial AF ordering has been shown in Mössbauer measurements at 4.2 K [29], with a gradual transition from a FM state into partial AF order with pressure. Another Mössbauer study concludes that the reduction in magnetization occurs mostly due to a loss of the spin orientation, rather then a decrease of their magnitudes [30]. Non-collinearity of spins in Invar has been observed by XMCD measurements [31], although this is not universally accepted [32].

Advances in *ab initio* methods enabled calculations with non-collinear spin configurations, beyond the itinerant model. Abrikosov et al. predicted a family of magnetic states in Fe-Ni Invar which are close in energy to each other. They include ferromagnetic, ferrimagnetic, anti-ferromagnetic, disordered non-collinear spins, and spin spiral states [15]. The Invar effect has been attributed to the non-collinearity of spins by Schilfgaarde et al. [33], a view that was recently supported by Ehn et al. [34]. As the volume is decreased, they observe first a spin-flip into local AF order with slightly reduced local moments. This catalyses a gradual transition to a non-collinear spin configuration as the volume is further decreased (see Fig. 5.8).

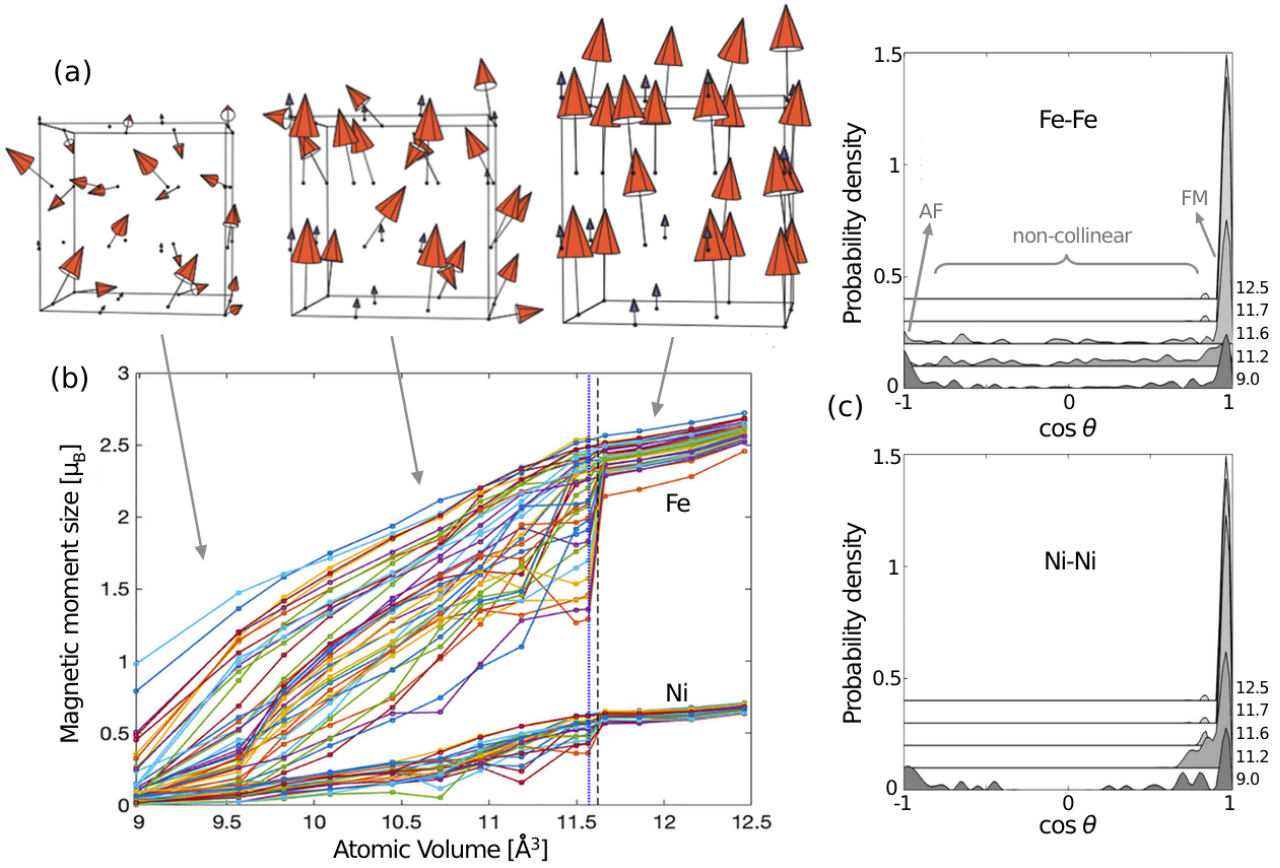

Figure 5.8: Noncollinear magnetism in Fe-Ni Invar. **(a)** Noncollinear spin configurations of Fe (orange) and Ni (blue) atoms in the Invar lattice [33]. As the volume decreases the spins become progressively disordered, especially those at Fe atoms. **(b)** Magnitude of induvidial magnetic moments as a function of volume [34]. Ni atoms have a much lower moment, less dependent on volume. **(c)** Angular correlation between Fe atoms and Ni atoms [34]. While Fe becomes non-collinear with decreasing volumes, the Ni moments remain mostly FM.

These new studies uncover important interactions between spins. They confirm that Fe atoms are responsible for most of the magnetic behavior. The magnetism decreases both because of orientational disorder and magnitude of the moments. Nickel atoms, with much weaker magnetic moments, remain mostly ferromagnetically aligned. The details are described in Fig. 5.8 showing (a) the increasing non-collinearity with decreasing volumes, (b) the magnitudes of the individual moments, and (c) the angular correlation between spins in Fe and Ni.

However, the calculated volume contraction due to magnetism is much larger than the lattice expansion expected from phonons. These calculations cannot quantify the Invar effect accurately. The magnetic component of the thermal expansion of Invar is not the only unknown. The thermal expansion from

phonons themselves have not been quantified in the literature. Without accounting for phonons, the near-zero thermal expansion of Invar cannot be explained.

Phonons in Invar theories

Early models of Invar recognized how electrons and their spin can be coupled to phonons to affect their vibrational modes [35]. Anomalous softening of the lattice near the Invar composition has been observed. They appeared as low Debye temperatures determined from specific heats of Invar alloys, for example [1]. The softening of phonons was later observed in the [110] direction by inelastic neutron scattering [36, 37] and *ab initio* calculations [38–40]. This low-energy transverse mode appears at lower energies than expected, resulting in a positive curvature of the phonon dispersion, called a Kohn anomaly.

Phonons are believed to assist the electronic spin-flip transitions between the e_g and t_{2g} orbitals that lead to the Invar effect. The band gap has a momentum mismatch in the [110] direction [38], the same region where a Kohn anomaly is observed. The phonon softening seems to be caused by thermal fluctuations of the magnetic moments through magnon-phonon interactions [39]. Instabilities of this transverse mode could also lead to the martensite transformation [38–40].

Phonons are the main drivers of thermal expansion in materials. How do these couplings of phonons with magnetic spins affect the volume and thermal expansion? Can they be responsible for the anomalous thermal behavior of the volume in Invar? The observation of soft phonons in Invar does not explain the Invar effect. We need to determine the consequences of the vibrations on the anomalous volume behaviour.

5.4 Thermal expansion from the entropy

Our goal is to quantify the individual contributions to the thermal expansion from phonon, electrons, and magnetism, and give a complete thermodynamic picture of the Invar effect.

These individual quantities are not accessible by directly measuring how the volume changes with temperature. We need techniques that are only sensitive to each specific excitation. Spectroscopy at different energy ranges is a solution, however it does not measure volume. It can give us the entropy, and we can extract the volume through the Maxwell relation derived in section 1.5, $(\partial V/\partial T)_P = -(\partial S/\partial P)_T$.

Assuming thermodynamic equilibrium, the thermal expansion can be broken down into its individual entropy contributions:

$$\beta_{\text{Invar}} = -\frac{1}{V}\left[\left(\frac{\partial S_{\text{ph}}}{\partial P}\right)_T + \left(\frac{\partial S_{\text{mag}}}{\partial P}\right)_T + \left(\frac{\partial S_{\text{el}}}{\partial P}\right)_T\right] \approx 0\ . \tag{5.1}$$

For Invar, with a near-zero thermal expansion, the different contributions must add up to zero. Note that by using the Maxwell relation, we change from a temperature to a pressure dependence. This approach allows us to determine the entropies with experiments using diamond anvil cells (see Chapter 2 for the experimental techniques). The disadvantage is that we do not know the range of Invar behavior in pressure yet. The thermal expansion has been extensively measured as a function of temperature (Fig. 5.3), but not as a function pressure.

First principles calculations, which explicitly include thermally disordered vibrational and spin degrees of freedom, and spin-lattice coupling, were performed to support the experiments and complete the analysis of Eq. 1.34. The computational methods are described in the appendix, for more details see [41, 42]. These calculations were important to investigate the effects of magnetism on the lattice vibrations, as they can artificially turn off the magnetic effects on phonons. The calculations also concluded that the contribution from electrons is small, and their entropy does not vary much over range of Invar behavior.

For zero thermal expansion, the changes of magnetic entropy with pressure need to be opposed by those from phonons by Eq. 5.1. Both pieces are essential. None of them have been previously quantified.

5.5 X-ray diffraction

First, to determine the range of Invar behavior, we performed x-ray diffraction (XRD) experiments under pressure. By measuring the lattice volume at two different temperatures we can determine the volumetric expansion, i.e., the thermal expansion. A temperature difference of about 100 K was chosen, which was large enough to reliably detect the small effects of temperature on the lattice parameter.

We prepared samples of fcc $Fe_{65}Ni_{35}$ through arc-melting, and rolled the material into thin films of 10-20 μm. Details of the sample preparation are included in the appendix of this chapter. High pressure experiments with diamond-anvil cells (DACs) require small samples, on the order of 50 μm (high pressure techniques were described in Chapter 2). For such small samples, the highly collimated x-ray beams provided by synchrotrons are necessary. The experimental setup for our diffraction measurements at beamline 16 BM-D of the Advanced Photon Source (APS) is described in Fig. 5.9.

The measured signal of Fig. 5.9 c has five diffracted rings corresponding to the fcc structure. The intensity of the rings is not fully homogeneous, showing some texture of preferred orientations of the crystals within the sample. After masking spots from x-rays diffracted from the diamonds and the DAC, we integrate intensities around the rings to obtain diffraction patterns. The diffraction peaks were then fitted by Gaussians, to accurately determine their diffraction angles.

Figure 5.10 shows the resulting lattice parameters calculated with Bragg's law. At ambient pressure we know that thermal expansion of Invar is zero from Fig. 5.3, so we set the lattice parameters at both temperatures to be the same (this calibration was necessary because of a small offset in the data, likely due to pressure uncertainties between the DACs used for the two different temperatures). Below 3 GPa the lattice parameter is unchanged by temperature, so there is no thermal expansion. The insert shows the volumetric thermal expansion coefficient, β, calculated from the volume difference between 295 K and 395 K. As the pressure approaches the Curie transition, the volume starts to increase with temperature, and the Invar effect is no longer observed. At 8 GPa the thermal expansion coefficient becomes $\beta = 3.4 \cdot 10^{-5}$ K^{-1}, typical of transition metals (Fe has a thermal expansion of $3.5 \cdot 10^{-5}$ K^{-1} at room temper-

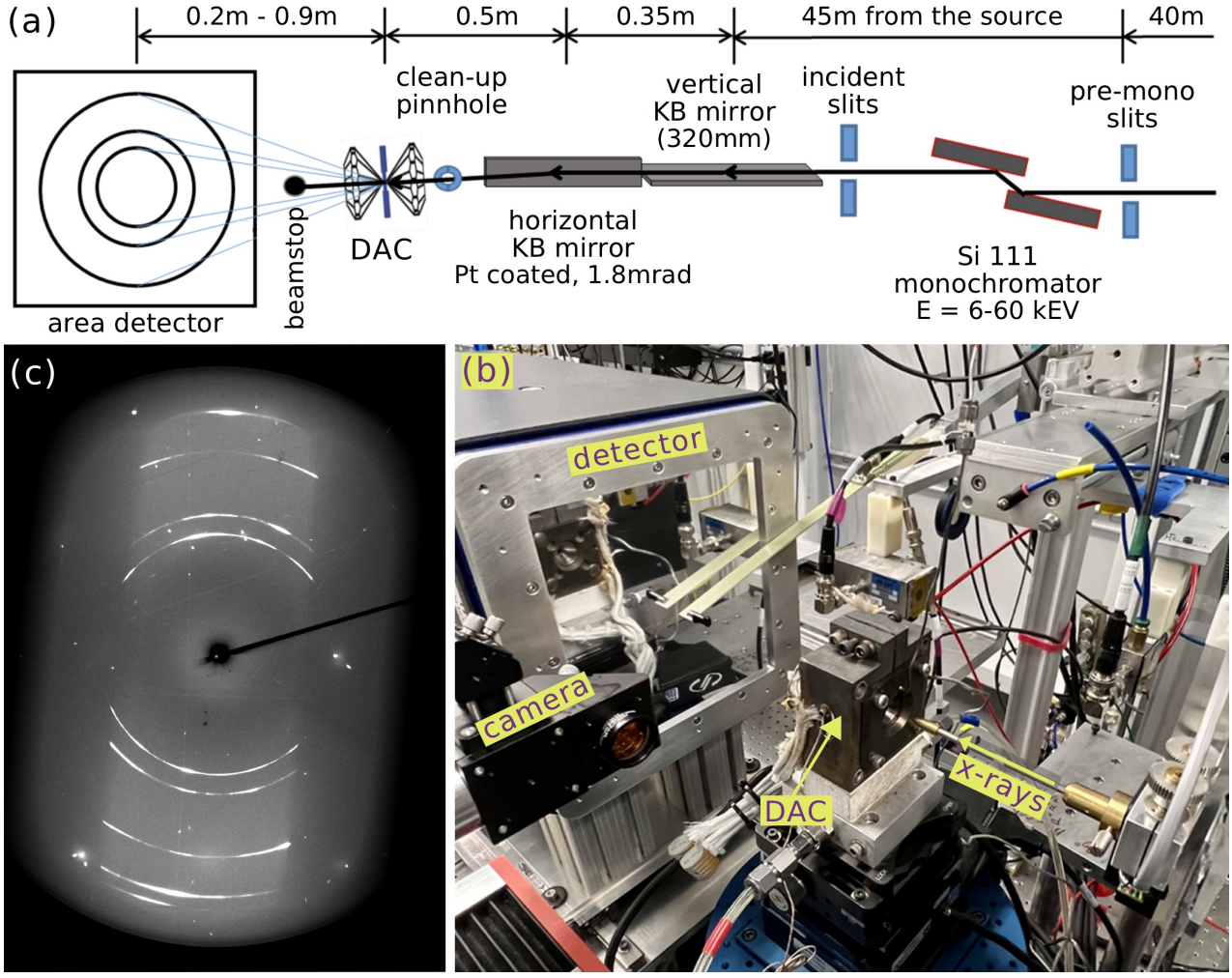

Figure 5.9: Diffraction experimental setup at beamline 16 BM-D at the APS. **(a)** Beamline schematic [43]. The x-ray beam was monochromated to 27 keV by Si mirrors with a resolution of about 1 eV. It was focused on the sample by KB mirrors with a beam size of $\sim 4\,\mu$m x $4\,\mu$m. **(b)** Our experimental setup. The x-ray beam comes out from the pinhole, is diffracted by the sample (inside the DAC) onto the area detector (we used a MAR345 detector, the one in the photo is the newer PILATUS 1M). The symmetric-type DAC is enclosed by a heating block, and sits on a rotating stage. A camera and a Raman spectrometer, that can move in and out of the beam path, were used to measure the pressure inside the DACS (by the fluorescence spectrum of Ruby spheres). The temperature was determined by thermocouples inside the heating-block. **(c)** Raw diffraction data of the area detector, showing five diffraction rings of fcc $Fe_{65}Ni_{35}$, along with some spots diffracted from the diamond and DAC. The downstream diamond-seat blocked part of the signal, resulting in a vertical strip of data. A beamstop blocked the forward beam to avoid saturation of the detector.

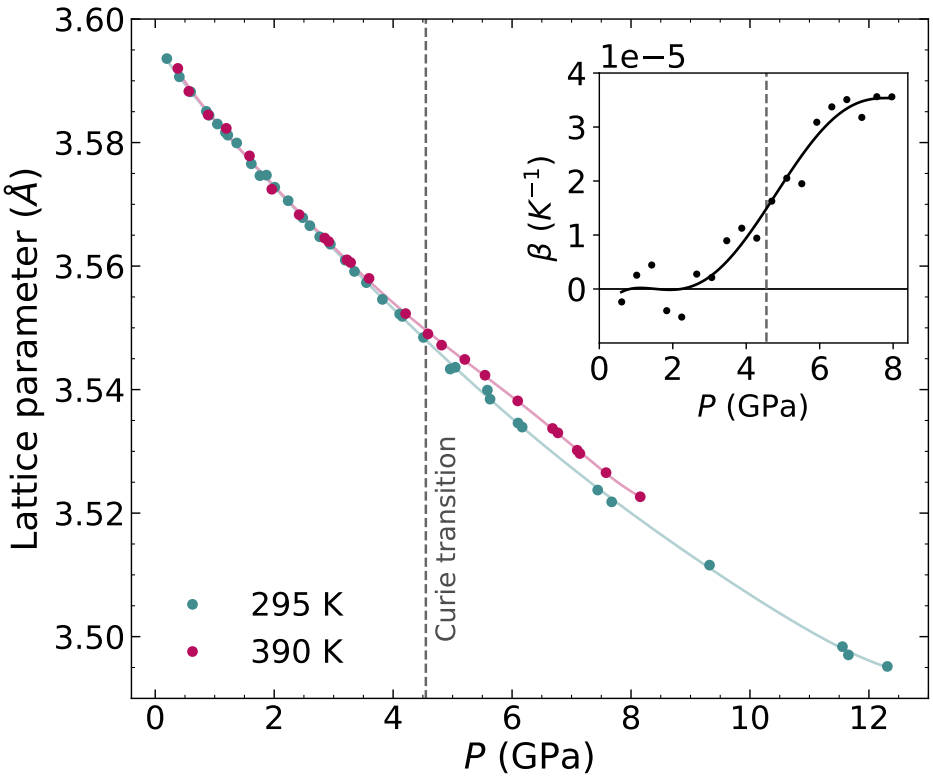

Figure 5.10: Lattice parameter vs. pressure measured by synchrotron x-ray diffraction at two temperatures. The insert shows the volumetric thermal expansion coefficient β from these data. Solid lines are polynomial fits. $Fe_{65}Ni_{35}$

ature and Ni $3.9 \cdot 10^{-5}$ K^{-1}). Note that the pressure dependence of the thermal expansion has a very similar behavior than its temperature dependence shown in Fig. 5.3.

We conclude that the Invar effect can be observed as a function of pressure up to about 3 GPa. In this range, the contributions from phonons and magnetism to the thermal expansion should cancel each other according to Eq. 5.1.

5.6 Magnetism

Invar materials have anomalous magnetic behavior. They do not have a strong preference for FM order over AF [25]. This might make the spins more susceptible to thermal fluctuations, and its magnetization has a stronger temperature dependence than other transition metals [1]. It results in a large magnetic heat capacity, even well below the Curie transition [12].

To quantify the precise balance between magnetism and phonons we perform our own pressure dependent measurement of the magnetization. As detailed in Chapter 2, our setup allows for measurements of both the lattice vibrations and spin dynamics in the same experimental conditions (see Fig. 2.9). This is especially important for Invar compositions, where the magnetization and Curie temperature are very sensitive to the composition and environmental conditions.

Mössbauer spectroscopy gives us the pressure dependence of the magnetization. For a quantitative analysis of magnetic entropy, however, we need to obtain absolute values separately. We calibrate the Mössbauer experiments by the total magnetic entropy measured by calorimetry.

Calorimetry

Calorimetry offers a fairly straightforward method to quantify the thermodynamic effects from magnetism. The disordering of spins through thermal excitations requires energy, which can be measured in a calorimeter.

We used differential scanning calorimetry (DSC) to measure the heat capacity of Invar, with a Perkin Elmer DSC 7. DSC measures the heat flow to the sample as its temperature is linearly increased. It can be compared to the heat flow measured on a reference material, with a known heat capacity, to quantify the heat capacity of the sample. Both our samples and sapphire references were heated inside aluminum crucibles, at a rate of 20 K/min from 340 K up to 873 K under a flow of nitrogen to enhance heat transfer and minimize oxidation.

Figure 5.11 a shows the resulting heat capacity, C_P, as a function of temperature (black curve). It is the total heat capacity, resulting from all excitations in the material. A good calibration and knowledge of the instrument baseline are essential for determining accurate values of C_P. To minimize baseline effects, we measured the heat capacity with empty crucibles before and after each heating run. We also repeated the measurement on samples four times. The error bars of Fig. 5.11 a reflect the standard deviation between these different runs.

The measured heat capacity has a peak at 515 K, typical of the heat released during a magnetic transition. Other materials, such as pure Fe or Ni have a much sharper peaks, however. Most of their 'magnetic heat' is released very

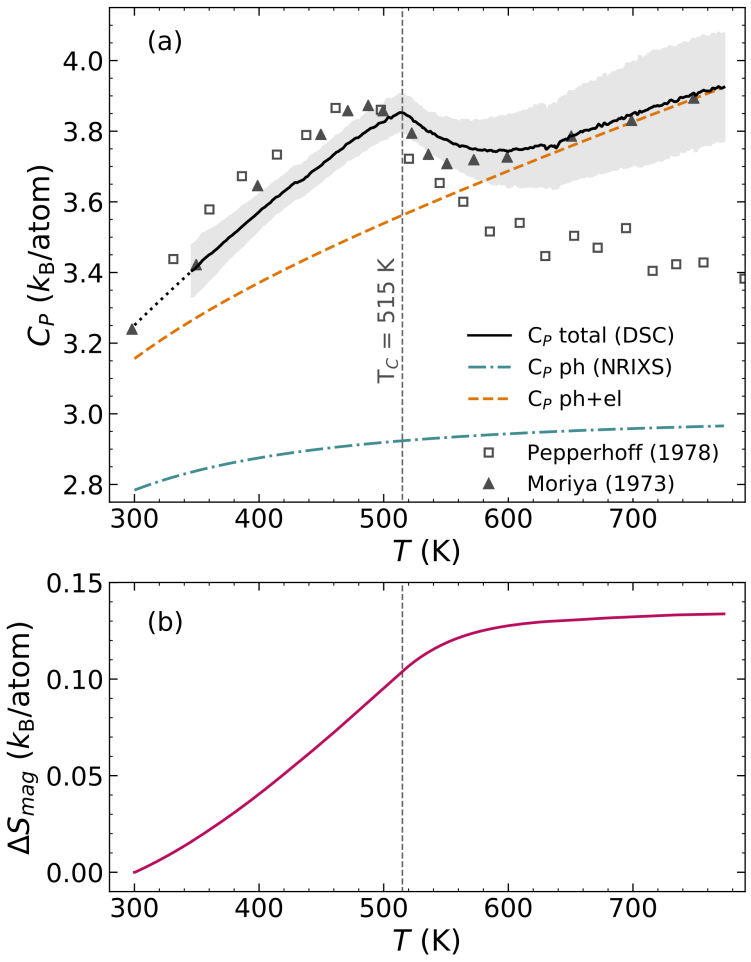

Figure 5.11: Heat capacity of Invar and its contributions. **(a)** Total heat capacity measured by DSC, compared the phonon contribution and fitted electronic heat capacity. Gray error bars show the uncertainty of four sequential measurements on two different samples. The black dotted curve is the extrapolation of C_P to room temperature. Data found in the literature is plotted for comparison [44, 45] **(b)** Change in magnetic entropy above 300 K computed from the magnetic heat capacity of panel a.

close to the Curie temperature. Invar is anomalous. The spins start disordering much earlier, and the magnetic heat capacity increases almost linearly with temperature, resulting in a broad magnetic peak [12]. The magnetic heat capacity also does not disappear abruptly at T_C, and there is some contribution from short-range ordering of spins up to about 640 K.

To isolate the magnetic contribution from the total heat capacity, we need to subtract the vibrational and electronic pieces. The contribution from phonons, C_P^ph, can be computed from measurements of the phonons DOS, $g(\varepsilon)$, as [27]:

$$C_P^\mathrm{ph}(T) = 3N\,k_\mathrm{B}\int_0^\infty g(\varepsilon)\,\left(\frac{\varepsilon}{k_\mathrm{B}T}\right)^2\frac{\mathrm{e}^{\varepsilon/k_\mathrm{B}T}}{\left(\mathrm{e}^{\varepsilon/k_\mathrm{B}T}-1\right)^2}\,\mathrm{d}\varepsilon\,. \tag{5.2}$$

The resulting phonon contribution is included in Fig. 5.11 a (and the NRIXS measurements are discussed further below).

At high temperatures above 640 K, where the magnetic contribution has completely died off, the heat capacity consist of only phonons and electrons. A typical linear electronic contribution ($C_P^\mathrm{el} = \gamma \cdot T$) is determined by fitting the total heat capacity at these high temperatures to the sum of phonon and electronic heat capacities (orange dashed curve in Fig. 5.11 a). This gave a coefficient of $\gamma = 0.0012\,k_\mathrm{B}/\mathrm{atom/K}$, in agreement with [46]. The remainder corresponds to the magnetic heat capacity.

The magnetic entropy can be computed from the magnetic heat capacity. Figure 5.11 b shows the resulting magnetic entropy calculated from the magnetic heat capacity. Up to the Curie transition it is:

$$\Delta S_\mathrm{mag}^{T_C} = \int_{300K}^{T_C}\frac{C_P^\mathrm{mag}}{T}\,\mathrm{d}T = 0.11\,k_\mathrm{B}/\mathrm{atom}\,. \tag{5.3}$$

The Curie temperature is an inflection point in S_mag, and the entropy gained above T_C originates from the magnetic short-range order (about $0.02\,k_\mathrm{B}$/atom). We use magnetic entropy change up to T_C (Eq. 5.3) to calibrate the pressure dependent magnetic entropy obtained from Mössbauer spectroscopy.

Synchrotron Mössbauer spectroscopy

Mössbauer spectroscopy is a technique that measures the local hyperfine magnetic field (HMF) at the ^{57}Fe nuclei. We prepared samples of Invar with this

isotope as $^{57}Fe_{65}Ni_{35}$. Since the HMF ^{57}Fe is proportional to the bulk magnetization [47], we used Mössbauer to obtain the pressure dependent magnetization of Invar.

Mössbauer is a resonant technique and only measures the field at ^{57}Fe nuclei. Adding Ni to the material lowers its net magnetization, but this is only indirectly measured through its effect on the Fe atoms. Fortunately, Ni plays only a minor role on the magnetization of Invar. As previously discussed, the magnetic moments of Ni atoms are much smaller than those of Fe [15, 33, 34, 48]. More importantly, both experiments [31] and calculations [33, 34] have shown that the orientation of the magnetic moments of Ni is less affected by pressure, remaining mostly ferromagnetic throughout the Invar transition (revisit Fig.5.8). Therefore, the magnetic entropy caused by spin disorder is mostly due to the Fe spins. A resonant technique, such as Mössbauer, is therefore suitable for quantifying the change of magnetization of Invar with pressure.

For high pressure experiments with samples inside DACs, we use synchrotron radiation monochromated to about 1 meV around the nuclear resonance of iron (14.413 keV). The experiments were performed at beamline 3 ID-D of the APS. At synchrotrons, the Mössbauer spectrum is obtained in time domain, and is called nuclear forward scattering (NFS). Magnetism splits the nuclear states of ^{57}Fe, and the interferences between these states create intensity modulations, or beats, in the signal (see Chapter 2 for details). These 'magnetic beats' are seen in the NFS spectra of Invar, shown Fig. 5.12 a, We measured the NFS signal between 0 and 21.3 GPa at room temperature. The figure also includes a measurement at 20 K and 0.3 GPa, corresponding to a fully ferromagnetic material.

As pressure is increased, the magnetic beats become progressively broader in time, with longer periods, showing a decline of the magnetization. At 4.4 GPa, the beats almost disappear and the signal is nearly an exponential decay. This is very close to the Curie transition, where the material becomes paramagnetic and the nuclear states are no longer split (no interference).

At highers pressures we observe very long modulation periods. These do not vary much with pressure up to 21.3 GPa. They could originate from a weak lingering magnetic field (magnetic short-range order would not persists to such high pressures above the Curie transition). They might also be an artifact from a finite sample thickness, or a 'thickness distortion'. If the sample is thick, x-

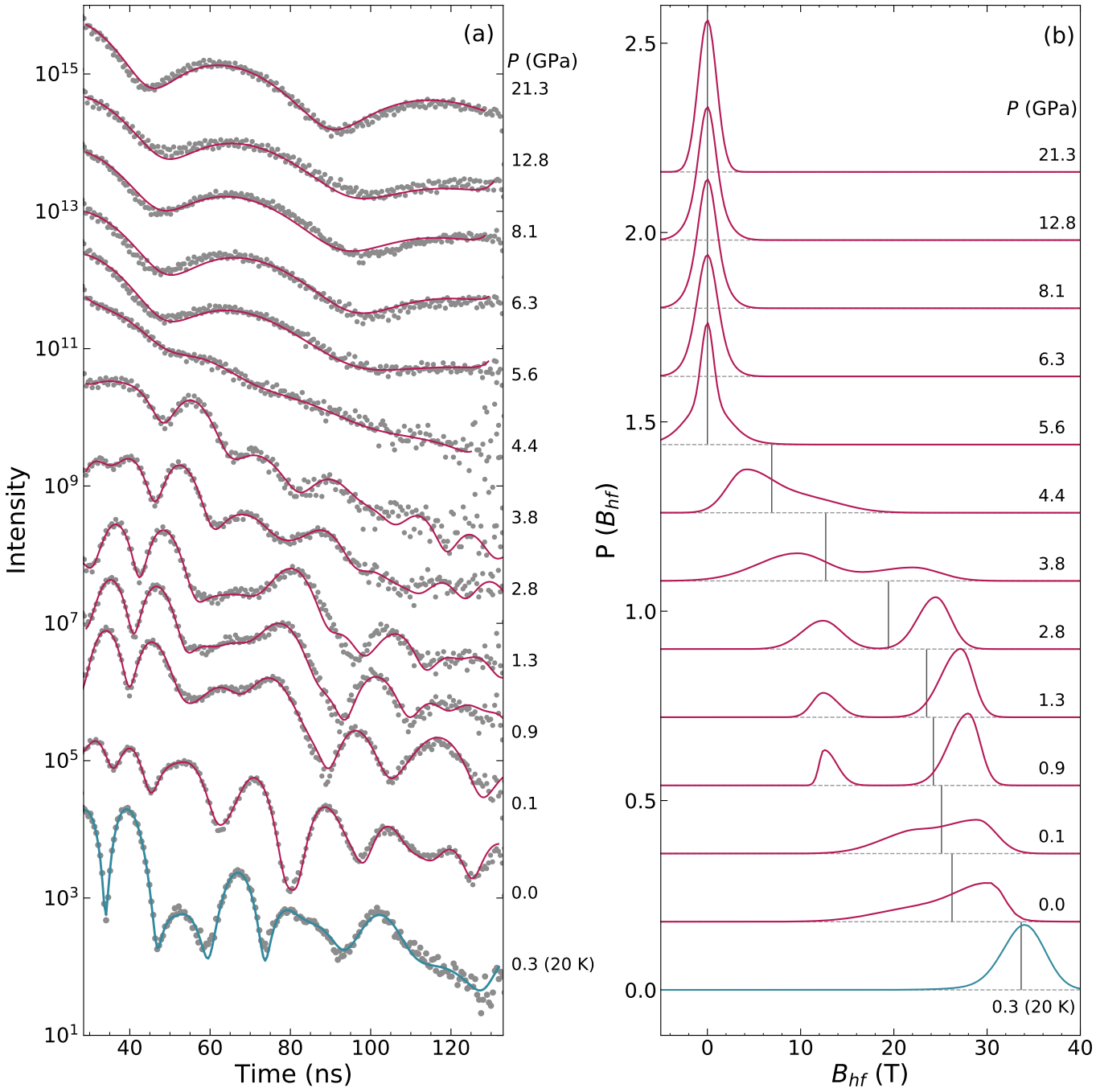

Figure 5.12: Pressure dependent hyperfine magnetic field (HMF) of $^{57}Fe_{65}Ni_{35}$. **(a)** NFS spectra of Invar at labeled pressures. Solid lines are the fits used to extract the hyperfine parameters. **(b)** HMF distributions, P($B_{\rm hf}$), found by fitting the NFS spectra of panel a. Vertical lines mark the mean of each distribution.

rays are absorbed by nuclei at different depths of the sample, and the radiation emitted coherently from these different nuclei can interfere with each other. It would also result in intensity modulations of the spectrum, or dynamical beats. The high pressure beats are either a result of such thickness distortions or they measure a real low magnetic field. We discuss these possibilities further below, however our NFS experiments can not discriminate between them.

Hyperfine magnetic field (HMF)

We can fit the Mössbauer (NFS) spectra to a model of the hyperfine interactions, to obtain recoil-free fractions, isomer shifts, quadrupole splitting, strength of the hyperfine magnetic field (HMF), along with other hyperfine parameters. We used the CONUSS software for fitting our data [49, 50]. Fits are shown as solid curves in Fig. 5.12 a. The distributions of the HMF, B_{hf}, were approximated by two asymmetric Gaussians as shown in Fig. 5.12 b.

At ambient conditions, the mean of the distribution is 26.2 Tesla, in agreement with the literature [51–54]. At 20 K it is stronger, 33.7 T, consistent with [29]. This shows a considerable loss of magnetization already at ambient conditions. As the pressure is increased, the distributions are broadened and progressively shift towards lower fields. Above 4.4 GPa, we attributed the beats of the NFS spectra to a thickness distortion effect. Their fits were obtained by the superposition of two nonmagnetic emissions (single absorption lines) from two different sample thicknesses, simulating a thickness distribution of the sample. This results in broadened HMF distributions around 0 T.

Conventional Mössbauer experiments at room temperature seem to confirm that no magnetism is left at 7 GPa [55]. This is not an unanimous result however. A low magnetic field up to about 12 GPa has been observed by x-ray circular magnetic dichroism (XMCD), owning to a possible low-spin state [56]. No field was measured above 15 GPa, however. Another Mössbauer study at 4.2 K also observed a low-field component around 3 T at 7 GPa [29]. It was attributed to an AF order, due its similarities with the AF field measured for fcc Fe [20] (revisit Fig. 5.5 a).

The intensity modulation of our NFS spectra at high pressures could correspond to such a low field. We therefore also fitted our spectra to a HMF distribution. Figure 5.13 show the results at 8.1 GPa (other pressures have very similar fields). Both fits, with a thickness distortion and with a weak

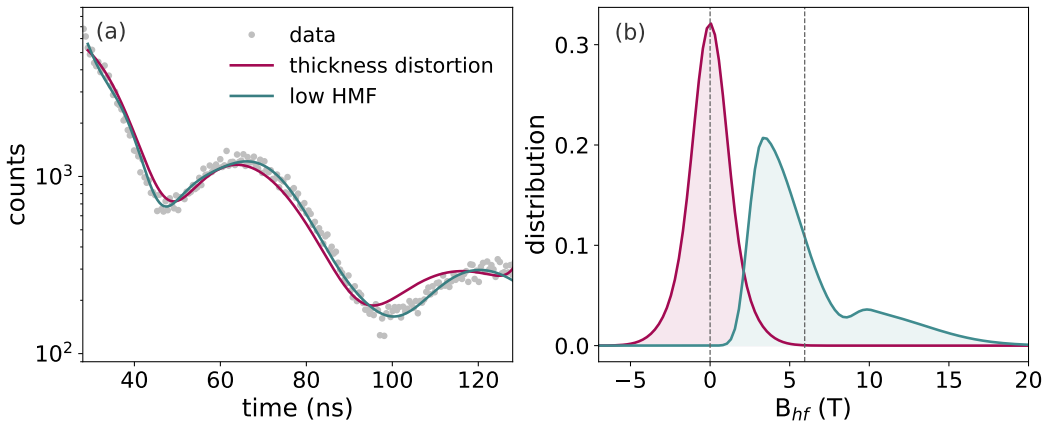

Figure 5.13: Hyperfine field of $^{57}Fe_{65}Ni_{35}$ at high pressures. **(a)** NFS spectrum at 8.1 GPa fitted by a thickness distortion with $B_{\mathrm{hf}} = 0$ and by a weak hyperfine magnetic field (HMF). **(b)** Distribution of the HMF for the non-magnetic case, broadened by a thickness distortion, and for the material with a weak magnetization. Vertical lines show the mean of the distributions.

HMF, are comparable. The HMF distribution has a mean at 6 T and a prominent peak at 3.5 T, consistent with AF order [20, 29]. Longer measurement windows to measure the intensity modulations over longer periods might be able to discern between the two explanations, but our current measurements can not.

A low-spin state at high pressures has little effect on the magnetic entropy. Our model includes only long-range order (below Curie transition), and is calibrated by calorimetry measurements. A remaining field would affect the entropy by only 0.007 k_B/atom or about 6% of the total magnetic entropy from long-range order.

Magnetization

Since magnetization of ^{57}Fe is proportional to its HMF [47], we computed the magnetization of Invar from the mean of its HMF distributions. Figure 5.14 a shows the resulting $M(P)$, normalized to ambient conditions. Starting at a near-ferromagnetic spin arrangement, the magnetization decreases with pressure. A mean-field model extrapolates the data to determine the Curie transition at 4.6 GPa. We assume a zero-field at higher pressure, although a residual low field has been reported [56]. The data scatter from the literature might reflect the sensitivity of magnetism in Invar, highly dependent on the

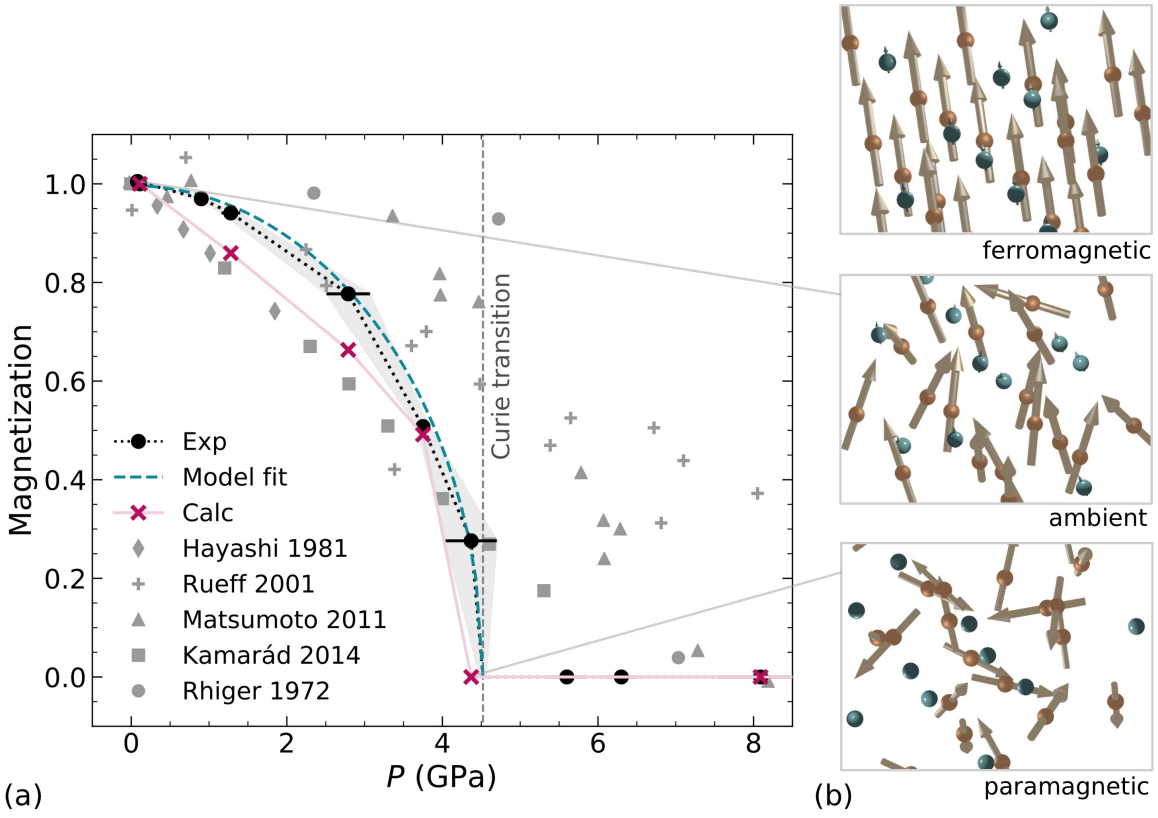

Figure 5.14: Magnetization of Fe-Ni Invar. **(a)** Exp: normalized ^{57}Fe hyperfine magnetic field (HMF) vs. P from NFS experiments, with Model fit. Error bars show the uncertainties in pressure. Calc: $M(P)$ calculated by our theory collaborator [41]. Gray symbols: literature data from different $M(P)$ measurements – Hayashi (pickup coil around piston-cell) [57], Rueff (XMCD) [56], Matsumoto (XMCD) [31], Kamarád (SQUID saturation magnetization) [58], Rhieger (Mössbauer spectroscopy) [55] **(b)** Calculated spin configurations at the Fe (orange) and Ni (blue) atoms for the fully ordered ferromagnetic, ambient and paramagnetic states. Arrow sizes are proportional to the calculated magnetic moments.

composition, the experimental conditions, and accuracy of pressure determination.

We also include the calculated magnetization curve from a local spin density model in the figure (details in Appendix). It has a slight stronger pressure dependence at low pressures than the experimental results. Figure 5.14 b shows some of the calculated spin configurations for the fully ordered (0 K), ambient, and fully disordered conditions. In agreement with the literature [15, 33, 34, 48], the magnitude of the Fe spins (orange) are much larger than those of Ni spins (blue). The orientation of Ni spins is also less affected by pressure [31, 33, 34].

At ambient conditions, there is already considerable spin disorder. The magnetization of Fig. 5.14 a was normalized to ambient conditions for comparison with the literature values. However, when compared to the measurements at 20 K it is M=0.75, in agreement with [59]. As a comparison, the magnetization of fcc Ni at ambient conditions is about 0.95 [59]. This shows the anomalous magnetic behavior of Invar, with spins disordering already at much lower temperatures then other transition metals.

Magnetic entropy

Magnetic entropy is a measure of spin disorder. An aligned ferromagnetic state has low entropy, whereas many equivalent configurations exist in a disordered state, corresponding to a high entropy.

To compute the magnetic entropy from the measured magnetization, we use a mean-field Ising model (Eq. 1.23) derived in Chapter 5. It gives the entropy to first order. We obtained the pressure dependence from measurements of $M(P)$, while absolute values were determined by calorimetry. In a mean-field model, the total change in entropy from ambient conditions up to the Curie temperature, $S_{mag}^{\Delta T_C}$, must be the same as the change in entropy due to pressure up to the Curie transition. This allows us to calibrate the Ising model with the calorimetry results, giving:

$$S_{\mathrm{mag}}(P) = -\frac{S_{mag}^{\Delta T_C}}{S_{\mathrm{Ising}}^{\Delta P_C}} \frac{1}{2} \left[(M(P)+1) \ln \frac{M(P)+1}{2} + (1-M(P)) \ln \frac{1-M(P)}{2} \right] \quad (5.4)$$

The resulting pressure dependence of S_{mag} is plotted in Fig. 5.15, compared to the temperature dependent magnetic entropy from calorimetry. As expected, the entropy rises with the pressure induced spin disorder up to the Curie transition. Since the mean-field model accounts only for long-range order, the entropy remains constant beyond the Curie transition.

5.7 Phonons

Phonons complete the picture. Their contributions to thermal expansion and entropy oppose those from magnetism. However, a careful quantification of their role in the Invar effect is missing in the literature. Here, we show measurements of the phonon spectrum and their dependence on pressure. These

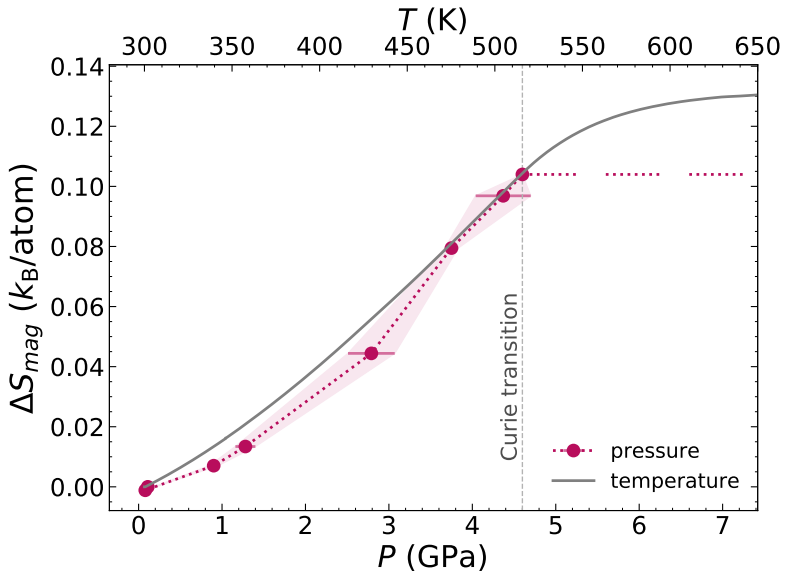

Figure 5.15: Magnetic entropy of Invar. Bottom axis: Pressure dependence of magnetic entropy calculated from the measured $M(P)$ with Eq. 5.4. Top axis: Temperature dependence of S_{mag} measured by calorimetry (Fig. 5.11).

enable us to quantify the contribution of phonon to the thermal expansion, and complete the thermodynamic explanation of the Invar effect.

Phonon DOS

The vibrational spectra of Invar were measured at pressures up to 21.3 GPa by nuclear resonant inelastic x-ray scattering (NRIXS). The phonon DOS can be computed from the NRIXS measurements after removing the elastic peak, separating the one-phonon from the multi-phonon contributions, and removing background noise. The details along with the full NRIXS spectra, and the multi-phonon contributions are found in the appendix. The experimental details and data analysis are described in Chapter 2.

Figure 5.16 compares the resulting phonon DOS of Invar at ambient conditions to those from (fcc) Ni. Van Hove singularities from two transverse phonon branches at around 16 and 23 meV result in a broad low energy peak in the phonon DOS of Invar. Another peak around 33 meV arises from the longitudinal branch. We confirm observations from the literature that the phonon DOS of Invar has anomalously soft modes at low energies. Both transverse phonon modes below 30 meV appear at lower energies than those measured for fcc Ni [10]. This observation alone does not explain the Invar effect, however.

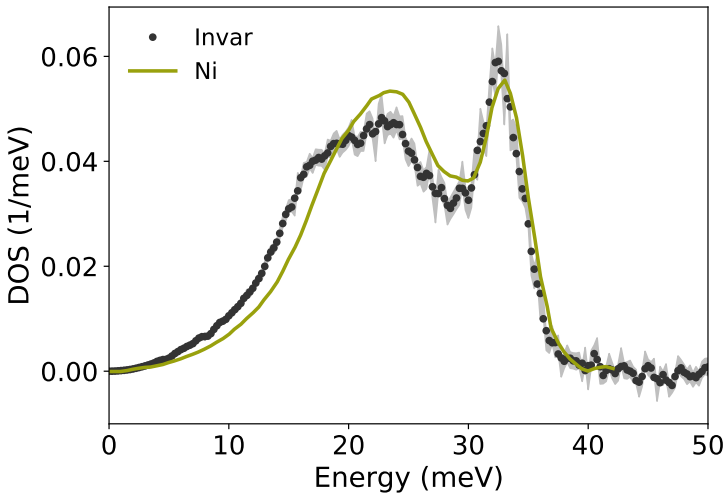

Figure 5.16: Phonon DOS of Fe-Ni Invar ($^{57}Fe_{65}Ni_{35}$) measured by NRIXS at ambient conditions, compared to the phonon DOS of fcc Ni [10]. A strong softening of the low-energy transverse phonons below 30 meV is observed in Invar.

We need to study how the phonon behavior is altered as the magnetization changes. We do this by varying the pressure.

The resulting pressure dependence of the phonon spectrum of Invar is presented in Fig. 5.17. The error bars were calculated from the standard deviation of sequential NRIXS measurements using a Monte-Carlo error propagation algorithm. As pressure is increased, the overall phonon energies increase, stiffening the material. However, not all phonon modes behave the same. The high energy peak from longitudinal modes remains constant with pressure up to 4 GPa. This is important for the Invar behavior and is discussed further below.

NRIXS is a resonant technique that measures only the partial DOS of the ^{57}Fe nuclei in the material. To investigate the effects of Ni, we also measured the vibrational spectrum of Invar with inelastic neutron scattering (INS), where Ni has a 50% larger cross-section than Fe. As shown in Fig. 5.17, the DOS measured by INS and by NRIXS at ambient conditions are almost the same. This shows that Fe and Ni have similar DOS curves, so the partial vibration of ^{57}Fe is representative of the full phonon spectrum of $^{57}Fe_{65}Ni_{35}$. The same result has been previously observed for other Fe-Ni alloys [10]. This is not necessarily surprising, given how close Fe and Ni are on the periodic table, and how similar their masses are.

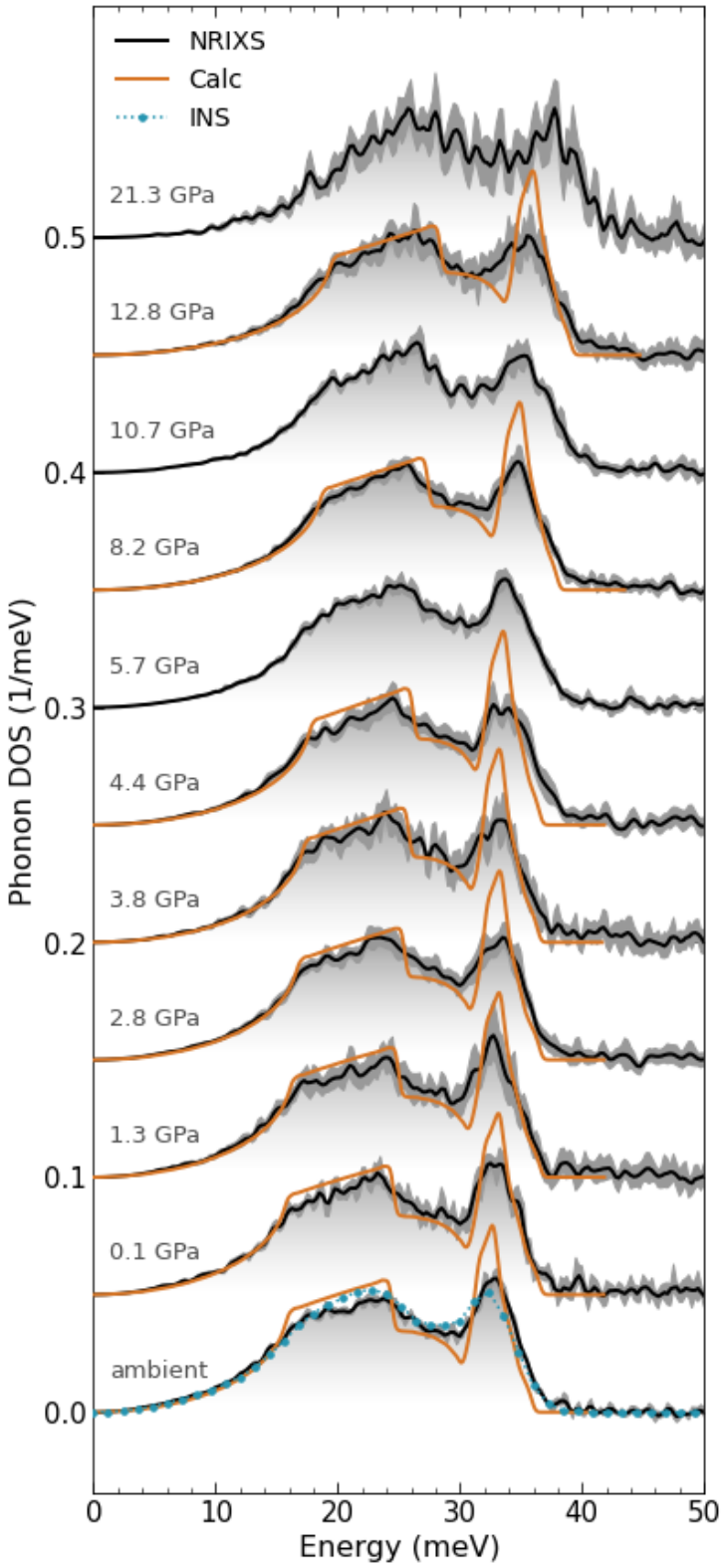

Figure 5.17: Phonon DOS of Fe-Ni Invar, $^{57}Fe_{65}Ni_{35}$, at different pressures as labeled. Experimental partial DOS curves measured by NRIXS (black curves) are compared to the calculated DOS (orange curves). Error bars show the standard deviation of sequential NRIXS scans. At ambient conditions the NRIXS measurement is in excellent agreement with the total phonon DOS measured by INS (blue markers).

The NRIXS measurements are also in excellent agreement with the *ab initio* calculations. This is especially seen by the agreement in the energies of their Van Hove singularities (the position of the peaks from the three branches of phonon polarization). Measurements and calculation also agree well at low energies, below 15 meV. This region is an important contributor to the phonon entropy, since there are more phonons occupying the low-energy modes. Calculations do have sharper features, partially due to broadening from the finite instrument resolution. However, both have nearly equal integrated areas under each of the vibrational modes. To show this, we plot the integrated (cumulative) DOS with increasing energies in Fig. 5.18 a for three representative pressures. Even though the calculated curves rise faster with the transverse modes around 20 meV, the measured DOS catches up around 30 meV. The same happens for the higher energy longitudinal vibrations between 30 and 40 meV.

To decompose the phonon DOS into contributions from the individual modes, we fitted the measured spectra to three asymmetric Lorentzians. These are able to to capture well the main features of the DOS as seen in Fig. 5.18 b. The area of the DOS is equally distributed between the three fitted distributions (as labeled in the figure). The mean energy of each of the Lorentzian (vertical lines) is plotted against pressure in Fig. 5.18 c. While the energies of both transverse branches increase monotonically with pressure, the longitudinal one remains fairly constant up to about 4 GPa, and increases above the Curie transition. This behavior is more evident in the calculations. A change in the vibrational behaviour near the magnetic transition indicates that phonons might be coupled to magnetism. The presence of ferromagnetic order in the spins affects the atomic vibrations and fixes the energies of the longitudinal modes at low pressures.

To confirm this claim, we turn to the calculations by our collaborators [41]. Full calculations include magnetism and spin-phonon coupling. They result in phonon DOS with unchanging longitudinal modes below the Curie transition, in agreement with experiments. This is especially evident when overlaying the phonon spectra as shown in Fig. 5.18 d. Calculations can also turn off the effects of magnetism, by artificially fixing the strength of the magnetization to its ambient values. The results of these calculations are different: the entire phonon DOS increases with pressure. The pressure-dependent behavior of

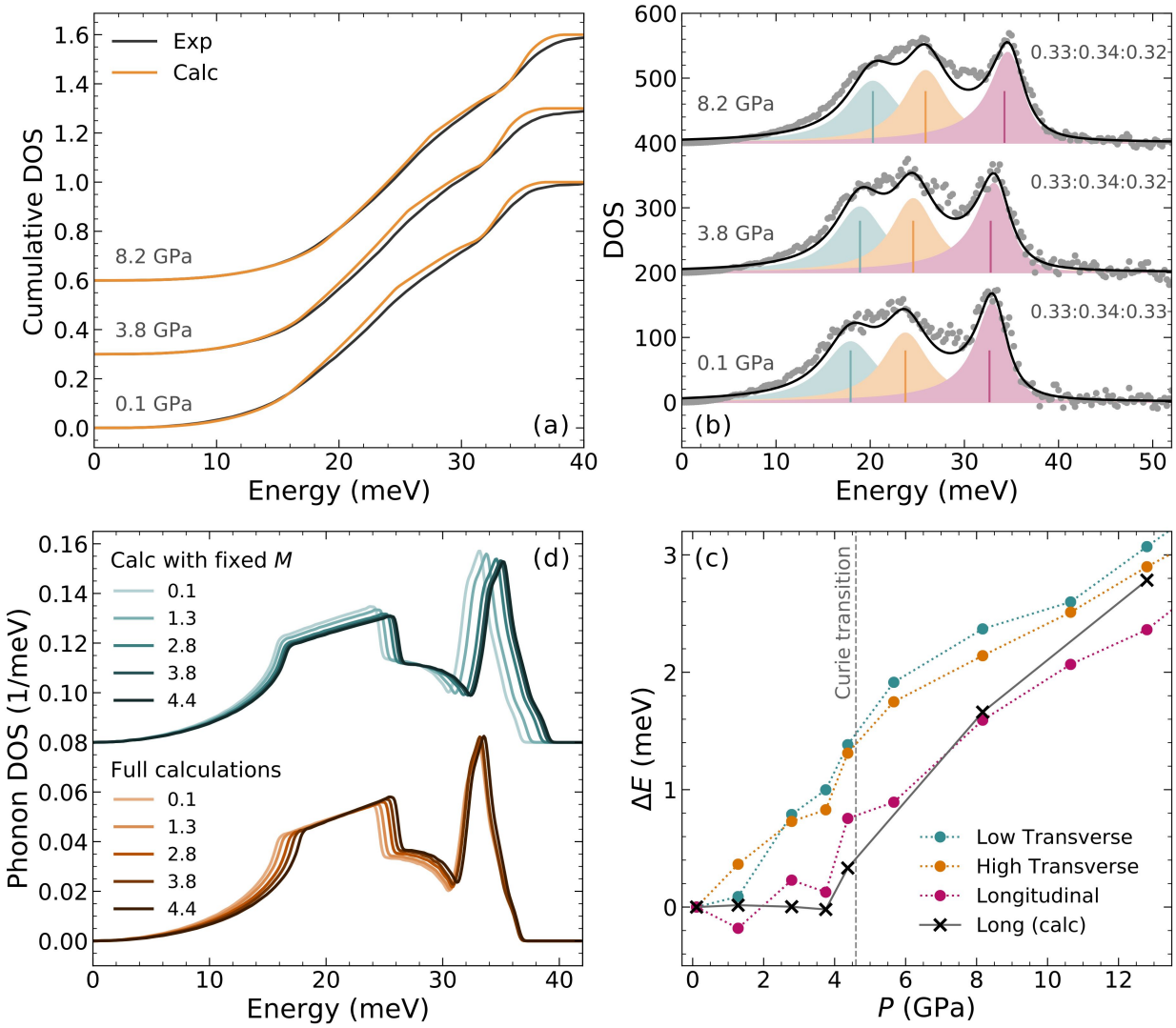

Figure 5.18: Phonon energies of Invar. **(a)** Cumulative phonon DOS of three representative NRIXS measurements and calculations. **(b)** Measured phonon DOS fitted by three asymmetric Lorentzians. Colored distributions show the individual fitted modes, and their mean energy is marked by vertical lines. The ratio of the areas of the distributions is labeled. **(c)** Mean energy of each phonon mode (from panel b) as a function of pressure. Calculations of the longitudinal branch show no energy changes up to about 4 GPa. **(d)** Calculated phonon DOS. Full calculations show little changes of the high-energy phonon peak around 34 meV below the Curie transition. This behavior is not seen when calculations turn off the effects of magnetism (fixed M), confirming that it arises from a spin-phonon coupling.

phonons has contributions from purely volumetric changes (calculations with fix M), but also from pressure-induced changes in magnetization through a spin-phonon coupling. Magnetism lowers the energy of the longitudinal modes with pressure, counteracting their energy stiffening due to volumetric changes. The net effect is a suppressed mode that remains at a fixed energy up to about 4 GPa.

Phonon entropy

The phonon entropy can be determined from the measured phonon DOS, $g(\varepsilon)$, as (Eq. 1.14):

$$S_{ph} = 3k_{\mathrm{B}} \int_0^\infty g(\varepsilon) \left[(1 + n_T(\varepsilon)) \ln(1 + n_T(\varepsilon)) - n_T(\varepsilon) \ln n_T(\varepsilon) \right] \mathrm{d}\varepsilon \,,$$

where ε is the phonon energy, and $n_{\varepsilon,T} = (\exp(\varepsilon/k_{\mathrm{B}}T) - 1)^{-1}$ is a Planck distribution for the phonon occupancy. The resulting phonon entropy is shown in Fig. 5.19 as a function of pressure. Calculations that incorporate the spin disorder agree very well with experiments (orange curve).

As pressure in increased, the atomic vibrations become confined to smaller volumes. The phonon energies increase (stiffen), which decreases the occupation of the vibrational modes, resulting in an overall reduction of the phonon entropy. Magnetism also play a role through the spin-phonon coupling, causing a change in behavior at the Curie transition. Below 4.6 GPa, the entropy has a concave-down curvature with a dip near the magnetic transition. Above 4.6 GPa, the entropy decreases almost linearly with pressure, corresponding to a quasi-harmonic behavior, where the phonon energies scale linearly with the decreasing volume.

Calculations with fixed magnetization give different results (teal curve). The dip near the Curie transition disappears, and the slope near ambient conditions decreases by about 30%. The presence of magnetism, therefore, suppresses the change in phonon entropy at low pressures. It is a reflection of the fixed energies of the longitudinal modes discussed before. As the magnetization decreases rapidly near the Curie transition, the vibrational entropy also changes faster above 3 GPa, resulting in the concave-down shape. This effect on phonons from their interactions with spins is at the core of the Invar effect, as discussed below.

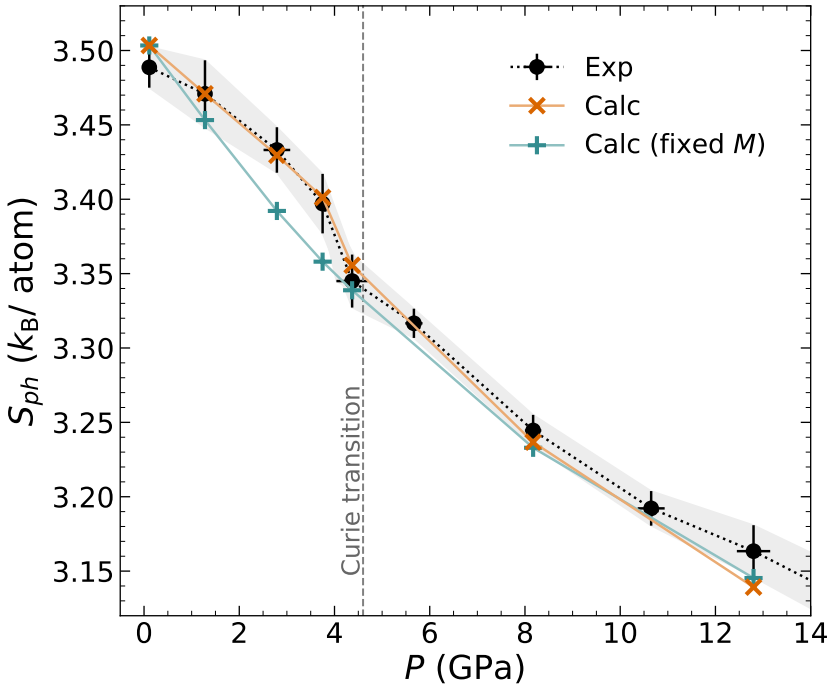

Figure 5.19: Phonon entropy vs. pressure calculated from experimental (Exp) and calculated (Calc) phonon density of states. Calc: full calculation including magnetic effects and spin-phonon coupling. Calc (fixed M): magnetization artificially fixed at the ambient value. (Calculated curves are shifted so their volumes coincide with the experimental ambient volume). Experimental errors were calculated by propagating the DOS errors of Fig. 5.17 using a Monte-Carlo method.

5.8 Electronic contribution

Electrons also absorb heat, and also contribute to the entropy. If the electronic states at the Fermi energy change with pressure, more or less states can become available for electronic excitations, affecting the electronic entropy. Within the Invar range, however, this effect does not contribute substantially to the total entropy.

Our collaborators computed the electronic entropy by *ab initio* calculations. At ambient conditions, a small value of 0.11 k_B/atom was obtained. More importantly, over the range of Invar behavior, the change in electronic entropy with pressure is 0.01 k_B/atom, about an order of magnitude smaller than changes in the phonon and magnetic entropies. Electronic entropy does not play a major role in the thermodynamics of the Invar effect.

5.9 Thermal expansion & Invar effect

The essence of the near-zero thermal expansion of Invar is the near-cancellation of contributions from phonons and magnetism in Eq. 5.1. Figure 5.20 a quantifies this cancellation as a function of pressure. As pressures are increased, the magnetic spins progressively lose their ferromagnetic order, increasing the magnetic entropy. Meanwhile, the lattice vibrations stiffen, causing a decrease in the phonon entropy. The opposing changes of phonon and magnetic contributions give a nearly pressure-independent entropy sum below at least 3 GPa as shown in Fig. 5.20 b. The spin-phonon coupling is essential. It alters the shape of the phonon entropy, improving the precision and extending the range at which phonons cancel the magnetic entropy. Above the Curie transition, the cancellation is lost and the total entropy decreases due to the stiffening of phonons.

Figure 5.20 c shows the thermal expansion measured by x-ray diffraction (orange markers) with a near-zero coefficient up to around 3 GPa. The individual contributions to the thermal expansion can be computed from their entropies by Eq. 1.33 ($\beta = -1/V(\partial S/\partial P)_T$). The resulting thermal expansion from the phonon and magnetic entropies, and from their sum is compared to the measured thermal expansion by x-ray diffraction in Fig. 5.20 c (electrons are not included here). The total thermal expansion computed from the entropy sum is indeed close to zero up to about 3 GPa, in agreement with the XRD measurements. The individual contributions from spins and phonons, however, are not at all close to zero or constant in pressure. Both approximately double in magnitude from 0 to 3 GPa, but in opposite directions, cancelling each other out. The phonon contribution seems to spike near the Curie transition, likely an artifact of our pressure resolution. A study with smaller pressure steps might uncover interesting details about the Curie transition behavior, where the magnetization changes rapidly, and where effects from spin-phonon coupling are likely to be strongest.

At pressures above 3 GPa, the accurate cancellation is lost, and so it the Invar effect. The sum of entropies begins to change with pressure, and β gradually becomes positive, even below the Curie transition at 4.6 GPa. At pressures above the Curie transition the thermal expansion computed from the entropies is in agreement with the value of 3.4×10^{-5} K^{-1} measured by XRD, a typical value for transition metals.

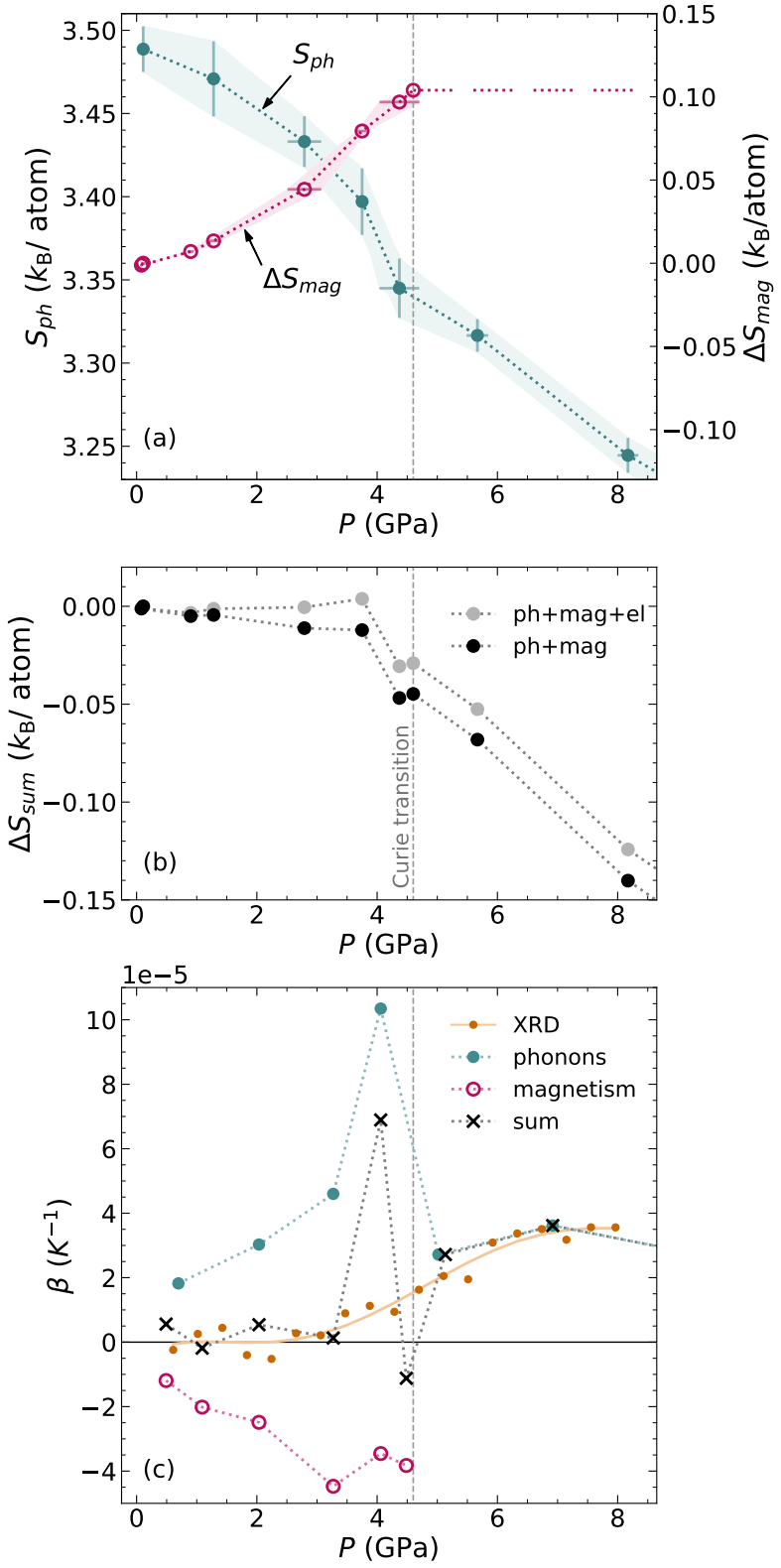

Figure 5.20: Contributions to the entropy and thermal expansion. **(a)** Experimental phonon entropy (S_{ph}, left axis) compared to experimental change in magnetic entropy (ΔS_{mag}, right axis) vs. P. The same scaling is used for the left and right axes. **(b)** Total entropy change (including and excluding the calculated contribution from electrons). **(c)** Volumetric thermal expansion coefficient β. Results from x-ray diffraction, XRD, are compared to individual contributions from phonons, and magnetic spins (calculated from entropies of panel a with Eq. 1.34) and their sum (from panel b, not including electrons).

5.10 Conclusion

We measured the individual contributions to the entropy from phonons and magnetism in the classic $Fe_{65}Ni_{35}$ Invar, by combining two complementary experimental techniques suitable for experiments in diamond-anvil cells. With increasing pressure, the changes in the phonon entropy counteracts the change of entropy from the spin disordering. We observe a precise cancellation of the phonon and magnetic contributions to the thermal expansion, leading to near-zero thermal expansion know as the Invar effect.

Electronic excitations contribute only with a minor entropy, and do not play an important role. Spin configurations, however, are key for understanding the Invar anomaly. This was recognized by thousands of studies. The Invar literature consists of almost exclusively electronic and magnetic explanations. The electronic structure of Invar might resemble that of γ-Fe, but is far more complex. Invar does not have a strong preference of FM over AF order, leading to several competing magnetic configurations close in energy. Non-collinear spins seem to be necessary to compute the magnetic states of Invar, however calculations are still unable to quantify the resulting effects on the lattice volume, and hence the anomalous thermal expansion. The calculations by our collaborators are therefore not fully *ab initio*, but take into account the measured magnetization curves to compute the spin configurations (see details in appendix).

Phonons are necessary to complete the thermodynamic picture. For the zero thermal expansion of Invar, phonons need to oppose the thermal contraction from magnetism. We provide the full thermodynamic picture, looking at all the individual excitations, and the first comprehensive study of the role of phonons in the Invar effect. While phonons have been previously measured in Invar materials [36, 37, 60, 61], their effects on the anomalous thermal expansion were not previously quantified or appreciated. Additionally, together with our theory collaborators, we see a spin-phonon coupling in Invar. It increases the precision of the cancellation of phonon and magnetic degrees of freedom, and is essential for the near-zero thermal expansion.

Apart from the anomalous thermal expansion, Invar materials also have an unusual temperature dependence of the magnetization [1]. The magnetic moments disorder much faster than expected from a Brillouin function (or than

observed for pure Ni or Fe). More energy than expected is absorbed by the spins at low temperatures. This is confirmed by the relatively large magnetic heat capacity of Fig. 5.11 even well below the Curie temperature. This excessive contribution to the magnetization has been previously attributed to 'hidden excitations' (because they were not detected by neutrons) [62], and by an anomalous spin-wave damping [63, 64]. Our experiments show that such a damping could be a result from scattering with phonons, through a spin-phonon coupling. While the magnetization has an anomalously large decrease, the phonon energy (especially from longitudinal modes) changes slower than expected. Even though we see this as a function of pressure, temperature-dependent phonon measurements [60, 61] seem to observe the same behavior. The coupling of phonons and spins could be responsible for transferring energy from lattice vibrations into the magnetic disordering, although further investigation is necessary.

As showcased for Invar, the interactions between phonons and magnetic spins can have significant thermodynamic effects, and result in macroscopic properties of magnetic materials. Including all relevant excitations is often not possible in theoretical treatments, so experiments become essential. We proposed an experimental methodology that captures effects from both phonons and spins, and it can be extended to other materials to understand their thermophysical properties. The concluding chapter of this thesis includes possible extensions of this work.

References

[1] E. F. Wasserman, in *Handbook of Ferromagnetic Materials*, Vol. 5 (Elsevier, 1990).

[2] A. W. Sleight, Endeavour **19**, 64 (1995).

[3] J. S. Evans, W. I. David, and A. W. Sleight, Acta. Crystallogr. B **55**, 333 (1999).

[4] M. Azuma, W. T. Chen, H. Seki, M. Czapski, S. Olga, K. Oka, M. Mizumaki, T. Watanuki, N. Ishimatsu, N. Kawamura, S. Ishiwata, M. G. Tucker, Y. Shimakawa, and J. P. Attfield, Nat. Commun. **2**, 1 (2011).

[5] J. Chen, L. Fan, Y. Ren, Z. Pan, J. Deng, R. Yu, and X. Xing, Phys. Rev. Lett. **110**, 1 (2013).

[6] C. Ablitt, S. Craddock, M. S. Senn, A. A. Mostofi, and N. C. Bristowe, Npj Comput. Mater. **3**, 1 (2017).

[7] M. T. Dove, V. Heine, and K. D. Hammonds, Mineral. Mag. **59**, 629 (1995).

[8] C. N. Saunders, D. S. Kim, O. Hellman, H. L. Smith, N. J. Weadock, S. T. Omelchenko, G. E. Granroth, C. M. Bernal-Choban, S. H. Lohaus, D. L. Abernathy, and B. Fultz, Phys. Rev. B **105**, 1 (2022).

[9] D. S. Kim, O. Hellman, J. Herriman, H. L. Smith, J. Y. Y. Lin, N. Shulumba, J. L. Niedziela, C. W. Li, D. L. Abernathy, and B. Fultz, Proc. Natl. Acad. Sci. U.S.A. **115** (2018).

[10] M. S. Lucas, L. Mauger, J. A. Muñoz, I. Halevy, J. Horwath, S. L. Semiatin, S. O. Leontsev, M. B. Stone, D. L. Abernathy, Y. Xiao, P. Chow, and B. Fultz, J. Appl. Phys **113**, 17 (2013).

[11] C.-É. Guillaume, Nobel Lectures in Physics, 444 (1920).

[12] E. F. Wassermann and M. Acet, in *Magnetism and structure in functional materials* (Springer, 2005), pp. 177–197.

[13] K. Ona, N. Sakaguchi, H. Ohno, and S. Utsunomiya, Trans. Jpn. Soc. Aeronaut. Space Sci. **18**, 32 (2019).

[14] E. F. Wassermann, M. Acet, P. Entel, and W. Pepperhoff, J. Magn. Soc. Jpn. **23**, 385 (1999).

[15] I. A. Abrikosov, A. E. Kissavos, F. Liot, B. Alling, S. I. Simak, O. Peil, and A. V. Ruban, Phys. Rev. B **76**, 1 (2007).

[16] M. Schröter, H. Ebert, H. Akai, P. Entel, E. Hoffmann, and G. G. Reddy, Phys. Rev. B **52**, 188 (1995).

[17] T. Miyazaki, Y. Ando, and M. Takahashi, J. Appl. Phys. **57**, 3456 (1985).

[18] J. Kübler, Phys. Lett. A **81**, 81 (1981).

[19] F. J. Pinski, J. Staunton, B. L. Gyorffy, D. D. Johnson, and G. M. Stocks, Phys. Rev. Lett. **56**, 2096 (1986).

[20] W. Keune, T. Ezawa, W. A. A. Macedo, K. P. Schletz, and U. Kirschbaum, Physica B **161**, 269 (1989).

[21] V. L. Moruzzi, P. M. Marcus, K. Schwarz, and P. Mohn, Phys. Rev. B **34** (1986).

[22] P. Entel, E. Hoffmann, P. Mohn, K. Schwarz, and V. L. Moruzzi, Phys. Rev. B **47**, 8706 (1993).

[23] R. J. Weiss, Proc. Phys. Soc. **82**, 281 (1963).

[24] L. Nataf, F. Decremps, M. Gauthier, and B. Canny, Phys. Rev. B **74**, 184422 (2006).

[25] E. F. Wassermann and P. Entel, J. Phys. IV **5** (1995).

[26] M. Schröter, E. Hoffmann, M. Yang, P. Entel, H. Akai, and A. Altrogge, J. Phys. IV **5** (1995).

[27] B. Fultz, *Phase Transitions in Materials* (Cambridge University Press, 2014).

[28] M. Acet, E. F. Wassermann, K. Andersen, A. Murani, and O. Schärpff, Europhys. Lett. **40**, 93 (1997).

[29] M. M. Abd-Elmeguid, B. Schleede, and H. Micklitz, J. Magn. Magn. Mater. **72**, 253 (1988).

[30] K. Lagarec, D.G. Rancourt, S.K. Bose, B. Sanyal, and R.A. Dunlap, J. Magn. Magn. Mater. **236**, 107 (2001).

[31] K. Matsumoto, H. Maruyama, N. Ishimatsu, N. Kawamura, M. Mizumaki, T. Irifune, and H. Sumiya, J. Phys. Soc. Japan **80**, 23709 (2011).

[32] N. Cowlam and A. R. Wildes, J. Phys. Condens. Matter. **15**, 521 (2003).

[33] M. van Schilfgaarde, I. A. Abrikosov, and B. Johansson, Nature **400** (1999).

[34] A. Ehn, B. Alling, and I. A. Abrikosov, Phys. Rev. B **107**, 104422 (2023).

[35] D. J. Kim, Phys. Rev. B **39** (1989).

[36] Y. Endoh, J. Magn. Magn. Mater. **10**, 177 (1979).

[37] E. Maliszewski and S. Bednarski, Phys. Status Solidi B **211**, 621 (1999).

[38] W. A. Adeagbo, A. Zayak, and P. Entel, Ph. Transit. **79**, 853 (2006).

[39] Y. Ikeda, F. Körmann, B. Dutta, A. Carreras, A. Seko, J. Neugebauer, and I. Tanaka, Npj Comput. Mater. **4** (2018).

[40] M. E. Gruner, W. A. Adeagbo, A. T. Zayak, A. Hucht, and P. Entel, Phys. Rev. B **81**, 1 (2010).

[41] M. Heine, O. Hellman, and D. Broido, Phys. Rev. Mater. **6**, 113805 (2022).

[42] M. Heine, O. Hellman, and D. Broido, Phys. Rev. B **100**, 104304 (2019).

[43] C. Park, D. Popov, D. Ikuta, C. Lin, C. Kenney-Benson, E. Rod, A. Bommananvar, and G. Shen, Rev. Sci. Instrum. **86** (2015).

[44] W. Bendick, H. H. Ettwig, and W. Pepperhoff, J. Phys. F: Met. Phys. **8**, 2525 (1978).

[45] Y. Tanji, H. Asano, and H. Moriya, Sci. Rep. Tohoku Univ. **24**, 205 (1972).

[46] R. Caudron, J.-J. Meunier, and P. Costa, Solid State Commun. **14**, 975 (1974).

[47] M. A. Kobeissi, Phys. Rev. B **24** (1981).

[48] A. V. Ruban, Phys. Rev. B **95**, 174432 (2017).

[49] W. Sturhahn, Hyperfine Interact. **125**, 149 (2000).

[50] W. Sturhahn, NRIXS Scientific Software (website).

[51] Abdel-Fatah, D. Lehlooh, and S. H. Mahmood, Hyperfine Interactions **139**, 387 (2002).

[52] C. E. Johnson, M. S. Ridout, and T. E. Cranshaw, Proc. Phys. Soc. **81**, 1079 (1963).

[53] M. Shiga and Y. Nakamura, J. Magn. Magn. Mater. **40**, 319 (1984).

[54] J. Y. Ping, D. G. Rancourt, and R. A. Dunlap, J. Magn. Magn. Mater. **103**, 285 (1992).

[55] D. R. Rhieger, "Mössbauer experiments in iron-nickel alloys at high pressures", PhD thesis (1972).

[56] J. P. Rueff, A. Shukla, A. Kaprolat, M. Krisch, M. Lorenzen, F. Sette, and R. Verbeni, Phys. Rev. B **63**, 132409 (2001).

[57] K. Hayashi and N. Mori, Solid State Commun. **38**, 1057 (1981).

[58] J. Kamarád, M. Míšek, and Z. Arnold, High Press. Res. **34**, 365 (2014).

[59] J. Crangle and G. Goodman, Proc. Roy. Soc. Lond. A **321**, 477 (1971).

[60] H. J. Giefers, "Unelastische Kernstreuung zur Untersuchung der Gitterdynamik in Eisen, Eisen-Invar-Systemen und Zinnmonoxid unter hohem Druck", PhD thesis (2004).

[61] H. Bremers, R. Rüffer, O. Leupold, and A. I. Chumakov, in Hyperfine interact. (2002), pp. 115–118.

[62] Y. Ishikawa, Y. Noda, K. Ziebeck, and D. Givord, Solid State Commun. **57**, 531 (1986).

[63] Y. Ishikawa, S. Onodera, and K. Tajima, J. Magn. Magn. Mater. **10**, 183 (1979).

[64] S. Onodera, Y. Ishikawa, and K. Tajima, J. Phys. Soc. Jpn. **50**, 1513 (1981).

Chapter 6

Conclusion and future directions

This thesis studied how the different atomic excitations affect the thermodynamics of magnetic materials. As seen for Fe-Ni alloys, most of the thermal energy is stored as vibrations of the nuclei, but electrons and magnetic excitations also play an important role. We explained macroscopic properties, such as the anomalous thermal expansion in Invar, by carefully quantifying the microscopic interactions of atomic vibrations, electrons, and their spins.

Our study started by quantifying the size effects of the crystalline structure on the heat absorption of nanocrystalline Ni_3Fe. All the excitations become enhanced and capable of storing more heat in nanostructured materials. In particular, the redistribution of spectral weights amplifies the heat capacity of phonons and increases the vibrational entropy. This increase in entropy is not sufficient to overcome the larger enthalpy from the extra grain boundaries of the nanostructure. Nanocrystalline Ni_3Fe is therefore in a metastable equilibrium compared to its bulk counterpart with larger grains.

We also examined the interactions between phonons and magnetic spins. Even though phonons have a larger absolute contribution to the free energy, changes due to magnetic disordering can be comparable to those from phonons. Since the magnetic order depends on the local environment (through the Pauli exclusion principle), magnetism is coupled to fluctuations of the lattice volume caused by phonons. Iron provides a good system to study such interactions. It has rich magnetic phase diagram, with spins excitations that can be coupled to changes in phonon energies. This observation led to the development of a magnetic quasi-harmonic model for Fe and Fe_3C, which accounts well for the deviation of phonon energies from pure volumetric effects of the conventional quasi-harmonic approximation.

Our studies of the interactions between phonons and magnetism also resulted in a thermodynamic explanation of the Invar effect. The anomalously low thermal expansion of fcc $Fe_{65}Ni_{35}$ has long been investigated since its discovery in 1985. Most studies focused on the complex magnetic nature of Fe in Invar, however thermal expansion cannot not be explained without including phonons. By combining different nuclear resonant scattering techniques, we quantified the changes in entropy from both phonons and magnetism as a function of pressure. They have opposite effects on the thermal expansion and cancel each other precisely in the range of Invar behavior. The precision of this cancellation is enhanced by the coupled behavior of phonons and the spins, leading to the Invar effect in a wide range of temperatures and pressures in Fe-Ni.

Future directions

The complex magnetic structure of Fe gives rise to several anomalous properties. They are not limited to the Invar (and anti-Invar) effect, and definitely not restricted to Fe-Ni materials.

Magnetic complexity often coincides with interesting anomalous themophysical behavior, and computational methods struggle particularly in those situations. Improvements in *ab initio* methods allow for increasingly complicated magnetic structures [1–4], but they are still unable to quantify accurately the thermophysical behavior because too many degrees of freedom need to be included in minimizing the free energy. For instance, to be able to describe the Invar behavior, our theory collaborators used experimental inputs for the volume dependence of the magnetization.

Experiments are especially valuable in these cases where the theory still needs to be developed. And even if the theory exists, computational methods often encounter limitations due to computing power. In real materials, the number of degrees of freedom grows quickly. Those arise from chemical configurations, defects, electronic structure, magnetic spins, phonons, but also interactions between all these excitations. Additionally, for thermophysical behavior, we need to understand how these are affected by finite temperatures and pressures. Calculations require large super-cells and become expensive, even for supercomputers. Experiments measure the net effect from all of these, although isolating specific degrees of freedom remains a challenge.

The successful experimental assessment of entropy contributions to explain the size dependence and thermal expansion of materials can be harnessed in a number of different directions. I conclude by exploring some possibilities for extending our experimental work.

Anomalous thermal expansion of transition metals

An obvious next step is to look at similar abnormal behaviour in transition metals. And there are plenty to look at. Anomalous thermal behavior tend to appear near compositions where spins do not have a strong preference between FM and AF exchange interactions, causing complicated non-collinear structures, with partially frustrated Fe-Fe correlations [5–8]. The resulting anomalies are not restricted to the thermal expansion. They are usually accompanied by anomalous Curie and Néel temperatures, anomalous temperature dependence of the magnetization and electrical resistivity, anomalous heat capacity, anomalous elastic constants in both longitudinal and transverse directions, and anomalous Young's and Bulk moduli [9].

Figure 6.1 shows a few examples of abnormal thermal expansion for Fe-bearing transition metals with different crystal structures. These include Fe-Pt, Fe-Pd, Fe-Ti, Fe-C, Fe-Mn, and Fe-Co (the specific compositions are labeled). Similarly to Fe-Ni, I expect the departure from the expected behavior can be understood as a competition between a volume expansion from phonons and a volume contraction from magnetic disordering.

Fe-32%Pd and Fe-28%Pt are ferromagnetic (FM) Invar materials (Fig. 6.1 a) [10, 13]. Near their respective Curie transitions, where the spin disordering is largest, the thermal expansion is suppressed. In Fe-Pt this effect is so pronounced that a very large negative thermal expansion coefficient is observed around room temperature. Compared to Fe-Pd and Fe-Pt, near-zero thermal expansion of Fe-Ni Invar extends for a wide range of temperatures. This is due to the spin-phonon coupling discussed in Chapter 5, that maintains the cancellation of phonon and magnetic excitations almost up to the Curie transition. Cementite, Fe_3C (Fig. 6.1 b), has an orthorhombic crystal structure, and is also an Invar material with a similar behavior as Fe-Pd [11, 13]. The anti-ferromagnetic (AF) Invar effect is observed in Fe-35%Ti, with Laves phase C14 hexagonal structure. It has a considerable volumetric contraction up to its Néel temperature [11]. Fe-30%Mn (Fig. 6.1 c), also AF, has an interesting

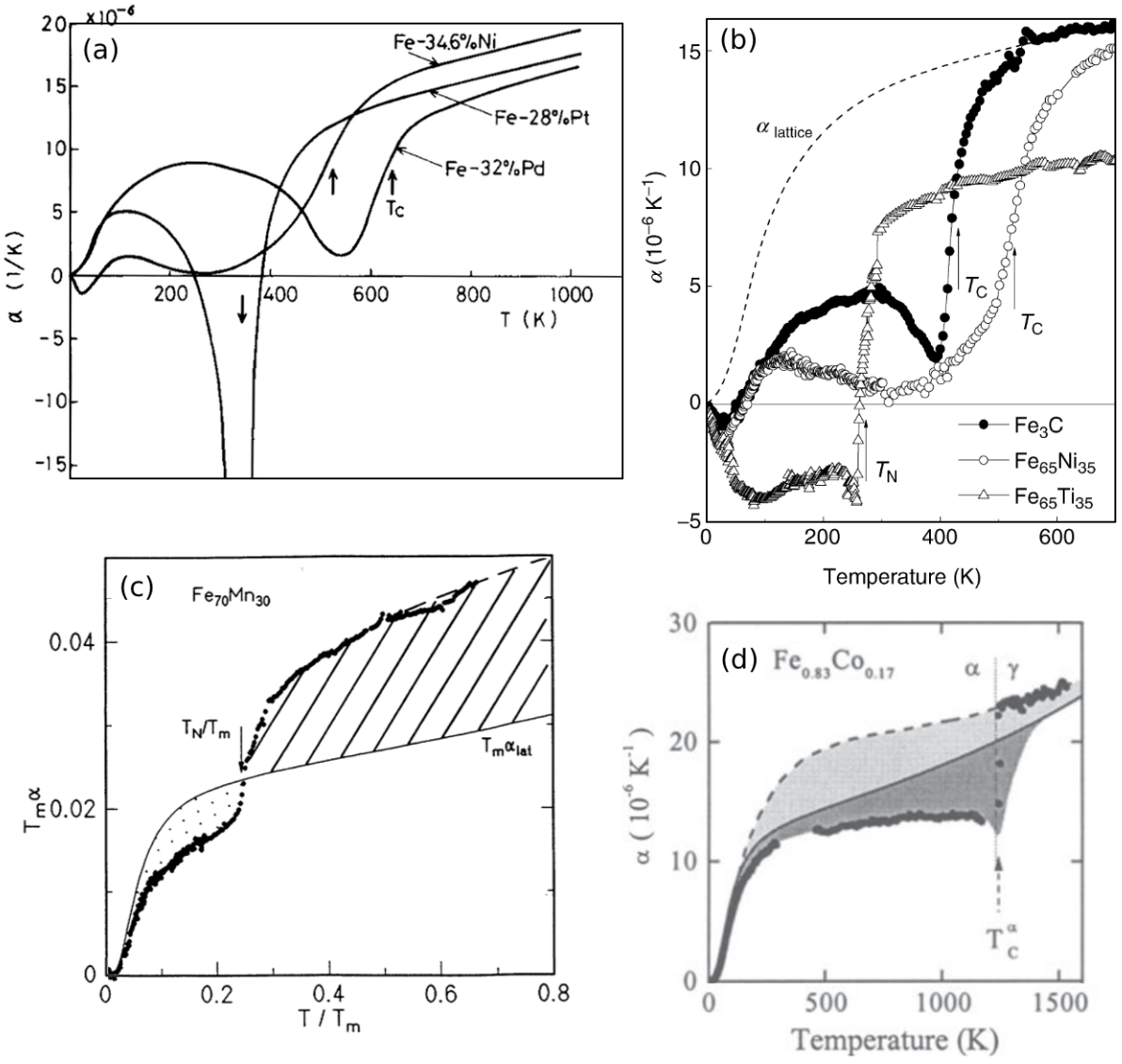

Figure 6.1: Anomalous thermal expansion behavior of different transition metals. **(a)** Fe-35%Ni, Fe-32%Pd, Fe-28%Pt [10]. **(b)** Fe-35%Ni, Fe-35%Ti, Fe_3C [11]. **(c)** Fe-30%Mn [12]. **(d)** Fe-17%Co [13].

thermal behavior which switches from a suppressed thermal expansion (Invar) to an excessive expansion (anti-Invar) at the Néel transition [12]. Fe-17%Co is FM with a bcc cystal structure (Fig. 6.1 d). Its thermal expansion has a very similar trend as Fe-30%Mn, however the transition from Invar to anti-Invar behavior at the Curie transition is accompanied by a structural transformation from bcc into the fcc structure [13]. Even pure Fe by itself has a dip in the thermal expansion near its Curie transition, due to the rapid decrease in magnetization (not shown) [13].

Understanding the Invar effect in Fe-Ni can give us clues on how to interpret the anomalous thermal behavior of other transition metals. It seems that the Fe-Fe correlations are the key. Even for non-crystalline solids; the Invar effect observed in metallic glasses is also correlated to Fe-Fe distances [14]. Further investigation is needed for tying these anomalies together, however. Mössbauer combined with NRIXS could be a good start to probe the importance of Fe in these anomalous behaviors.

Thermal behavior of Fe-Perovskites

There is growing interest in controlling the volume expansion of perovskites for their technical applications. This remains a challenge, given that negative thermal expansion (NTE) is rarely seen in these materials [15]. In the past years, however, anomalous NTE has been found in different types of perovskites, such as in $LaCu_3Fe_4O_{12}$ [16], or in $BiNiO_3$ [17] and $PbTiO_3$ [15]. These have been associated with charge transfers and ferroelectric transitions.

What is more interesting is that doping these compounds with different amounts of Fe controls the thermal expansion. In general, larger amounts of Fe tend to enhance the NTE. Substituting Mn for Fe in $SrCu_3Fe_{4-x}Mn_xO_{12}$ systematically changes the thermal expansion from positive ($x > 1.75$), to near-zero ($x = 1.5$), to negative ($x < 1.25$) [18]. In MgSiO3, a major components the Earth's lower mantle, partially replacing Mg by Fe lowers the (positive) thermal expansion [19]. In $PbTiO_3$, a prototype ferroelectric, the NTE is significantly enhanced in a wide range of temperatures when partially substituted by $BiFeO_3$ [15, 20]. On the other hand, when Fe is replaced by Zn and Ti, the NTE weakens, enabling near-zero thermal expansion. $BiFeO_3$ itself has attracted attention because it might be the only multiferroic material at room temperature with both ferroelectric properties and magnetic order [21]. Their

properties can be tailored by decreasing the particle size [22], with a spontaneous polarization that is enhanced by almost an order of magnitude in thin films [23].

Explanations of the thermal expansion behavior in perovkistes are still lacking. Fe-Fe correlations are not the source of the anomalous behaviour here, since the Fe atoms are usually isolated at the center of the octahedra. The magnetic states of Fe, however, affect the octahedral tilts [19, 24] and the tetragonality [15], which distorts the lattice and has been related to NTE. Such geometric arguments can fall short for explaining a dynamic behavior such as NTE, and here again, phonons have rarely been considered in the explanations. Distortions of the lattice with different valence and spin sates of Fe do indicate a coupling of magnetism with vibrations the lattice [24]. Additionally, the crystalline size influences the thermal behavior of perovskites. Reducing the particle size of $PbTiO_3$-$BiFeO_3$ shifts the strong NTE into positive expansion of the lattice [25]. This is likely related to the enhanced the phonon vibrations and magnetic fluctuations of small-sized crystals studied in Chapter 3.

The experimental methods described in this thesis could help shed light on the anomalous thermal behavior, and their size dependencies. For perovskites, Mössbauer and NRIXS cannot give a full thermodynamic description, because of their resonant nature. But these techniques are ideal for targeting the Fe atoms and studying how they contribute to abnormal behavior. In particular, Mössbauer spectrometry is sensitive to the local chemical environment of Fe. It can discern between distinct Fe site occupations and their spin states. NRIXS could complements this with local vibrational information, related to the forces of the octahedral cage on the Fe atoms.

Magnetocaloric effect

Precise knowledge of the individual entropy contributions opens possibilities for understanding other thermophysical properties. In magnetocaloric materials, a change in entropy is tied to a variation of the temperature.

When such a material is exposed to an external magnetic field, its spins are aligned, lowering the magnetic entropy. When the field is reduced under adiabatic conditions (adiabatic demagnetization), the magnetic entropy increases, while the phonon entropy decreases to maintain a constant total entropy. The spin disordering hence lowers the atomic vibrations, resulting in a cooling ef-

fect. When coupled to a heat sink, this effect can be exploited for magnetic refrigeration. It is used to cool materials down to the milli-Kelvin range [26], but has recently gained attention due to the realistic perspective for room temperature refrigeration [27, 28]. Cooling through the magnetocaloric effect can have a superior efficiency compared to conventional vapor-compression refrigeration, which could help minimizing the climate impact of our growing demands on cooling devices [29].

Similarly to the Invar effect, the magnetocaloric effect relies on a interactions between magnetism and phonons, and precise knowledge of their entropy behavior is key. A material with a large changes in magnetic entropy, and strong couplings of spins with phonons is desired, ideally with a small thermal hysteresis for practical implementations. Apart from the classic $Gd_5Si_2Ge_2$ [30], the most promising candidates are Fe_2P and $La(Fe,Si)_{13}$ [28, 29, 31, 32], but FeRh [33, 34] also shows large magnetocaloric effects. Iron-containing materials are again at the spotlight.

The maximum attainable temperature reduction in an adiabatic demagnetization process is limited by the maximum isothermal entropy change [29]:

$$|\Delta T_{\mathrm{ad}}^{\mathrm{max}}| = |\Delta S_T^{\mathrm{max}}|\, T/C_P\,.$$

Usually, only the magnetic entropy is affected by an external field, as is the case for Gd based materials. However, the magnetocaloric effect can be enhanced if other excitations also contribute [29]. This requires a coupling between the magnetic disordering and other excitations. Spin-phonon coupling has been accordingly observed in all of the promising Fe-containing magnetocaloric materials: FeRh [33], Fe_2P [35], and $La(Fe,Si)_{13}$ [29, 31].

Micro-structural size also matters here. Reducing the structure to thin-films affects the magnetic entropy in $(Mn,Fe)_2(P,Si)$ [32], as well as the lattice dynamics [33] and the thermal hysteresis [34] in FeRh.

By tuning the individual entropies, exotic effects can be observed. In Ni-Mn-Sn alloys, the change of magnetic entropy has the opposite sign, resulting in a inverse magnetocaloric effect, or magnetic heating [36], analogous to the anti-Invar effect.

$La(Fe,Si)_{13}$ is an interesting material. Its magnetic transition from ferromagnetic to paramagnetic is accompanied by a significant drop in the volume of

1%. The phonons undergo an anomalous softening through the transition despite the volume decrease, adding to the entropy change and enhancing the magnetocaloric effect [29]. The volume of $La(Fe,Si)_{13}$ depends on the occupation of Fe in two inequivalent sites with different magnetic states [29], strikingly similar to Invar materials. As a result, thermal expansion anomalies are also observed in $La(Fe,Si)_{13}$, with a suppressed volume change in the FM phase [31]. Here again, the thermal expansion can be tuned by varying the amount of Fe, and a near-zero thermal expansion was achieved for $LaFe_{13-2.4}Si_{2.4}$ [37].

In $LaFe_{13}$, the Fe^{I} is surrounded by an icosahedron cage of 12 Fe^{II} atoms. Their precise distance is changed by doping with Si, which affects the magnetic exchange interactions and structural properties. Mössbauer spectrometry is ideal to probe such local changes, and can give the magnetic entropy associated with the Fe atoms. Since spin-phonon coupling is important for the magnetocaloric effect, complementary information of the Fe vibrational spectrum through NRIXS could help complete the thermodynamic picture.

The knowledge of the individual contributions from phonons and spins are important for building thermodynamic models of thermophysical behavior, particularly in iron-containing materials with complex magnetic properties. We showed how the stability of nanocrystals and the Invar effect can be explained in terms of their underlying microscopic excitations. There is still a lot to be uncovered.

References

[1] M. Heine, O. Hellman, and D. Broido, Phys. Rev. Mater. **6**, 113805 (2022).

[2] A. Ehn, B. Alling, and I. A. Abrikosov, Phys. Rev. B **107**, 104422 (2023).

[3] M. van Schilfgaarde, I. A. Abrikosov, and B. Johansson, Nature **400** (1999).

[4] A. V. Ruban, Phys. Rev. B **95**, 174432 (2017).

[5] E. F. Wassermann and P. Entel, J. Phys. IV **5** (1995).

[6] I. A. Abrikosov, A. E. Kissavos, F. Liot, B. Alling, S. I. Simak, O. Peil, and A. V. Ruban, Phys. Rev. B **76**, 1 (2007).

[7] T. Miyazaki, Y. Ando, and M. Takahashi, J. Appl. Phys. **57**, 3456 (1985).

[8] K. Lagarec, D.G. Rancourt, S.K. Bose, B. Sanyal, and R.A. Dunlap, J. Magn. Magn. Mater. **236**, 107 (2001).

[9] E. F. Wasserman, in *Handbook of Ferromagnetic Materials*, Vol. 5 (Elsevier, 1990).

[10] M. Matsui and K. Adachi, Physica B Condens. **161**, 53 (1990).

[11] E. F. Wassermann and M. Acet, in *Magnetism and structure in functional materials* (Springer, 2005), pp. 177–197.

[12] T. Schneider, M. Acet, B. Rellinghaus, E. F. Wassermann, and W. Pepperhoff, Phys. Rev. B **51**, 8917 (1995).

[13] W. Pepperhoff and M. Acet, *Constitution of Iron and its Alloys* (Springer, 2001).

[14] A. Firlus, M. Stoica, S. Michalik, R. E. Schäublin, and J. F. Löffler, Nat. Commun. **13**, 1 (2022).

[15] J. Chen, K. Nittala, J. S. Forrester, J. L. Jones, J. Deng, R. Yu, and X. Xing, J. Am. Chem. Soc. **133**, 11114 (2011).

[16] Y. W. Long, N. Hayashi, T. Saito, M. Azuma, S. Muranaka, and Y. Shimakawa, Nature **458**, 60 (2009).

[17] M. Azuma, W. T. Chen, H. Seki, M. Czapski, S. Olga, K. Oka, M. Mizumaki, T. Watanuki, N. Ishimatsu, N. Kawamura, S. Ishiwata, M. G. Tucker, Y. Shimakawa, and J. P. Attfield, Nat. Commun. **2**, 1 (2011).

[18] I. Yamada, S. Marukawa, N. Hayashi, M. Matsushita, and T. Irifune, Appl. Phys. Lett. **106** (2015).

[19] A. S. Wolf, J. M. Jackson, P. Dera, and V. B. Prakapenka, J. Geophys. Res. **120**, 7460 (2015).

[20] J. Chen, X. R. Xing, G. R. Liu, J. H. Li, and Y. T. Liu, Appl. Phys. Lett. **89**, 87 (2006).

[21] G. Catalan and J. F. Scott, Adv. Mater. **21**, 2463 (2009).

[22] D. Carranza-Celis, A. Cardona-Rodríguez, J. Narváez, O. Moscoso-Londono, D. Muraca, M. Knobel, N. Ornelas-Soto, A. Reiber, and J. G. Ramírez, Sci. Rep. **9**, 1 (2019).

[23] J. Wang, J. B. Neaton, H. Zheng, V. Nagarajan, S. B. Ogale, B. Liu, D. Viehland, V. Vaithyanathan, D. G. Schlom, U. V. Waghmare, N. A. Spaldin, K. M. Rabe, M. Wuttig, and R. Ramesh, Science **299**, 1719 (2003).

[24] H. Hsu, K. Umemoto, P. Blaha, and R. M. Wentzcovitch, Earth Planet. Sci. Lett. **294**, 19 (2010).

[25] J. Chen, L. Fan, Y. Ren, Z. Pan, J. Deng, R. Yu, and X. Xing, Phys. Rev. Lett. **110**, 1 (2013).

[26] Y. Tokiwa, S. Bachus, K. Kavita, A. Jesche, A. A. Tsirlin, and P. Gegenwart, Commun. Mater. **2**, 1 (2021).

[27] K. A. Gschneidner and V. K. Pecharsky, Int. J. Refrig. **31**, 945 (2008).

[28] M. F. Boeije, P. Roy, F. Guillou, H. Yibole, X. F. Miao, L. Caron, D. Banerjee, N. H. Van Dijk, R. A. De Groot, and E. Brück, Chem. Mater. **28**, 4901 (2016).

[29] F. Scheibel, T. Gottschall, A. Taubel, M. Fries, K. P. Skokov, A. Terwey, W. Keune, K. Ollefs, H. Wende, M. Farle, M. Acet, O. Gutfleisch, and M. E. Gruner, Energy Technol. **6**, 1397 (2018).

[30] V. K. Pecharsky and K. A. Gschneidner, Phys. Rev. Lett. **78**, 4494 (1997).

[31] M. E. Gruner, W. Keune, J. Landers, S. Salamon, M. Krautz, J. Zhao, M. Y. Hu, T. Toellner, E. E. Alp, O. Gutfleisch, and H. Wende, Phys. Status Solidi B **255** (2018).

[32] F. Zhang, C. Taake, B. Huang, X. You, H. Ojiyed, Q. Shen, I. Dugulan, L. Caron, N. van Dijk, and E. Brück, Acta Mater. **224**, 117532 (2022).

[33] M. Wolloch, M. E. Gruner, W. Keune, P. Mohn, J. Redinger, F. Hofer, D. Suess, R. Podloucky, J. Landers, S. Salamon, F. Scheibel, D. Spoddig, R. Witte, B. Roldan Cuenya, O. Gutfleisch, M. Y. Hu, J. Zhao, T. Toellner, E. E. Alp, M. Siewert, P. Entel, R. Pentcheva, and H. Wende, Phys. Rev. B **94**, 1 (2016).

[34] Y. Liu, L. C. Phillips, R. Mattana, M. Bibes, A. Barthélémy, and B. Dkhil, Nat. Commun. **7**, 1 (2016).

[35] J. Cedervall, M. S. Andersson, E. K. Delczeg-Czirjak, D. Iuşan, M. Pereiro, P. Roy, T. Ericsson, L. Häggström, W. Lohstroh, H. Mutka, M. Sahlberg, P. Nordblad, and P. P. Deen, Phys. Rev. B **99**, 1 (2019).

[36] T. Krenke, E. Duman, M. Acet, E. F. Wassermann, X. Moya, L. Manosa, and A. Planes, Nat. Mater. **4**, 450 (2005).

[37] W. Wang, R. Huang, W. Li, J. Tan, Y. Zhao, S. Li, C. Huang, and L. Li, Phys. Chem. Chem. Phys. **17**, 2352 (2015).

Appendix A

Nanocrystalline Ni_3Fe - x-ray diffraction analysis

A.1 Lattice parameters

In principle, the lattice parameter, a_0, can be determined from the diffraction angles, θ, using Bragg's law:

$$2d \sin\theta = \lambda, \tag{A.1}$$

where d is the spacing between the diffracting planes and is related to the lattice parameter for each (hkl) diffraction peak through

$$d_{hkl} = \frac{a_0}{\sqrt{h^2 + k^2 + l^2}}. \tag{A.2}$$

In practice however, the accuracy of the lattice parameter calculated using Bragg's law may suffer due to experimental errors. These include misalignment caused by the sample positioning, or by irregularities of the sample surface, which lead to the center of diffraction not being at the center of the diffractometer's goniometer. Nelson and Riley proposed a correction based partially on empirical observations (see [1]). According to the Nelson-Riley method, the error in the lattice parameter, Δa_0, has the following angle dependence:

$$\frac{\Delta a_0}{a_0} \propto \frac{\cos^2\theta}{\sin\theta} + \frac{\cos^2\theta}{\theta}. \tag{A.3}$$

A.2 Grain growth

We observed the grain growth of the nanocrystalline material by annealing it to different temperatures. To avoid oxidation, the materials were sealed inside quartz tubes under vacuum to be heated. x-ray diffraction was collected for

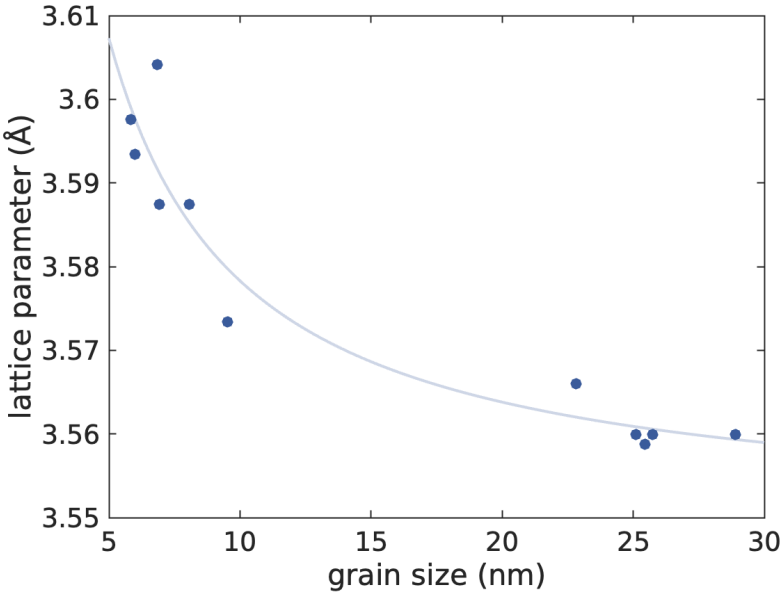

Figure A.1: Grain sizes vs. lattice parameters. The fitted curve shows an inverse grain size dependency of the lattice parameters in our Ni_3Fe samples.

all annealed samples and the results are shown in Fig. A.2. As the annealing temperature is increased, the diffraction peaks become narrower and sharper. This is indicative of increasing grain sizes (which are labeled in the figure).

The broadening of the peaks is dependent on the number of atomic planes, at a distance d from each other, are contributing to the diffraction. In a bulk material with large crystals, a large number of planes are diffracting, and constructive interference of the diffracted waves from each plane occurs only at very specific angles, given by Bragg's law (Eq. A.2). These result in sharp diffraction peaks. On the other hand, if only a few planes are diffracting at each nanocrystallite, partially-constructive wave interference can occur even for relatively large deviations of θ from the Bragg angles.

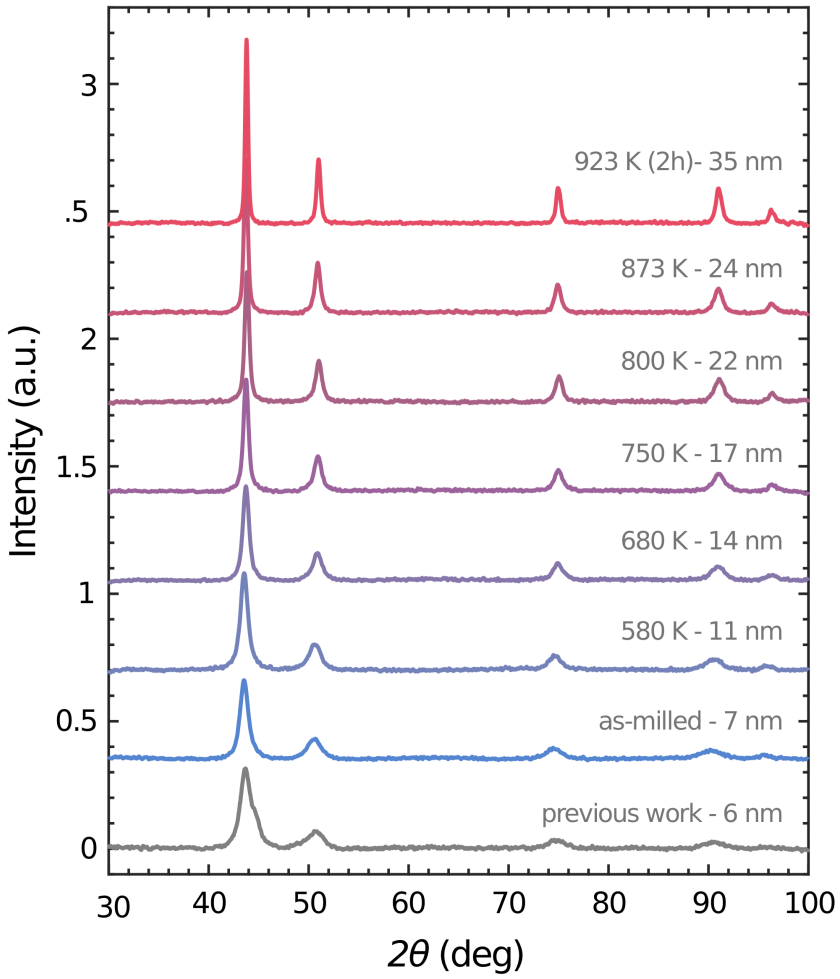

Figure A.2: X-ray diffraction patterns of the as-milled nanomaterial before and after annealing to different temperatures. The annealing temperatures and the calculated grain sizes are labeled.

Shape factor and grain size

To understand this effect, we explicitly write the equation for a scattered wave ψ as a function of the diffracted wavevector $\Delta\mathbf{k}$ as [1]:

$$\begin{aligned}\psi(\Delta\mathbf{k}) &= \mathcal{S}(\Delta\mathbf{k})\mathcal{F}(\Delta\mathbf{k}) \\ &= \sum_{\mathbf{r}_g}^{lattice} \mathcal{F}(\Delta\mathbf{k})e^{-i2\pi\Delta\mathbf{k}\cdot\mathbf{r}_g},\end{aligned} \tag{A.4}$$

where the sum is over all the unit cells at positions $\mathbf{r}_g$ in the lattice. The structure factor $\mathcal{F}(\Delta\mathbf{k})$ gives the position of the atoms within each unit cell and hence the type of crystal structure. In the case of Ni_3Fe, the crystal takes on a fcc structure, and $\mathcal{F}(\Delta\mathbf{k})$ gives the allowed diffraction angles for such a

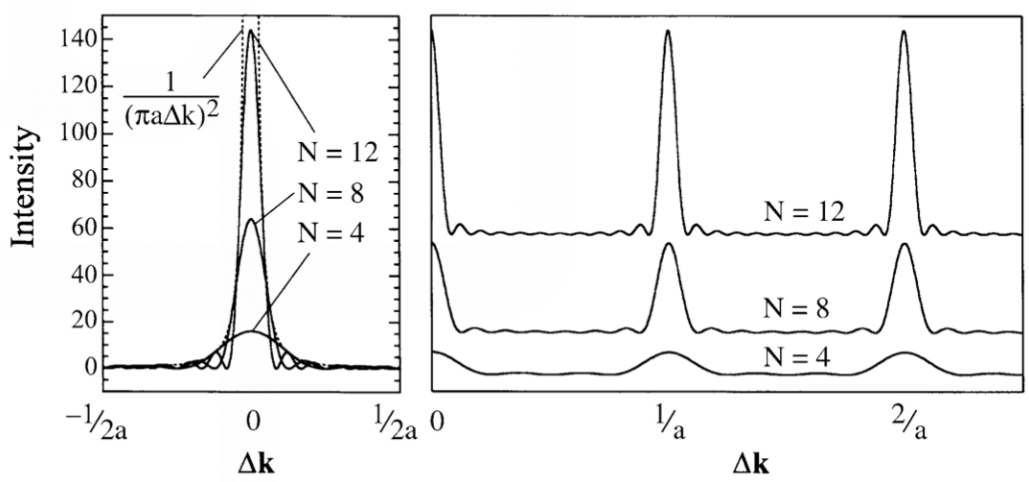

Figure A.3: Effect of the number of diffracting planes, N, on the width of diffraction peaks [1].

structure, resulting in the 2θ diffraction angles seen in Fig. A.2. The shape factor, $\mathcal{S}(\Delta\mathbf{k})$, does not affect the diffraction angles, but gives the number of unit cells (or planes) that contribute to the diffraction. It therefore describes the overall shape and size of the crystal, and the resulting broadening of the diffraction peaks. The diffracted intensities, as those plotted in a diffraction pattern of Fig. A.2, are given by

$$I(\Delta\mathbf{k}) = \psi(\Delta\mathbf{k})^*\psi(\Delta\mathbf{k}). \tag{A.5}$$

If we assume a cubic lattice (as in a FCC crystal), the shape factor can be expanded in a geometric series and simplified. For the x direction (and equivalently in y and z) it contributes to the intensities as

$$\mathcal{S}(\Delta k_x)^*\mathcal{S}(\Delta k_x) = \frac{\sin^2(\pi\Delta k_x a_x N_x)}{\sin^2(\pi\Delta k_x a_x)} \approx \frac{\sin^2(\pi\Delta k_x a_x N_x)}{(\pi\Delta k_x a_x)^2}. \tag{A.6}$$

The resulting effect of the number of diffracting planes, N, on the shape factor and consequently on the shape of the diffraction peaks is illustrated in Fig. A.3.

Grain size and strain broadening

Equation A.6 can be modified and simplified to a more appropriate form for analysing experimental data [1]. The resulting Scherrer equation

$$\beta_L = \frac{K\lambda}{L\cos\theta}, \tag{A.7}$$

explicitly relates the full width half maximum (FWHM), β_L, of the diffraction peaks to a mean grain size, L ($= aN$). The constant λ is the wavelength of the radiation used for the diffraction experiment, and K is a constant that depends on the specific crystal shape (for a flat crystallite with constant thickness it is equal to 0.89, for example).

The size of the grains is not the only cause of broadening, however. Strains can also broaden the diffraction peaks, and are definitely present in ball-milled samples that were severely plastically deformed. Fortunately, these have different θ angle dependencies and can therefore be separated. Following the Williamson-Hall method [2] and assuming Lorentzian profiles, the broadening due to small grain sizes (β_L) and due to strains (β_ε) add linearly [1]:

$$\begin{aligned} \beta_{\text{tot}} &= \beta_L + \beta_\varepsilon \\ &= \frac{K\lambda}{L\cos\theta} + 4\varepsilon\tan\theta\,. \end{aligned}$$

Multiplying both sides by $\cos\theta$ gives the Williamson-Hall equation:

$$\beta_{\text{tot}}\cos\theta = \frac{K\lambda}{L} + 4\varepsilon\sin\theta\,, \tag{A.8}$$

where ε represents an an isotropic strain field within the sample. Our samples do not have such an isotropic behavior, so we modified the Williamson-Hall method to include elastic anisotropy. Using the Young's moduli measured along different directions in a Ni_3Fe single crystal [3], we rewrite the strain as $\varepsilon_{hkl} = \sigma/E_{hkl}$. Assuming an isotropic stress field, σ, the Williamson-Hall equation becomes

$$\beta_{\text{tot}}\cos\theta = \frac{K\lambda}{L} + \frac{4\sigma}{E_{hkl}}\sin\theta\,. \tag{A.9}$$

By plotting $\beta_{\text{tot}}\cos\theta$ vs. $4\sin\theta/E_{hkl}$ a linear dependency can be seen, where the slope corresponds to the contribution from stress (or strains) and the vertical offset represents the grain size broadening.

Fig. A.4 shows the Williamson-Hall plot of our samples, as-milled and annealed, together with linear fits. The colors match those from from Fig. A.2 and the gray lines are measurements on additional samples as comparison. As expected, the nanocrystalline as-milled samples show larger grain size broadening (larger vertical offset) and also larger slopes due to strains compared to the annealed samples. While the as-milled samples show a distribution of grain sizes and strains, the bulk control samples are very similar to each other.

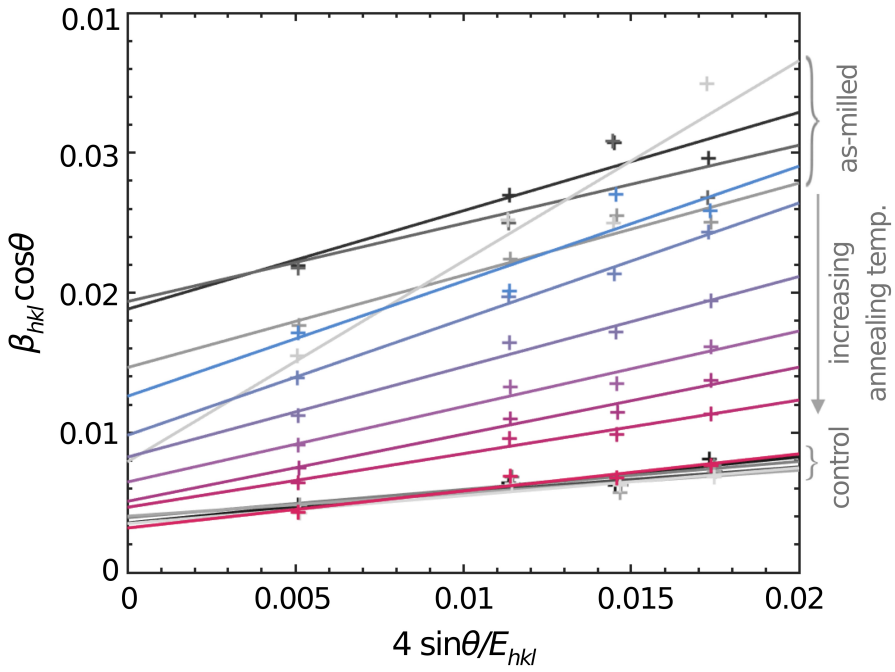

Figure A.4: Williamson-Hall plot of the XRD data (+) and linear fits to the data (solid lines). Colored lines represent samples annealed at increasing temperatures (see Fig. A.2), from as-milled nanocrystalline samples (blue) to bulk control samples (red). Gray lines correspond additional as-milled and bulk samples as comparison.

Absolute values of the grain sizes were determined by comparing the broadening of our samples with those from previous work with crystallites of 6 nm [4] using the Scherrer Equation. The resulting grain sizes and RMS strains are shown in Fig. A.5 as a function of the annealing temperature. The resulting RMS strain of the as-milled nanocrystalline sample is 0.77%, very similar to the 0.75% strain reported in [5].

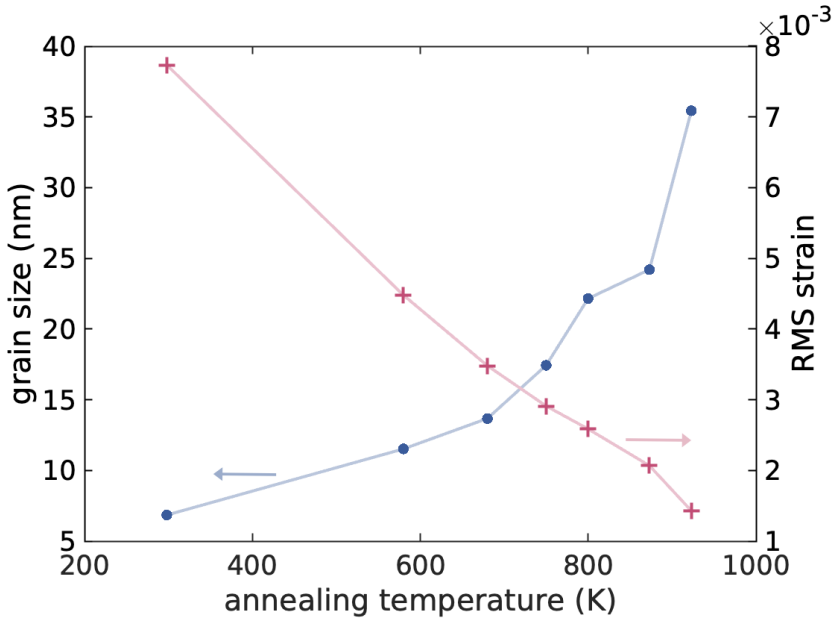

Figure A.5: Grain sizes (•) and RMS strains (+) as functions of the annealing temperature, determined by the anisotropic Williamson-Hall method.

Appendix B

Thermodynamic origin of the Invar effect

Sample and DAC preparation

The $^{57}Fe_{65}Ni_{35}$ Invar materials (in atomic %) were prepared by arc-melting iron and high-purity nickel (99.99 %). Arc-melting was performed under an argon atmosphere with a titanium getter to avoid oxidation of the samples. The experimental techniques used, NRIXS and NFS, are only sensitive to the ^{57}Fe isotope of iron, which has a natural abundance of 2.2 %. To enhance the measured signal, the alloys were prepared with ^{57}Fe enriched by 95.73 % (from Isoflex).

The arc-melted ingots were then rolled to thin foils of material, as required by the experimental techniques. For x-rays of 14.41 keV (energy used for NRIXS and NFS) the attenuation length is about 20 μm for Fe and 15 μm for Ni. This is the depth at which the x-ray intensity falls to $1/e$, still strong enough to be detected. An intensity of $\sim 1/e$ also implies that enough energy was absorbed by the sample to excite the inelastic spectrum of phonons. The attenuation length therefore represents a good sample thickness for NRIXS experiments.

To achieve samples thicknesses between 10-20 μm, the material had to be rolled in a rolling mill several times. Rolling, however, introduces internal stresses, which stiffen the material and impede further thickness reduction. To reduce the thickness further, the stresses need to be released through a heat treatment. Samples were annealed at 600°C for a few hours inside vacuum-sealed quartz tubes (to avoid oxidation). This process of rolling and annealing was repeated until the desired sample thickness was achieved. A final annealing for about 15 h after is important, so that the experiments are performed on relaxed samples. It also reduces texturing of diffraction patterns, which occurs when crystals within the sample have a preferred orientation.

NRIXS data anaylisys

To acquire an NRIXS spectra, we scan the energy of the incoming x-ray beam to excite the phonons. An average of 6 scans were performed from −60 to 80 meV, with 561 points and 3 s acquisition time per point. A larger number of scan is typically needed as the pressure is increased. The raw NRIXS data, with the added counts for all scans, is shown in Fig. B.1. The error bars correspond to the standard deviation between the different scans. The data at 21.3 GPa was collected at the last remaining hours of a beamtime (4 scans), so the statistical quality is impaired.

Due to the resonant nature of the NRIXS technique, there is no background signal (except for a constant background from detector noise). This results in very low intensities at low and high energies. The weak signal seen at energies beyond ±40 meV stem mostly from multi-phonon contributions, where an incoming x-ray excites more than one phonon.

The process of computing the phonon DOS from the NRIXS spectrum is explained in Chapter 2. First, we remove the elastic peak by fitting the resolution function of the instrument to the NRIXS signal. Then, a constant background from detector noise is subtracted from the signal. We define a cutoff energy and integrate the resulting DOS above the cutoff. A background that minimizes the integral above the cutoff is chosen through an automated iterative process. We then use the PHOENIX software [6, 7] to separate the one-phonon from the multi-phonon contributions. These are shown in Fig. B.2.

The error bars of the computed phonon DOS (shown in Fig. 5.17) were propagated from the standard deviation of sequential NRIXS scans. PHOENIX defines, by default, an error for the NRIXS data that follows a Gaussian distribution with an uncertainty of $\sqrt{N}$, where N is the number of counts. It propagates this error into the computed phonon DOS and entropy. We find that this Gaussian error underestimated the errors calculated by the standard deviation of our NRIXS scans. Moreover, PHOENIX does not allow us to define a cutoff energy for the entropy calculation. We therefore propagated the standard deviation errors of the NRIXS scans to the phonon DOS and the entropy by a Monte-Carlo method.

For calculating the entropy with Eq. 1.14, we need to truncate the energy integral and define a cutoff energy. We could integrate the entire measured

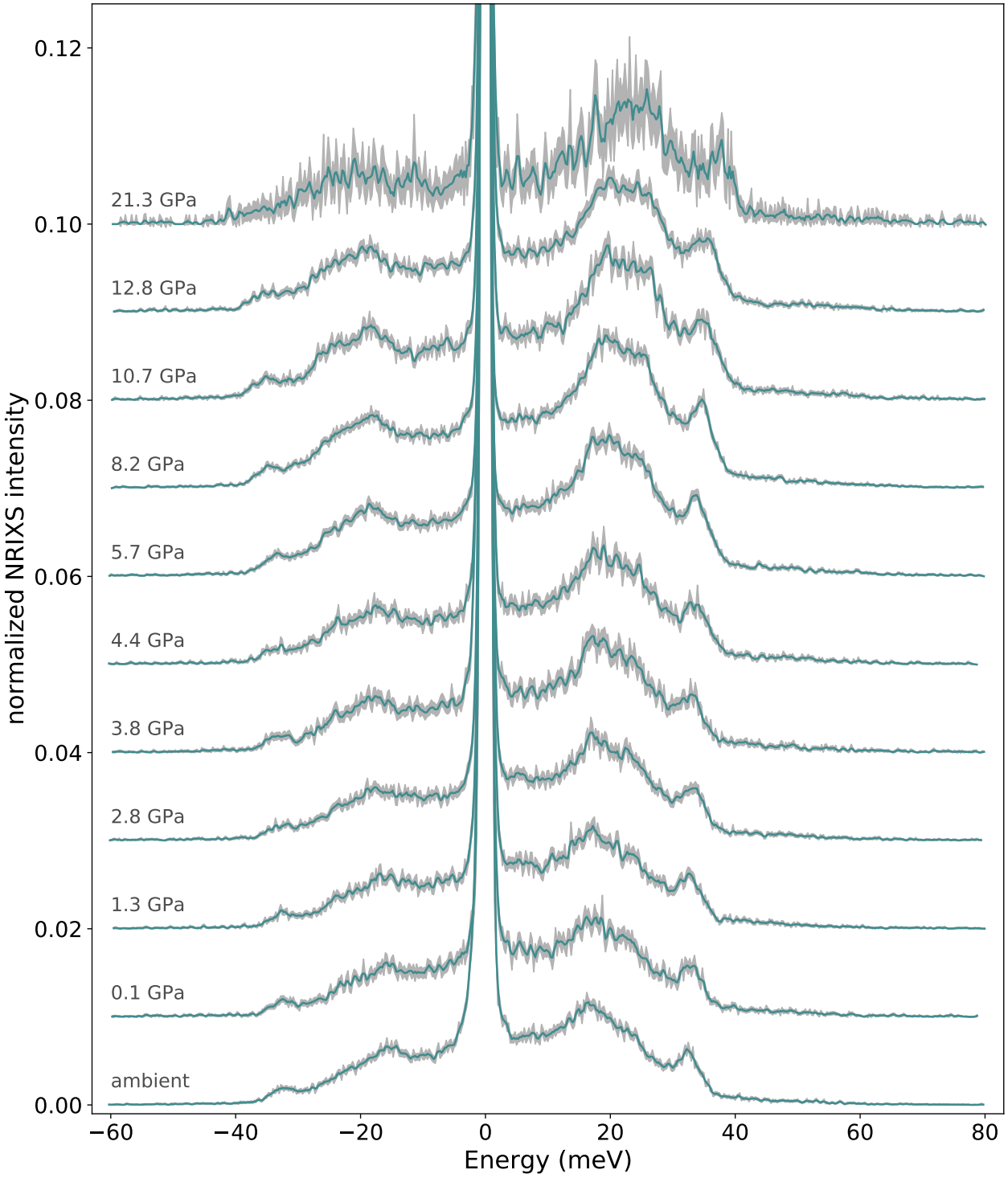

Figure B.1: Raw NRIXS spectra of $^{57}Fe_{65}Ni_{35}$, showing the inelastic spectrum of phonons in Invar. The data were collected at beamline 3 ID-D of the APS with samples inside diamond-anvil cells. The strong elastic peak at $E = 0$ is about two orders-of-magnitude larger than the inelastic signal.

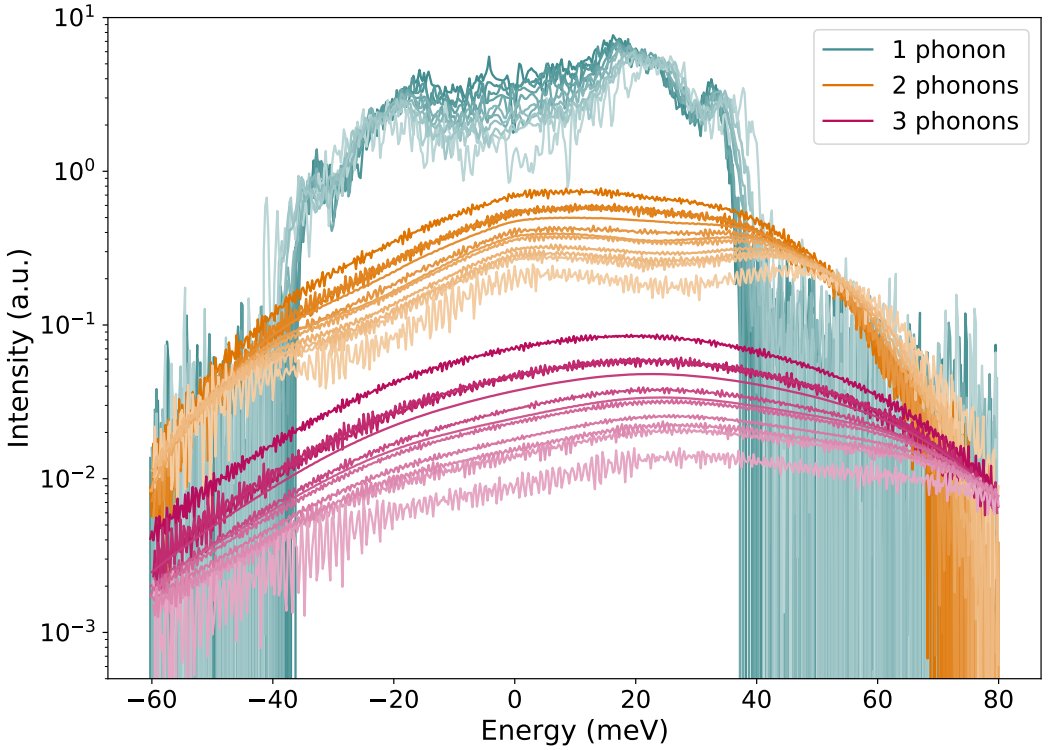

Figure B.2: Contributions from one-phonon and multi-phonon scattering events to inelastic spectrum of $^{57}Fe_{65}Ni_{35}$. Lighter tints correspond to higher pressures. The one-phonon contribution (with removed elastic peak) has a clear cutoff at about 40 meV. Multi-phonon contributions, where an x-ray excites more than one phonon, become more prominent at higher energies.

DOS (up to 80 meV), however the spectrum at high energy contains only noise without phonon information. The distribution of phonon occupancy is not flat with energy; it is much larger at low energies due to the bosonic nature of phonons. When computing the entropy, we calculate a weighted integral of the DOS with the phonon occupancy factor, and even a zero-mean noise can have a non-zero contribution. To choose a cutoff energy consistently for all pressures, we defined a cutoff at 10 meV above the energy of the longitudinal mode. The positions of this mode were found by fitting the DOS to three asymmetric Lorentzians (see Fig. 5.18). This same cutoff was used for determining the constant background discussed above. Other cutoff criteria were tested, but they all gave similar results. Some shifted the entire phonon entropy by a little amount, in the order of 0.01 kB/atoms at most (less than the error bars reported in Fig. 5.19). For determining the thermal expansion and the Invar effect we need to compute accurate entropy shifts. This requires a precise entropy and not necessarily highly accurate absolute values.

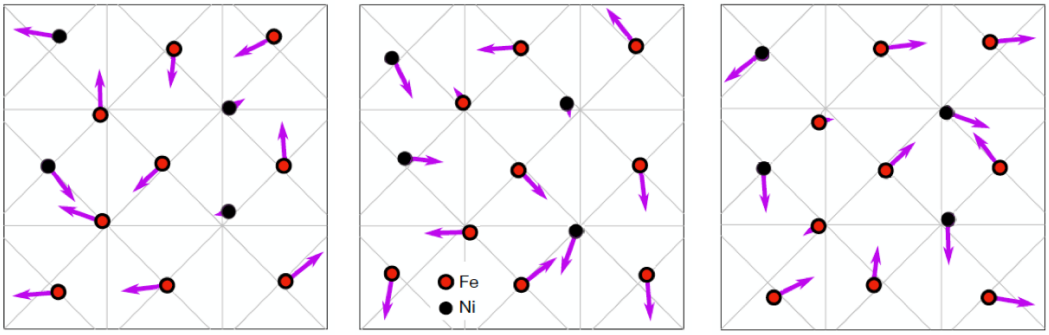

Figure B.3: Examples of snapshots used in the TDEP calculations at 300 K. These include chemical disorder of the Fe and Ni atoms, temperature and pressure induced vibrational disorder (displacements of nuclei in the supercell) and magnetic disorder (randomness of the non-collinear spins).

Measurement guided *ab initio* calculations

The calculations described here were performed by Matthew Heine[1] under the supervision of David Broido[1] and Olle Hellman[2]. The methods are described in more depth in [8, 9].

As reviewed in section 5.3, Invar has a complex magnetic phase, with multiple sates close by in energy that compete with each other. As a result, there is still no fully accepted theory to describe magnetism in Invar systems. To circumvent this problem, no specific physical mechanism for the magnetic interactions is assumed. A hybrid approach is adopted that integrates the measured magnetization data into the calculations, and computes the phonons from first principles.

The calculations were performed at room temperature within the framework of the Temperature Dependent Effective Potential (TDEP) approach [9–11]. This method incorporates the renormalization of phonon modes by chemical disorder (i.e., alloys), temperature and pressure-induced vibrational and magnetic disorder, spin-lattice coupling, and local environment effects. Fully non-collinear magnetism with spin-orbit coupling was included. Magnetism adds several new coordinates to the phonon calculations in TDEP. They become therefore expensive requiring large computing power.

[1]Dept. of Physics, Boston College, Chestnut Hill, MA 02467, USA
[2]Dept. of Molecular Chemistry and Materials Science, Weizmann Institute of Science, Rehovoth 76100, Israel

In short, several snapshots atomic configurations are generated for each pressure/volume as exemplified in Fig. B.3. The atomic displacements from their equilibria is consistent with the thermal disorder of phonons. Only snapshots with spin configurations that are consistent with the measured magnetization at that volume are used. This ensures that all snapshots represent thermodynamically relevant microstates, without relying on a specific magnetic model. The macrostate of the material is then computed by the an ensemble average of those. For each snapshot, *ab initio* calculations of the forces on the atoms are performed using DFT (VASP). Phonon modes can be computed from the interatomic force constants (IFCs) by diagonalizing the dynamical matrix. These phonon modes are then used to generate a new set of snapshots, and the procedure is repeated until self-consistency is achieved. Spin-lattice effects are captured implicitly in the effective IFCs, since these are fitted to reproduce all effects present in the DFT calculations.

Calculations were very important to study the effects of magnetism on the lattice vibrations. By artificially fixing the spin orientations and magnitudes, for example, we were able study how the lattice would behave without magnetic effects. It gave us direct evidence of a spin-lattice coupling in $Fe_{65}Ni_{35}$, which is at the core of the Invar effect.

Appendix C

Invar effect at low temperatures

In addition to the room temperature analysis of Chapter 5, we also conducted experiments on $^{57}Fe_{65}Ni_{35}$ Invar at 30 K with samples inside a mini-panoramic DAC that can be cooled (see Chapter 2 for methods). The Curie transition happens at higher pressures at 30 K, allowing us to study whether the Invar region of near-zero thermal expansion is also extended in pressure.

The phonon density of states (DOS) computed from the NRIXS spectra are shown in Fig. C.1 a. The count rate of cryogenic experiments is lower than those at room temperature. Only two detectors (instead of three) can be used due to the geometric constraints of the cryogenic setup. The DAC also has to be insulated inside a shroud, with windows that attenuate the signal. This results in noisier data with larger error bars than at room temperature.

At 30 K, phonons are mostly excited at very low energies below 3 meV. The Planck distribution describing the phonon occupancy is accordingly only large at low energies as shown in Fig. 1.5. When calculating the phonon entropy, the DOS is weighted by the Planck distribution in Eq. 1.14, so the low energy region of the DOS is crucial to compute the entropy at 30 K. The subtraction of the elastic peak of the NRIXS spectrum, which extends to about 4 meV (see Fig. B.1), becomes the critical step in the data analysis. We therefore, subtracted the elastic peaks with two alternative methods: (1) by fitting the resolution function of the instrument to the elastic line using the PHOENIX software [6, 7], and (2) by choosing an energy range to replace the elastic peak by an interpolated baseline function using the SciPhon software packed [12]. SciPhon gives slightly smoother phonon DOS below 7 meV. The phonon entropies calculated with both methods are consistent, with nearly the same pressure dependence, with SciPhon resulting in entropies that are offset by

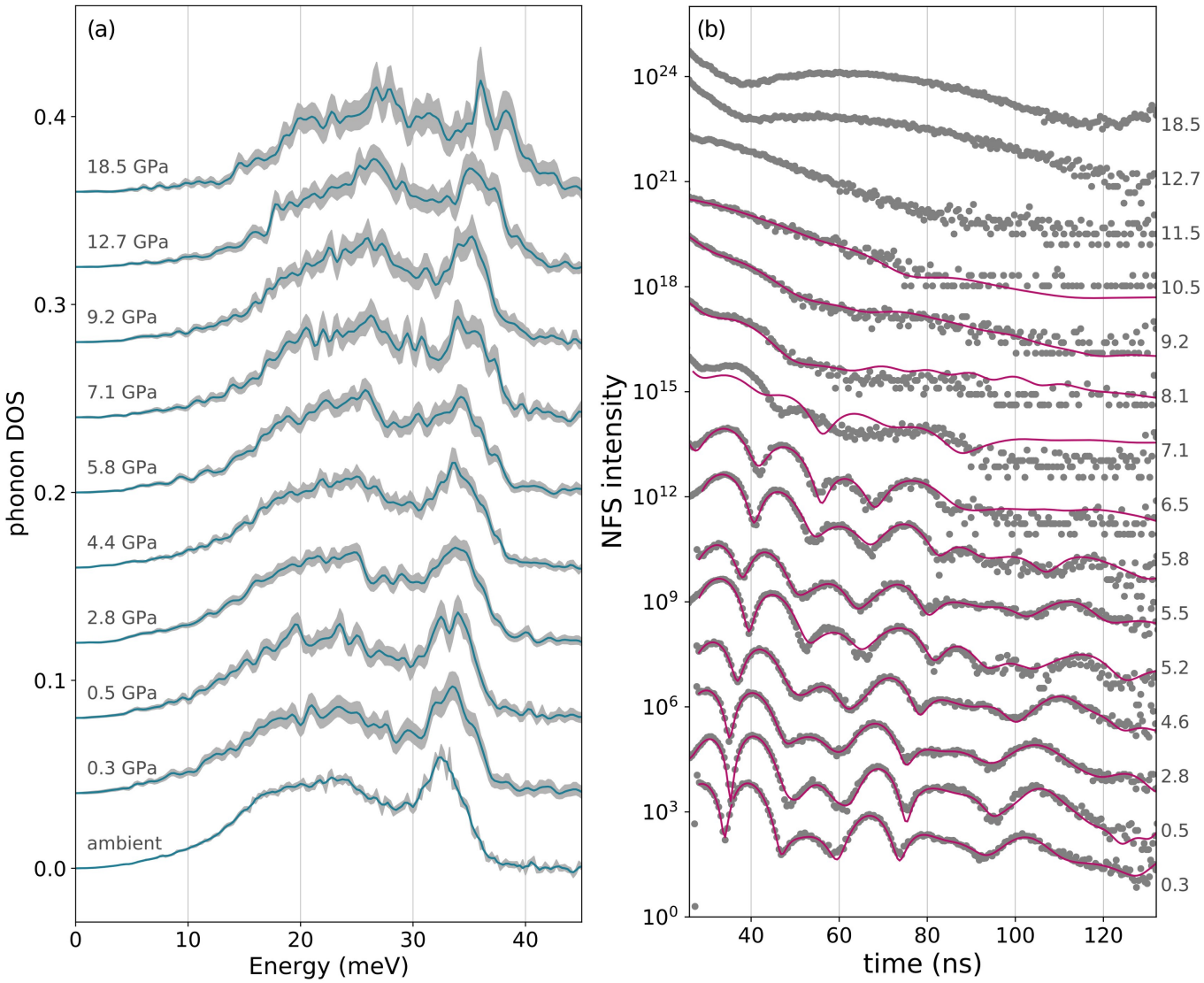

Figure C.1: Nuclear resonant measurements on Invar at 30 K. **(a)** Partial phonon DOS of ^{57}Fe at increasing pressures computed from NRIXS measurements using the PHOENIX software package. **(b)** Time interference of nuclear states due to magnetic splitting measured by NFS. The intensity modulations disappear around 11 GPa corresponding to the Curie transition.

about 0.01 k_B/atom with respect to the PHOENIX analysis. For studying the thermal expansion and the Invar effect, only the pressure dependence matters, so for consistency with the data set at room temperature, we present the data analysis using PHOENIX. The resulting entropy as a function of pressure is shown in Fig. C.2 b. The change in phonon entropy between 0.3 and 7.1 GPa is approximately 0.08 k_B/atom, about half of the entropy change in the Invar region at room temperature.

To complement the phonon analysis we also measured the magnetic state of the material through synchrotron Mössbauer experiments. The intensity modulations of the time-domain Mössbauer spectra of Invar at 30 K are presented in Fig. C.1 b. The magnetic beat patterns extend to approximately 10 GPa. Above 11.5 GPa the material is paramagnetic. Fits of the Mössbauer spectra using the CONUSS software package [6, 7] are shown as solid lines in Fig. C.1 b. These fits allow us to compute the distribution of the hyperfine magnetic field (HMF) around the ^{57}Fe nuclei. The mean of these distributions, proportional to the magnetization of the iron atoms, are shown in Fig. C.2 a. A mean-field model fit gives Curie transition at approximately 11 GPa. The fits of the HMF of Fig. C.1 b can be further optimized, especially those at 7.1 and 8.1 GPa, but this would not have a significant effect on the mean of the HMF distributions of Fig. C.2 a.

The magnetic entropy was computed from the normalized hyperfine magnetic fields of Fig. C.2 a using Eq. 5.4. As for the analysis at room temperature, we calibrate the total magnetic entropy at the Curie transition by heat capacity measurements. We extrapolated the heat capacity of Fig. 5.11 to 0 K giving a total entropy change of 0.15 k_B/atom between 0 K and the Curie transition. The resulting magnetic entropy as a function of pressure is shown in Fig. C.2 b. It opposes the decreasing phonon entropy with pressure.

The sum of both contributions from phonons and spins gives a nearly unchanging entropy up to approximately 7 GPa (black curve in Fig. C.2 b). Electrons should have only a small contribution to the entropy, as is the case at room temperature. The nearly unchanging total entropy below 7 GPa should result in a near-zero thermal expansion by Eq. 5.1, i.e. the Invar effect. Curiously, in contrast to the analysis at room temperature, the entropy increases above the region of Invar behavior. This is due to the increase of the magnetic entropy up to the Curie transition, which overcomes the decrease of the phonon entropy. Above the Curie transition, the behavior is dominated by phonons and the total entropy decreases accordingly.

The data analysis presented here is preliminary and requires further refinement. In particular, the phonon entropy is very sensitive to the noise in the data at low energies as discussed above. Additional x-ray diffraction experiments that can explicitly measure the thermal expansion would be helpful for the analysis of the Invar behavior at 30 K. However, our analysis of the entropy

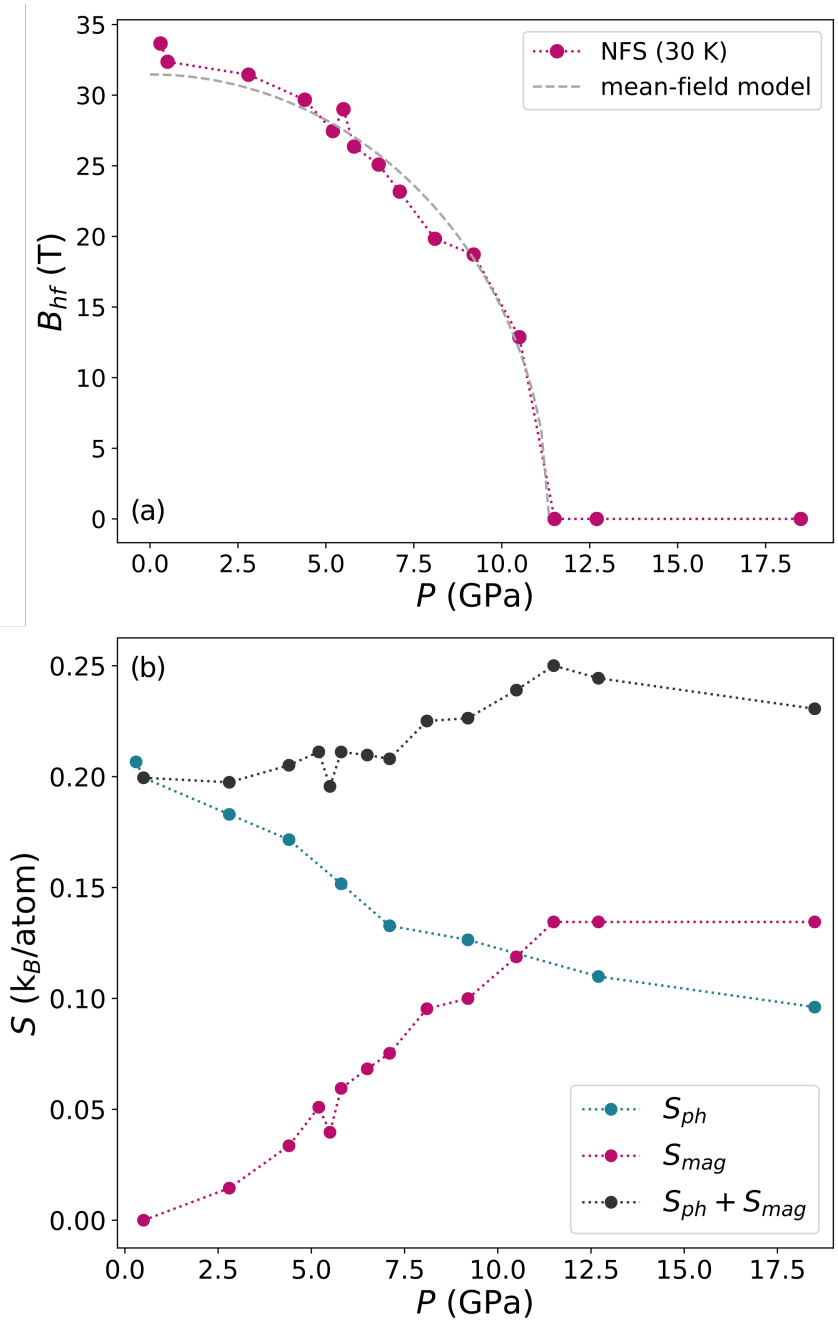

Figure C.2: Magnetism and entropies of Invar at 30 K **(a)** Mean hyperfine magnetic field, B_{hf}, obtained by fitting the data of Fig. C.1 b. **(b)** Phonon entropy, S_{ph}, computed from the phonon DOS of Fig. C.1 a, compared to magnetic entropy, S_{mag}, calculated from the normalized hyperfine magnetic field of panel a and calibrated by heat capacity measurements. The sum of both entropies remains mostly unchanged up to about 7 GPa, the region where the Invar effect is expected to be observed.

contributions from phonons and spin 30 K is consistent with the analysis of Invar behavior at room temperature. It seems like the Invar effect in $Fe_{65}Ni_{35}$ is extended up to 7 GPa at these low temperatures.

References

[1] B. Fultz and J. M. Howe, *Transmission Electron Microscopy and Diffractometry of Materials* (Springer, 2013).

[2] H. Klug and L. E. Alexander, *X-Ray Diffraction Procedures* (Wiley, 1974).

[3] P. Turchi, Y. Calvayrac, and F. Plicque, Phys. Status Solidi A **45**, 229 (1978).

[4] H. Frase, B. Fultz, and J. L. Robertson, Phys. Rev. B **57**, 898 (1998).

[5] C. Chinnasamy, A. Narayanasamy, K. Chattopadhyay, and N. Ponpandian, Nanostruct. Mater. **12**, 951 (1999).

[6] W. Sturhahn, Hyperfine Interact. **125**, 149 (2000).

[7] W. Sturhahn, NRIXS Scientific Software (website).

[8] M. Heine, O. Hellman, and D. Broido, Phys. Rev. Mater. **6**, 113805 (2022).

[9] M. Heine, O. Hellman, and D. Broido, Phys. Rev. B **100**, 104304 (2019).

[10] O. Hellman, I. A. Abrikosov, and S. I. Simak, Phys. Rev. B **84** (2011).

[11] O. Hellman and I. A. Abrikosov, Phys. Rev. B **88**, 144301 (2013).

[12] N. Dauphas, M. Y. Hu, E. M. Baker, J. Hu, F. L. H. Tissot, E. E. Alp, M. Roskosz, J. Zhao, W. Bi, J. Liu, J.-F. Lin, N. X. Nie, and A. Heard, J. Synchrotron Radiat. **25**, 1581 (2018).